Flavor decomposition of the nucleon spin at HERMES

Maria Chiara Simani

VRIJE UNIVERSITEIT

Flavor decomposition of the nucleon spin

at HERMES

ACADEMISCH PROEFSCHRIFT

ter verkrijging van de graad van doctor aan
de Vrije Universiteit te Amsterdam,
op gezag van de rector magnificus
prof.dr. T. Sminia,
in het openbaar te verdedingen
ten overstaan van de promotiecommissie
van faculteit der Exacte Wetenschappen
op maandag 7 october 2002 om 15:45 uur
in de aula van de universiteit,
De Boelelaan 1105

door

Maria Chiara Simani

geboren te Ferrara, Italië

promotor: prof.dr.ing. J.F.J. van den Brand

The work described in this thesis is part of the research program of the "Stichting voor Fundamenteel Onderzoek der Materie (FOM)", which is financially supported by the "Nederlandse Organisatie voor Wetenschappelijk Onderzoek (NWO)".

Contents

1 Introduction

Studies of nucleon spectra performed throughout the 1950s showed the existence of many possible excited states for the proton and neutron which appeared as resonances in photon-nucleon scattering and in pion-nucleon scattering [1]. In addition, the proliferation of new particle states discovered during the 1950s and the 1960s pointed the way to a possible substructure of hadrons in terms of more fundamental objects.
A model proposed by Gell-Mann [2] and Zweig [3] described the hadron as a composite system of only three kinds of particles which Gell-Mann called "quarks" (u, d and s) and of their corresponding antiparticles. Static properties of the observed hadronic structure could be derived from the flavor, spin and charge of these quarks. Gell-Mann called this classification "The Eightfold Way", since octets of nucleons and mesons naturally appeared. The nucleons were found to belong to a supermultiplet of eight particles, $i.e.$ an octet. For the mesons an octet was proposed where the π- and K-mesons filled seven places.
This idea was experimentally verified in the late 1960s at the Stanford Linear Accelerator Center (SLAC) in the first deep-inelastic scattering experiments led by Friedman, Kendall and Taylor. Reminiscent of the experience of Rutherford in 1911, they investigated the internal structure of the proton by scattering high-energy electrons from a target of liquid hydrogen. From the analysis of the scattering angles and energies of the electrons after the collision, it was observed that when the process was inelastic and the protons were struck with sufficient energy to produce new particles, such as pions, the electrons were deflected through much wider angles than expected. A possible explanation for the SLAC results was proposed in 1968 by Feynmann, who suggested the existence of point-like particles within the proton: the "partons". In the deep-inelastic energy regime, the weak dependence of the scattering cross-section on the momentum transfer was interpreted as evidence for the existence of the partons. This dependence defines the so-called scaling behaviour already predicted earlier by Bjorken [4]. From such charged objects, electrons could be elastically scattered through large angles. Furthermore, it followed that the partons must have spin-$\frac{1}{2}$.
The quark and parton interpretations of the nucleus were subsequently merged together in the Quark-Parton Model. Within this framework, the process of electron-proton scattering could be expressed in terms of two structure functions, F_1 and F_2, which behave in accordance with Bjorken scaling. The identification of partons with quarks led to the expectation that the integral of the structure function F_2 over the fractional momentum carried by the constituent quarks would result in unity. In 1972, measurements of the structure function F_2 of the nucleon revealed that the quarks only contribute for about

50% to the total momentum of the nucleon. The remaining momentum was later associated with new constituent partons: the spin-1 gluons.
From the theoretical developments of new non-Abelian gauge field theories, Quantum Chromodynamics (QCD) was established as the more suitable candidate to explain the interaction of quarks and gluons in terms of a strong force between color-charged particles. The idea of "color" was already postulated as an extra degree of freedom to resolve the violation of the Pauli principle in the formation of the Δ^{++} out of three u quarks with the same symmetry in spin and angular momentum. The extension of the global color model to QCD (see *e.g.* Ref. [5]) could naturally describe the binding forces between quarks within hadrons.
The distinctive feature of QCD is that the coupling of the strong force is predicted to become weaker at small distances (asymptotic freedom). This behavior is consistent with the experimental observations in deep-inelastic lepton-nucleon scattering in which the constituent quarks behaved almost as free particles at high momentum transfer. At large distances, the coupling would become progressively stronger and could presumably lead to color confinement.
In the asymptotic limit, *i.e.* when the strong coupling constant is small, QCD can be approached perturbatively and quantitative predictions can be formulated. In particular, a violation of Bjorken scaling of the structure functions is accurately predicted within QCD. It arises from the interaction between quarks by exchange of gluons. The momentum distributions of valence and sea quarks within the nucleon have been determined to a certain level of accuracy, and provide further evidence for the important role of gluonic degrees of freedom.
However, the intuitive picture of the QPM can be regarded as the zeroth order approximation of perturbative QCD.

The existence of a rich internal structure of the nucleon challenged physicists during the past few decades with the task of explaining the origin of the spin of the nucleon in terms of its constituents. The total spin of the nucleon can be decomposed as

$$\frac{1}{2} = \frac{1}{2}\Delta\Sigma + \Delta g + L_z \, , \tag{1.1}$$

where $\Delta\Sigma$ and Δg are the net spin contributions from the quarks and the gluons, respectively, and L_z is the contribution from the orbital angular momentum of the partons. Since quarks carry an intrinsic spin of $\frac{1}{2}$, it is possible to naively assume that only the three valence quarks carry the nucleon spin, while the sea quarks and gluons are supposed to be unpolarized and thus do not contribute.
Since the first SLAC-MIT experiments, the DIS process with charged lepton beams has been widely used to probe the structure of the nucleon and to enhance our understanding of QCD. With the technological development of polarized beams and targets the spin structure of the nucleon became accessible. The nucleon spin composition can be probed by studying the dependence of the cross-sections on the relative orientations of the helicity of the lepton beam and the nucleon polarization in DIS. Experimentally, the determination of the ratio between the difference in the cross-sections and their sum is exploited to extract an asymmetry. In fact, the systematic uncertainties in an asymme-

try measurement are much more favorable than in the measurement of a cross-section difference alone.
Starting from the late 1970s, a variety of experiment have been carried out to investigate the nucleon spin structure. The SLAC experiments E80 [6, 7] and E130 [8] measured asymmetries in DIS of polarized electrons from polarized protons. Their results confirmed the general ideas of scaling and QPM interpretation of the nucleon structure. In addition, the Ellis-Jaffe sum rule prediction for the integral of the proton spin structure was verified, though within large experimental uncertainties.
In 1987, a high precision measurement of the proton spin structure function was performed by the European Muon Collaboration (EMC) [9] with a polarized muon beam. Their result significantly deviated from the prediction of the Ellis-Jaffe sum rule. As a consequence, if no polarization of the strange quark sea is assumed, the EMC data imply that only 12% of the nucleon spin is carried by the quarks. This surprising result lead to the proposal of a new series of experiments which could test the validity of the EMC measurement with increased accuracy and add information on the structure functions for neutron and deuteron. Also the second generation of experiments (Spin Muon Collaboration [10, 11] at CERN and E142 [12] and E143 [13, 14] at SLAC) confirmed the deviation from the naive parton model predictions found in the previous polarized scattering experiments.
The newly born "spin crisis" in the parton model is nowadays established rather as the "nucleon spin puzzle". In order to have a complete picture of the nucleon spin, also the spin contributions from the gluons and the sea quarks in the nucleon must be taken into account.
Essentially, all the experimental information so far was gained through inclusive DIS where only the kinematics of the scattered lepton were measured. In particular, the integral of the spin structure functions is not a measure of only the intrinsic component of the nucleon spin carried by the quarks, since also the gluon polarization directly contributes. Further insight into the nucleon structure may be obtained through semi-inclusive DIS events in which a forward hadron is detected in coincidence with the scattered positron. The identification of the particle in the hadronic final state gives a unique insight in the individual quark flavor contributions. With appropriate kinematic constraints it is possible to tag the flavor of the struck quark, allowing the separation of the contributions of the different quark flavors to the nucleon spin. In this way, semi-inclusive pion asymmetries are sensitive to the polarization of the light-sea quarks in the nucleon. Furthermore, since the K^- meson consists of only sea quarks, the K^- asymmetry directly probes the spin content of the strange quarks in the nucleon. A direct measurement of the spin contributions of the light-sea and strange sea quarks is expecially interesting for a definitive interpretation of the nucleon spin puzzle.
The HERMES (HERa MEasurement of Spin) experiment, together with the SLAC experiments E154 [15, 16] and E155 [17, 18], belongs to a new generation of polarized DIS experiments designed to optimize the study of the spin nuclear structure. In particular, HERMES specialized its efforts not only on precise inclusive measurements but also on the semi-inclusive physics via the measurement of semi-inclusive pion and kaon asymmetries. The experiment is located at the Deutsches Elektronen Synchrotron (DESY) laboratory in Hamburg, Germany. The longitudinally self-polarized 27.5 GeV positron beam cir-

culating in the HERA (Hadronen Electronen Ring Anlage) storage ring interacts with a longitudinally polarized atomic gas of the HERMES target. For the experimental set-up the novel technique of an open-ended storage cell target internal to the positron beam pipe is used. In the HERMES experiment the reduction in luminosity due to the limited thickness of the gaseous target is compensated by the multiple interactions of the circulating positron beam.
The HERMES large acceptance spectrometer detects the forward going positrons and the corresponding hadronic fragments resulting from the interactions. A good hadron/positron separation is achieved by four particle identification detectors: a lead-glass calorimeter combined with a preshower, a threshold Čerenkov counter and a transition radiation detector (TRD). Pion identification was possible with the threshold Čerenkov counter. Since 1998 a Ring Imaging Čerenkov detector has been in operation, allowing full hadron identification over a wide momentum range.
The spin distribution of the sea quarks can be directly accessed through the measured pion and kaon semi-inclusive asymmetries. Since the commissioning of the experiment in 1995, three different polarized targets have been used: ^{3}He (1995), hydrogen (1996-1997) and deuterium (1998-2000).

The work presented in this thesis is organized as follows. In Chapter 2 an overview is given of the theoretical framework of polarized deep-inelastic scattering. The interpretation of observables within the Quark-Parton Model and its extension to the theory of Quantum Chromodynamics is also reviewed. The HERMES experimental setup is presented in Chapter 3. Essential to measurements of spin-dependent observables is a precise information on the target polarization. This requires a good determination of the fraction of molecules and atoms present in the target. In Chapter 4 the HERMES polarized hydrogen/deuterium target set-up is detailed and the formalism to determine the target polarization is described. At HERMES the Target Gas Analyzer is used to measure the relative atomic and molecular content of a sample of gas extracted from the target cell. In particular, a new method developed for the calibration of the device is presented. The future physics program of HERMES includes the investigation of the structure of the nucleon with its spin transversely polarized with respect to the beam helicity. Here, the studies performed with a test dipole magnet to achieve a transversely polarized hydrogen target are discussed. In Chapter 5 the analysis methods necessary to extract the double-spin asymmetries are presented for the inclusive and semi-inclusive channels. The data analyzed for this thesis comprise the 1996-97 hydrogen target data and the 1998-2000 deuterium target data. The results of systematic studies performed on deuterium data are presented. In Chapter 6, the formalism is introduced that allows one to relate the measured semi-inclusive asymmetries to the quark flavor polarizations. Finally, the results for the flavor decomposition of the nucleon spin and the polarized quark densities are presented and discussed on the basis of different theoretical models. Furthermore, the integrals of the polarized quark distributions are evaluated, providing a measurement of the fraction of the nucleon spin carried by the different quark flavors.

2 Polarized deep-inelastic scattering

In this chapter, the formalism of polarized deep-inelastic scattering (DIS) is discussed. The kinematics are given in Section 2.1 for the DIS of a charged lepton from a nucleon. The polarized cross-section for this process is discussed in Section 2.2 for the inclusive case. It will be shown how the measurement of polarized cross-section asymmetries can be related to spin observables. The structure functions are interpreted in terms of point-like constituents of the nucleon within the framework of the Quark Parton Model (Section 2.3). In Section 2.4, the role of gluons in the nucleon structure and their dynamical coupling to quarks is explained in the theory of Quantum Chromodynamics. Section 2.5 presents the sum rules for the spin structure of the nucleon by using the Operator Product Expansion formalism. Finally, in Section 2.6 the importance of the polarized semi-inclusive asymmetries is discussed. It is shown that they provide essential information on the flavor dependence of the polarized quark distributions.

2.1 Deep-inelastic scattering kinematics

The general form of the lepton-nucleon DIS reaction can be denoted by

$$\ell + N \longrightarrow \ell' + X \ , \tag{2.1}$$

where ℓ and ℓ' are the initial and final states of the charged lepton, N is the target nucleon, and X represents the final hadronic state. The energy transfer involved in the process is such that the nucleon breaks apart incoherently. The charged lepton interacts with the charged components inside the nucleon via neutral currents which are mediated by photons or Z^0 bosons. At HERMES energy ($\sqrt{s} \sim 7$ GeV in the center of mass) the dominant process is one-photon exchange, since Z^0-exchange only contributes significantly when the experimental energy transfer is comparable to the weak boson mass ($m_{Z^0} = 91$ GeV). The lowest order contribution to deep-inelastic lepton-nucleon scattering is schematically depicted in Fig. 2.1.
The corrections due to multi-photon exchange are suppressed by the smallness of the fine structure constant $\alpha_{EM} \sim 1/137$. The interference between one- and two-photon exchange is sensitive to the charge of the lepton beam. Therefore, the importance of contributions from multi-photon exchange processes can be measured by comparing results from DIS experiments which use oppositely charged leptons. Experimentally there is no evidence that the cross-section ratio $\sigma_{e^+}/\sigma_{e^-}$ deviates from unity [19].

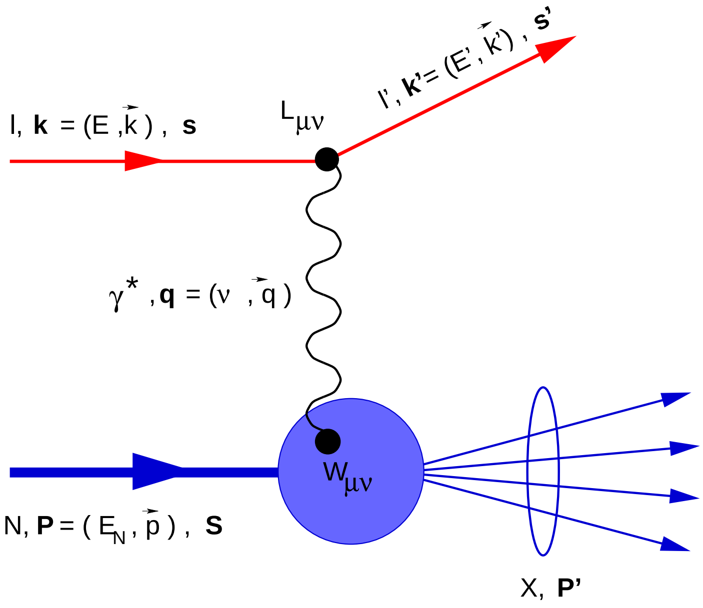

Figure 2.1: *Diagram of the deep-inelastic lepton-nucleon scattering in the one-photon exchange approximation.*

Note that in a fixed target experiment as HERMES, neglecting the thermal motion of the target atoms and the Fermi motion of the nucleons, the laboratory frame coincides with the nucleon rest frame. In addition, since the energies of incident and scattered leptons are large compared to their mass, the lepton mass may also be neglected. Both these approximations are used in the derivation of the DIS kinematic quantities listed in Table 2.1.

The initial-state lepton ℓ in Eq. (2.1) is characterized by the four-momentum, $\mathbf{k}$, and the spin four-vector, s. Both quantities are Lorentz-invariants. In the same way, $\mathbf{k}'$ and s' respectively represent four-momentum and spin four-vector of the scattered lepton ℓ'. For the target nucleon N these kinematic variables are indicated by $\mathbf{P}$ and $\mathbf{S}$.
The negative square of the four-momentum of the exchanged virtual photon equals

$$Q^2 \equiv -\mathbf{q}^2 = -(\mathbf{k} - \mathbf{k}')^2 > 0\,. \tag{2.2}$$

Since the exchanged photon is virtual, it can be either longitudinally or transversely polarized. In contrast, real photons have zero mass and are completely transversely polarized.
The transferred momentum and energy are carried away by the hadronic final state X, which has a squared invariant mass of

$$W^2 \equiv (\mathbf{P} + \mathbf{q})^2 \stackrel{Lab}{=} M^2 + 2\,M\,\nu - Q^2 \geq M^2 = \mathbf{P}^2\,. \tag{2.3}$$

Here, M is the nucleon mass and ν is the energy transferred by the photon.
Introducing the dimensionless Lorentz-invariant Bjorken variable

$$x \equiv \frac{-\,\mathbf{q}^2}{2\,\mathbf{P}\cdot\mathbf{q}} = \frac{Q^2}{Q^2 + W^2 - M^2} \stackrel{Lab}{=} \frac{Q^2}{2\,M\,\nu}\,, \tag{2.4}$$

it is possible to define a measure for the inelasticity of the scattering process. Since the invariant mass of the final hadronic state is larger than (or equal to) the mass of the target (see Eq. (2.3)), the kinematically allowed range for the Bjorken variable is $0 \leq x \leq 1$. The limit $x = 1$ corresponds to elastic scattering ($W^2 = M^2$). The deep-inelastic region is defined by the conditions $Q^2 > 1$ GeV^2 and $W > 2$ GeV.

Deep-inelastic scattering processes are classified according to the part of final state that is detected. A measurement is called *inclusive* if only the outgoing lepton ℓ' is detected, while in the *semi-inclusive* case also particles of the hadronic final state X are recorded in coincidence. If the final state is completely determined, then the measurement is called *exclusive*.

In the case of semi-inclusive measurements, the Lorentz-invariant scaling variable z is introduced which in the lab frame relates the energy E_h of the hadron h (detected in coincidence with the scattered lepton) to the maximum available energy ν:

$$z \equiv \frac{\mathbf{P} \cdot \mathbf{P_h}}{\mathbf{P} \cdot \mathbf{q}} \stackrel{Lab}{=} \frac{E_h}{\nu} \,. \tag{2.5}$$

Furthermore, by indicating with $\mathbf{P_h} = (E_h, \vec{p}_h)$ the four-momentum of a final state hadron, the three-momentum vector $\vec{p}_h$ can be decomposed into the longitudinal, $\vec{p}_{\|}$, and transverse , $\vec{p}_T$, components with respect to the virtual photon momentum $\vec{q}$. In the virtual photon-nucleon center of mass system the Feynman variable, x_F, is defined by

$$x_F \equiv \frac{|\vec{p}_{\|}|}{|\vec{q}|} \approx \frac{2|\vec{p}_{\|}|}{W} \,, \tag{2.6}$$

which scales the longitudinal hadron momentum with respect to its maximum possible value. The kinematically allowed ranges for the variables z and x_F are $0 < z < 1$ and $-1 < x_F < 1$, respectively. The kinematic dependence of the semi-inclusive hadrons and the struck quarks in the parton model is discussed in Section 2.6.

2.2 Inclusive deep-inelastic scattering

In the one-photon exchange approximation, the deep-inelastic cross-section for detecting the scattered lepton in the solid angle $d\Omega$ and in the energy range $[E', E' + dE']$ can be written in terms of leptonic and hadronic tensors, which describe the structure of the leptonic and hadronic vertices [19, 20]:

$$\frac{\mathrm{d}\sigma}{\mathrm{d}\Omega \mathrm{d}E'}(\mathbf{k}, \mathbf{s}, \mathbf{P}, \mathbf{S}\,; \mathbf{k}', \mathbf{s}') = \frac{\alpha_{EM}^2}{2MQ^4} \frac{E'}{E} L_{\mu\nu}(\mathbf{k}, \mathbf{s}\,; \mathbf{k}', \mathbf{s}')\, W^{\mu\nu}(\mathbf{q}\,; \mathbf{P}, \mathbf{S}) \,. \tag{2.7}$$

The leptonic tensor, $L_{\mu\nu}$, represents the emission of a photon by a lepton and is calculable in Quantum Electrodynamics. The unknown hadronic tensor $W^{\mu\nu}$ models the absorption of a photon by a nucleon.

The leptonic tensor can be split into a symmetric (S) part and an antisymmetric (A)

Experimental Observables	
Lepton:	
$\mathbf{k} = \left(E,\, \vec{k}\right)$	Four-momentum of the incident lepton
$\mathbf{k}' = \left(E',\, \vec{k}'\right)$	Four-momentum of the scattered lepton
$(\theta,\, \phi)$	Polar and azimuthal angles of the scattered lepton
Hadron:	
$\mathbf{P} \overset{Lab}{=} \left(M,\, \vec{0}\right)$	Four-momentum of the target nucleon
$\mathbf{P_h} \overset{Lab}{=} \left(E_h,\, \vec{P}_h\right)$	Four-momentum of a detected final state hadron h
Derived Quantities	
Inclusive DIS:	
$\mathbf{q} = \mathbf{k} - \mathbf{k}' = (\nu,\, \vec{q})$	Four-momentum of the virtual photon
$\nu = E - E'$	Energy of the virtual photon in the lab frame
$\vec{q} = \vec{k} - \vec{k}'$	Three-momentum of the virtual photon in the lab frame
$Q^2 \equiv -\mathbf{q}^2 \overset{Lab}{=} 4EE' \sin^2(\theta/2)$	Squared invariant mass of the virtual photon
$W^2 \equiv (\mathbf{P} + \mathbf{q})^2 \overset{Lab}{=} M^2 + 2M\nu - Q^2$	Squared invariant mass of the final hadronic system
$x \equiv -\mathbf{q}^2 / (2\, \mathbf{P} \cdot \mathbf{q}) \overset{Lab}{=} Q^2 / (2\, M\, \nu)$	Bjorken scaling variable
$y \equiv \mathbf{P} \cdot \mathbf{q} / \mathbf{P} \cdot \mathbf{k} \overset{Lab}{=} \nu / E$	Fractional energy transfer of the photon
Semi-inclusive DIS:	
$z \equiv \mathbf{P} \cdot \mathbf{P}_h / \mathbf{P} \cdot \mathbf{q} \overset{Lab}{=} E_h / \nu$	Fractional energy of the photon carried by the hadron h
$\vec{p}_{\parallel} \equiv (\vec{p}_h \cdot \hat{n}_q)\, \hat{n}_q$	Longitudinal momentum of a hadron h in γN c.m. frame
$\vec{p}_T = \vec{p}_h - \vec{p}_{\parallel}$	Transverse momentum of a hadron h in γN c.m. frame
$x_F \equiv \lvert\vec{p}_{\parallel}\rvert / \lvert\vec{q}\rvert \approx 2\vec{p}_{\parallel}/W$	Feynman scaling variable in γN c.m. frame

Table 2.1: *Definition of the DIS kinematic variables. The hadronic quantities related to the semi-inclusive DIS will be used in Section 2.6. For the derivation of the formulas in the laboratory frame the lepton mass was neglected.*

part under the exchange of the indices μ and ν:

$$\begin{aligned} L_{\mu\nu}(\mathbf{k},\mathbf{s}\,;\,\mathbf{k}') &\equiv \sum_{\mathbf{s}'} L_{\mu\nu}(\mathbf{k},\mathbf{s}\,;\,\mathbf{k}',\mathbf{s}') \\ &= L^{(S)}_{\mu\nu}(\mathbf{k}\,;\,\mathbf{k}') + i\,L^{(A)}_{\mu\nu}(\mathbf{k},\mathbf{s}\,;\,\mathbf{k}')\,. \end{aligned} \tag{2.8}$$

Here, a summation over the states s$'$ was performed. This is equivalent to the experimental situation in which the polarization of the scattered lepton cannot be measured. The symmetric part is spin-independent

$$L^{(S)}_{\mu\nu}(\mathbf{k}\,;\,\mathbf{k}') = 2\left[\mathbf{k}_\mu \mathbf{k}'_\nu + \mathbf{k}'_\mu \mathbf{k}_\nu - g_{\mu\nu}\left(\mathbf{k}\cdot\mathbf{k}' - m^2\right)\right]\,, \tag{2.9}$$

while the spin information is contained in the antisymmetric part

$$L^{(A)}_{\mu\nu}(\mathbf{k},\mathbf{s}\,;\,\mathbf{k}') = 2\,m\,\epsilon_{\mu\nu\alpha\beta}\,\mathbf{s}^\alpha\left(\mathbf{k}-\mathbf{k}'\right)^\beta\,. \tag{2.10}$$

In Eqs. (2.9) and (2.10), m is the lepton mass, $g_{\mu\nu}$ is the metric tensor, and $\epsilon_{\alpha\beta\gamma\delta}$ is the totally antisymmetric Levi-Civita tensor (with $\epsilon_{0123} = +1$).
The hadronic tensor $W_{\mu\nu}$, instead, cannot be derived from first principles. Using Lorentz covariance, parity and current conservation of the electromagnetic current, as well as invariance under time reversal, the hadronic tensor for a spin-$\frac{1}{2}$ target can also be decomposed [19, 20] into a spin-independent symmetric part and a spin-dependent antisymmetric part:

$$W_{\mu\nu}(\mathbf{q}\,;\,\mathbf{P},\mathbf{S}) = W^{(S)}_{\mu\nu}(\mathbf{q}\,;\,\mathbf{P}) + i\,W^{(A)}_{\mu\nu}(\mathbf{q}\,;\,\mathbf{P},\mathbf{S})\,. \tag{2.11}$$

The symmetric part is defined by the unpolarized structure functions $W_1(\mathbf{P}\cdot\mathbf{q},\mathbf{q}^2)$ and $W_2(\mathbf{P}\cdot\mathbf{q},\mathbf{q}^2)$, while the antisymmetric term is described by the polarized structure functions $G_1(\mathbf{P}\cdot\mathbf{q},\mathbf{q}^2)$ and $G_2(\mathbf{P}\cdot\mathbf{q},\mathbf{q}^2)$:

$$\begin{aligned} \frac{1}{2M}W^{(S)}_{\mu\nu}(\mathbf{q}\,;\,\mathbf{P}) &= \left(-\,g_{\mu\nu} + \frac{\mathbf{q}_\mu\mathbf{q}_\nu}{\mathbf{q}^2}\right) W_1(\mathbf{P}\cdot\mathbf{q},\mathbf{q}^2) \\ &+ \left[\left(\mathbf{P}_\mu - \frac{\mathbf{P}\cdot\mathbf{q}}{\mathbf{q}^2}\mathbf{q}_\mu\right)\left(\mathbf{P}_\nu - \frac{\mathbf{P}\cdot\mathbf{q}}{\mathbf{q}^2}\mathbf{q}_\nu\right)\right]\frac{W_2(\mathbf{P}\cdot\mathbf{q},\mathbf{q}^2)}{M^2}\,, \end{aligned} \tag{2.12}$$

$$\begin{aligned} \frac{1}{2M}W^{(A)}_{\mu\nu}(\mathbf{q}\,;\,\mathbf{P},\mathbf{S}) &= \epsilon_{\mu\nu\alpha\beta}\mathbf{q}^\alpha\left\{M\mathbf{S}^\beta G_1(\mathbf{P}\cdot\mathbf{q},\mathbf{q}^2)\right. \\ &+ \left.\left[(\mathbf{P}\cdot\mathbf{q})\,\mathbf{S}^\beta - (\mathbf{S}\cdot\mathbf{q})\,\mathbf{P}^\beta\right]\frac{G_2(\mathbf{P}\cdot\mathbf{q},\mathbf{q}^2)}{M}\right\}\,. \end{aligned} \tag{2.13}$$

The structure functions W_1, W_2, G_1, and G_2 parametrize the hadronic current. Since they are Lorentz-invariant scalars, they are functions of two independent Lorentz-invariant scalar combinations of $\mathbf{q}$ and $\mathbf{P}$ which can be chosen to be x and Q^2. In addition, one can redefine W_1, W_2, G_1, and G_2 in terms of dimensionless structure functions as

$$\begin{aligned} F_1(x,Q^2) &= MW_1(\mathbf{P}\cdot\mathbf{q},\mathbf{q}^2)\,, & g_1(x,Q^2) &= \tfrac{(\mathbf{P}\cdot\mathbf{q})^2}{\nu}\,G_1(\mathbf{P}\cdot\mathbf{q},\mathbf{q}^2)\,, \\ F_2(x,Q^2) &= \nu\,W_2(\mathbf{P}\cdot\mathbf{q},\mathbf{q}^2)\,, & g_2(x,Q^2) &= \nu(\mathbf{P}\cdot\mathbf{q})\,G_2(\mathbf{P}\cdot\mathbf{q},\mathbf{q}^2)\,. \end{aligned} \tag{2.14}$$

An intuitive interpretation of these structure functions is given within the framework of the quark parton model in Section 2.3.
For high energies ($Q^2 \geq m_{Z^0}$), the weak interaction contribution is not negligible, and only Lorentz and CP invariance can be used to reduce the number of degrees of freedom in the hadronic tensor. The most general form for $W_{\mu\nu}$, then, is represented by eight scalar structure functions [20] of which three are unpolarized (F_1, F_2, F_3), and five are polarized (g_1, g_2, g_3, g_4, g_5).
The physical interpretation of the structure functions can be given in terms of the amplitudes for the process of photo-absorption of a polarized virtual photon by a polarized nucleon [19, 21]. Thus, the hadronic tensor $W_{\mu\nu}$ can be related to the forward virtual Compton scattering through the optical theorem. In this approach, four independent amplitudes are involved, which are specified by the helicities of the virtual photon (λ_γ) and the nucleon (Λ_{N}). All other amplitudes are related to those by parity and time-reversal invariance. Conventionally the four transitions are labeled by the total angular momentum J_z of the photon-nucleon system, and the labels "L" or "T" indicate a longitudinal ($\lambda_\gamma = 0$) or transverse ($\lambda_\gamma = \pm\, 1$) polarized photon, as summarized in Table 2.2. Right-handed photons have $\lambda_\gamma = +\,1$ and left-handed photons have $\lambda_\gamma = -\,1$. The term "transverse" refers to both helicity states taken together, thus $\lambda_\gamma = 1$.

Initial λ_γ	Λ_{N}	Final λ'_γ	Λ'_{N}	Label J_z	
1	$\frac{1}{2}$	1	$\frac{1}{2}$	$\frac{3}{2}$	T
1	$-\frac{1}{2}$	1	$-\frac{1}{2}$	$\frac{1}{2}$	T
0	$-\frac{1}{2}$	1	$\frac{1}{2}$	$\frac{1}{2}$	LT
0	$\frac{1}{2}$	0	$\frac{1}{2}$	$\frac{1}{2}$	L

Table 2.2: *Notation for transitions amplitudes in forward virtual Compton scattering.*

The virtual photon-nucleon absorption cross-sections are defined through the imaginary parts of the virtual Compton amplitudes $A(\lambda'\Lambda'\,;\,\lambda\Lambda)$. It can be shown that they are related to the structure functions F_1, F_2, g_1, and g_2 as follows [1]

$$\begin{array}{lclcl}
\sigma^{\mathsf{T}}_{\frac{1}{2}}(x,Q^2) & \propto & \mathrm{Im}\,A(1,\frac{1}{2}\,;\,1,\frac{1}{2}) & = & \frac{1}{M}\left(F_1 + g_1 - \gamma^2\, g_2\right)\,, \\
\sigma^{\mathsf{T}}_{\frac{3}{2}}(x,Q^2) & \propto & \mathrm{Im}\,A(1,-\frac{1}{2}\,;\,1,-\frac{1}{2}) & = & \frac{1}{M}\left(F_1 - g_1 + \gamma^2\, g_2\right)\,, \\
\sigma^{\mathsf{L}}_{\frac{1}{2}}(x,Q^2) & \propto & \mathrm{Im}\,A(0,\frac{1}{2}\,;\,0,\frac{1}{2}) & = & \frac{1}{M}\left(\frac{1+\gamma^2}{2x}F_2 - F_1\right)\,, \\
\sigma^{\mathsf{LT}}_{\frac{1}{2}}(x,Q^2) & \propto & \mathrm{Im}\,A(0,-\frac{1}{2}\,;\,1,\frac{1}{2}) & = & \frac{1}{M}\,\gamma\,\left(g_1 + g_2\right)\,,
\end{array} \qquad (2.15)$$

where $\gamma^2 = \frac{4M^2x^2}{Q^2}$. A factor $4\pi^2\alpha/K$ is implicitly assumed in all four equations of (2.15), with K being the flux of virtual photons generated by the incident lepton beam. In a

[1] For brevity, the dependences on x and Q^2 are implied on the right-hand side of all the following equations of this Section.

possible convention introduced by Hand [22] it is evaluated as $K = \nu - Q^2/2M$.
Taking convenient combinations of the cross-sections listed above, the virtual photon-nucleon asymmetries can be expressed as

$$A_1(x, Q^2) \equiv \frac{\sigma^{\mathsf{T}}_{\frac{1}{2}} - \sigma^{\mathsf{T}}_{\frac{3}{2}}}{\sigma^{\mathsf{T}}_{\frac{1}{2}} + \sigma^{\mathsf{T}}_{\frac{3}{2}}} = \frac{1}{F_1}\left(g_1 - \gamma^2\, g_2\right) , \tag{2.16}$$

and

$$A_2(x, Q^2) \equiv \frac{\sigma^{\mathsf{LT}}_{\frac{1}{2}}}{\frac{1}{2}\left(\sigma^{\mathsf{T}}_{\frac{1}{2}} + \sigma^{\mathsf{T}}_{\frac{3}{2}}\right)} = \frac{1}{F_1}\gamma\ (g_1 + g_2) . \tag{2.17}$$

The asymmetry A_1 quantifies the difference in the cross-sections involving a helicity change of the nucleon without a helicity change of the photon. Instead, the asymmetry A_2 accounts for a change of the photon helicity. The term σ^{LT} in A_2 arises from the interference between the transverse and longitudinal amplitudes.
From Eqs. (2.16) and (2.17) the polarized structure functions can be derived in terms of A_1, A_2 and the spin averaged structure function F_1 as follows

$$g_1(x, Q^2) = \frac{F_1}{1+\gamma^2}\ (A_1 - \gamma A_2) , \tag{2.18}$$

$$g_2(x, Q^2) = \frac{F_1}{1+\gamma^2}\left(-A_1 + \frac{A_2}{\gamma}\right) . \tag{2.19}$$

Rewriting the longitudinal and the transverse photo-absorption cross-sections as

$$\sigma_{\mathsf{L}}(x, Q^2) \equiv \sigma^{\mathsf{L}}_{\frac{1}{2}} , \tag{2.20}$$

$$\sigma_{\mathsf{T}}(x, Q^2) \equiv \tfrac{1}{2}\left(\sigma^{\mathsf{T}}_{\frac{1}{2}} + \sigma^{\mathsf{T}}_{\frac{3}{2}}\right) , \tag{2.21}$$

an expression for the ratio of the unpolarized structure functions F_1 and F_2 can be defined

$$R(x, Q^2) \equiv \frac{\sigma_{\mathsf{L}}}{\sigma_{\mathsf{T}}} = \left(1+\gamma^2\right)\frac{F_2}{2xF_1} - 1 . \tag{2.22}$$

Constraints on the virtual photon asymmetries A_1 and A_2 have been investigated [23] establishing the following positivity limits:

$$|A_1| \leq 1 , \tag{2.23}$$

$$|A_2| \leq \sqrt{R} . \tag{2.24}$$

On the basis of the positivity study done by Doncel and de Rafael, Soffer and Teryaev [24] derived a stronger bound for the transverse asymmetry:

$$|A_2| \leq \sqrt{\frac{R(1+A_1)}{2}} . \tag{2.25}$$

In the following, the expressions which allow to extract the polarized and unpolarized structure functions from experimental measurable quantities are discussed.

2.2.1 Unpolarized cross-section

The unpolarized DIS cross-section is obtained by averaging Eq. (2.7) over the spin states of the initial particles and summing over the spin states of the scattered lepton. Only the symmetric parts of the leptonic and hadronic tensors contribute to the cross-section

$$\frac{\mathrm{d}\sigma_{\text{unp}}}{\mathrm{d}\Omega\mathrm{d}E'}(\mathbf{k},\mathbf{P}\,;\,\mathbf{k}') = \frac{\alpha^2}{2MQ^4}\frac{E'}{E}L^{(S)}_{\mu\nu}(\mathbf{k}\,;\,\mathbf{k}')W^{\mu\nu(S)}(\mathbf{q}\,;\,\mathbf{P})\,. \tag{2.26}$$

Using Eqs. (2.9) and (2.12), the dependence of the cross-section on the scattering angle θ of the outgoing lepton can be derived

$$\frac{\mathrm{d}\sigma_{\text{unp}}}{\mathrm{d}\Omega\mathrm{d}E'} = \underbrace{\frac{4\,\alpha^2\,E'^2\,\cos^2(\frac{\theta}{2})}{Q^4}}_{\sigma_{Mott}}\left[\frac{2}{M}\,F_1(x,Q^2)\,\tan^2(\frac{\theta}{2}) + \frac{1}{\nu}\,F_2(x,Q^2)\right]. \tag{2.27}$$

The leading term, σ_{Mott}, is the Mott cross-section for elastic scattering of spinless electrons from spinless point-like nuclei.
Equation (2.27) can be rewritten as

$$\frac{\mathrm{d}\sigma_{\text{unp}}}{\mathrm{d}x\mathrm{d}Q^2} = \frac{4\pi\alpha^2}{xQ^4}\left[1 - y - \frac{Q^2}{4E^2} + \frac{(1+\gamma^2)}{(1+R(x,Q^2))}\frac{(y^2+\frac{Q^2}{E^2})}{2}\right]F_2(x,Q^2)\,, \tag{2.28}$$

where Eq. (2.22) was used and a change from the variable E' to Q^2 was also applied. Precise measurements of the structure function F_2 of proton and deuteron have been performed by a series of experiments covering a wide kinematic range in x and Q^2 ($10^{-6} \le x \le 0.9$ and $0.1\,\mathrm{GeV}^2 \le Q^2 \le 5\cdot 10^3\,\mathrm{GeV}^2$). World data for F_2^p from fixed target experiments are shown in Fig. 2.2.

2.2.2 Cross-section asymmetries

The polarized structure functions of the nucleon can be accessed once the antisymmetric parts of leptonic and hadronic tensor in Eq. (2.7) are singled out. This can be achieved by taking the difference of the cross-sections with opposite target spin orientations $-\mathbf{S}$ and $\mathbf{S}$ with respect to the incident lepton spin and averaging over the spin states of the scattered lepton:

$$\sum_{s'}\left[\frac{\mathrm{d}\sigma}{\mathrm{d}\Omega\mathrm{d}E'}(\mathbf{k},\mathbf{s},\mathbf{P},-\mathbf{S}\,;\,\mathbf{k}',\mathbf{s}') - \frac{\mathrm{d}\sigma}{\mathrm{d}\Omega\mathrm{d}E'}(\mathbf{k},\mathbf{s},\mathbf{P},\mathbf{S}\,;\,\mathbf{k}',\mathbf{s}')\right] = \frac{\alpha^2}{2MQ^4}\frac{E'}{E}L^{(A)}_{\mu\nu}(\mathbf{k},\mathbf{s}\,;\,\mathbf{k}')W^{\mu\nu(A)}(\mathbf{q}\,;\,\mathbf{P},\mathbf{S})\,. \tag{2.29}$$

Using the definitions of the scattering angles given in Fig 2.3, the cross-section difference for a longitudinally polarized lepton with spin along the direction of motion ($\rightarrow$) is given by

$$\frac{\mathrm{d}\sigma^{\rightarrow,-\mathbf{S}}}{\mathrm{d}\Omega\mathrm{d}E'} - \frac{\mathrm{d}\sigma^{\rightarrow,\mathbf{S}}}{\mathrm{d}\Omega\mathrm{d}E'} = \frac{4\,\alpha^2_{\text{EM}}}{M\,\nu\,Q^2}\frac{E'}{E}\left[(E\cos\alpha + E'\cos\theta)\,g_1 + \frac{2\,E\,E'}{\nu}\,(\cos\Theta - \cos\alpha)\,g_2\right], \tag{2.30}$$

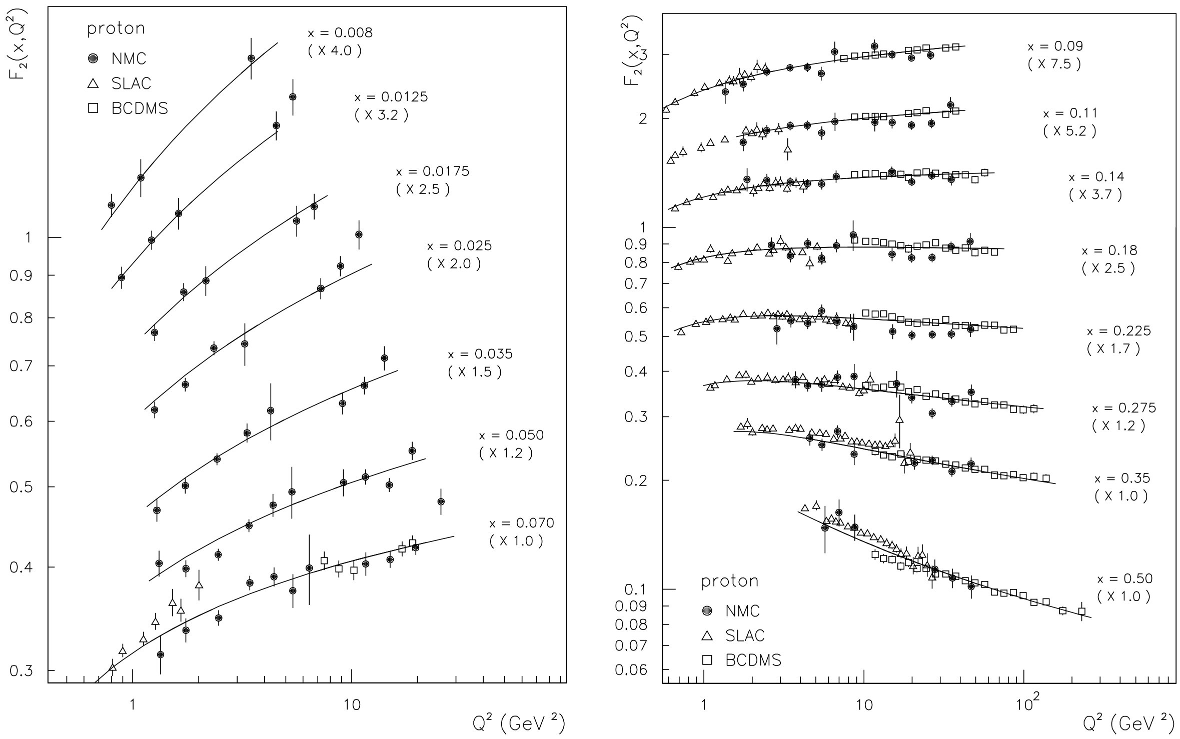

Figure 2.2: *Comparison of world data on the proton structure function F_2^p from the fixed target experiments NMC [25](muon scattering), SLAC [26](electron scattering) and BCDMS [27](muon scattering). The solid curves represent a fit to all three data sets performed by NMC [25]. In the figure, the data in each x-bin have been scaled by the factor indicated in the brackets for clarity.*

where $\cos\Theta \equiv \sin\theta\sin\alpha\cos\phi + \cos\theta\cos\alpha$ and α is the polar angle of the nucleon spin direction. The term α_{EM} is the electromagnetic coupling constant.

Experimentally, the interesting cases are when in the lab frame $\alpha = 0$ and when $\alpha = \pi/2$. In the former case ($\alpha = 0$ and $\Theta = \theta$) the lepton and nucleon spins are aligned parallel ($\rightrightarrows$) or antiparallel ($\rightleftarrows$) leading to the relation

$$\frac{\mathrm{d}\left(\sigma^{\rightleftarrows} - \sigma^{\rightrightarrows}\right)}{\mathrm{d}\Omega\mathrm{d}E'} = \frac{4\,\alpha^2}{M\,\nu\,Q^2}\frac{E'}{E}\left[(E + E'\cos\theta)\,g_1 - \frac{Q^2}{\nu}\,g_2\right], \tag{2.31}$$

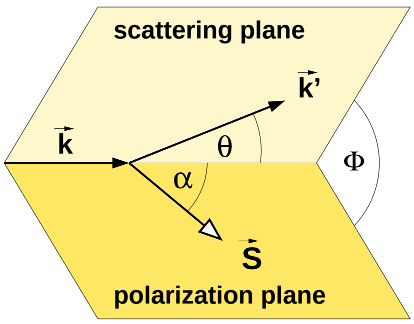

Figure 2.3: *Angles relevant to the polarized scattering process are here indicated. The scattering plane (defined by the vectors $\vec{k}$ and $\vec{k}'$) and the polarization plane (determined by $\vec{k}$ and $\vec{S}$) define the azimuthal angle ϕ. The polar angle α is fixed by the spin direction $\vec{S}$ and the direction of $\vec{k}$. The angle of the scattered lepton is indicated by θ.*

while in the second case the target spin (indicated by the thick arrow, $\Uparrow$) is transversely oriented with respect to the lepton spin:

$$\frac{\mathrm{d}\,(\sigma^{\rightarrow\Downarrow} - \sigma^{\rightarrow\Uparrow})}{\mathrm{d}\Omega \mathrm{d}E'} = \frac{4\,\alpha^2}{M\,\nu\,Q^2}\frac{(E')^2}{E}\left[\cos\theta\, g_1 + \frac{2\,E}{\nu}\,\cos\Theta\, g_2\right] . \tag{2.32}$$

The measure of the cross-section differences expressed in the previous equations would in principle allow to extract g_1 and g_2 individually. However, this method is experimentally difficult due to the precision required in the measurement of cross-sections.
Instead, one measures the longitudinal, $A_\parallel$, and transverse, $A_\perp$, double-spin asymmetries defined by

$$A_\parallel \equiv \frac{\sigma^{\rightleftarrows} - \sigma^{\rightrightarrows}}{\sigma^{\rightleftarrows} + \sigma^{\rightrightarrows}} , \quad A_\perp \equiv \frac{\sigma^{\rightarrow\Downarrow} - \sigma^{\rightarrow\Uparrow}}{\sigma^{\rightarrow\Downarrow} + \sigma^{\rightarrow\Uparrow}} . \tag{2.33}$$

These asymmetries are related to the virtual photo-absorption asymmetries A_1 and A_2 through

$$A_\parallel = D\,(A_1 + \eta\,A_2) , \quad A_\perp = D\left(\xi A_2 - \frac{\eta}{\xi}\,A_1\right) . \tag{2.34}$$

The kinematic factors appearing in the previous equations are defined as

$$D \equiv \frac{y(2-y)}{y^2 + 2(1-y)(1+R)} , \tag{2.35}$$

$$\epsilon \equiv \frac{4\,(1-y) - \gamma^2\,y^2}{4\,(1-y) + 2\,y^2 + \gamma^2\,y^2} , \tag{2.36}$$

$$\xi \equiv \sqrt{\frac{2\,\epsilon}{1+\epsilon}} , \tag{2.37}$$

$$\eta \equiv \frac{2\gamma(1-y)}{(2-y)} . \tag{2.38}$$

The coefficient D can be interpreted as the depolarization factor in the spin transfer from the initial lepton to the virtual photon, and ϵ represents the ratio of probabilities for the emission of a longitudinally or transversely polarized photon.
The spin structure functions g_1 and g_2 can be solved in terms of the longitudinal and transverse asymmetries as

$$g_1(x,Q^2) = \frac{F_1}{D}\left[A_\parallel + A_\perp \tan\left(\frac{\theta}{2}\right)\right] , \tag{2.39}$$

$$g_2(x,Q^2) = \frac{F_1}{D}\frac{y}{2\sin\theta}\left[-A_\parallel \sin\theta + A_\perp \frac{(E + E'\cos\theta)}{E'}\right] . \tag{2.40}$$

Due to the factor $\tan(\theta/2)$ in Eq. (2.40) the contribution of $A_\perp$ to g_1 is suppressed for small scattering angles. Measuring $A_\parallel$ at small θ yields primarily information about g_1. Similarly, the $A_\parallel$ contribution to g_2 is suppressed by a factor of $\sin\theta$ relative to the contribution from $A_\perp$.

At HERMES, longitudinally polarized nucleons are used as target. Therefore, it is convenient to derive the interesting experimental quantity, $A_\parallel$, as a function of g_1 and g_2. Using Eqs. (2.16) and (2.17), the experimental target-beam asymmetry $A_\parallel$ is given by

$$A_\parallel = \frac{D}{F_1}\left[g_1(1+\eta\gamma) + g_2(\eta\gamma - \gamma^2)\right] . \tag{2.41}$$

Assuming $g_2 = 0$, the relation between the polarized structure function g_1 and the asymmetry $A_\parallel$ significantly simplifies:

$$\frac{A_\parallel}{D(1+\eta\gamma)} \approx \frac{g_1}{F_1} \approx A_1 . \tag{2.42}$$

As it will be discussed later in Section 5.5.4, the assumption for g_2 is supported by the fact that this quantity is measured to be close to zero for proton and neutron in the kinematic region of the HERMES experiment. In addition, the contribution of g_2 to A_1 is suppressed by the kinematic factors γ^2 and $\eta\gamma$ which in the HERMES kinematic domain are small (0.003 $< \gamma^2 <$ 0.15, 0.001 $< \eta\gamma <$ 0.15).

2.3 Quark Parton Model

In the previuos sections only the general scattering formalism has been presented. The underlying physics of deep-inelastic scattering was born out of the results of DIS experiments performed at SLAC in the late 1960s. It was observed that for large momentum transfer Q^2 and large hadronic invariant mass W, the unpolarized structure functions F_1 and F_2 are to a large extend independent of Q^2 [28, 29].
At the same time Bjorken [4] predicted Q^2-invariance of the structure functions for $\nu, Q^2 \to \infty$ with $x = \frac{Q^2}{2M\nu}$ fixed (the *Bjorken-limit*). In this limit, the functions F_1 and F_2 exhibit dependence only on the variable x, which is often referred to as Bjorken-x:

$$F_{1,2}(\nu, Q^2) \quad = \quad F_{1,2}(x) . \tag{2.43}$$

This property is known as *scaling*, since the quantities are independent of the energy scale, Q^2, of the interaction.
In order to give an interpretation of deep-inelastic scattering and its scale invariance Bjorken and Paschos [30], and Feynman [31] developed the *Quark Parton Model* (QPM). In the QPM, deep-inelastic lepton-nucleon scattering is interpreted as elastic scattering of the lepton from point-like constituents of the nucleon with spin $\frac{1}{2}$ and charge $e_q \neq 0$: the *partons*. Later the partons were identified with the *quarks* proposed by Gell-Mann [2] and Zweig [3] to describe the hadronic spectra.
A convenient coordinate system used to define the kinematics of the scattering process in the QPM is the so-called *Breit frame* (see Fig. 2.4). In this frame the energy transfer equals zero, and the nucleon momentum is large compared to parton masses and parton transverse momenta. The scattering is then interpreted as the absorption of the virtual

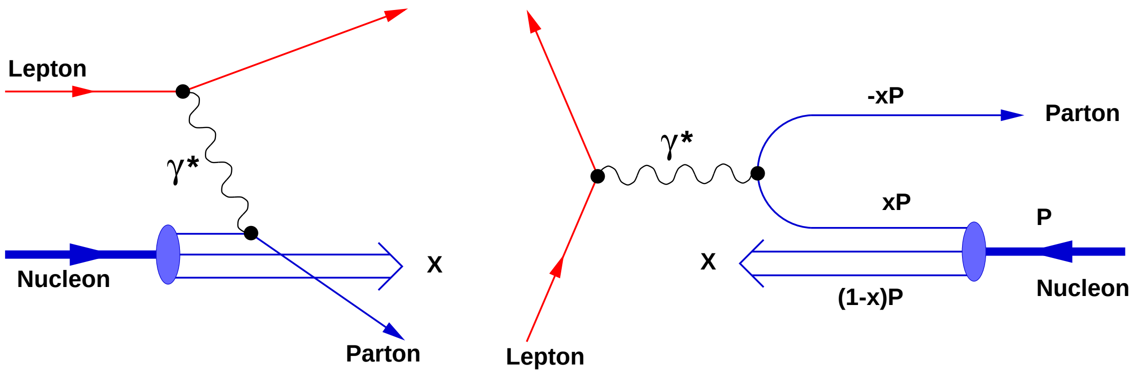

Figure 2.4: *Deep-inelastic lepton-nucleon scattering in the parton model: general (left) and Breit frame (right).*

photon by one of the partons which move collinearly within the nucleon [32]. The scaling variable, x, corresponds to the fraction of the total nucleon momentum, P, carried by the struck quark: $p_q = xP$. Taking the mass of the quark as a fraction of the nucleon mass, $m_q = xM$, the Bjorken scaling can be viewed as a consequence of momentum conservation in elastic scattering: $Q^2 = 2m_q\nu = 2xM\nu$.
Since the measured structure functions exhibit a smooth dependence on x, many partons have to be present in the nucleon. In the Bjorken-limit, the wavelength of the exchanged virtual photon is small ($\lambda \propto 1/Q$). Correspondingly, the time scale ($\tau \propto 1/\nu$) of the parton-photon interaction is much shorter than the time scale over which the partons may interact with other partons inside the nucleon [30]. Therefore, the picture of the DIS process in the QPM is that of an incoherent scattering from the individual partons as free constituents, each carrying a fraction x of the nucleon momentum. The nucleon may then be described by *parton momentum distribution functions* $q_f(x) = \frac{dP_i}{dx}$, which define the probability of finding in the nucleon a parton with fractional momentum x. Physically, $q_f(x)dx$ represents the number density of a quark q_f with momentum fraction $[x, x+dx]$. The nucleon structure functions in the QPM are then expressed in terms of sums of the parton density functions.
Defining the *unpolarized parton distribution function* as

$$q_f(x) \equiv q_f^{\rightrightarrows}(x) + q_f^{\rightleftarrows}(x)\,, \tag{2.44}$$

the term $q_f^{\rightrightarrows(\rightleftarrows)}(x)$ denotes the probability to find a parton of type f with momentum fraction x in the nucleon with spin parallel (antiparallel) to the nucleon spin. Therefore, for the unpolarized structure functions one has

$$F_1(x) = \frac{1}{2}\sum_f e_f^2\, q_f(x) \quad , \quad F_2(x) = x\sum_f e_f^2\, q_f(x)\,, \tag{2.45}$$

where the sum runs over all the quark flavors available in the nucleon $f = u, \bar{u}, d, \bar{d}, s, \bar{s}$,..., and e_f is the charge of the parton of flavor f. Similarly, the polarized structure functions can be written as

$$g_1(x) = \frac{1}{2}\sum_f e_f^2\, \Delta q_f(x) \quad , \quad g_2(x) = 0\,, \tag{2.46}$$

where the *polarized parton distribution functions* are defined as

$$\Delta q_f(x) \equiv q_f^{\overset{\rightarrow}{\Rightarrow}}(x) \; - \; q_f^{\overset{\leftarrow}{\Rightarrow}}(x) \,. \tag{2.47}$$

In Eq. (2.44), $q_f(x)$ defines the unpolarized distributions as the spin degrees of freedom are averaged. Instead, $\Delta q_f(x)$ represents the difference of the momentum distributions of partons with different helicity states within the nucleon. The measure of g_1 with polarized DIS is sensitive to the helicity distribution of the partons in the nucleon.
Note that in the QPM, which considers non-interacting partons moving collinearly within the nucleon, the contribution from structure function g_2 is zero. In the operator product expansion formalism (Section 2.5), the function g_2 is described as a twist-3 contribution. Its role is interpreted in terms of binding effects in the nucleon and it is related to transverse degrees of freedom of the quarks in the nucleon [20].
The parton densities are normalized so that the net number of each kind of valence quark corresponds to the uud combination of the constituent quarks in the proton

$$\begin{aligned} \int_0^1 u(x) - \bar{u}(x) dx &= 2\,, \\ \int_0^1 d(x) - \bar{d}(x) dx &= 1\,, \\ \int_0^1 s(x) - \bar{s}(x) dx &= 0\,. \end{aligned} \tag{2.48}$$

Here, the subtraction of the antiquark distribution from the quark distribution for the same flavor, yields the number of valence quarks in the proton.
The distributions for the neutron are derived from those of the proton applying isospin symmetry rotations: $u^n(x) = d(x)$, $d^n(x) = u(x)$, and $s^n(x) = s(x)$, and analogously for antiquarks.
The assumption of the spin-$\frac{1}{2}$ nature of the partons is motivated by the experimental evidence that the photo-absorption cross-section ratio $R = \sigma_{\mathsf{L}}/\sigma_{\mathsf{T}}$ is small [26]. As a consequence from Eq. (2.22) it follows that

$$F_2(x) = 2x\, F_1(x)\,, \tag{2.49}$$

which is known as the Callan-Gross relation [33]. In the QPM approximation only one independent unpolarized structure function remains.
In the hypothesis that the scattering occurs from a spin-0 parton, the Callan-Gross relation would lead to the result $2xF_1(x)/F_2(x) = 0$. This results from the fact that a photon cannot couple transversely to spin-0 partons. Thus, $\sigma^{\mathsf{T}} \to 0$ and $R \to \infty$, contrary to the experimental results.
The cross-section ratio R has been measured for proton and deuteron targets (*e.g.* [26, 25, 34]) over the kinematic range 0.6 GeV$^2 < Q^2 <$ 20 GeV^2 and 0.1 $< x <$ 0.9.
Using $F_2^d R_d = F_2^n R_n + F_2^p R_p$, a relation for the neutron can be obtained,

$$R_n = R_d + \frac{\delta}{F_2^n/F_2^p}\,, \tag{2.50}$$

where $\delta = R_d - R_p$. The data for the cross-section difference δ was determined to be consistent with zero within the statistical uncertainties [26, 25, 34]. This implies that $R_d \sim R_n \sim R_p$.

The QPM assumes the universality of the parton description as fundamental components of the hadronic structure. This implies that the cross-section of any deep-inelastic probe of the hadron structure should be proportional to the parton distribution. This assumption is used to fit universal parton distributions to measured cross-sections from a variety of processes, including DIS, Drell-Yan scattering, W-boson production, high-p_t-jet production and neutrino experiments. Figure 2.5 shows the unpolarized parton distribution fits obtained by the CTEQ collaboration [35] from world data.

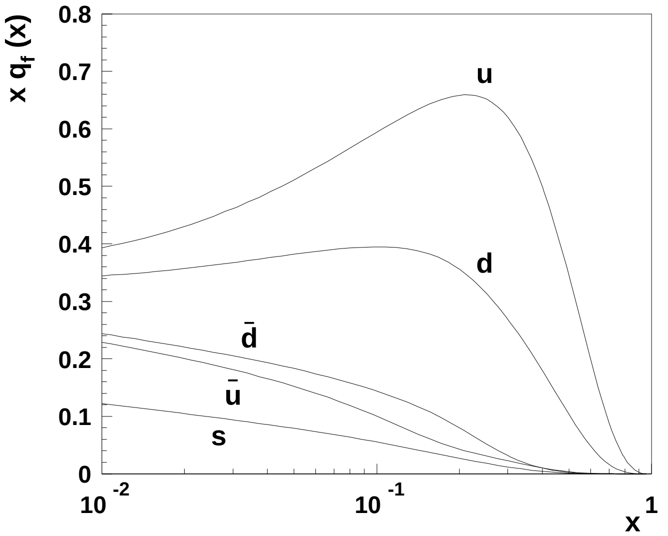

Figure 2.5: *The unpolarized quark distributions in the proton as a function of x for a Q^2 = 2.5 GeV^2, resulting from a fit to world data performed by the CTEQ collaboration [35].*

2.4 Quantum Chromodynamics in DIS

The result in Eq. (2.49) for spin-$\frac{1}{2}$ partons rules out the existence of additional non-fermionic charged partons. However, if these charged partons would be the only constituents of the nucleon, the total nucleon momentum should be reproduced when integrating over their momentum distribution

$$I = \int_0^1 \sum_f e_f^2 \, x \, q_f(x) \, \mathrm{d}x = \int_0^1 F_2(x) \, \mathrm{d}x \,. \tag{2.51}$$

Experimentally it was found that the charged partons only account for about half of the nucleon momentum [36].
Furthermore, from Fig. 2.2 it is obvious that the scaling property of the partonic model is only approximately valid.
A more complete treatment of the parton behavior inside a nucleon is described by *Quantum Chromodynamics* (QCD), which is a non-Abelian quantum field theory describing the strong interaction of the partons in a hadron within the Standard Model.

In this framework, the partons are identified as quarks that possess one of the three color charges of the strong force, commonly: red, green, and blue. The $SU(3)_{color}$ group describes the symmetry of the color charges. Colored quarks interact with each other through the exchange of a new parton, which is identified with the massless spin-1 $gluon$. In addition, gluons themself carry color charge.
A quark emitting a gluon reduces its momentum. The gluon can subsequently convert into a quark-antiquark pair. In addition, due to the non-Abelian property of QCD, also three or four gluons can couple to each other. The basic vertices of the QCD theory are depicted in Fig. 2.6.

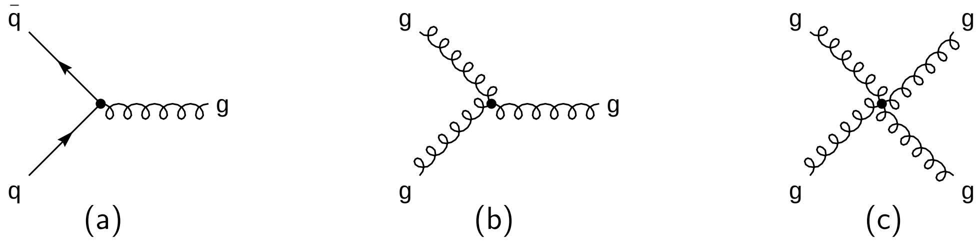

Figure 2.6: *Elementary Feynman diagrams for QCD processes: quark-gluon vertex (a), and self-coupling of three (b) and four gluons (c) vertices.*

In QCD the $scaling\ violation$ of the structure functions is expected due to the coupling of the quarks to the gluons, while in the QPM non-interacting partons were assumed. As a result a Q^2-dependence enters in the parton distribution functions and thus in the structure functions. Intuitively, the scaling violation may be schematically represented in Fig. 2.7 and explained as follows. The value of Q^2 determines the wavelength of the virtual photon and, therefore, the resolution of the probe. For a certain value $Q^2 = Q_0^2$, the measured quark distribution is $q_f(x, Q_0^2)$. Increasing the resolution of the virtual photon by using $Q^2 > Q_0^2$, one can resolve that the quark momentum has changed due to the emission of a gluon. Thus, in the DIS process the quark with momentum fraction x' is now probed, which originated from a parent quark with momentum fraction $x > x'$. In the same way, the virtual photon can couple to a quark which was generated by a gluon splitting into a $q\bar{q}$ pair.
As consequence of these processes the probability to find a parton with large x decreases with increasing Q^2 since the momentum fraction can be shared amongst several partons. The scaling violation observed in the unpolarized structure function F_2 in Fig. 2.2 [37] is the experimental evidence of the argumentation above. For small values of x the unpolarized structure functions increase logarithmically with Q^2, while at large values of x the opposite behaviour is observed.
The $running$ coupling constant, α_s, of QCD quantitatively describes the strength of the vertices of the strong interaction. The coupling α_s varies with the renormalization energy scale, μ, of the field theory.
In the calculation to the first order (Leading Order), α_s is given by [38]

$$\alpha_s^{(LO)}(\mu^2) = \frac{4\,\pi}{\beta_0\,\ln(\mu^2/\Lambda^2)}\,, \tag{2.52}$$

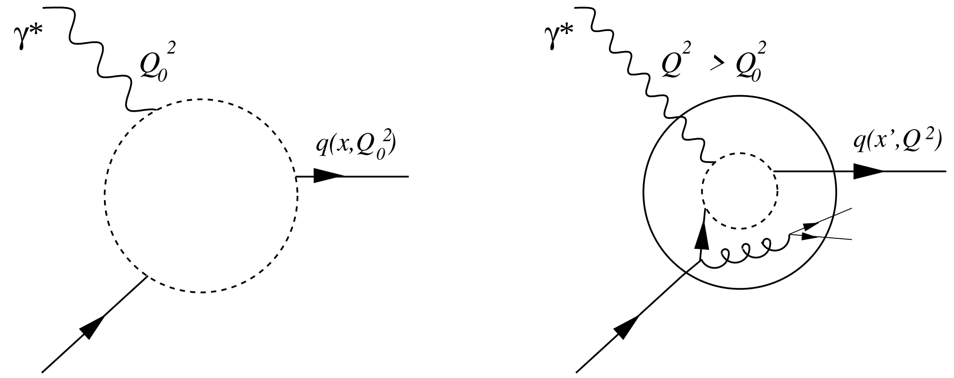

Figure 2.7: *Schematic representation of the Q^2-dependence of the quark distributions due to the increasing resolving power of the virtual photon. In the left diagram the virtual photon with momentum Q_0^2 probes the quark distribution $q_f(x, Q_0^2)$. For $Q^2 > Q_0^2$ (right diagram) the photon probes $softer$ quarks due to the emission of a gluon.*

and to the Next-to-Leading Order (NLO) by

$$\alpha_s^{(NLO)}(\mu^2) = \alpha_s^{(LO)}(\mu^2)\left[1 - \frac{\beta_1 \ln\ln(\mu^2/\Lambda^2)}{\beta_0^2 \ln(\mu^2/\Lambda^2)}\right] . \tag{2.53}$$

The coefficients β_0 and β_1 are calculated from QCD as

$$\beta_0 = 11 - \frac{2}{3}n_f \,, \quad \beta_1 = 102 - \frac{38}{3}n_f \,, \tag{2.54}$$

respectively. Here, n_f denotes the number of active quark flavors which have a mass less than the energy scale μ. The parameter Λ in Eqs. (2.52) and (2.53) is known as the QCD scale parameter. It does not depend on the scale μ, but it depends on the number of active quark flavors and the order of the calculation. At the NLO, and fixing the energy scale dependence at $\mu_{\text{fixed}} \equiv M_{Z^0} = 91.187$ GeV, the average value from Ref. [39] is $\alpha_s(M_{Z^0}) = 0.118 \pm 0.002$, which corresponds for $n_f = 5$ to $\Lambda_{QCD}^{(5)} = 208\ ^{+25}_{-23}$MeV. In DIS experiments, the value of μ is taken to be equal to the virtual photon mass Q.
The coupling constant scales as $\alpha_s(Q^2) \approx 1/\ln(Q^2/\Lambda^2)$, in agreement with the behavior observed for the scaling violation. This implies that $\alpha_s(Q^2) \rightarrow 0$ for $Q^2 \rightarrow \infty$, which is known as the $asymptotic\ freedom$ property in QCD. In this limit, in the DIS process the quarks freely interact with the virtual photons, and the partonic picture is reproduced by QCD in the Bjorken limit.
In practice, all the experiments are performed at some finite value of Q^2 and perturbative corrections are necessary to adjust the parton model interpretation.
In analogy to QED, QCD corrections to DIS comprise the gluon bremsstrahlung, the vertex and the vacuum polarization corrections. In addition, the photon-gluon fusion process is present, in which the virtual photon interacts with a quark produced from the splitting of a gluon into a $q\bar{q}$ pair.
The value of Λ_{QCD} represents the limit of the scale at which the strong coupling constant would diverge. In this domain the perturbative QCD approach cannot be applied any more and only non-perturbative calculation techniques may be used to understand the strong

interaction. This could be an indication of the *confinement* property of quarks and gluons inside the hadrons as a consequence of the increase of the α_s coupling at low scales [38]. The Q^2-dependence of the parton distributions is quantitatively described in QCD by the *evolution equations*. Introducing the variables

$$t \equiv \ln(Q^2/\Lambda^2)\,, \quad \text{and} \quad \langle e^2 \rangle \equiv \frac{1}{n_f}\sum_f e_f^2\,, \tag{2.55}$$

the unpolarized singlet and non-singlet combinations of the quark and antiquark distributions are defined as

$$\Sigma(x,t) \equiv \sum_f q_f(x,t)\,, \tag{2.56}$$

$$q^{NS}(x,t) \equiv \sum_f \left[\frac{e_f^2}{\langle e^2 \rangle} - 1\right] q_f(x,t)\,. \tag{2.57}$$

In the same way, a distribution function $g(x,t)$ for the gluons can be introduced. Using the definition of the convolution product

$$[f \otimes h]\,(x,t) \equiv \int_x^1 \frac{\mathrm{dy}}{y} f(\frac{x}{y},t)h(y,t)\,, \tag{2.58}$$

the evolution of the parton distributions as a function of Q^2 is given by the Dokshitzer–Gribov–Lipatov–Altarelli–Parisi (DGLAP) equations [40, 41, 42].

$$\frac{\mathrm{d}}{\mathrm{dt}} q^{NS}(x,t) = \frac{\alpha_s(t)}{2\pi}\left[P_{qq}^{NS} \otimes q^{NS}\right](x,t)\,, \tag{2.59}$$

$$\frac{\mathrm{d}}{\mathrm{dt}} \left[\begin{array}{c} \Sigma \\ g \end{array}\right](x,t) = \frac{\alpha_s(t)}{2\pi}\left[\begin{array}{cc} P_{qq}^{S} & P_{qg} \\ 2\,n_f\,P_{gq} & P_{gg} \end{array}\right] \otimes \left[\begin{array}{c} \Sigma \\ g \end{array}\right](x,t)\,. \tag{2.60}$$

The functions P_{ij} are the QCD *splitting functions* for the unpolarized parton densities. They represent the probability that a quark with momentum fraction x' originates from a parent quark with momentum fraction x and is given by $\alpha_s(t)P_{qq}(x'/x,t)$ while the probability that it is the result of a $q\,\overline{q}$ pair production from a gluon with momentum fraction x is given by $\alpha_s(t)P_{qg}(x'/x,t)$. Similar explanations hold for P_{gq} and P_{gg}. The processes described by the splitting functions are depicted in Fig. 2.8.

The expressions in Eqs. (2.59) and (2.60) allow the determination of the parton density functions at any value of Q^2 once they are determined for a fixed value Q_0^2. In addition, from these equations it can be seen that only the singlet combination Σ of the quarks couples to the gluon density, g, while the non-singlet part, q^{NS}, does not.

In analogy to the unpolarized case, distributions for the polarized non-singlet, Δq^{NS}, singlet $\Delta\Sigma$ and gluon, Δg, can be defined. They formally evolve in the same way as the corresponding unpolarized distributions. Therefore, given the splitting functions for polarized parton distributions, $\Delta P_{q\bar{q}}^{NS}$, $\Delta P_{q\bar{q}}^{S}$, ΔP_{qg} and ΔP_{gg}, the evolution equations follow from Eqs. (2.59) and (2.60) with the replacements $q^{NS} \rightarrow \Delta q^{NS}$, $\Sigma \rightarrow \Delta\Sigma$, and $g \rightarrow \Delta g$. The polarized gluon distribution, Δg, is defined according to that of the quark

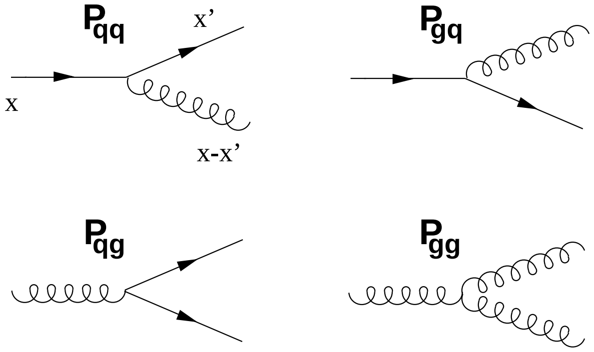

Figure 2.8: *The lowest order splitting functions. The function $P_{qq}(x'/x)$ gives the probability that by an increase of unit t a parton q with momentum fraction x emits a gluon and is left with momentum fraction $x' < x$. The same interpretation is valid for the other functions. In particular P_{qg} dynamically generates the sea quark distribution.*

distribution in Eq. (2.47): $\Delta g \equiv g^{\overrightarrow{\rightarrow}}(x) - g^{\overleftarrow{\rightarrow}}(x)$.
The polarized evolution equations provide information about the evolution of the differences of the parton helicity states. The expressions for the polarized and unpolarized structure functions Eqs. (2.45) and (2.46) in the parton model are given in a perturbative QCD calculation by Altarelli [43]

$$F_1(x,t) = \frac{1}{2}\langle e^2\rangle \left\{c^{NS}\otimes q^{NS} + c^S \otimes \Sigma + 2n_f c^g \otimes g\right\}(x,t)\,, \quad (2.61)$$

$$g_1(x,t) = \frac{1}{2}\langle e^2\rangle \left\{\Delta c^{NS}\otimes \Delta q^{NS} + \Delta c^S \otimes \Delta\Sigma + 2n_f \Delta c^g \otimes \Delta g\right\}(x,t)\,, \quad (2.62)$$

where $c^{S,NS,g}$ ($\Delta c^{S,NS,g}$) denote the so-called unpolarized (polarized) flavor singlet, non-singlet and gluon coefficient functions. Coefficients and splitting functions are usually expanded in a power series of the coupling α_s and the DGLAP equations hold in each order of the expansion. Coefficients and splitting functions for unpolarized and polarized cases have been computed up to next-to-leading order [44, 45]. This allows a complete NLO QCD analysis of the scaling violations of F_1 and g_1.
At LO in α_s, the unpolarized and polarized singlet and non-singlet coefficient functions are given by the delta function $\delta(1 - x'/x)$, while the gluon coefficient function vanishes. Thus, at LO the structure functions in the QCD formalism recover the expressions given in Eqs. (2.45) and (2.46), with the parton model quark densities $q_f(x)$ being replaced by Q^2-dependent densities $q_f(x,t)$.
The currently available measurements of the unpolarized structure functions (on different nuclear targets and with different probes) cover a broad range in x and Q^2. This enables one to test the predictions of the QCD evolution calculations. Evolution equations for parton distributions are used to extract a set of universal parton distribution from a fit to world data of many physical processes ($e.g.$ by the CTEQ collaboration [35] or by Germann $et\ al.$ [46]). The possibility of performing a global fit analysis tests the consistency of the assumed theoretical picture of hard scattering, based on factorization and on the universality of the parton distributions.
However, since in QCD there is no direct lepton-gluon coupling, the DIS process is directly sensitive to the gluon distribution only through the photon-gluon fusion. A quantitative analysis of the gluon distribution can be carried out at the NLO level by examining the Q^2-evolution of the gluon contribution to the unpolarized structure functions in experiments at different Q^2.
In analogy, parametrizations of polarized distributions for $\Delta\Sigma$, Δq_{NS}, and Δg can be obtained from fits to data of the spin asymmetry A_1 ($e.g.$ from Ref. [47]). However,

polarized inclusive DIS data alone do not provide enough information for a complete separation of the distributions for the different quark and antiquark flavors. In addition, the smaller amount of available polarized data compared to the unpolarized case imposes limitations on the precision of the fitting procedure of the QCD scale evolution.

2.5 Operator product expansion and sum rules

Sum rules establish relationships between the total integrated quark and antiquark densities and the macroscopic properties of the nucleon. For example, Eq. (2.48) provides the number of valence u and d quarks in the nucleon.
The importance of the sum rules relies on the fact that they do not depend on any model of hadronic structure, and provide a direct test of QCD. The Operator Product Expansion (OPE) [48, 49] formalism allows one to directly derive QCD sum rules for the structure functions.
As was shown in Section 2.2, the hadronic tensor $W_{\mu\nu}$ is related, via the optical theorem, to the helicity amplitudes for the forward photon-nucleon Compton scattering (see Eq. (2.15)). The amplitudes may be calculated as

$$A(\lambda'\Lambda'\,;\,\lambda\Lambda) = \varepsilon^{\mu}_{\lambda'}\varepsilon^{\nu}_{\lambda}T_{\mu\nu}\,, \tag{2.63}$$

and thus $W_{\mu\nu} = \frac{1}{2\pi}\mathrm{Im}T_{\mu\nu}$. Here, ε_λ denote the three polarization states of a photon with energy ν and squared mass Q^2 moving along the z-axis

$$\varepsilon^{\mu}_{\pm} = \mp\frac{1}{\sqrt{2}}(0,\,1,\,\pm i,\,0)\,, \quad \varepsilon^{\mu}_{0} = \frac{1}{\sqrt{Q^2}}(\sqrt{Q^2+\nu^2},\,0,\,0,\,\nu)\,. \tag{2.64}$$

The tensor $T_{\mu\nu}$ is written in terms of the time-ordered product of two electromagnetic currents as

$$T_{\mu\nu} = i\int d^4x e^{iqx}\langle PS|\mathcal{T}(J_\mu(x)J_\nu(0))|PS\rangle\,, \tag{2.65}$$

where S^μ is the covariant spin vector that defines the nucleon state of momentum P^μ.
The basic ideas of OPE is that in the limit $x \to 0$, the product of two electromagnetic currents can be written as an expansion in terms of a sum of local operators

$$\lim_{x\to 0} J_\mu(x)J_\nu(0) = \sum_k c_{\mu\nu k}(x)O_k(0)\,. \tag{2.66}$$

It follows that

$$T_{\mu\nu} = \frac{1}{4\pi}\sum_k c_{\mu\nu k}(Q^2)\langle PS|O_k(0)|PS\rangle\,, \tag{2.67}$$

where the Wilson coefficients $c_{\mu\nu k}(Q^2)$ are the Fourier transform of $c_{\mu\nu k}(x)$.
The operators O_k are the quark and gluons operators, and are specified by an arbitrary dimension, d, and spin, s. The contribution of any operator O_k to the hadronic tensor, and, therefore, to the cross-section, is defined by its *twist*: $t \equiv d - s$. The higher orders of twist are suppressed by $(\frac{M}{Q})^{t-2}$. In the Bjorken limit, only twist-2 functions contribute

to the cross-section, while for experimental values of Q^2, higher twist contributions may become significant.
In the OPE formalism, the n^{th} moment of a function $f(x)$ can be expressed in terms of operator and coefficient functions as

$$\int_0^1 x^{n-1} f(x)dx = \sum_i c_i(Q^2)\langle PS|O_i|PS\rangle \,. \tag{2.68}$$

To the leading twist, the first moment ($n = 1$) of g_1 for the proton and the neutron are given by [20]

$$\Gamma_1^{p\,(n)}(Q^2) = \int_0^1 g_1^{p\,(n)}(x)dx = \frac{1}{12}\left[+(-)a_3 + \frac{1}{3}a_8\right]\Delta C^{NS}(Q^2) + \frac{1}{9}a_0(Q^2)\Delta C^S(Q^2)\,. \tag{2.69}$$

Here, ΔC^{NS} and ΔC^S are the first moment of the flavor non-singlet and singlet coefficient functions, respectively:

$$\Delta C^{NS\,(S)}(Q^2) = \int_0^1 \Delta c^{NS\,(S)}(x, Q^2)dx\,. \tag{2.70}$$

The coefficient functions are scheme-dependent, in the *modified minimal subtraction* scheme ($\overline{\text{MS}}$) with $n_f = 3$ they are expanded as [50, 51]

$$\begin{aligned}
\Delta C^{NS} &= 1 - \frac{\alpha_s}{\pi} - 3.583\left(\frac{\alpha_s}{\pi}\right)^2 - 20.22\left(\frac{\alpha_s}{\pi}\right)^3 + \mathcal{O}(\alpha_s^4)\,, &(2.71)\\
\Delta C^S &= 1 - \frac{\alpha_s}{\pi} - 1.096\left(\frac{\alpha_s}{\pi}\right)^2 - \mathcal{O}(\alpha_s^3)\,. &(2.72)
\end{aligned}$$

In Eq. (2.69), $a_j S^\mu \equiv \langle PS|J_\mu^j|PS\rangle$ are the matrix elements for the proton expectation values of the axial-vector currents

$$J_\mu^j = \bar{\psi}\gamma_\mu\gamma_5\left(\frac{\lambda_j}{2}\right)\psi\,, \text{ with } j = 1, ..., 8\,, \tag{2.73}$$

and the flavor singlet current

$$J_\mu^0 = \bar{\psi}\gamma_\mu\gamma_5\psi\,. \tag{2.74}$$

In the previous equations, the vectors ψ are the quark fields in flavor space, and the matrixes λ_j are the generators of $SU(3)_f$ in the Gell-Mann notation, with $\lambda_0 = 2I$. The elements a_3 and a_8 are independent of Q^2, while a_0 depends upon Q^2.
In the QPM, the fields are treated as free fields, thus the a_j are related to the first moments $\Delta q_f = \int_0^1 dx\Delta q_f(x)$ of the polarized quark and antiquark distributions as

$$\begin{aligned}
a_0 &= \Delta\Sigma = \Delta u + \Delta\bar{u} + \Delta d + \Delta\bar{d} + \Delta s + \Delta\bar{s}\,,\\
a_3 &= \Delta q_3 = \Delta u + \Delta\bar{u} - (\Delta d + \Delta\bar{d})\,,\\
a_8 &= \Delta q_8 = \Delta u + \Delta\bar{u} + \Delta d + \Delta\bar{d} - 2(\Delta s + \Delta\bar{s})\,. &(2.75)
\end{aligned}$$

In this formalism, a_0 equals the fraction $\Delta\Sigma$ of the nucleon spin carried by the quark spins.

Assuming $SU(3)_f$ and isospin symmetries, the axial-vector currents of flavor octet of $SU(3)_f$, a_3 and a_8, can be expressed in terms of the decay constants F and D obtained from hyperon decay rates:

$$\begin{aligned} a_3 &= F + D = \left|\frac{g_A}{g_V}\right| = 1.2670 \pm 0.0035\,, \\ a_8 &= 3F - D = 0.584 \pm 0.032\,. \end{aligned} \tag{2.76}$$

The values given above are from Ref. [39]. The matrix element a_3 is directly determined from the ratio of the axial-vector coupling, g_A, and the vector coupling, g_V, in the neutron β-decay.
The matrix element a_0 cannot be calculated from decay constants, but may be determined from the measured values of $\Gamma_1^{p(n)}$ in Eq. (2.69) together with Eq. (2.76).
The axial currents J_μ^3 and J_μ^8 are conserved, while the flavor singlet current J_μ^0 is not ($\partial^\mu J_\mu^0 \neq 0$), and its matrix element is renormalization-scale dependent. Since the physical parameters are independent of scale, the axial-coupling a_0 cannot be interpreted as the total spin carried by quarks in the nucleon.
Adler, Bell and Jackwin showed in Refs. [52, 53] that an anomalous contribution arises in the calculation of the axial current matrix element a_0, which introduces a point-like interaction between J_μ^0 and gluons. through this *axial anomaly* $\Delta\Sigma$ becomes dependent on the factorization scheme. For instance, in the Adler-Bardeen (AB) scheme [54] the modified singlet axial-vector current element is given by

$$a_0(Q^2) = \Delta\Sigma - n_f \frac{\alpha_s(Q^2)}{2\pi} \Delta g(Q^2)\,. \tag{2.77}$$

Here, $\Delta\Sigma$ is independent of Q^2, but the value of $a_0(Q^2)$ can be obtained only providing an input value for $\Delta g(Q^2)$. In the $\overline{\text{MS}}$ scheme [55], $\Delta\Sigma = a_0(Q^2)$ and it depends on Q^2. The differences between the two schemes do not vanish in the limit $Q^2 \to \infty$ since the term $\alpha_s(Q^2)\Delta g(Q^2)$ remains finite for $Q^2 \to \infty$ [56].
Using the relations in Eqs. (2.75) and (2.76), constraints can be obtained on the flavor decomposition of the nucleon spin.

In the OPE formalism the structure function $g_2(x)$ is defined as a twist-3 contribution. In the Wandzura-Wilczek decomposition for g_2 [57]

$$g_2(x, Q^2) = g_2^{WW}(x, Q^2) + \hat{g}_2(x, Q^2)\,, \tag{2.78}$$

the term g_2^{WW} is given as a function of g_1 as follows

$$g_2^{WW}(x, Q^2) = -g_1(x, Q^2) + \int_x^1 g_1(t, Q^2) \frac{dt}{t}\,. \tag{2.79}$$

The term $\hat{g}_2$ is due to a twist-3 contribution in the operator product expansion [20] and is a measure of long-distance, non-perturbative effects like quark-quark or quark-gluon correlations in the nucleon.

2.5.1 Bjorken sum rule

The Bjorken sum rule [58] relates the difference between the first moment for proton and neutron spin structure functions to the axial-vector coupling g_A and g_V in neutron β decay:

$$\Gamma_{Bj} = \Gamma_1^p - \Gamma_1^n = \frac{1}{6}\left|\frac{g_A}{g_V}\right| \Delta C^{NS} = \frac{1}{6}\Delta q_3 \,. \tag{2.80}$$

Here, the QCD corrections are needed only for the non-singlet channel. The expansion of the non-singlet coefficient function is given by Eq. (2.72).
The Q^2 dependence of the Bjorken sum rule is driven by the scale dependence of $\alpha_s(Q^2)$ only. Therefore, the fact that Δq_3 does not depend on the renormalization scale implies that the Bjorken sum rule can provide a fundamental test of QCD. The Bjorken sum rule is experimentally confirmed with a precision of about 10%.

2.5.2 Ellis-Jaffe sum rule

Ellis and Jaffe [59] derived sum rules for Γ_1^p and Γ_1^n separately, with the assumption on the polarization of the strange sea $\Delta s = 0$. This leads to the relation $a_0 = a_8$.
Exploiting isospin symmetry and $SU(3)_f$ symmetry, Eq. (2.69) can be written as

$$\Gamma_1^{p\,(n)} = \frac{1}{12}\left[+(-)\left|\frac{g_A}{g_V}\right| + \frac{1}{3}(3F-D)\right]\Delta C^{NS}(Q^2) + \frac{1}{9}(3F-D)\Delta C^S(Q^2)\,, \tag{2.81}$$

where the relation $\Delta\Sigma = a_8 = 3F - D$ follows from the assumption on the contribution of strange sea. Also the Ellis-Jaffe sum rule requires QCD corrections both for the non-singlet, ΔC^{NS}, and singlet, ΔC^S, channels.

In the late '80s, the value for the integral of the spin structure function of the proton calculated by the EMC collaboration [9] was found to be in disagreement with the prediction for the Ellis-Jaffe sum rule. The interpretation of the measured value in the framework of the *naive parton model* led to the surprising result that only 12% of the spin of the proton arises from the spin of its constituent quarks [60]. In addition, as a consequence the strange quarks had also to be polarized antiparallel to the proton spin. This was the beginning of the so-called *Spin Crisis* in the parton model. Subsequent data from SLAC [12, 13, 14] and SMC [11, 10] confirmed the violation of the Ellis-Jaffe sum rule at the 3σ level also for the neutron.
However, the result in Eq. (2.77) leads to the fundamental implication that the small measured value of a_0 does not imply that $\Delta\Sigma$ is small.

2.6 Semi-inclusive deep-inelastic scattering

Semi-inclusive deep-inelastic scattering is a subprocess of inclusive scattering in which the additional high-momenta hadrons are detected in coincidence with the DIS lepton:

$$\ell + N \to \ell' + h + X\,. \tag{2.82}$$

Table 2.1 summarizes the definition of the kinematic variables used in semi-inclusive scattering, which is depicted in Fig. 2.9.

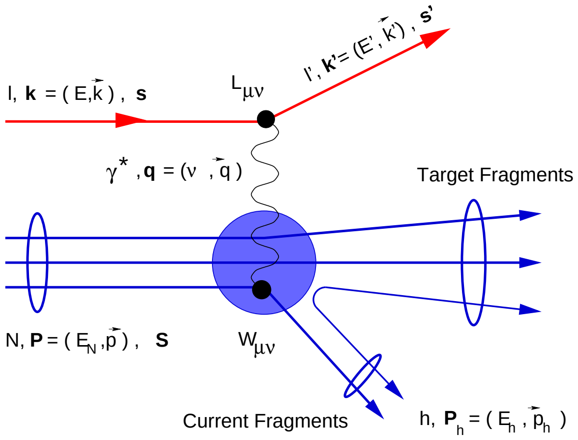

Figure 2.9: *Schematic diagram of semi-inclusive deep-inelastic lepton-nucleon scattering.*

Hadron production in DIS is described by the absorption of the virtual photon by the quark and the subsequent *fragmentation* into a final state hadron h.

The general approach to fragmentation is known as the *local parton-hadron duality* (LPHD) hypothesis [61], in which it is assumed that the flow of momentum and quantum numbers at the hadron level tend to follow the flow established at the parton level. Quantitative agreement between calculated parton spectra and measured hadron distributions have been experimentally confirmed, *e.g.* in e^+e^- [62] and DIS [63] processes.

The hadrons in the final state produced in the DIS process can be separated into two main kinematic classes according to the hadron momenta: the *current fragments* and the *target fragments* [64]. In the LPHD hypothesis, in the current fragmentation region one expects a strong correlation between the flavor of the struck quark and the types of produced hadrons, in particular for the hadrons whose valence quarks contain the flavor of the struck quark. Instead, the target fragments relate to the spectator remnant of the nucleon. Experimental evidence of a clean kinematic separation of the two fragmentation regions was demonstrated by the EMC collaboration [65] and . In addition, it was also found that the fast-forward hadron in the DIS event has a very high probability of containing the struck quark.

The existence of such a correlation between the struck quark and the hadron from the current fragmentation region is the underlying assumption in order to apply the quark flavor tagging method [66]. This method allows to extract information on the polarization of the quarks in the nucleon by using semi-inclusive measurements.

To achieve experimental sensitivity to the information on the spin structure of the nucleon carried by the detected semi-inclusive hadronic state, selection criteria are applied on the kinematic variables z and x_F, introduced in Section 2.1 (Eqs. (2.5) and (2.6)). The hadron produced in the fragmentation of the struck quark typically has a high forward momentum in the $\gamma^* N$ center of mass system ($x_F > 0$ and $z > 0.2$). Instead, hadrons originating from the target fragments have $x_F < 0$ and low momenta in the laboratoty system.

The fragmentation process is not calculable in perturbative QCD since it involves long

distance processes with low Q^2. Instead it is parametrized by *fragmentation functions* $\mathrm{D}_f^h(z)$ which denote the probability density of a quark of flavor f to produce a hadron h with an energy fraction z of the energy of the virtual photon.
Due to momentum conservation the fragmentation functions are normalized to conserve the total particle multiplicity, n_h, and total energy:

$$\sum_h \int_0^1 \mathrm{dz}\, \mathrm{D}_f^h(z) \;=\; n_h\,, \tag{2.83}$$

$$\sum_h \int_0^1 \mathrm{dz}\, z\, \mathrm{D}_f^h(z) \;=\; 1\,. \tag{2.84}$$

In the QPM picture, the partons in the nucleus are free and the hard-scattering process factorizes from the hadron-formation mechanism. The fragmentation process, where colored partons are transformed into color-neutral hadrons, is governed by long distance dynamics ($r \sim \frac{1}{\Lambda_{QCD}}$), where perturbation theory breaks down. Since it is not possible to compute the fragmentation process from first principles, it is necessary to resort to phenomenological models. The comparison of results on particle production resulting from experiments which employ different hard scattering processes allows to test the universality of the fragmentation functions predicted by the factorization theorem. QCD predicts the Q^2-scale dependence also for D_f^h which arises from gluon radiation from the final quark. This process is similar to the scaling violations of the quark distribution functions q_f by gluon radiation from the initial quark. Additionally, the exchange of gluons between the initial and final quarks can break the factorization assumption. However, these effects are small in NLO QCD calculations [67, 68].
The fragmentation functions implicitly contain the probabilities to create quark-antiquark pairs from the vacuum. Because of the uncertainty principle these probabilities are inversely proportional to the squared quark masses. At HERMES energies, the fragmentation of six quarks and antiquarks (u, d, s, $\bar{u}$, $\bar{d}$ and $\bar{s}$) dominantly produces six charged hadrons: π^+, π^-, K^+, K^-, p and $\bar{p}$. The strange quarks are suppressed by about a factor 3-5 compared to up and down quarks, while the creation of charmed and third generation quark pairs can be neglected in the fragmentation process. Thirty-six independent fragmentation functions then describe semi-inclusive particle production. However, isospin and charge conjugation invariance are usually used to reduce the number of independent fragmentation functions. In the case of charged pions it is possible to define the following functions:

$$\begin{array}{lcllllllll} \mathrm{D}^+ & \equiv & \mathrm{D}_u^{\pi^+} & = & \mathrm{D}_{\bar{d}}^{\pi^+} & = & \mathrm{D}_d^{\pi^-} & = & \mathrm{D}_{\bar{u}}^{\pi^-}\,, \\ \mathrm{D}^- & \equiv & \mathrm{D}_d^{\pi^+} & = & \mathrm{D}_{\bar{u}}^{\pi^+} & = & \mathrm{D}_u^{\pi^-} & = & \mathrm{D}_{\bar{d}}^{\pi^-}\,, \\ \mathrm{D}_s & \equiv & \mathrm{D}_s^{\pi^+} & = & \mathrm{D}_{\bar{s}}^{\pi^+} & = & \mathrm{D}_s^{\pi^-} & = & \mathrm{D}_{\bar{s}}^{\pi^-}\,. \end{array} \tag{2.85}$$

The function D^+ is called favored as the pion produced by each quark has that quark in its ground state wave function. This fragmentation is more probable than the unfavored and strange quark fragmentation functions described by D^- and D_s. The D^+ and D^- fragmentation functions have been measured in semi-inclusive DIS with pions in the forward region [69, 70].

2.6.1 Fragmentation models

Since it is not possible to calculate the fragmentation functions in perturbative QCD directly from first principles, several phenomenological models have been developed to predict the fragmentation functions.
The strategy adopted in general in these models is to break the fragmentation process into several phases [71]. Initially, a quark in the nucleon is struck by a virtual photon on a short time scale determined by $1/Q^2$. From the initial quark splitting $q \rightarrow qg$ a cascade of quarks develops from the emitted gluon as $g \rightarrow q\bar{q}$. The cascade is modeled perturbatively until the parton energies fall below a cutoff scale $t_0 \gg \Lambda_{QCD}$. At the end, the quarks are assigned to hadrons by an effective model of soft hadronization and are confined in a final state of color singlet hadrons.
Two models are used to describe hadron production at HERMES.

Independent fragmentation model
The independent fragmentation (IF) model, developed by Field and Feynman [72], assumes that each parton fragments independently from the others. In this scheme, the struck quark q_0 combines with the antiquark $\bar{q}_1$ of a pair $q_1\bar{q}_1$ created out of the vacuum. The $q_0\bar{q}_1$ pair produces a primary meson with energy fraction z, and the remaining quark q_1 is left with energy $1-z$. The process continues in the same way with the formation of the $q_1\bar{q}_2$ state from another $q_2\bar{q}_2$ pair. This process of meson formation proceeds until the remaining energy falls below a certain cutoff energy. The remaining quarks are then neglected, which leads to an explicit non-conservation of color and flavor quantum numbers in the hadronization.

Lund string model
The Lund string fragmentation (SF) model [73] is based on the idea that a fragmenting quark system is connected by color flux tubes, or strings. In QCD a linear confinement potential is expected at long distances. The string potential energy increases as the $q\bar{q}$ pair separates back-to-back stretching the srting. The string may then break into pieces by forming other $q\bar{q}$ pairs along the sting length. Each q and $\bar{q}$ form the end points of two new srtings which continue to hadronize following this model. The process ends when the string-connected quark pair reaches the on-shell mass of a hadron.
In this way, the SF conserves color and flavor quantum numbers, but as a consequence of the string-breaking method the baryon production is not naturally accommodated in the model. This feature is common also to the IF model. The SF model allows the radiation of gluons from strings, which produce "kinks" in the fragmentation. The problem of divergences in the cross-section is then circumvented by using cutoff parameters.

Both the LUND string and the independent fragmentation models have been implemented into the JETSET Monte Carlo generator [74] and tuned to reproduce HERMES particle multiplicities [70, 75, 76].

2.6.2 Cross-sections and asymmetries

In LO QCD the differential cross-section $d\sigma^h/dz$ for the production of a hadron of type h can be expressed in terms of fragmentation functions and unpolarized quark distribution functions as

$$\frac{\mathrm{d}\sigma^{\mathrm{h}}}{\mathrm{dz}}(z,Q^2) = \sigma_{\mathrm{INCL}}(x,Q^2)\left[\frac{\sum_f e_f^2\, q_f(x,Q^2)\,\mathrm{D}_f^h(z,Q^2)}{\sum_f e_f^2\, q_f(x,Q^2)}\right], \tag{2.86}$$

where $\sigma_{\mathrm{INCL}}(x,Q^2)$ is the inclusive DIS cross-section. The previous equation explicitly displays the factorization property by dividing the cross-section into two terms which depend separately on z and on x.

The fragmentation process is assumed to be spin-independent, *i.e.* that the probability to produce a hadron h from a struck quark q_f is independent on the relative orientation of the quark spin and on the nucleon spin. Hence, it is possible to define generalized structure functions F_1^h and g_1^h relevant to the semi-inclusive scattering. In the QPM, these may be written as

$$F_1^h(x,Q^2;z) = \frac{1}{2}\sum_f e_f^2\, q_f(x,Q^2)\,\mathrm{D}_f^h(z,Q^2)\,, \tag{2.87}$$

$$g_1^h(x,Q^2;z) = \frac{1}{2}\sum_f e_f^2\, \Delta q_f(x,Q^2)\,\mathrm{D}_f^h(z,Q^2)\,, \tag{2.88}$$

in complete analogy to the inclusive case.

Assuming $g_2^h = 0$, the z-integrated semi-inclusive spin asymmetries are related to the polarized and unpolarized quark distributions and fragmentation functions as follows

$$\begin{aligned} A_1^h(x,Q^2) &= \frac{\int dz\, g_1^h(x,Q^2;z)}{\int dz\, F_1^h(x,Q^2;z)} = \frac{\sum_f e_f^2\,\Delta q_f(x,Q^2)\,\int dz\,\mathrm{D}_f^h(z,Q^2)}{\sum_{f'} e_{f'}^2\, q_{f'}(x,Q^2)\,\int dz\,\mathrm{D}_{f'}^h(z,Q^2)}, \\ &= \frac{A_\parallel^h(x,Q^2)}{D(1+\eta\gamma)}, \end{aligned} \tag{2.89}$$

where the boundaries of the integration are $z \in [z_{min}, z_{max}]$ The region over which z is integrated is defined by the kinematic criteria applied to select hadrons from the current fragmentation region.

Semi-inclusive asymmetries offer more direct information on the individual contributions of the different quark flavors. Within the QPM, the charge and the valence quark composition of the hadron detected in coincidence with the scattered lepton provide sensitivity to the flavor of the struck quark.

In Chapter 5, a method of accessing quark polarization in semi-inclusive data will be presented. From a set of measured semi-inclusive asymmetries the complete flavor decomposition of the nucleon spin can be performed at the LO QCD by using Eq. (2.89) in combination with an input parametrization for the unpolarized parton distributions $q_f(x,Q^2)$ and the integrated fragmentation functions.

3 The HERMES experiment

The primary objective of the HERMES experiment is to study the spin structure of the nucleon by using deep-inelastic scattering of polarized positrons on a polarized gas target. High polarization of both beam and target is thus required to enhance the sensitivity to spin observables. The experiment was installed and commissioned in 1995, and DIS data were taken on a polarized ^{3}He target. In the following years a hydrogen polarized target (1996-1997) and a deuterium polarized target (1998-2000) were used.
The detector [77] is located in the East section of the HERA positron-proton collider facility at DESY in Hamburg (Germany). HERMES operates in fixed target mode and only the 27.5 GeV polarized positron beam interacts with the HERMES target, while the 820 GeV proton beam passes through the apparatus without interference. A schematic of the HERA positron ring is shown in Fig. 3.1. The polarization of the positron beam and the polarimetry methods are described in Section 3.1.
The storage-cell target employed at HERMES (Section 3.2) allows to achieve a luminosity of about 10^{32} $e^+\cdot$ nucleons/(cm$^2\cdot$s). Compared to polarized solid targets, the use of pure gas target species (hydrogen,deuterium, and ^{3}He) minimizes the dilution from unpolarized material in the beam-target interaction. The presence of this material contributes as background to the measurement. In addition, to minimize systematic uncertainties, the relative orientation of target and beam polarizations was frequently alternated (once every minute for hydrogen and deuterium targets, once every 10 minutes for the ^{3}He target).
Inclusive and semi-inclusive spin-dependent scattering events were measured simultaneously in the HERMES forward angle spectrometer with high precision and good particle identification. In Section 3.3, a description of the sub-detectors of the experimental set up is given. The performance of the particle identification (PID) system is discussed in Section 3.4. An overview of the triggering and data acquisition systems is given in Section 3.5.

3.1 The polarized positron beam at HERA

Either electrons or positrons can be stored in the HERA ring (6.3 km circumference). All the data collected during the running periods studied in this thesis, except for the year 1998, were produced with a positron beam.
In a storage ring a positron beam builds up a transverse polarization as a consequence of

a small asymmetric spin-flip amplitude in the emission of synchrotron radiation (Sokolov-Ternov effect [78]). The positron beam will be polarized parallel (antiparallel for electrons) with respect to the magnetic guide field in the ring.
For an ideal ring the polarization of the beam, $P_{beam}(t)$, increases exponentially in time, with a characteristic rise-time constant τ, according to

$$P_{beam}(t) = P_\infty(1 - e^{-t/\tau}) \ . \tag{3.1}$$

The constant τ depends on the geometry of the ring and the beam energy, and P_∞ is the asymptotic polarization value. Taking into account beam-depolarizing effects, the rise-time constant measured at HERA was $\tau =$ 22 min for a beam energy of $E_{beam} =$ 27.5 GeV. The average beam polarization is $P_{beam} =$ 40 – 60% [79]. Figure 3.2 shows a typical polarization rise-time curve obtained at HERA .
Longitudinal beam polarization at HERMES is accomplished by means of two spin rotators located at the entrance and exit of the HERMES section [80]. The rotators precess the spin direction from vertical to longitudinal at the target position and back to the vertical position as shown in Fig. 3.1. The spin rotators may themselves be rotated in order to reverse the positron beam helicity, thus reducing systematic uncertainties in the asymmetry measurements.
Two laser Compton back-scattering polarimeters are employed at HERMES for a precise measurement of the positron polarization. The transverse polarization is measured by a polarimeter located close to the West section of HERA . Near the HERMES region, another polarimeter (installed in 1997) independently monitors the longitudinal polarization of the beam.
The *transverse polarimeter* [79] is based on the principle that the Compton cross-section for transversely polarized leptons has a spin-dependent azimuthal distribution. A position

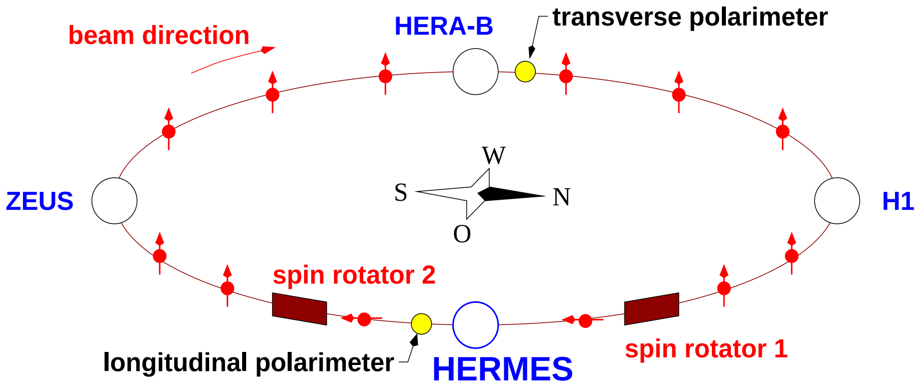

Figure 3.1: *Overview of the electron storage ring of HERA at DESY . Two spin rotators located in front and after the interaction point at HERMES allow for longitudinal polarization of the otherwise transversely polarized beam. The spin of the circulating electrons is indicated by the small arrows. The transverse and longitudinal polarizations are measured by two independent polarimeters located in the West and East areas. The proton ring of HERA is not shown.*

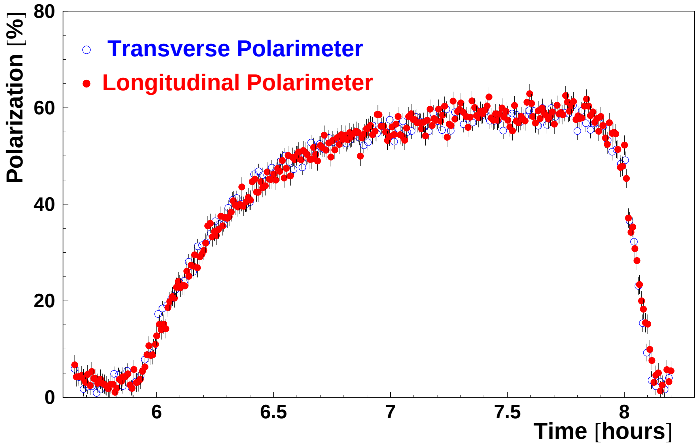

Figure 3.2: *Rise-time curve of the polarization at HERA as measured by the two polarimeters. The polarization of the beam was destroyed on purpose at the end of the plateau by using resonant depolarization.*

sensitive calorimeter measures the center of gravity of the back-scattered laser photons. The top-bottom asymmetry of the position distribution is used to derive the beam polarization [81]. Correlations between the position and energy of the Compton photons are used to study the precision of the polarization measurement with a systematic uncertainty of 3.4%.
A so-called *longitudinal polarimeter* [82] measures the longitudinal polarization of the beam near the HERMES interaction point. The longitudinal polarimeter uses the spin-dependent angular distribution of the Compton cross-section for longitudinally polarized leptons, which corresponds to a spin-dependent energy spectrum. By using laser pulses of high intensity several thousand photons are back-scattered per bunch of the positron beam. Hence, the energy-weighted spin asymmetry can provide a measurement of the polarization of each individual bunch [83]. The fractional systematic uncertainty associated with the longitudinal polarimeter is $\Delta P_{beam}/P_{beam} = 1.6\%$.
The measured polarization values are fitted for each fill in order to decrease the sensitivity to statistical fluctuations of the polarimeter measurements.

3.2 The HERMES polarized gas target

The HERMES experiment employs the *storage cell technique* to confine the polarized target atoms within a volume around the path of the positron beam [84]. The first internal polarized gas target with a storage cell was used at the *VEPP-3* electron storage ring facility in Novosibirsk [85].
Figure 3.3 illustrates the method: a polarized atomic beam is injected into an open-ended tube, and the atoms bounce a few hundred times within the cell volume before leaving from one of the extremities. This method allows for an increase of the target density by about two orders of magnitude compared to conventional polarized jet targets, which can obtain a target thickness of typically $\sim 10^{12}$ nucleons/cm^2 [86]. In addition, by cooling the storage cell, the target density can be further increased. At HERMES, for a cell temperature of 100K a target thickness of $\sim 10^{14}$ polarized nucleons/cm^2 is obtained in the case of hydrogen or deuterium gas, and of $\sim 10^{15}$ polarized nucleons/cm^2 in the case of ^{3}He gas.

Despite the low target thickness, polarized gas targets present several advantages compared to solid state polarized targets. For instance, the polarized target used by the SMC experiment had a thickness of 6.8×10^{24} atoms/cm^2 [87]. A solid state polarized target is characterized by chemical compounds (e.g., NH_3, and butanol) in a magnetic holding field of a few Tesla and at cryogenic temperature.
In a polarized gas target, a relatively low magnetic holding field is required to provide spin alignment. In addition, due to the high purity of the gases employed, negligible levels of contamination from chemical and isotopical compounds can be achieved. The use of radio frequency transitions for the selection of the injected atomic states allows for the reversal of the target polarization on a time scale of seconds. Therefore, systematic uncertainties are minimized.
Finally, taking into account the average current stored in the HERA positron ring ($\sim$30 mA), a sufficiently high luminosity of $\sim10^{32}$ $e^+\cdot$atoms/(cm$^2\cdot$s) can be achieved. As a consequence of the low target thickness, the operation of the HERMES internal target does not significantly affect the lifetime of the circulating beam, minimizing the impact of HERMES on the luminosity of the two collider experiments.
At HERMES two different setups have been used to realize polarized hydrogen, deuterium, and ^{3}He targets. Each target is characterized by a different atomic beam source and polarimetry technique, though the storage cells are similar for both.
In 1995, an infrared laser was used to polarized ^{3}He atoms through metastability-exchange optical-pumping in a quartz cell [88, 89]. The polarized atoms were then fed into the storage cell via a capillary tube. The operating target density at the temperature of 15 K was about $\sim10^{15}$ nucleons/cm^2. Conventional copper Helmholtz coils provided a magnetic holding field of 1mT in order to define the polarization quantization axis. The polarization of the ^{3}He target was determined in the pumping cell by measuring the degree of circular polarization of the photons emitted in the 667 nm transition. Typical polarization values of about 50% were achieved. The spin direction of the target was changed every 10 minutes by reversing the polarization of the laser light.
In 1996 and 1997, a polarized hydrogen target was used, while from 1998 to 2000 a polarized deuterium target was employed. The description of the HERMES polarized hydrogen/deuterium gas target and the determination the target polarization is discussed extensively in Chapter 3.

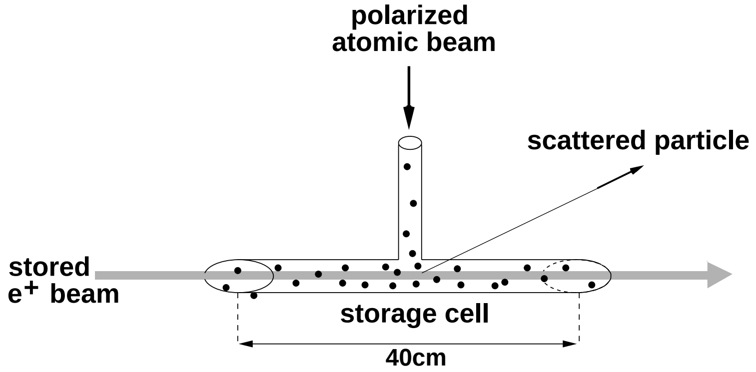

Figure 3.3: *Schematic representation of the storage cell technique implemented at the HERA positron ring for the HERMES experiment.*

3.3 The HERMES spectrometer

A schematic drawing of the HERMES spectrometer [90] is shown in Fig. 3.4. It consists of two identical halves above and below the positron ring plane. Each spectrometer half is equipped with the same sequence of detectors. This configuration allows to perform two independent measurements to control the systematic uncertainties. The origin of the HERMES coordinate system is defined at the center of the target. The positive z-axis is oriented along the positron beam direction, the y-axis is pointing vertically upwards, and the x-axis is pointing towards the outside of the ring, making a right-handed orthogonal axis system.
The particle momenta are measured by means of a dipole magnet with a magnetic bending field integral of $\int B \cdot dl = 1.3$ T·m. Tracking chambers situated before the magnet, inside the magnetic field, and behind the magnet measure the trajectories of charged particles. A system of segmented hodoscopes and a lead-glass calorimeter realize the trigger for deep-inelastic events. The particle identification section comprises, in addition to the calorimeter, a preshower detector, of a threshold Čerenkov counter and a transition radiation detector (TRD). The angular acceptance of the experiment is 40 mrad $\leq \theta \leq$ 220 mrad. At small angles this quantity is limited by the geometrical acceptance of the steel plate in the spectrometer magnet, which shields proton and positron beams from the field of the dipole magnet. The scattering angles in the vertical and horizontal plane result in an acceptance of 40 mrad $\leq |\theta_y| \leq$ 140 mrad and $|\theta_x| \leq$ 170 mrad respectively. The accessible kinematic range is 0.02 $< x <$ 0.8 and 0.2 GeV$^2 < Q^2 <$ 20 GeV^2.

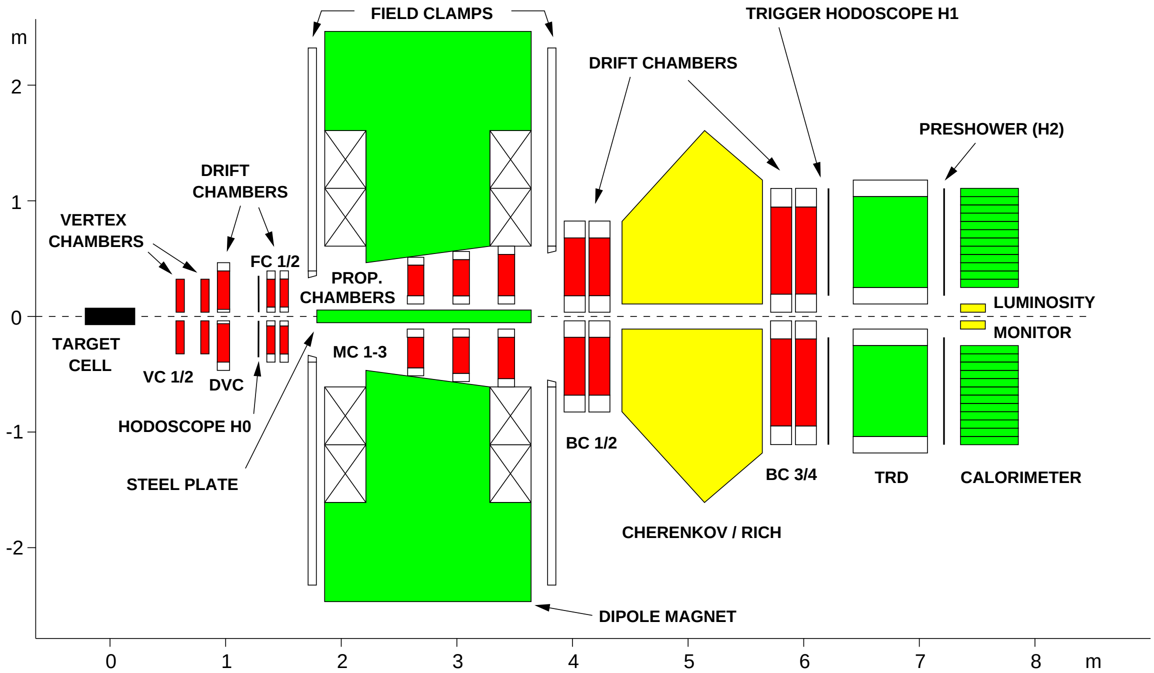

Figure 3.4: *Side view of the HERMES spectrometer. The various detector components are described in the text.*

3.3.1 Tracking system

The tracking system provides the measurement of the kinematics of the event. It determines the scattering angles, the interaction point at the target, and, in combination with the dipole spectrometer magnet, the particle momentum.
The tracking at HERMES may be divided into three sections with respect to the spectrometer magnet: the front region, the magnet region, and the back region. In front of the bending magnet the system is composed of two 3-plane microstrip gas counters (VC), a 6-plane drift chamber (DVC), and a pair of 6-plane drift chambers near the magnet (FC 1/2). The VC has been removed from the HERMES detector in 1998. Three proportional chambers are mounted within the gap of the magnet (MC 1-3). They are used in the reconstruction of low momentum tracks that do not completely pass the magnet. The tracking system behind the magnet consists of two pairs of large planar 6-plane drift chambers (BC 1/2 and BC 3/4).
In each tracking plane, the wires are oriented either vertical (for the measurement of the X coordinate) or tilted $\pm 30^o$ with respect to the vertical (U and V planes). To resolve left-right ambiguities, each plane is provided with a corresponding second plane with the same wire orientation, which is staggered by half the cell size. The HERMES track-reconstruction program is described in Section 3.5. The momentum resolution, $\Delta p/p$, is limited by the loss of energy of the particle in the material, and by multiple scattering in the tracking detector. For a scattered positron $\Delta p/p$ is about 1-3$\%$ depending on the kinematics. The scattering-angle resolution is better than 0.6 mrad. In terms of DIS kinematics, x and Q^2 can be determined from the scattered positron with an accuracy of 4-8$\%$ and 2$\%$, respectively [90].

3.3.2 Particle identification detectors

Particle identification at HERMES is accomplished by using four independent detectors: a threshold Čerenkov counter, a transition radiation detector (TRD), and an electromagnetic calorimeter (CALO) coupled to a preshower-hodoscope counter (Presh). The Čerenkov counter was used from 1995 to 1997, and in 1998 it was replaced by a Ring Imaging Čerenkov detector. All the PID detectors are located in the back region of the spectrometer. For each detector the response to positrons and hadrons is different. By combining the responses of all the detectors, hadrons and positrons can be separated.

Threshold Čerenkov detector

A charged particle, traversing a medium of refraction index n with a velocity v_p greater than the phase velocity of light (v_{ph}) in that medium, emits Čerenkov radiation under an angle θ_C according to

$$cos\,\theta_C = \frac{v_{ph}}{v_p} = \frac{1}{\beta n}\;. \tag{3.2}$$

The emission of Čerenkov radiation is characteristic of the threshold velocity of the particle in the medium $v_t = c/n$, and depends on the refraction index. Therefore, the threshold momentum p_t for a particle of mass m can be defined as

$$p_t = \beta_t \gamma_t m c \,, \tag{3.3}$$

where, $\beta_t = 1/n$ and $\gamma_t = 1/\sqrt{1-\beta_t^2}$. Different particle types with the same momentum will have different threshold momenta p_t, and the Čerenkov radiation will be emitted at different angles θ_C. This property is used in the threshold Čerenkov detector to separate particles based on their masses.
At HERMES the Čerenkov radiation emitted along the particle trajectory is focused by an array of 20 spherical mirrors mounted at the rear of each detector half. An array of 20 photomultipliers is used to detect the light. During the different periods of operation, the detector volume was filled with N_2 gas or mixtures of N_2 and C_4F_{10} gases, corresponding to less than 0.035 radiation lengths. Therefore, the Čerenkov detector could be located between the two sets of back tracking chambers without compromising the momentum measurement. Figure 3.5 shows a schematic drawing of the upper Čerenkov detector. Due to the different gas mixture used in each year, each period of data taking had a significantly different detector response. A summary of the radiator compositions for the different years together with the observed threshold momenta for the different particle types are given in Table 3.1.

	1995	1996	1997
Radiator	N_2	30% C_4F_{10}, 70% N_2	30% C_4F_{10}, 70% N_2
n_{radiator}	1.00031264	1.00066181	1.00066181
p_t (e) [GeV]	0.021	0.015	0.015
p_t (π) [GeV]	5.6	3.94	3.87
p_t (K) [GeV]	19.8	13.6	13.7
p_t (p) [GeV]	37.6	25.8	26.2

Table 3.1: *Observed parameters for the Čerenkov detector for the years 1995-1997.*

The signal in a photomultiplier is proportional to the number of generated photo-electrons N_{pe} and depends on the particle momentum. The positron signal is characterized by a continuous distribution in N_{pe} over the entire momentum range. The hadron signal shows a peak around zero N_{pe}, which is formed mostly by pions below threshold and kaons with momenta below 14 GeV. The N_{pe} distribution of pions above threshold largely overlaps with the positron distribution (see Fig. 3.6).

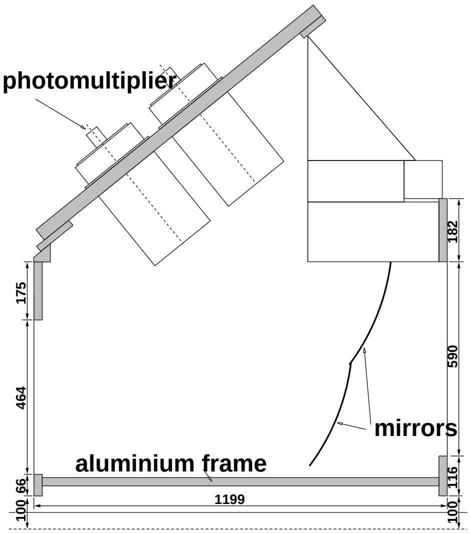

Figure 3.5: *Side view of the upper half of the Čerenkov detector.*

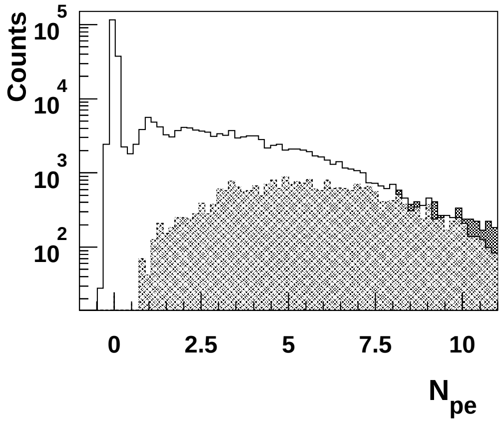

Figure 3.6: *Čerenkov signal in terms of generated photo-electrons N_{pe} for positrons (dark area) and for hadrons (shaded area) integrated over the entire momentum range.*

Ring Imaging Čerenkov detector (RICH)

HERMES employed the single-radiator Čerenkov counter described before for the data taking period 1995-1997. In 1998, the Čerenkov detector was replaced by a double-radiator RICH detector [91].

The angular distribution of the Čerenkov light can be used by a RICH detector to determine β, providing particle identification for pions, kaons, and protons. The use of two radiators allows the discrimination of different particle types over a wide momentum range (at HERMES 2-15 GeV).

In each half of the HERMES RICH, placed above and below the beam pipe, pure C_4F_{10} gas fills the same detector volume used for the threshold Čerenkov . In addition, a wall of silica aerogel located at the entrance window of the detector provides for the second radiator medium. A side view of one half of the RICH detector is shown in Fig. 3.7. The resulting threshold momenta for pions, kaons, and protons are listed in Table 3.2 for the two radiator types. The aerogel radiator is assembled in 5 stacks of 5×17 silica aerogel tiles, for a total thickness of 5.5 cm. For each detector half, an array of 8 spherical mirrors reflects the Čerenkov radiation cones on a 74×26 photomultipliers matrix, where the cones appear as quasi-elliptical rings. For particle identification with the HERMES RICH, a method based on the fitting of the Čerenkov ring is not feasible, since non-linearities of the imaging system distort the simple ring shape of the reflected Čerenkov cone.

In addition, it is important to note that the HERMES RICH operates "digitally" since the pulse-height information in the PMTs (that is proportional to the number of incident photo-electrons) is not stored. A PMT *fired* or has been *hit* if the signal exceeded a predetermined threshold. Two methods are currently available at HERMES for the recon-

struction of the Čerenkov angle: the direct ray tracing (DRT) method and the indirect ray tracing (IRT) method [92]. For both, the reconstruction procedure is event-based, and it uses as input information a list of fired PMTs and the parameters of the particle track incident on the RICH as determined by the tracking detectors. The number of fired PMTs strongly depends not only on the radiator type, but also on the position of the track on the detector. Therefore, effects related to detector acceptance and event topology need to be taken into account.
The principal characteristics of operation of two methods can be described as follows:

- DRT: assuming that the emission point of the Čerenkov radiation and the particle momentum are known, the DRT algorithm determines the reflection points of the rays on the mirrors and hits at the PMTs. This approach requires a Monte Carlo simulation of the path of Čerenkov photons along the particle track and the reflection on the mirrors. The process is done for each particle hypothesis. Finally, the particle hypothesis probability is determined from a comparison of the simulated hits and the actual fired PMT pattern.

- IRT: for each fired PMT, the Čerenkov angle associated with each track is calculated assuming all particle hypotheses. Imposing a window on the angular distributions obtained for each particle type around the expected Čerenkov angle, the average reconstructed angle is determined. A probability is assigned to the track for each particle hypothesis.

The DRT method is more effective at low momenta and in the range of the particle thresholds. However, the required relatively high number of simulated photon trajectories makes it slower in the data reconstruction as compared to the IRT method. An algorithm (*RICH PID Scheduler*, RPS) was developed [93] to assign to each track of the event the particle type hypothesis as calculated either by the IRT or the DRT depending on the specific track momentum and topology.

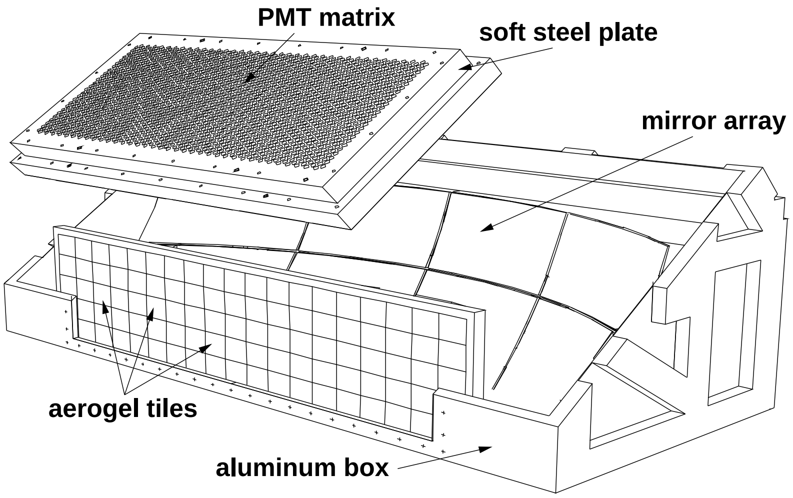

Figure 3.7: *Schematic view of the upper RICH detector*

	Radiator	
	Aerogel	C_4F_{10}
n_{radiator}	1.0304	1.00137
$\beta_t\gamma_t$	4.03	19.10
$\Delta\theta$ [mrad]	7.6	7.5
p_t (π) [GeV]	0.6	2.7
p_t (K) [GeV]	2.0	9.4
p_t (p) [GeV]	3.8	17.9

Table 3.2: *The HERMES RICH parameters for the two radiators. The angular resolution, $\Delta\theta$, and the particle thresholds are indicated.*

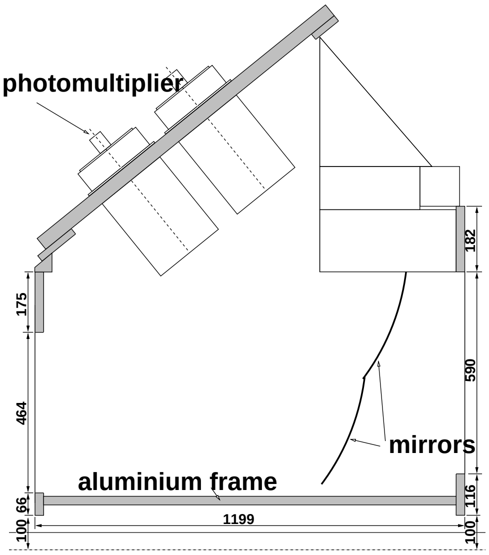

Figure 3.8: *Momentum dependence of the reconstructed Čerenkov angles for the silica aerogel and gas radiators in the HERMES RICH detector.*

Particle identification with the RICH is available for both methods for the 1999 and 2000 data sets, and also the RPS selection information is there incorporated. Instead, the 1998 set has been reconstructed with IRT only. In this thesis, the particle identification type assigned by the IRT method was chosen. The probability analysis used for hadron identification with the IRT is discussed in Section 3.4. Figure 3.8 shows the average reconstructed angles for the two radiators separately with the IRT method.

Transition Radiation Detector

Transition radiation is emitted when a relativistic charged particle crosses a boundary between media of different dielectric constants. Similar to bremsstrahlung radiation, transition radiation is emitted in the forward direction, and the angle ϑ between the radiation and the particle trajectory is inversely proportional to the Lorentz factor: $\vartheta \propto 1/\gamma$. The mean energy radiated is in the range of X-ray photons (several keV) and it is directly proportional to γ. Positrons at HERMES have $\gamma >$ 6000, compared to hadrons which have $\gamma <$ 200. Therefore, hadron/positron separation is possible by detecting the emitted X-ray radiation.

The HERMES TRD consists of 2 sandwich structures located above and below the beam line, each realized by 6 modules of radiators and X-ray detectors. In each module the radiator is placed in front of a conventional multiwire proportional chamber (MWPC). The radiator is made of a two-dimensional matrix of polyethylene/polypropylene fibers. The thickness of each radiator is 6.5 cm, which corresponds to an average of 267 dielectric layers. Positrons deposit on average two times more energy than hadrons in the MWPCs, due to the additional ionization from transition radiation. The signal from the TRD is realized by combining the information from all the modules but the one that produced the largest signal. This method, called the *truncated-mean average*, reduces the overlapping region in the hadron and positron distributions.
The response of the TRD to positrons and hadrons integrated over all momenta is shown in Fig. 3.10. Hadron/positron separation is obtained by placing constrains on the signals of the other PID detectors.

Calorimeter and preshower detector

Particle identification with a calorimeter is based on the topological difference between the development of electromagnetic and hadronic showers.
The HERMES calorimeter consists of 840 radiation-hard lead-glass blocks, coupled to photomultipliers, arranged in two walls symmetrically located with respect to the beam pipe, as shown in Fig. 3.9. Each block has an area of 9×9 cm^2 and a length of 50 cm, corresponding to about 18 radiation lengths. This block size meets the requirements that $\simeq$ 90% of the shower is contained in a single block for an electron incident in the center at straight angles. The measured characteristics of the calorimeter comprise a 1% linearity in energy response to electrons over the range 1−30 GeV, an energy resolution $\sigma(E)/E[\%] = 5.1\sqrt{E}+1.5$, and an energy uniformity within 1%.

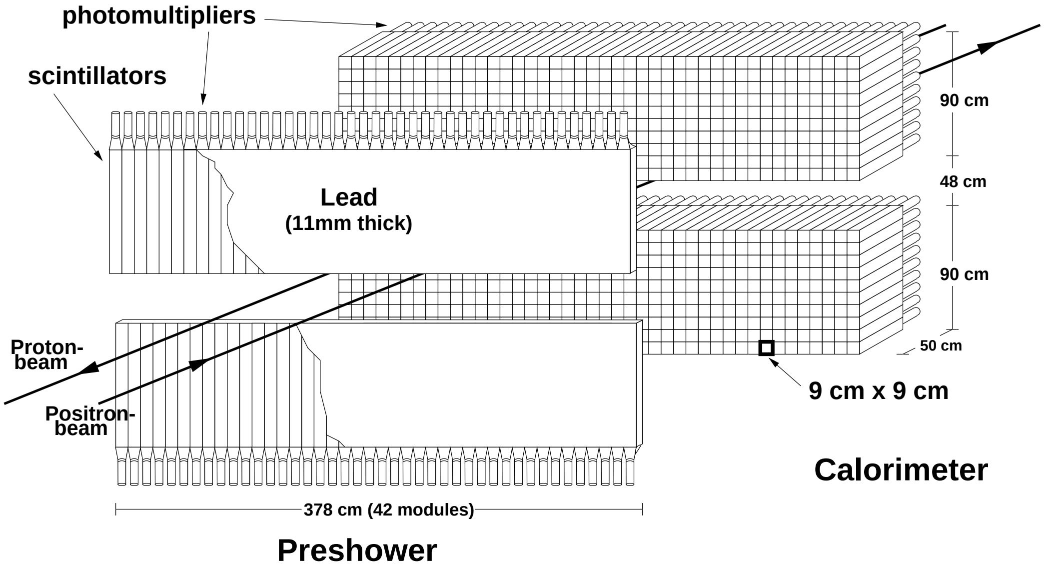

Figure 3.9: *Overview of the preshower and the calorimeter.*

The preshower detector (also called hodoscope H2) consists of 1 cm of lead ($\sim$ 2 radiation lengths) and 1 cm of plastic scintillators, and it is placed directly in front of the calorimeter. The preshower can be seen as an integrated part of the calorimeter itself, providing information on the longitudinal development of the electromagnetic shower. The complete calorimeter-preshower system accounts for $\sim$20 radiation lengths in total and can completely contain electromagnetic showers. On the other hand, 1 cm of lead corresponds to about 0.064 nuclear interaction length. Therefore, hadrons typically induce a minimum ionizing signal in the preshower detector. Figure 3.10 shows the response of the preshower for hadrons and positrons integrated over all momenta. The preshower signal allows for a better positron/hadron discrimination. With the calorimeter-preshower combination a hadron rejector factor is obtained of $\simeq(2.5 \pm 1.2)\times 10^3$ integrated over all energies, for a positron detection efficiency of 95%.
The calorimeter signal and preshower signal are used, together with the signals of the other hodoscopes, for making the trigger decision at first level on scattered positrons (see Section 3.5).

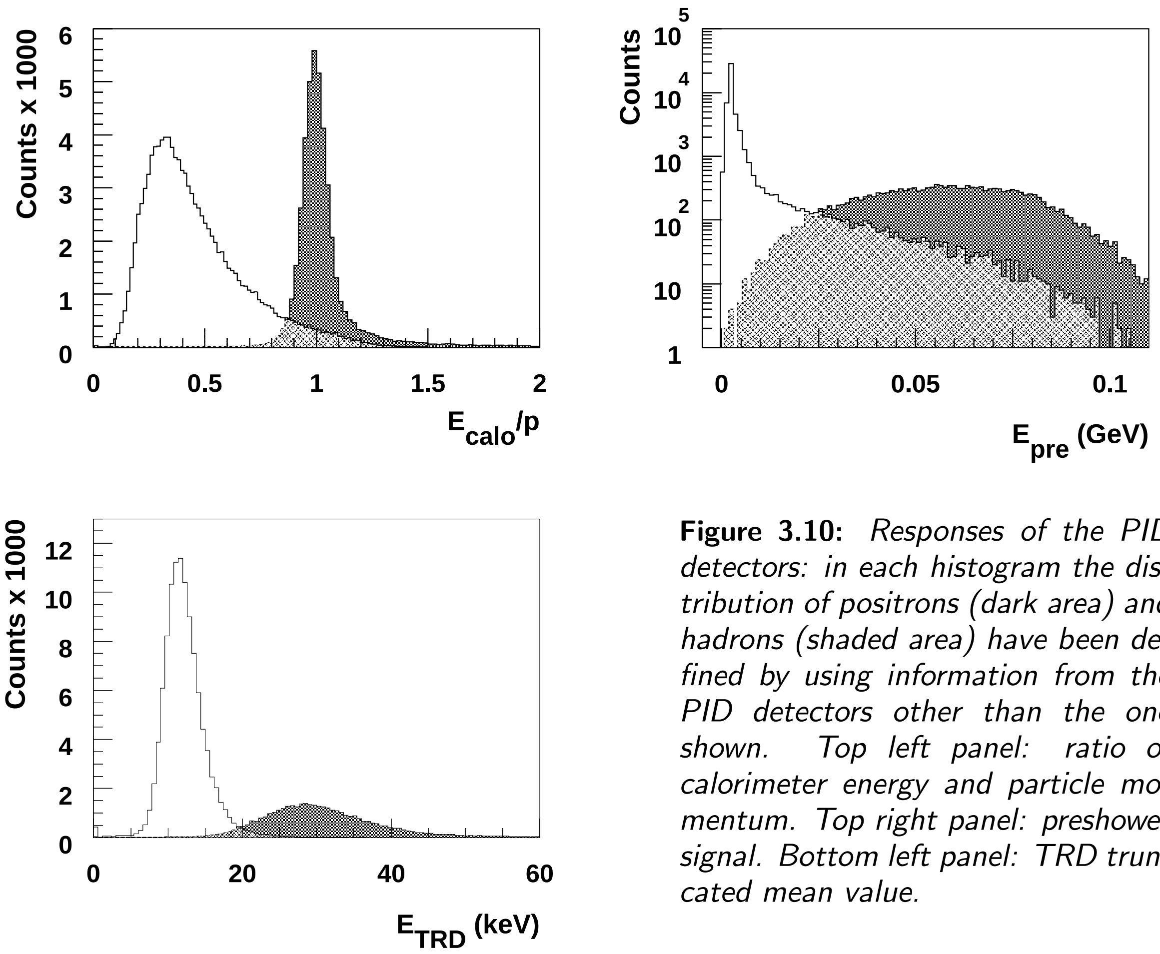

Figure 3.10: *Responses of the PID detectors: in each histogram the distribution of positrons (dark area) and hadrons (shaded area) have been defined by using information from the PID detectors other than the one shown. Top left panel: ratio of calorimeter energy and particle momentum. Top right panel: preshower signal. Bottom left panel: TRD truncated mean value.*

3.3.3 Luminosity monitor

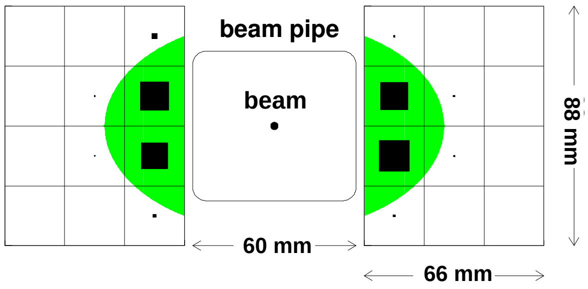

Figure 3.11: *The HERMES luminosity monitor. The beam pipe acceptance is shown by the gray area. The size of the black boxes is proportional to the number of track hits per detector crystal.*

For the measurement of the luminosity at HERMES the elastic scattering of the beam particles with the electrons in the target gas is used. The cross-sections for elastic scattering $e^+e^- \rightarrow e^+e^-$ (Bhabha scattering) and the annihilation into photon pairs $e^+e^- \rightarrow \gamma\gamma$ are known precisely from QED, including radiative corrections. In the case of an electron beam, Møller scattering $e^-e^- \rightarrow e^-e^-$ is used.
The scattered particles are detected in coincidence by a pair of calorimeters symmetrically placed on either side of the beam pipe at a distance of 7.21 m downstream of the target center. Figure 3.11 schematically represents the HERMES luminosity monitor. Each calorimeter module consists of 3×4 NaBi $(WO_4)_2$ crystals, which are radiation hard. The coincidence is made by requiring two simultaneous signals of approximately equal energy, about half the beam energy each, corresponding to elastic scattering at about $\theta_{CM} = 90^o$. The coincidence rate is about 130 Hz for a beam current of 20 mA and for an areal target density of 10^{15} nucleons/cm^2. This allows to measure the luminosity with a statistical uncertainty of about 1% within 100 s.
Residual electron polarization in the nuclear polarized target gas (about 1-2% for hydrogen and less that 0.2% for deuterium) produces an asymmetry in the luminosity yields for the different target states. To avoid a bias in the luminosity measurement due to this asymmetry, the coincidence rates are fitted over time intervals much longer than the typical spin-reversal time of the target. The fitting curve is an exponential function representing the time dependence of the beam current for a constant density in the target.

3.3.4 Hodoscopes

In the HERMES back region two hodoscopes are installed: H1 and H2. The latter is part of the Preshower detector, and was already introduced in Section 3.3.2. The hodoscopes are used for triggering and particle identification. For each detector half, both counters are composed of 42 vertical plastic-scintillator paddles, 9.3 cm wide and 91 cm long. In H2, each paddle is aligned with a corresponding column of blocks in the calorimeter. The paddles are staggered and overlap each other by 2-3 mm.
A front region hodoscope (H0) was installed in 1996 mainly for trigger purposes. H0 is comprised of a single sheet of plastic scintillator 3.2 mm thick (0.7% radiation length), and it is located before the front chambers. The H0 hodoscope distinguishes forward and backward going particles by using time-of-flight information in combination with the rear hodoscopes.

3.4 Performance of the PID system

The PID analysis scheme at HERMES is based on a Bayesan probability analysis of the responses from the PID detectors which were described in Section 3.3.2. A combination of the PID detector signals allows for the identification of positrons with a hadron contamination less that 1% over the HERMES kinematic range.
In this approach the responses from each detector D are converted into *conditional probabilities* $\mathcal{L}^i_{\mathrm{D}}$, which give the probability that a given signal is recorded by the detector D when a particle of type i passes the detector. At HERMES the probability distribution for each PID detector (so-called *parent distribution*) is derived by comparing the responses for positrons and hadrons by using a clean sample of data. These samples are obtained by imposing restrictive selection criteria on the PID detectors other than the one considered. The individual conditional probabilities for each PID detector are combined to form overall conditional probabilities

$$\mathcal{L}^i \equiv \prod_{\mathrm{D}} \mathcal{L}^i_{\mathrm{D}} \,. \tag{3.4}$$

Assuming that the incident flux ϕ^i of particles of type i is known, then the true probabilities P^i that a track originated from a particle of type i can be derived as

$$\mathcal{P}^i = \frac{\phi^i \, \mathcal{L}^i}{\sum_j \phi^j \, \mathcal{L}^j} \,, \tag{3.5}$$

In the case of only two particle types (positrons e and hadrons h) the probability that the detected particle is a positron is given by

$$\mathcal{P}^e = \frac{\mathcal{L}^e}{\phi \, \mathcal{L}^h + \mathcal{L}^e} \,, \tag{3.6}$$

where only the parent distributions for positrons and hadrons and the flux ratio $\phi = \phi^h/\phi^e$ need to be known. In general, ϕ is function of particle momentum, p, and scattering angle, θ, as well as of the particle charge. The value of ϕ for positive and negative charges is derived from data with an iterative Bayesian approach and parametrized as a function of p and θ [94].

Hadron/Positron Separation

At HERMES hadron/positron separation is made by introducing the likelihood PID. This quantity is defined as the logarithm of the ratio of the true probabilities $\mathcal{P}^e$ and $\mathcal{P}^h$:

$$PID \equiv \log_{10} \frac{\mathcal{P}^e}{\mathcal{P}^h} = \log_{10} \frac{\mathcal{L}^e}{\mathcal{L}^h} - \log_{10} \phi \,. \tag{3.7}$$

The PID distribution for each detector intuitively resembles the detector response. At $PID = 0$, the probability for a particle to be a positron or a hadron is equal for an equal incident flux of positrons and hadrons. If the flux ratio ϕ in Eq. (3.7) is neglected, the resulting PID distribution is shifted by $\log_{10} \phi$. The logarithmic likelihood for different detectors can be combined. For instance, the responses of calorimeter, preshower counter, and threshold Čerenkov detector form the logarithmic likelihood PID_3

$$PID_3 \equiv \log_{10} \frac{\mathcal{L}^{e}_{\mathsf{CAL}} \cdot \mathcal{L}^{e}_{\mathsf{CER}} \cdot \mathcal{L}^{e}_{\mathsf{PRE}}}{\mathcal{L}^{h}_{\mathsf{CAL}} \cdot \mathcal{L}^{h}_{\mathsf{CER}} \cdot \mathcal{L}^{h}_{\mathsf{PRE}}} . \tag{3.8}$$

As the TRD detector consists of six modules, according to the truncated mean method (see TRD description in Section 3.3.2) the responses from 5 individual modules are combined into the logarithmic likelihood PID_5:

$$PID_5 \equiv \log_{10} \frac{\mathcal{L}^{e}_{\mathsf{TRD}}}{\mathcal{L}^{h}_{\mathsf{TRD}}} \equiv \log_{10} \frac{\prod_{m=1}^{5} \mathcal{L}^{l}_{\mathsf{TRD}\,,m}}{\prod_{m=1}^{5} \mathcal{L}^{h}_{\mathsf{TRD}\,,m}} , \tag{3.9}$$

For the analysis these two quantities are usually joined together

$$PID \equiv \log_{10} \frac{\mathcal{L}^{e}_{\mathsf{CAL}} \cdot \mathcal{L}^{e}_{\mathsf{CER}} \cdot \mathcal{L}^{e}_{\mathsf{PRE}} \cdot \mathcal{L}^{e}_{\mathsf{TRD}}}{\mathcal{L}^{h}_{\mathsf{CAL}} \cdot \mathcal{L}^{h}_{\mathsf{CER}} \cdot \mathcal{L}^{h}_{\mathsf{PRE}} \cdot \mathcal{L}^{h}_{\mathsf{TRD}}} = PID_3 + PID_5 . \tag{3.10}$$

Since 1998, when the threshold Čerenkov detector was replaced by the RICH, the quantity related to PID_3 was modified into the quantity PID_2 as follows

$$PID_2 \equiv \log_{10} \frac{\mathcal{L}^{e}_{\mathsf{CAL}} \cdot \mathcal{L}^{e}_{\mathsf{PRE}}}{\mathcal{L}^{h}_{\mathsf{CAL}} \cdot \mathcal{L}^{h}_{\mathsf{PRE}}} , \tag{3.11}$$

as the RICH detector is not used in the standard PID scheme. The quantities PID_2, PID_3, and PID_5 are not equivalent to the real probabilities, because they do not include the flux ratio. For each track the corrected probability is derived by subtracting from the PID term the value of the flux ratio $\log_{10} \phi(p, \theta)$, where momentum p and angle θ are specific for the track. The distributions of PID_2, PID_5, and their sum are shown in Fig. 3.12 for a sample of data. The effect of the inclusion of the flux ratio ϕ is illustrated. In the data analysis, positrons are identified by requiring $PID_2 + PID_5 - \log_{10} \phi \geq 2$, while hadrons are selected for a criteria $PID_2 + PID_5 - \log_{10} \phi \leq 0$.
Applying this PID scheme, the positron identification efficiency is above 97% and the contamination of hadrons in the positron sample remains below 0.01% over the entire kinematic range. For hadrons, the average efficiency is 99% with a positron contamination below 0.6%. A hadron rejection factor better than 10^4 is necessary since the rate of low momentum hadrons from photo-production is much higher than the rate of DIS electrons with the same momentum.

Pion/Kaon Separation

For the years 1995 till 1997, the threshold Čerenkov detector was used in the likelihood analysis for the hadron/positron separation. The detector mainly allows for selection of pions from other hadrons between the pion momentum threshold and the kaon threshold. Thresholds for kaons and protons are too high to achieve a statistically significant sample for these particles.
The pion identification efficiency could be determined from a selection of diffractively

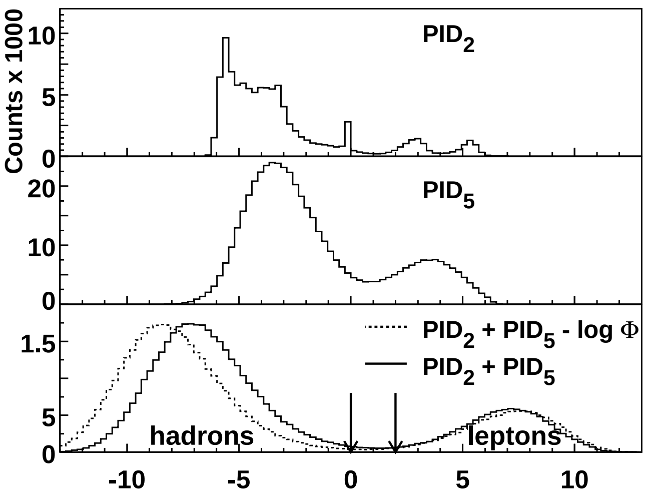

Figure 3.12: *PID parameters for all particle momenta from 1999 data: PID_2 is the combined responses of calorimeter and preshower counter; PID_5 is realized from the responses of the individual TRD modules. The sum of the two parameters is shown with and without flux factor ratio. The arrows in the bottom panel indicate the criteria used in the analysis to separate hadrons from leptons. The counts are given in arbitrary units.*

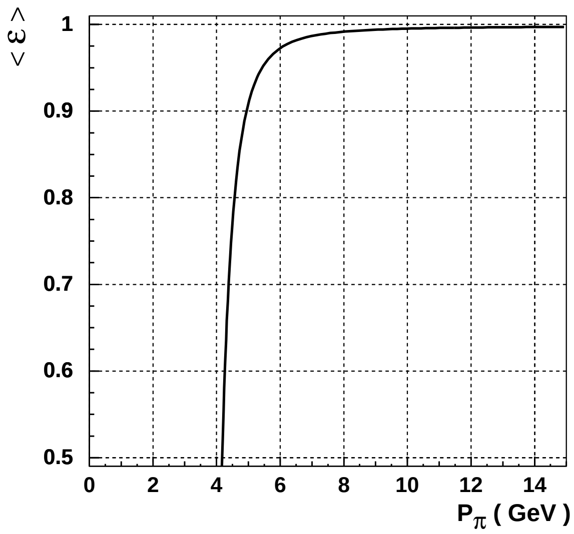

Figure 3.13: *Average pion identification efficiency for the Čerenkov detector as a function of the pion momentum (1997 data set).*

produced ρ^0 mesons decaying into two pions: $\rho^0 \rightarrow \pi^+\pi^-$. Unfortunately, at HERMES no sufficient statistics for a reliable extraction can be obtained in this channel. Instead, a parametrization of the pion efficiency can be obtained in terms of the average number of photo-electrons, N_0, detected for a particle with $\beta \approx 1$, and as a function of the pion momentum threshold:

$$\epsilon = 1 - e^{-N_0\left(1-\frac{\gamma_t^2}{\gamma^2}\right)} . \tag{3.12}$$

Here, $\gamma = \sqrt{1-\beta^2}$ and $\beta = p/E$. The number for N_0 can be determined with a high statistics sample of positrons, and the momentum threshold is defined with a clean hadron sample. Figure 3.13 shows the pion identification efficiency as a function of the pion momentum for the 1997 data taking period [95]. The pion identification efficiency is about 80% for particle momenta greater than 4.5 GeV, and asymptotically increases to unity. For momenta larger than 7.5 GeV efficiencies above 99% are achieved.

For the years 1998-2000, the RICH detector allows to separate pions, kaons and protons from other hadrons for particle momenta between 2 and 15 GeV. The parti-

cles to be identified by the RICH have been already defined as hadrons by the other PID detectors. In addition, muons are neglected, as they only form a small contamination of the pion sample.
As described in Section 3.3.2, the inverse ray tracing method (IRT) reconstructs one Čerenkov angle for each combination of fired-PMT/track per radiators, *i.e.* one so-called "gas angle" and one "aerogel angle". Depending on the track momentum, the IRT likelihood algorithm assigns identification probabilities to the track by using both the threshold aspects of the detector and the imaging techniques [96]. Over the distributions of the measured angles for each particle hypothesis i, a window $[\theta^i_{th} - \sigma_w, \theta^i_{th} + \sigma_w]$ is imposed on the angular distributions centered around the theoretically expected Čerenkov angle θ^i_{th}. From the angles within this window the average angle $\langle\theta^i\rangle$ is calculated. The value of θ^i_{th} depends on the radiator, particle type, and track momentum. The width σ_w is set to four times the single-photon resolution of the RICH.
For each particle type, the normalized distribution of the measured averaged angles forms a conditional probability. Assuming known relative particle fluxes, for a Gaussian distribution of the average reconstructed angles, the likelihood for the particle hypothesis i is calculated as

$$L_i(\langle\theta^i\rangle) = \exp\left[-\frac{(\theta^i_{th} - \langle\theta^i\rangle)^2}{2\sigma^2_{\langle\theta^i\rangle}}\right] . \tag{3.13}$$

At the denominator, $\sigma_{\langle\theta\rangle}$ is the average angle resolution, which is calculated from the single photon resolution $\sigma_{\langle\theta\rangle} = \sigma_\theta/\sqrt{N_{PMT}}$. The likelihoods for the two radiators are combined by multiplication to obtain an overall likelihood. The particle type is assigned to the particle hypothesis with the highest likelihood.
In addition, the quality parameter rqp,

$$rqp = \log_{10}\left(\frac{L_1}{L_2}\right) , \tag{3.14}$$

defines the likelihood ratio of the most likely, L_1, and the second most likely, L_2, particle type hypothesis. In particular when $L_1 = L_2$ the particle type is considered *undefined*. The request of a minimum value for rqp can be used to reduce contamination, at the expense of the efficiency.
The likelihood analysis employed by the IRT algorithm assigns to each track a probability for each particle type. Therefore, efficiencies and contaminations in the RICH detector depend on all the particle hypotheses at the same time. This is explained in the following. If N^i_t is the number of particles of type t that cross the detector and that are identified as particles of type i, then it is possible to define the *identification probabilities* P^i_t as

$$P^i_t = \frac{N^i_t}{\sum_j N^j_t} . \tag{3.15}$$

For example, P^i_π with $i = \pi$, K, p, X, defines the identification probability that a pion is identified as a pion, kaon, proton or unknown particle. Considering pion, kaon and proton as the only particle types incident on the RICH, the values $P^i_{\pi,K,p}$ form a matrix:

$$P = \begin{pmatrix} P^\pi_\pi & P^\pi_K & P^\pi_p \\ P^K_\pi & P^K_K & P^K_p \\ P^p_\pi & P^p_K & P^p_p \\ P^X_\pi & P^X_K & P^X_p \end{pmatrix} . \tag{3.16}$$

By definition, the columns of the P-matrix are normalized to one.
In order to study the RICH response to different particle types, clean samples of pions and kaons were selected from decaying particles [97]: $\rho^0 \rightarrow \pi^+\pi^-$ and $K_s \rightarrow \pi^+\pi^-$ for pions, and $\phi \rightarrow K^+K^-$ for kaons. In addition, the decay of the Λ hyperon $\Lambda \rightarrow p\pi^-$ was used to obtain information on the proton response.
Due to the limited statistics for decaying particles and the strong dependence on the event topology, the identification efficiency has been additionally determined from Monte Carlo methods and compared to data. In this way, the P identification matrix can be extracted for every track multiplicity per detector half and event topology as a function of the momentum. Pion identification efficiency, P^π_π, for single track is above 92% even at low momenta, and above 98% for momenta larger than 4 GeV. For kaons, the efficiency decreases for particle momenta at the gas threshold, between 9 and 10 GeV. In this range, kaons produce too few Čerenkov photons, and from the corresponding number of fired PMTs in the gas window the particle is not identified as a kaon but as a subthreshold proton.
Complementary information on the detector performance, directly connected to the identification efficiency matrix, is given by the *contamination matrix*. The elements of this matrix are the *true type probabilities*, Q^i_t, that a particle identified as type i is really of type t. The elements of the Q-matrix are related to those of the P-matrix as

$$Q^i_t = \frac{P^i_t \cdot \phi_t}{\sum_k P^k_t \cdot \phi_k} , \tag{3.17}$$

where ϕ_t is the relative flux for hadrons of type t. Figure 3.14 shows the values of the Q-matrix as a function of the momentum for pions and kaons for one and two tracks per detector half.

The P-matrix and therefore the Q-matrix are defined for each event topology as a function of the momentum. In the semi-inclusive analysis the selection of pions and kaons candidates is performed on a track-by-track basis considering the particle momentum and the track multiplicity of the event. Depending on the track characteristics, the vector $\vec{N} = (N_\pi, N_K, N_p)$ containing the fractional numbers of true hadron types is extracted from the vector $\vec{I} = (I_\pi, I_K, I_p, I_X)$ of the identified hadron as [98]:

$$\vec{N} = Q \cdot \vec{I} , \tag{3.18}$$

where the Q-matrix contains the elements specific for this track. Details on the selection of the semi-inclusive events are discussed in Section 5.1.3.

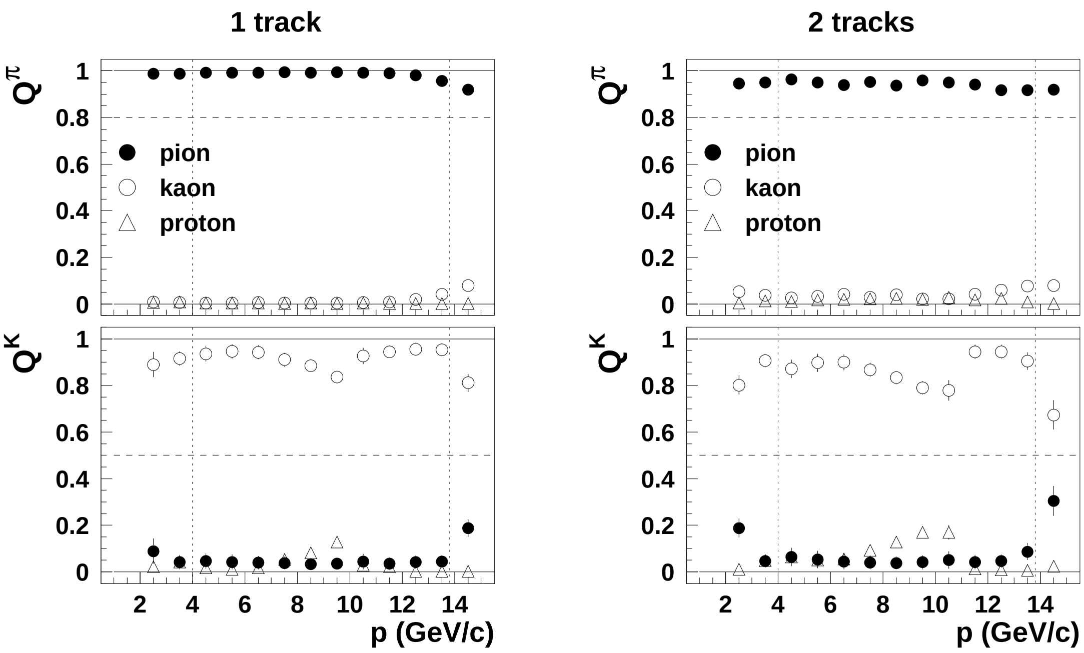

Figure 3.14: *Elements of the Q-matrix for pions and kaons as a function of the track momentum, for one (left panel) and two (right panel) tracks per detector half. The vertical dotted lines indicate the momentum window of the selected hadron tracks for the semi-inclusive analysis. The horizontal dashed lines represent the criteria applied to the Q-matrix elements as described in the text.*

3.5 The trigger and the data acquisition system

The trigger system used during data acquisition at HERMES is a first-level trigger. It initiates digitization and readout of the detector signals in correspondence to interesting physics events. The typical data taking rate for polarized gas target mode is $\sim$ 50 Hz.
Different trigger schemes are implemented in the experiment for the different physics analyses or for detector monitoring and calibration. For the inclusive and semi-inclusive asymmetries the DIS positron candidates are selected by using the *deep-inelastic trigger* (also called *trigger 21*). This requires a scattered beam particle with an energy deposit of at least 3.5 GeV in two adjacent columns of the calorimeter. The calorimeter response should be in coincidence with the signals in the hodoscopes H0, H1, and H2 in the correct time relationship (only H1 and H2 in 1995).
When a positive trigger decision is reached, the Data AcQuisition system (DAQ) initializes the readout of all the detectors information relative to the event. The data are compressed and sent to the online workstation system, which stores them on disk and on tape. The HERMES DAQ consists of front-end FASTBUS crates holding the electronic equipment (ADC, TDC, *etc.*) that performs the digitization of the signals coming from each detector. During the time needed for the digitization and the readout of the detec-

tor components, no new trigger can be accepted, leading to a *dead time* of the trigger system.
The raw events collected online are separated in *runs*, corresponding to about 50 Mbyte of recorded data. The time length of a run is about 2 minutes at the beginning of the fill, and 10 minutes at the end of the fill of data taking. Scalers are internal counters of the DAQ-system, which store the numbers of generated and accepted triggers. The readout of the scalers is synchronized by the *slow-control system*, and the information is acquired every 10 s, defining a *burst*. In addition to the detector readout initiated by a physics trigger, the slow-control system provides the continuous monitoring of information such as target status, chambers pressure, beam current, *etc.* The slow-control ensures that on a time scale of typically a few seconds all these data are also stored on disk and on tape.
The stored raw data need to be further processed and synchronized with the slow-control information before they can be used for physics analyses. This process is performed *offline* by a chain of software packages. The HERMES decoder (HDC) converts the raw data written in EPIO [99] format into ADAMO format [100], which is the database used at HERMES. Mapping information and calibration files are applied to the data at this stage.
The HERMES reconstruction software (HRC) [101] uses the HDC data to perform track reconstruction in two steps. First a *tree-search* pattern recognition algorithm recursively identifies track hits in each tracking-detector plane. Straight partial tracks in the chambers are formed independently for the front and back tracking regions. Then, the set of front and back partial tracks are matched at the magnet center (with some pre-specified tolerance) to form the reconstruction of a *full track*. The matching condition consists of well specified tolerances in the coordinates x and y (5 cm in each direction). In addition, the slope dy/dz is required to be within 0.05 for both partial tracks. This technique results in a momentum resolution of $\Delta p/p \sim$ 1-3%.
The reconstructed track information from HRC is synchronized with the slow-control data and stored in so-called μDST (Data Summary Tape) format. The μDSTs contain all the information of the triggered events and detector status, and are used in the further physics analyses.

4 The polarized internal gas target at HERMES

As introduced in Section 3.2, at HERMES spin dependent structure functions are studied by using the internal target technique. The storage cell internal to the HERA beam pipe increases the target density without affecting the quality of the circulating positron beam. A flux of highly polarized atomic hydrogen or deuterium gas is injected into the cell by means of an Atomic Beam Source (ABS). In this chapter, a short review of the hyperfine splitting mechanism for hydrogen and deuterium atoms is given in Section 4.1, and the several components of the HERMES longitudinally polarized target are described individually. A schematic layout of the polarized target is shown in Fig. 4.1.

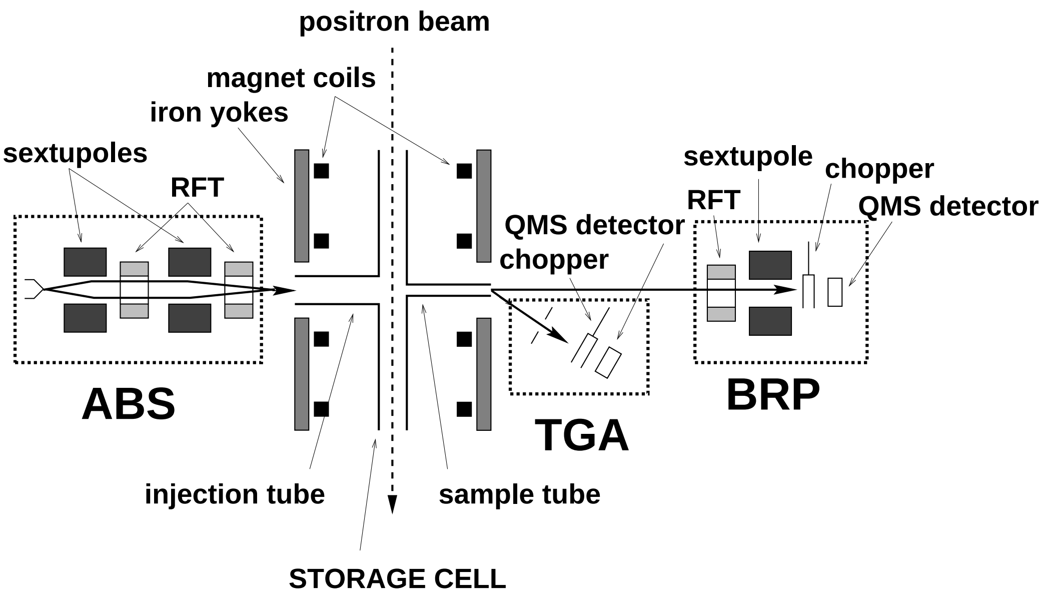

Figure 4.1: *Schematic layout of the components of the HERMES polarized target: the Atomic Beam Source (ABS), the Target Gas Analyzer (TGA) and the Breit-Rabi Polarimeter (BRP). The radio-frequency transition units (RFT) and the quadrupole mass spectrometer detector (QMS) are also indicated.*

Polarized atoms are fed by the ABS into the center of the storage cell through the injection tube. A fraction of the gas (about 2%) is extracted via the sample tube and diffuses into the Target Gas Analyzer (TGA) and into the Breit-Rabi Polarimeter (BRP) to be analyzed (Sections 4.4 and 4.5, respectively). The TGA measures the relative atomic and molecular content of the sampled gas, and the BRP measures the polarization of the sampled atoms. This information is needed in order to accurately estimate the polarization of the target (Section 4.6). Finally, Section 4.7 presents results of a study performed on a transversely polarized target. In a future phase of the HERMES physics program this target configuration will allow the investigation of spin observables related to transverse degrees of freedom of the nucleon.

4.1 Hyperfine structure of hydrogen and deuterium

The interaction Hamiltonian of an atom in the presence of a static magnetic field $\vec{B}$ can be written as

$$\mathcal{H}_{stat} = A_{HFS}\vec{I}\cdot\vec{S} + \frac{g_S\mu_B}{\hbar}\vec{S}\cdot\vec{B} + \frac{g_I\mu_B}{\hbar}\vec{I}\cdot\vec{B}\ . \tag{4.1}$$

In the equation above the first term represents the coupling between the electron spin $\vec{S}$ and nucleon spin $\vec{I}$, with strength A_{HFS}. The second and the third term represent, respectively, the interaction of the electron and of the nucleus with the external magnetic field. The Bohr magneton is denoted by μ_B, while $g_S = 2.0023$, and $g_I^H = -0.00152$ are the gyromagnetic factors for electron and proton, respectively. In the case of the deuteron $g_I^D = -0.00047$.
For a hydrogen atom the energy eigenvalues of the static Hamiltonian, $\mathcal{H}_{stat}$, in Eq. (4.1) equal:

$$\begin{aligned} E_1 &= \tfrac{E^H_{HFS}}{4}(1+2x(1-\epsilon_H))\ ,\\ E_2 &= \tfrac{E^H_{HFS}}{4}(-1+2\sqrt{x^2(1+\epsilon_H)^2+1}\,)\ ,\\ E_3 &= \tfrac{E^H_{HFS}}{4}(1-2x(1-\epsilon_H))\ ,\\ E_4 &= \tfrac{E^H_{HFS}}{4}(-1-2\sqrt{x^2(1+\epsilon_H)^2+1}\,)\ . \end{aligned} \tag{4.2}$$

Here, $x = B/B_c^H$, and B_c^H is the critical field for hydrogen which is defined as

$$B_c = \frac{A^H_{HFS}\hbar}{g_S\mu_B} = 50.7\ \text{mT}\ . \tag{4.3}$$

In addition, the term $\epsilon_H = g_I^H/g_S$ is small and it is neglected in the following. The critical field B_c characterizes the strength of the interaction between the spin of the electron and the spin of the proton. For $x = 0$, the two possible spin states with total spin $\vec{F} = \vec{I} + \vec{S} = \frac{1}{2} \pm \frac{1}{2}$ are $(2F+1)$-fold degenerate. The energy splitting between the two levels is $E^H_{HFS} = A^H_{HFS}\hbar^2 = 5.87\cdot10^{-6}$ eV, corresponding to a frequency ν^H_{HFS} of 1420.4 MHz. The introduction of the external magnetic field $\vec{B}$ leads to the removal of the degeneracy of the states with $F = 1$. Two limits of the magnetic field strength may be considered. In the weak field limit ($B \ll B_c$), the terms in Eq. (4.1) representing

Hydrogen	Deuterium
$\|1\rangle = \|\frac{1}{2}, \frac{1}{2}\rangle$ $\|2\rangle = \cos\theta\|\frac{1}{2}, -\frac{1}{2}\rangle + \sin\theta\| - \frac{1}{2}, \frac{1}{2}\rangle$ $\|3\rangle = \| - \frac{1}{2}, -\frac{1}{2}\rangle$ $\|4\rangle = \sin\theta\|\frac{1}{2}, -\frac{1}{2}\rangle - \cos\theta\| - \frac{1}{2}, \frac{1}{2}\rangle$	$\|1\rangle = \|\frac{1}{2}, 1\rangle$ $\|2\rangle = \cos\theta_+\|\frac{1}{2}, 0\rangle + \sin\theta_+\| - \frac{1}{2}, 1\rangle$ $\|3\rangle = \cos\theta_-\|\frac{1}{2}, -1\rangle + \sin\theta_-\| - \frac{1}{2}, 0\rangle$ $\|4\rangle = \| - \frac{1}{2}, -1\rangle$ $\|5\rangle = \sin\theta_-\|\frac{1}{2}, -1\rangle - \cos\theta_-\| - \frac{1}{2}, 0\rangle$ $\|6\rangle = \sin\theta_+\|\frac{1}{2}, 0\rangle - \cos\theta_+\| - \frac{1}{2}, 1\rangle$
$\cos\theta = \sqrt{\frac{1}{2}\left(1 + \frac{x}{\sqrt{x^2+1}}\right)}$	$\cos\theta_\pm = \sqrt{\frac{1}{2}\left(1 + \frac{3x\pm1}{\sqrt{(3x\pm1)^2+8}}\right)}$

Table 4.1: *Energy eigenstates of the static Hamiltonian in Eq. (4.1) for hydrogen (left column) and deuterium (right column) atoms in the basis defined by* $|m_S, m_I\rangle$.

the interaction with the external magnetic field can be treated as a perturbation with respect to the coupling term $\vec{I} \cdot \vec{S}$. In this case the states $|F, m_F\rangle$ form a suitable basis for describing the energy states of the Hamiltonian. For large values of B ($B \gg B_c$), the electronic and nuclear spins decouple as the interaction with the external magnetic field becomes dominant. In this limit the states $|m_S, m_I\rangle$ form a good basis for the Hamiltonian. The energy eigenstates of $\mathcal{H}_{stat}$ for a hydrogen atom, expressed as linear combination of the eigenvectors of the spin operators $\vec{S}$ and $\vec{I}$, are listed in the left column of Table 4.1.

In analogy to the hydrogen atom, the energy eigenvalues of $\mathcal{H}_{stat}$ for a deuterium atom are given by

$$
\begin{aligned}
E_1 &= \frac{E^D_{HFS}}{3}(1 + \frac{3}{2}x(1 - 2\epsilon_D)) \,, \\
E_2 &= \frac{E^D_{HFS}}{6}(-1 + \sqrt{9x^2(1 + 2\epsilon_D)^2 + 6x(1 + 2\epsilon_D) + 9}\,) \,, \\
E_3 &= \frac{E^D_{HFS}}{6}(-1 + \sqrt{9x^2(1 + 2\epsilon_D)^2 - 6x(1 + 2\epsilon_D) + 9}\,) \,, \\
E_4 &= \frac{E^D_{HFS}}{3}(1 - \frac{3}{2}x(1 - 2\epsilon_D)) \,, \\
E_5 &= \frac{E^D_{HFS}}{6}(-1 - \sqrt{9x^2(1 + 2\epsilon_D)^2 - 6x(1 + 2\epsilon_D) + 9}\,) \,, \\
E_6 &= \frac{E^D_{HFS}}{6}(-1 - \sqrt{9x^2(1 + 2\epsilon_D)^2 + 6x(1 + 2\epsilon_D) + 9}\,) \,,
\end{aligned}
\tag{4.4}
$$

where $x = B/B^D_c$, and the critical field for deuterium is $B^D_c = 11.7$ mT. Also in this case the term $\epsilon_D = g^D_I/g_S$ is neglected in the following. The energy due to the hyperfine splitting is $E^D_{HFS} = A^D_{HFS}\hbar^2 = 1.35 \cdot 10^{-6}$ eV, corresponding to $\nu^D_{HFS} = 327.4$ MHz. The energy eigenstates of the Hamiltonian in Eq. (4.1) are listed in the right column of Table 4.1. The hyperfine splitting levels as a function of the strength of the external magnetic field are represented in Fig. 4.2 for both hydrogen and deuterium atoms.

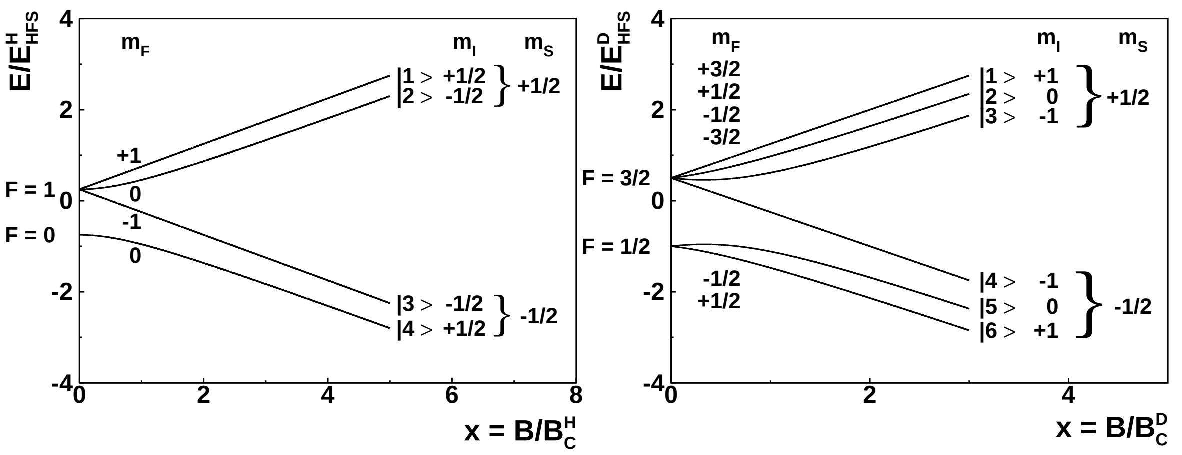

Figure 4.2: *Hyperfine structure of hydrogen (left) and deuterium (right) in units of the critical field $x = B/B_c$. The quantum numbers F, m_F (m_I, m_S) are indicated for the weak (strong) field limit on the left (right) side of each panel.*

The electron polarization, P_e, and the nuclear polarization, P_z, of a set of atoms is given by the expectation value

$$P_{e,z} = \sum_i n_i \langle i|\mathcal{P}_{e,z}|i\rangle \ , \tag{4.5}$$

where n_i is the relative occupation number of the hyperfine state $|i\rangle$ in the ensemble, and $\mathcal{P}_{e,z}$ are the projection operators of the electron and proton polarization, respectively. For hydrogen atoms the electron and the nuclear polarization equal:

$$\begin{aligned}
\langle 1|\mathcal{P}_e|1\rangle &= +1 \ , & \langle 1|\mathcal{P}_z|1\rangle &= +1 \ , \\
\langle 2|\mathcal{P}_e|2\rangle &= +cos2\theta \ , & \langle 2|\mathcal{P}_z|2\rangle &= -cos2\theta \ , \\
\langle 3|\mathcal{P}_e|3\rangle &= -1 \ , & \langle 3|\mathcal{P}_z|3\rangle &= -1 \ , \\
\langle 4|\mathcal{P}_e|4\rangle &= -cos2\theta \ , & \langle 4|\mathcal{P}_z|4\rangle &= +cos2\theta \ .
\end{aligned} \tag{4.6}$$

Using the identity cos$2\theta = \frac{x}{\sqrt{1+x^2}}$, the average polarization of the ensemble can be written as

$$\begin{aligned}
P_e &= n_1 - n_3 + (n_2 - n_4)\tfrac{x}{\sqrt{1+x^2}} \ , \\
P_z &= n_1 - n_3 - (n_2 - n_4)\tfrac{x}{\sqrt{1+x^2}} \ .
\end{aligned} \tag{4.7}$$

The dependence of nuclear and electron polarization on the external magnetic field strength for a set of hydrogen atoms is shown in Fig. 4.3.
Correspondingly, the expectation values for the nuclear and electron polarization in a

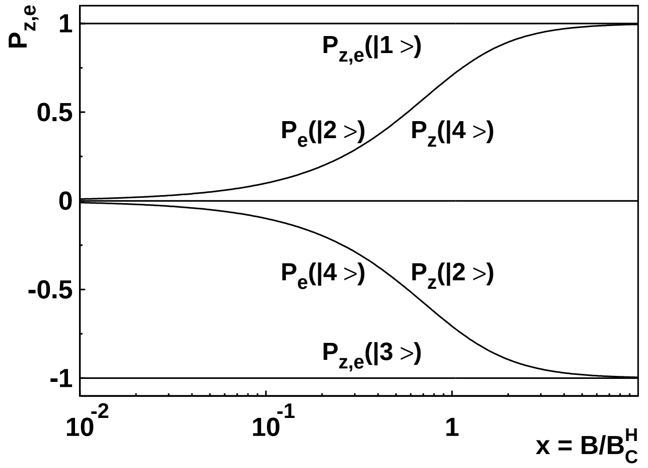

Figure 4.3: *Expectation values for nuclear and electron polarization of the four hyperfine states of a set of hydrogen atoms in the ground state, as a function of external magnetic field.*

sample of deuterium atoms is given by:

$$\begin{aligned}
\langle 1|\mathcal{P}_e|1\rangle &= +1\,, & \langle 1|\mathcal{P}_z|1\rangle &= +1\,,\\
\langle 2|\mathcal{P}_e|2\rangle &= +\cos 2\theta_+\,, & \langle 2|\mathcal{P}_z|2\rangle &= +\tfrac{1}{2}\left(1-\cos 2\theta_+\right)\,,\\
\langle 3|\mathcal{P}_e|3\rangle &= +\cos 2\theta_-\,, & \langle 3|\mathcal{P}_z|3\rangle &= -\tfrac{1}{2}\left(1+\cos 2\theta_-\right)\,,\\
\langle 4|\mathcal{P}_e|4\rangle &= -1\,, & \langle 4|\mathcal{P}_z|4\rangle &= -1\,,\\
\langle 5|\mathcal{P}_e|5\rangle &= -\cos 2\theta_-\,, & \langle 5|\mathcal{P}_z|5\rangle &= -\tfrac{1}{2}\left(1-\cos 2\theta_-\right)\,,\\
\langle 6|\mathcal{P}_e|6\rangle &= -\cos 2\theta_+\,, & \langle 6|\mathcal{P}_z|6\rangle &= +\tfrac{1}{2}\left(1+\cos 2\theta_+\right)\,,
\end{aligned} \tag{4.8}$$

In the previous equations the identity

$$\cos 2\theta_\pm = \frac{3x \pm 1}{\sqrt{9x^2 \pm 6x + 9}} \tag{4.9}$$

has been used. The deuterium nucleus has $I = 1$, therefore in a magnetic field there are three possible projections for $\vec{I}$: $m_I = +1$, 0 and -1. The determination of the nuclear *vector* polarization, P_z, is not sufficient for an univocal determination of the occupation probabilities for the three quantum states. The so-called *tensor* polarization, P_{zz}, is defined as a function of the relative occupation numbers corresponding to the three possible m_I values:

$$P_{zz} = n_{(m_I=+1)} + n_{(m_I=-1)} - 2n_{(m_I=0)} = 1 - 3n_{(m_I=0)}. \tag{4.10}$$

The tensor polarization expectation values are obtained from the tensor polarization projector operator, $\mathcal{P}_{zz}$, on the deuterium atom hyperfine states:

$$\begin{aligned}
\langle 1|\mathcal{P}_{zz}|1\rangle &= +1\,, & \langle 4|\mathcal{P}_{zz}|4\rangle &= +1\,,\\
\langle 2|\mathcal{P}_{zz}|2\rangle &= -\tfrac{1}{2}\left(1+3\cos 2\theta_+\right)\,, & \langle 5|\mathcal{P}_{zz}|5\rangle &= -\tfrac{1}{2}\left(1+3\cos 2\theta_-\right)\,,\\
\langle 3|\mathcal{P}_{zz}|3\rangle &= -\tfrac{1}{2}\left(1-3\cos 2\theta_-\right)\,, & \langle 6|\mathcal{P}_{zz}|6\rangle &= -\tfrac{1}{2}\left(1-3\cos 2\theta_+\right)\,.
\end{aligned} \tag{4.11}$$

The values of both polarizations P_z and P_{zz} determine the distribution of the three spin states in a sample of deuterium nuclei. Equations (4.5), (4.8), and (4.11) imply for the

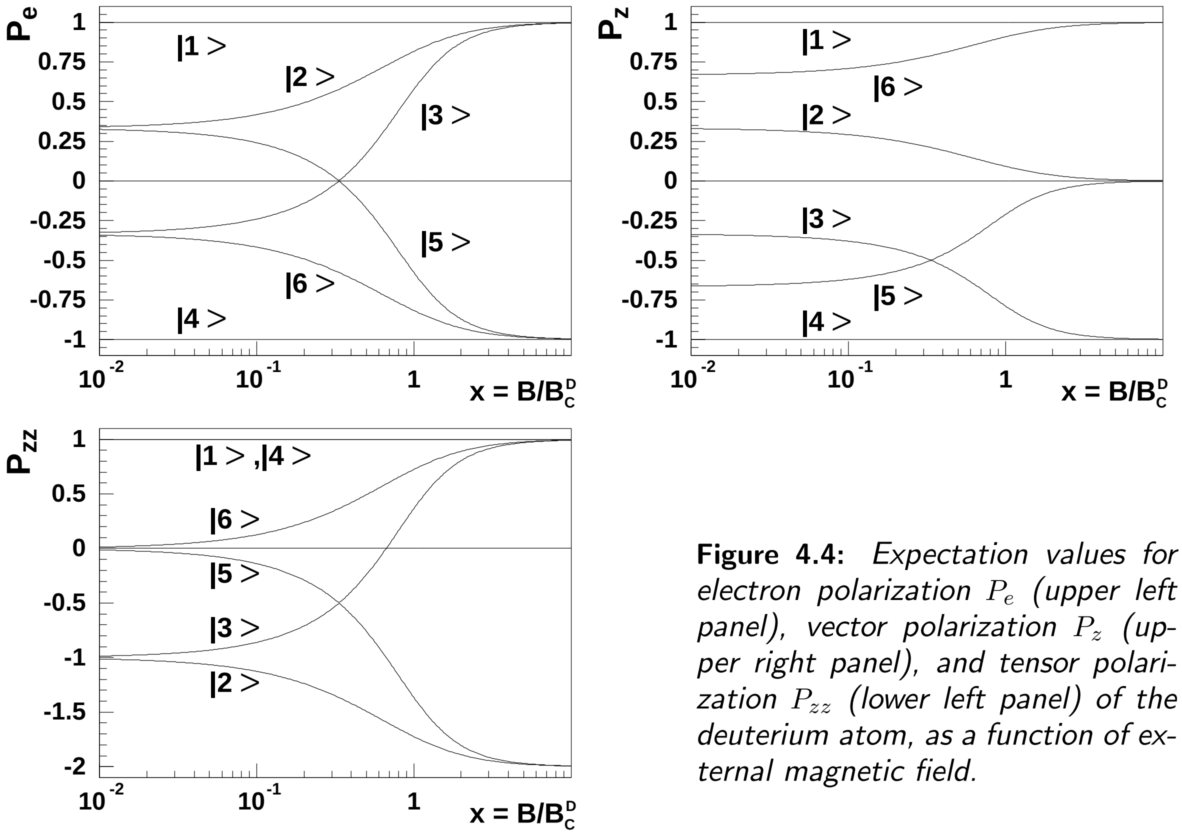

Figure 4.4: *Expectation values for electron polarization P_e (upper left panel), vector polarization P_z (upper right panel), and tensor polarization P_{zz} (lower left panel) of the deuterium atom, as a function of external magnetic field.*

polarization values of an of deuterium atoms as a function of an external magnetic field:

$$\begin{aligned}
P_e &= n_1 - n_4 \\
&\quad + (n_2 - n_6)\cos 2\theta_+ + (n_3 - n_5)\cos 2\theta_- \\
P_z &= n_1 - n_4 + \tfrac{1}{2}(n_2 + n_6 - n_3 - n_5) \\
&\quad -\tfrac{1}{2}(n_2 - n_6)\cos 2\theta_+ - \tfrac{1}{2}(n_3 - n_5)\cos 2\theta_- \\
P_{zz} &= n_1 + n_4 - \tfrac{1}{2}(n_2 + n_3 + n_5 + n_6) \\
&\quad -\tfrac{3}{2}(n_2 - n_6)\cos 2\theta_+ + \tfrac{3}{2}(n_3 - n_5)\cos 2\theta_- \; .
\end{aligned} \tag{4.12}$$

Figure 4.4 shows P_e, P_z, and P_{zz} for a set of deuterium atoms as a function of the magnetic field strength.

4.1.1 Principles of RF transitions for hydrogen and deuterium

Introducing an additional oscillating magnetic field $\vec{B}_{RF}$ of frequency ν and amplitude $B_{RF}(z(t))$ along the trajectory $z(t)$ of the atom, the interaction Hamiltonian takes the form

$$\mathcal{H} = \mathcal{H}_{stat} + \mathcal{H}_{RF} \; , \tag{4.13}$$

where the term

$$\mathcal{H}_{RF}(t) = \mu_B(g_I\vec{I} + g_S\vec{S}) \cdot \vec{B}_{RF}(z(t))cos(2\pi\nu t) \tag{4.14}$$

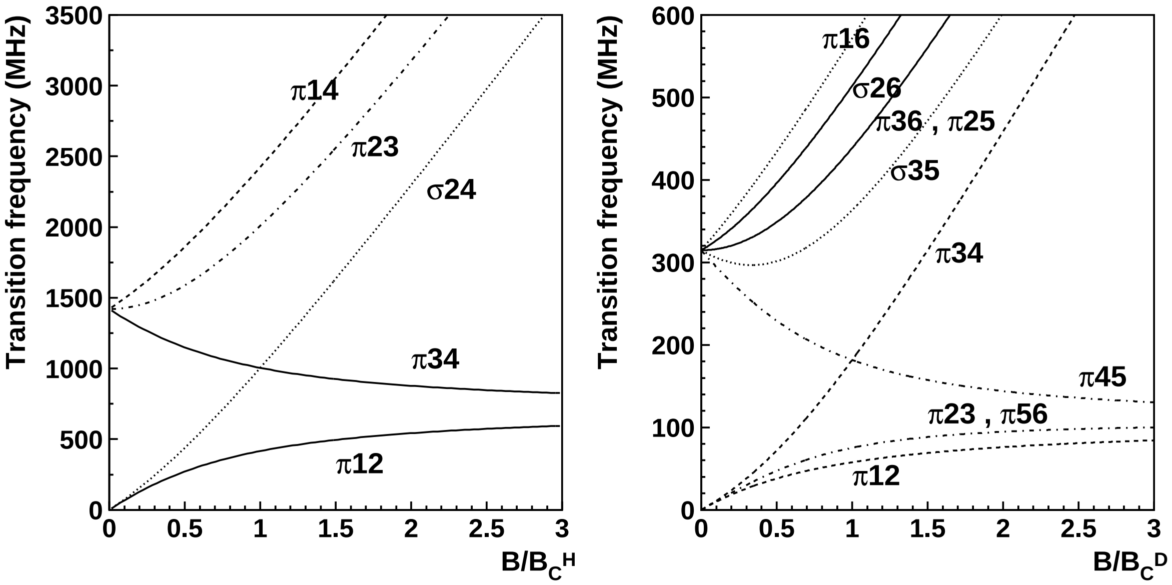

Figure 4.5: *Transition frequencies for the hydrogen (left panel) and deuterium (right panel) hyperfine states as a function of B/B_c.*

describes the interaction of the atom with the oscillating magnetic field.
The static Hamiltonian, $\mathcal{H}_{stat}$, gives the energy levels in the static magnetic field as discussed in Eq. (4.1). At a given value of the static field a transition between hyperfine sub-states can occur when the RF field matches the energy splitting between the two hyperfine states $|a\rangle$ and $|b\rangle$:

$$h\nu_{RF} = \Delta E_{ab} \; . \tag{4.15}$$

In Fig. 4.5, the transition frequencies are shown as a function of B/B_c for hydrogen and deuterium. The transition probability is proportional to the amplitude of the corresponding matrix element $V_{ab} = \langle a|\mathcal{H}_{RF}|b\rangle$. Figure 4.6 shows the matrix elements for hydrogen and deuterium as a function of the static magnetic field. In both cases it is possible to observe that for static fields much larger than the critical field the transitions involving only the nuclear spin are suppressed with respect to the pure electron spin-flip transitions. A transition is called either a σ or π transition depending on the relative orientation of the static field with respect to the oscillating field. A π-transition can occur if the two fields are perpendicular to each other and $\Delta m_F = \pm 1$, while a σ-transition can occur if the static field is parallel to the oscillating field and $\Delta m_F = 0$. The possible hyperfine transitions for hydrogen and deuterium atoms and their nomenclature are listed in Table 4.2.

4.2 The atomic beam source

The polarized gas in the Hermes target is provided by an Atomic Beam Source. The ABS is based on the well-known principle of Stern-Gerlach separation of an atomic hydrogen or deuterium beam [84]. Figure 4.7 shows a side view drawing of the Hermes ABS. Hydrogen or deuterium molecules are dissociated into atoms in a quartz tube by means of an RF

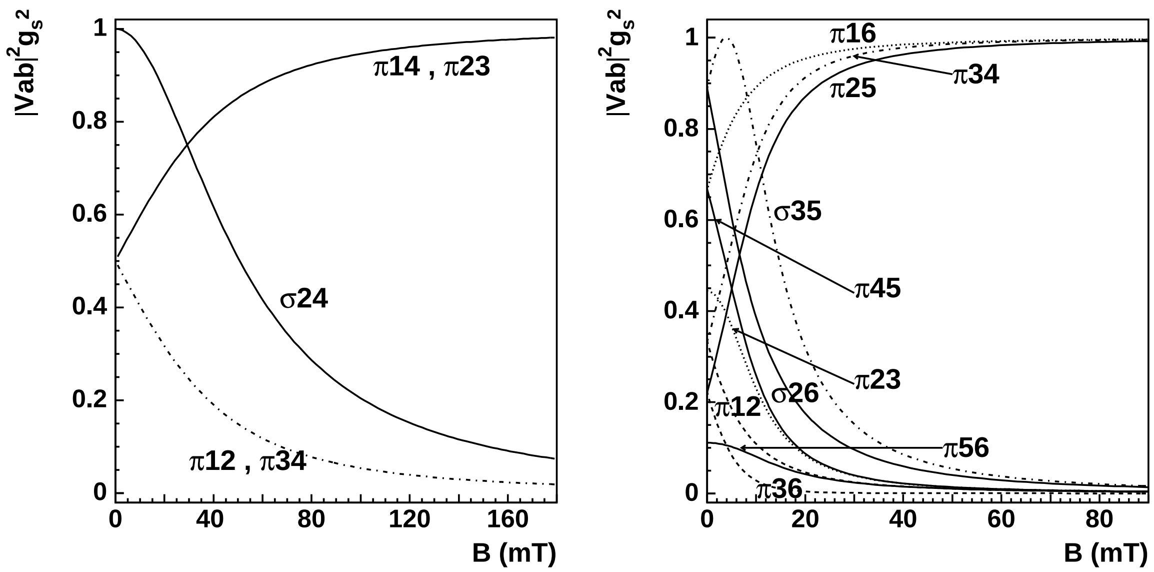

Figure 4.6: *Matrix elements for hyperfine transitions in hydrogen (left panel) and deuterium (right panel) as a function of the static magnetic field.*

	Hydrogen		Deuterium	
Nuclear transitions	$\vert 1 > \leftrightarrow \vert 2 >$	$\pi 12$	$\vert 1 > \leftrightarrow \vert 2 >$	$\pi 12$
	$\vert 3 > \leftrightarrow \vert 4 >$	$\pi 34$	$\vert 2 > \leftrightarrow \vert 3 >$	$\pi 23$
			$\vert 4 > \leftrightarrow \vert 5 >$	$\pi 45$
			$\vert 5 > \leftrightarrow \vert 6 >$	$\pi 56$
Electronic transitions	$\vert 1 > \leftrightarrow \vert 4 >$	$\pi 14$	$\vert 1 > \leftrightarrow \vert 6 >$	$\pi 16$
	$\vert 2 > \leftrightarrow \vert 3 >$	$\pi 23$	$\vert 2 > \leftrightarrow \vert 5 >$	$\pi 25$
			$\vert 3 > \leftrightarrow \vert 4 >$	$\pi 34$
Nuc. and Elec.			$\vert 3 > \leftrightarrow \vert 6 >$	$\pi 36$
σ transitions	$\vert 2 > \leftrightarrow \vert 4 >$	$\sigma 24$	$\vert 2 > \leftrightarrow \vert 6 >$	$\sigma 26$
			$\vert 3 > \leftrightarrow \vert 5 >$	$\sigma 35$

Table 4.2: *Hyperfine transitions for hydrogen and deuterium classified according to the type of transition together with the corresponding nomenclature.*

discharge. The atomic beam is formed by expanding the dissociated gas through a cooled aluminum nozzle with a circular aperture of $\varnothing = 2$ mm. Beam shaping is performed by a skimmer ($\varnothing = 6.4$ mm) and a collimator ($\varnothing = 11$ mm).
The atoms diffuse into the high vacuum provided by a powerful differential pumping system with a nominal pumping speed of 5600 l/s in the dissociator chamber and 2000 l/s in the skimmer chamber. At the working point, the gas throughput through the nozzle is typically 1.25 mbar·l/s, the pressure in the discharge tube 1 mbar, the nozzle temperature 100 K and the applied RF power 300 W. The degree of dissociation at the nozzle is about 80%.
In order to generate a nuclear polarized beam, the hyperfine states of the formed atomic beam are selected with a system of magnets and RF transition units. The first set of sextupole magnets (with pole tip fields of about 1.5 T) focus the atoms of the upper hyperfine states (with $m_J = +\frac{1}{2}$): $|1\rangle$ and $|2\rangle$ for hydrogen, and $|1\rangle$, $|2\rangle$, and $|3\rangle$ for deuterium. The lower hyperfine states (with $m_J = -\frac{1}{2}$) are defocused and pumped away from the system. The second set of sextupole magnets focuses the atomic beam into

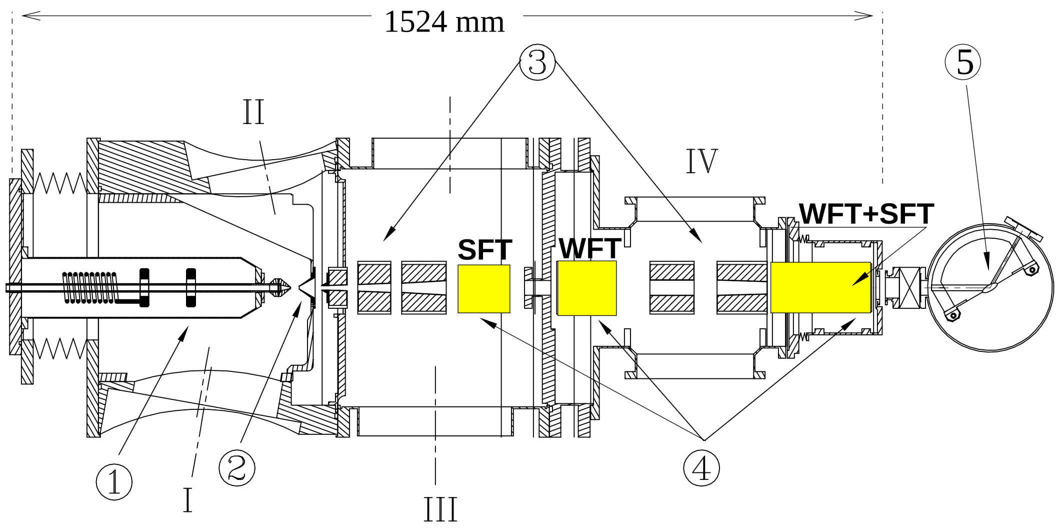

Figure 4.7: *Side view of the HERMES ABS. The circled numbers indicate: ① the RF dissociator, ② the skimmer and collimator, ③ two sets of sextupole magnets, ④ Strong field and Weak field transition units, and ⑤ the storage cell inside the target chamber. The roman numbers indicate the different pumping stages: I dissociator chamber, II skimmer chamber, and III and IV are the two sextupole chambers.*

the target cell. The required nuclear polarization is obtained by adiabatic RF transitions which are induced between the hyperfine levels. By switching on and off selected RF transition units, the polarization can be rapidly changed. The possible hyperfine state selection and the resulting polarizations for the HERMES ABS are listed in Table 4.3. The measured efficiency of the RF transitions is better than 98% [102]. The maximum output flux for polarized hydrogen (2 states injected) is 6.6×10^{16} atoms/s, and for deuterium (3 states injected) 4.5×10^{16} atoms/s [103]. To maximize the output intensity an oxygen admixture of 0.04% is added to the input flux. This leads to the formation of water molecules, which are adsorbed on the cold surface of the nozzle. The ice formation at the nozzle exit results in a decrease in output intensity after 7-8 days of continuous operation. After this period, the ABS nozzle is warmed up to remove the ice layer, and cooled down to restore the normal operating mode. This operation typically requires a couple of hours.

4.3 The storage cell

The HERMES storage cell consist of an open ended 400 mm long tube with an elliptical cross section of 29.0×9.8 mm^2. These dimensions are optimized for high target density and good shielding of the storage cell from synchrotron radiation. The cell is made of 75 μm thick ultra-pure aluminum. Aluminum was chosen because it is not possible to employ magnetic material. The polarized atomic gas is injected into the cell through a side tube 100 mm long and 10 mm in diameter. A small fraction (2%) of the gas is directed to the polarimeter system for analysis via a sample tube of 100 mm long and

	ABS transition	Injected states	P_e	P_z	P_{zz}
Hydrogen	off	$\|1\rangle, \|2\rangle$	$+1$	0	—
	WFT 1-3	$\|2\rangle, \|3\rangle$	0	-1	—
	SFT 2-4	$\|1\rangle, \|4\rangle$	0	$+1$	—
	MFT 2-3, SFT 2-4	$\|1\rangle$	$+1$	$+1$	—
	MFT 1-3, WFT 1-3	$\|2\rangle$	$+1$	$+1$	—
	MFT 2-3, WFT 1-3	$\|3\rangle$	-1	-1	—
	MFT 1-3, SFT 2-4	$\|4\rangle$	-1	$+1$	—
Deuterium	off	$\|1\rangle, \|2\rangle, \|3\rangle$	$+1$	0	0
	SFT 3-5, SFT 2-6	$\|1\rangle, \|6\rangle$	0	$+1$	$+1$
	SFT 3-5, WFT 1-4/2-3	$\|3\rangle, \|4\rangle$	0	-1	$+1$
	MFT 1-4, SFT 2-6	$\|3\rangle, \|6\rangle$	0	0	$+1$
	MFT 1-4, SFT 3-5	$\|2\rangle, \|5\rangle$	0	0	-2
	SFT 2-6, MFT 3-4	$\|1\rangle$	$+1$	$+1$	$+1$
	SFT 2-6, WFT 1-4/2-3	$\|2\rangle$	$+1$	0	-2
	SFT 3-5, WFT 1-4/2-3	$\|3\rangle$	$+1$	-1	$+1$
	SFT 2-6, MFT 3-4, WFT 1-4/2-3	$\|4\rangle$	-1	-1	$+1$
	SFT 3-5, WFT 1-4/2-3, SFT 3-5	$\|5\rangle$	-1	0	-2
	SFT 2-6, WFT 1-4/2-3, SFT 2-6	$\|6\rangle$	-1	$+1$	$+1$

Table 4.3: *RF transition schemes available at the HERMES ABS for hydrogen and deuterium atoms. For each scheme, the hyperfine states injected in the target and the corresponding polarizations are indicated.*

5 mm of diameter. Injection and sample tubes are mounted off axis so that gas atoms cannot flow directly from the ABS to the TGA and BRP without having at least one collision on the cell walls. Drawings of the cell are shown in Figs. 4.8 and 4.9.

The storage cell confines the target atoms near the HERA positron beam axis, thus increasing the target density. After diffusing through the cell the atoms are pumped away by a powerful pumping system (~9000 l/s), which guarantees the ultra-high vacuum conditions in the HERA beam pipe. The pressure in the target chamber is maintained at about 1.5×10^{-7}mbar, compared to the 10^{-9} to 10^{-10} mbar vacuum in HERA. The target density is inversely proportional to the square root of the temperature, therefore an increase of the target thickness is achieved by cooling the cell by means of cold helium gas flowing through the cell support structure. Platinum-resistance temperature sensors

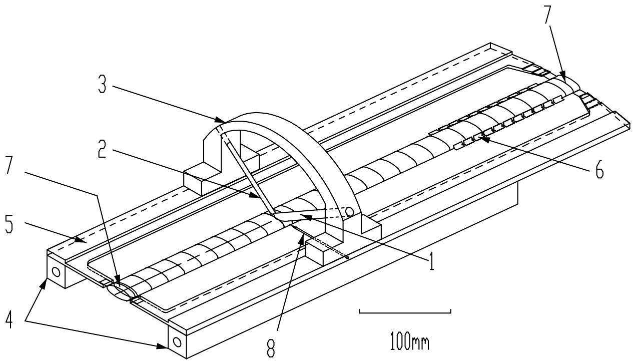

Figure 4.8: *The HERMES storage cell. The following components are indicated: 1) H/D feed tube; 2) sample tube; 3) arch support for feed and sampling tubes; 4) cryogenic cooling and support rails; 5) support plates; 6) cell extension with holes; 7) cell end support collar; 8) capillary for unpolarized gas inlet.*

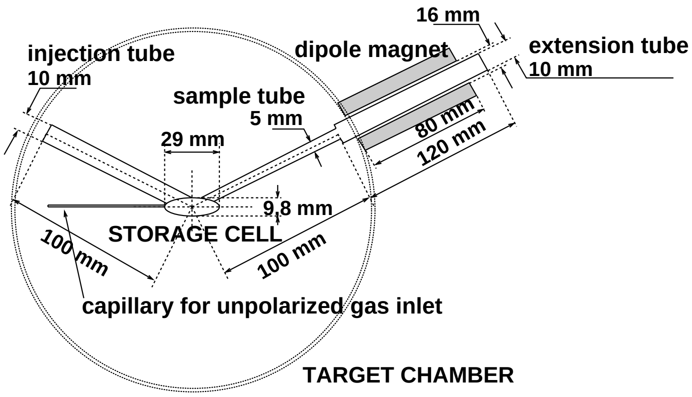

Figure 4.9: *Front view of the storage cell inside the target chamber. The dimensions of the injection, sample and extension tube are indicated. The dipole magnet on the extension tube is represented by the gray area.*

are fixed on the cell support. The operating range of the HERMES cell cooling system is 35-260 K.

The hydrogen or deuterium atoms interact with the walls of the storage cell and have a finite probability to loose their nuclear polarization by depolarizing processes such as atomic recombination and spin relaxation caused by wall collisions [103, 104]. These effects depend on the cell temperature, which is therefore optimized to achieve maximal density without decreasing polarization. At HERMES the nominal operating temperature of the cell is 100 K for atomic hydrogen and 90 K for atomic deuterium. In addition, the cell surface is homogeneously coated with "Drifilm" which is found to give better performance against depolarizing processes than a bare aluminum surface and is radiation harder than Teflon [105, 106, 107].

In order to shield the target from synchrotron radiation originating from the lepton beam, two sets of movable and fixed collimators are placed in front of the target area. The downstream and the upstream ends of the cell are bridged to the fixed collimator and to the beam pipe respectively by eight phosphore-bronze fingers. The fingers, providing a good electrical connection from the cell to the beam pipe, allow the suppression of the electromagnetic *wake fields* that can be generated by the bunched HERA beam in the storage cell. Wake fields in the target chamber would result in loss of beam energy which could cause beam instabilities. In addition, they would generate heat within the target cell which is undesirable as the cell is required to be at uniform low temperature. The fingers are optimized for low thermal conductivity, in order to minimize the heat leak from the (room temperature) beam-pipe to the cold cell body. A layout of the target area in the HERA beam line is shown in Fig. 4.10. To maximize the nuclear polarization of the target a strong magnetic longitudinal holding field is realized over the target region. A superconducting magnet consisting of four coils generates a nominal axial field of 0.35 T. The uniformity of the longitudinal target field is about $\pm 1.5\%$ as shown in Fig. 4.11. Iron flux-return yokes minimize the stray field at the position of the ABS and TGA (see Fig. 4.1). The holding field provides a well defined polarization axis for the spins of the atoms in the cell and decouples the nuclear and electron spins.

The working point of the magnetic field has been carefully chosen in order to avoid resonant depolarizations induced by the circulating lepton beam. The value of the holding field defines the energy eigenvectors of the spin states of the atoms in the cell, and thus defines whether or not the RF field generated by the beam will excite a resonance.

Depolarizing effects induced by the HERA lepton beam will be discussed in detail in Section 4.7.

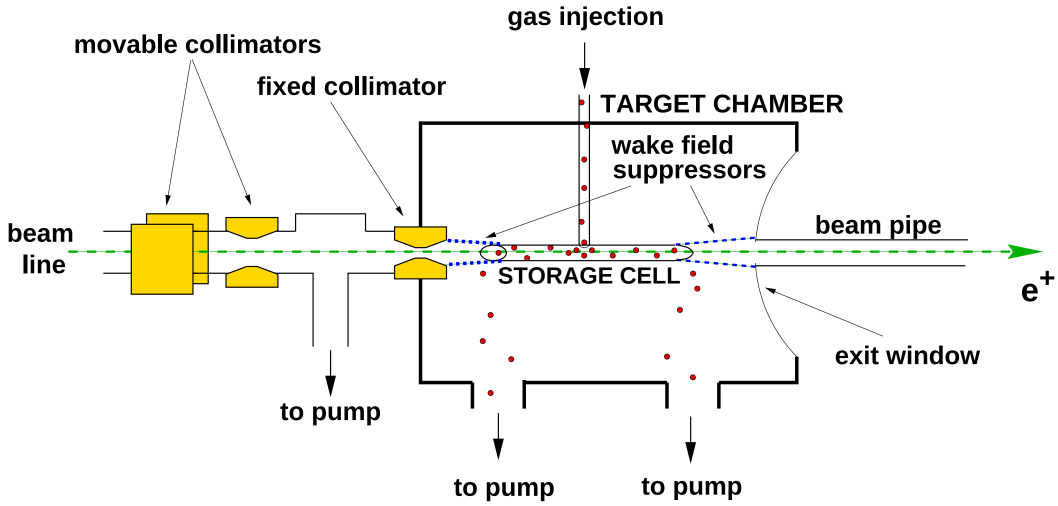

Figure 4.10: *Schematic diagram of the HERMES target area in the HERA positron beam line. Positrons enter from the left.*

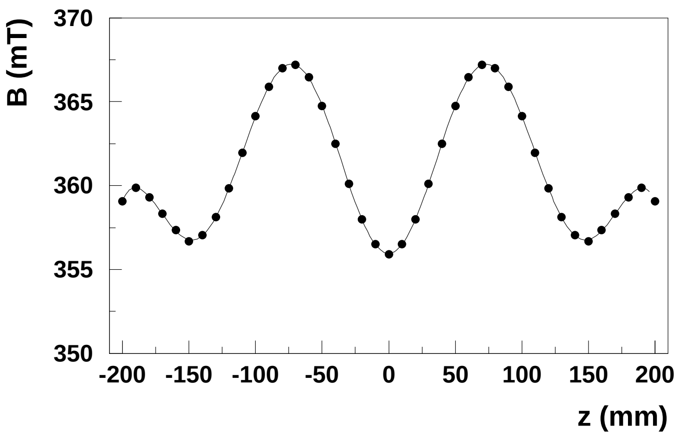

Figure 4.11: *Strength of the longitudinal target holding field as a function of the position along the axis of the storage cell, for a current in the coils of 50 A.*

4.4 The target gas analyzer

The evaluation of the polarization of the target requires not only the knowledge of the polarization of the atomic beam injected in the cell, but also the determination of the fraction of atoms and molecules present in the target. The TGA serves to determine the relative content of atoms and molecules present in the gas sampled from the cell. This is essential for obtaining precise information on the target polarization, since molecules provide a background which, in general, dilutes the target polarization. A schematic outline of the TGA system is shown in Fig. 4.12.

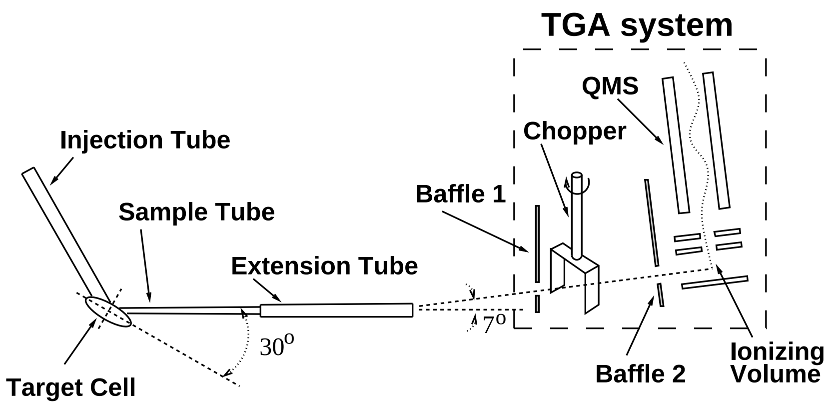

Figure 4.12: *Schematic diagram of the target cell coupled to the TGA system.*

The TGA is mounted at an angle of 7 degrees with respect to the axis of the extension tube, so as not to interfere with the beam entering the BRP. The TGA chamber is pumped by a titanium sublimation pump with a pumping speed of ≈2000 l/s. During operation the pressure in the chamber is typically 3×10^{-9}mbar. A pair of baffles collimates the beam which enters the TGA ionizing volume ensuring that the atoms entering the volume cannot strike the inner walls of the ionizer. An atom striking the ionizer structure would have a finite probability to recombine and, after re-emission, to be detected causing a background which is not distinguishable from the signal coming from the beam. The quadrupole mass analyzer (QMS, BALZERS QMA 430), equipped with a crossed beam ionizer, alternately measures the flux of gas with hydrogen (deuterium) atomic and molecular mass. The ionizer operates at a potential of 70 V in order to maximize the cross sections both for hydrogen (or deuterium) atoms and molecules [108, 109]. A chopper in front of the QMS operating at 5.5 Hz allows for background subtraction. A continuous dynode electron multiplier (CDEM, DeTech 401A) is used for the detection of the ionized atoms and molecules. Figure 4.13 shows a schematic layout of the TGA ion-optic system.

Figure 4.13: *Outline of the ion optic system employed in the TGA.*

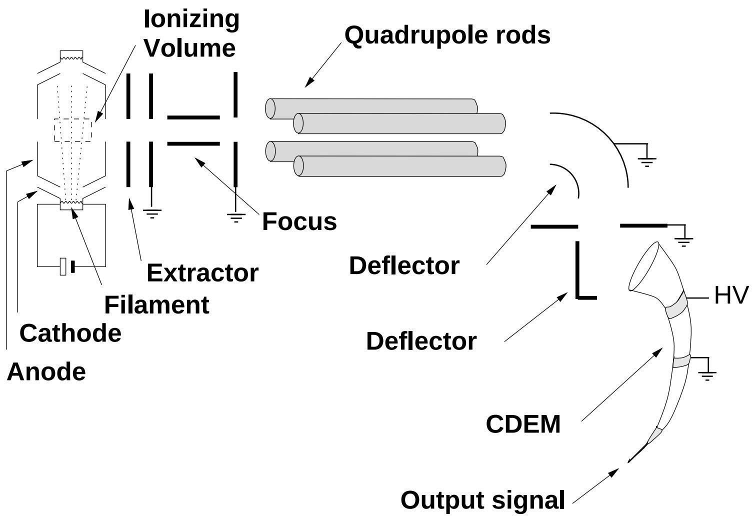

The measurement of the count rates is made by means of a time resolving counter with 2048 bins. Figure 4.14 shows a typical time-resolved count rate spectrum of the TGA for atomic hydrogen. A trigger signal produced by the chopper is used for the definition of the chopper positions: *open, closed* and *undefined*, as indicated by the vertical lines in Fig. 4.14. The TGA signal is formed by the difference between the count rates in the period of open and closed chopper.

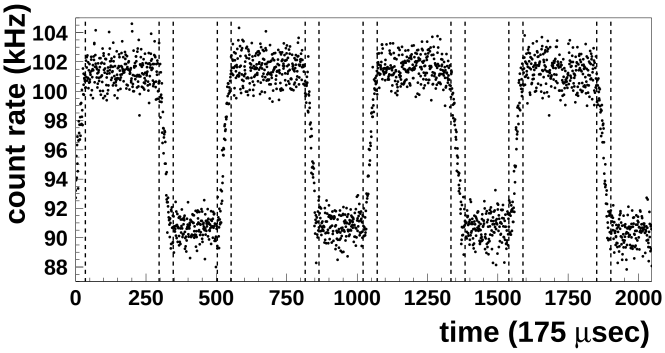

Figure 4.14: *TGA time-resolved count rate for atomic hydrogen. The vertical dashed lines define the chopper positions open, closed and undefined.*

The count rates measured by the TGA are in general a non-linear function of the emission current I_{emis} in the ionizing volume. A polynomial function of the emission current, $f(I_{emis})$, is taken to normalize the TGA count rates. The $f(I_{emis})$ is determined by injecting a constant gas flux into the cell and measuring the dependence of the count rates on the emission current [103]. In Fig. 4.15 the TGA rate is shown as a function of the emission current for a constant flux entering the TGA. The temperature of the storage cell was constant within 1K during the measurement. At normal running conditions the value of the emission current is around $400\ \mu$A to minimize the variations in the count rate from instability of the electron emitter.

4.4.1 Degree of dissociation measured by the TGA

The relative atomic flux of hydrogen (or deuterium), measured in nuclei per second, entering the TGA can be expressed by the ratio

$$\alpha^{TGA} = \frac{\phi_a}{\phi_{tot}}, \tag{4.16}$$

where ϕ_a is the atomic flux, and ϕ_{tot} is the total atomic and molecular flux leaving the sample tube and passing through the QMS ionizing volume. The quantity indicated in Eq. (4.16) is also referred to as degree of dissociation of the sampled gas. Under normal working conditions of the target, the gas dynamics in the target is described by molecular flow [110]. The total flux of nuclei is expressed by the sum of the atomic flux and two times the molecular flux:

$$\phi_{tot} = \phi_a + 2 \cdot \phi_m. \tag{4.17}$$

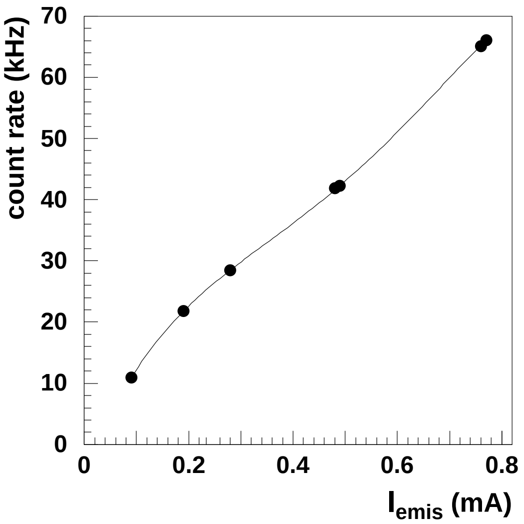

Figure 4.15: *The measured TGA count rates as a function of the emission current, I_{emis}. The solid curve represents a polynomial fit of 4th degree to the data.*

The TGA count rates S_i^{TGA} (with $i = a, m$ for atoms and molecules, respectively) are proportional to the density of particles inside the ionizing volume and, after background correction, can be related to the fluxes in the following way

$$S_i^{TGA} \propto \phi_i^{TGA} \cdot f(I_{emis}) \cdot \sigma_i^{ion} \cdot \frac{1}{< v_i >} \cdot \varepsilon_i \ . \tag{4.18}$$

Here, σ_i^{ion} is the ionization cross section, $< v_i >$ is the average velocity of the particles passing through the ionizing volume, and ε_i represents the detection probability for atoms and molecules. In particular, ε_i depends on the transmission probability through the QMS ion optics and the detection probability in the CDEM.
The average velocity for hydrogen (or deuterium) atoms and molecules in thermal equilibrium is expressed by

$$< v_a >= \sqrt{2} \cdot < v_m > \ . \tag{4.19}$$

Therefore, the total nuclear flux entering the TGA can be written as

$$\phi_{tot} \propto S_a^{TGA} + \frac{2}{\sqrt{2}} \cdot \frac{\sigma_a^{ion} \cdot \varepsilon_a^{ion}}{\sigma_m^{ion} \cdot \varepsilon_m^{ion}} \cdot S_m^{TGA} \ . \tag{4.20}$$

The constant κ defined as

$$\kappa = \frac{\sigma_a^{ion} \cdot \varepsilon_a^{ion}}{\sigma_m^{ion} \cdot \varepsilon_m^{ion}} \ . \tag{4.21}$$

takes into account the relative sensitivity of the TGA system in detecting atoms and corresponding molecules. The relative atomic ratio in Eq. (4.16) can now be rewritten as

$$\alpha^{TGA} = \frac{S_a^{TGA}}{S_a^{TGA} + \sqrt{2} \cdot \kappa \cdot S_m^{TGA}} \ . \tag{4.22}$$

In the following the procedure that is used to determine κ is described.

4.4.2 TGA calibration procedure

In order to obtain the calibration constant κ the flux of the particles entering the target cell is kept constant while the relative amount of atoms and molecules is varied by changing the amount of recombination in the cell. The corresponding atomic and molecular rates are measured during the process. For a constant flux entering the TGA the relation between the atomic and molecular signal is linear (see Eq. (4.20))

$$S_m^{TGA} = -\frac{1}{\sqrt{2}\kappa} S_a^{TGA} + const. \tag{4.23}$$

The graph in Fig. 4.16 illustrates the molecular count rate S_m^{TGA} versus the atomic count rate S_a^{TGA} for a constant TGA flux while the amount of recombination in the target cell is varied.

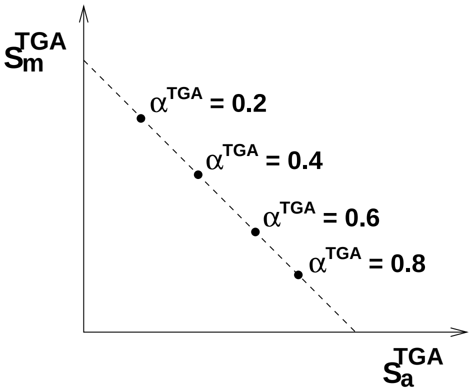

Figure 4.16: *Graphical representation of the atomic count rate S_a^{TGA} versus the molecular count rate S_m^{TGA} (filled circle) for a constant flux entering the TGA. The slope of the dashed line is equal to $-1/\sqrt{2}\kappa$.*

Points at different values of α^{TGA} lie on the dashed line of which the slope is related to κ by:

$$\frac{\mathrm{d}S_m^{TGA}}{\mathrm{d}S_a^{TGA}} = -\frac{1}{\kappa \cdot \sqrt{2}} \; . \tag{4.24}$$

A change in the amount of recombination in the target cell can be achieved by changing the cell temperature, as the recombination of atoms on the walls of the cell is strongly temperature dependent. This process is illustrated in Fig. 4.17 where a typical scan of the temperature of the cell, T_{cell}, is shown versus time, and the corresponding variations in the TGA for molecular signal, S_m^{TGA}, and atomic signal S_a^{TGA} are shown as well. Since the TGA count rates additionally depend on the average velocities of atoms and molecules in the ionizing volume (see Eq. (4.18)) a temperature correction has to be applied in order to take this effect into account. The last wall bounce of the particles sampled from the cell and entering the TGA is located in the extension tube. Therefore, the average velocity of a particle entering the TGA ionizing volume is determined by the temperature of the extension tube, T_{ex}, which is measured by means of a thermocouple. The measured count rates in Eq. (4.18) are related to the temperature of the extension tube in the following way:

$$S_i^{TGA} \propto \frac{1}{\left\langle \sqrt{T_{ex}} \right\rangle} . \tag{4.25}$$

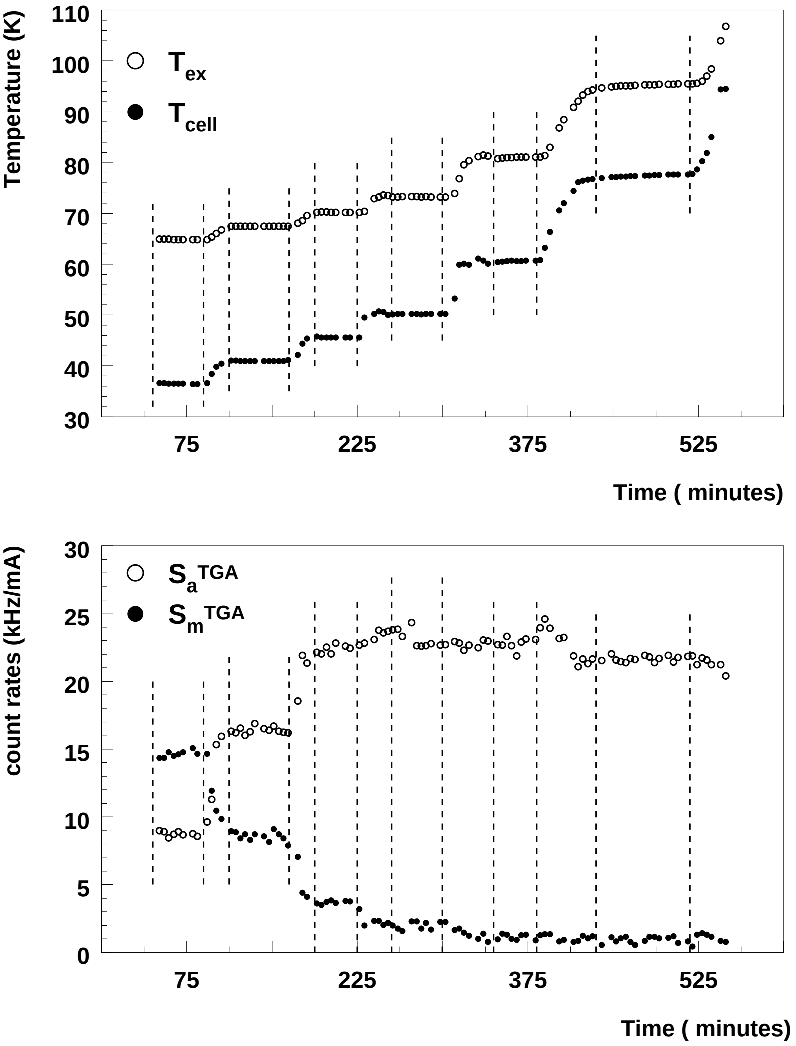

Figure 4.17: *The upper panel shows a scan of the temperature of the cell, T_{cell}, versus time (filled circles). The temperature of the extension tube, T_{ex}, (open circles) is shown as well. In the lower panel the count rates for molecular signal, S_m^{TGA} (filled circles), and atomic signal, S_a^{TGA} (open circles), are shown as the temperature scan of the cell is performed.*

As example of the method, Fig. 4.18 shows the result of the fit of S_m^{TGA} versus S_a^{TGA} with injected polarized deuterium for $T_{ex} < 100$ K. The molecular and atomic count rates, corrected for $f(I_{emis})$ and for the temperature dependence, are averaged for each interval range in which the temperature of the extension tube is constant within 0.5 K. A fit of the data according to Eq. (4.24), resulted in

$$\kappa = 0.862 \pm 0.014 \ . \tag{4.26}$$

An accidental loss of part of the HERA lepton beam near the HERMES target region can cause a drastic modification of the cell surface, leading to a sudden decrease of α^{TGA} due to the recombination of the atoms. Normally, after a couple of hours of ABS running the value of α^{TGA} recovers due to the regeneration of the water coating on the cell walls which evaporated because of the beam loss. During the whole process the temperature of the extension tube is constant. In such conditions it is possible to monitor the variation of α^{TGA} in order to extract the value of κ, without applying a temperature correction. As example, the result of the fit of the molecular signal, S_m, versus the atomic signal, S_a, is shown in Fig. 4.19. The value for κ extracted with this method after a HERA beam loss is

$$\kappa = 0.869 \pm 0.030\ . \tag{4.27}$$

A summary of the values of κ resulting from TGA calibrations performed during the HERMES running period 1998-1999 is presented in Table 4.4 and Fig. 4.20.
Note that the two calibration approaches lead quantitatively to the same result for κ, indicating an overall stability of the TGA throughout a wide range of time. For this reason, all the extracted κ values from both methods have been used to estimate the weighted average for the period 1998-1999, which resulted in

$$\kappa = 0.848 \pm 0.008\ . \tag{4.28}$$

The error is calculated by taking the corresponding error of the weighted average and increasing it by a factor $[\chi^2/(N-1)]^{1/2} = 2.24$ to take into account the large value of the χ^2 resulting from the fit of all the data. The relative error $\Delta\kappa/\kappa$ is 1%, introducing a negligible error in the ultimate determination of the average target polarization.

DATE	κ from temp. scan	κ from beam loss
27 Aug. '98	0.862 $\pm$ 0.014	
19 Nov. '98		0.869 $\pm$ 0.030
7 Aug. '99		0.846 $\pm$ 0.023
14 Aug. '99	0.838 $\pm$ 0.012	
19 Aug. '99	0.857 $\pm$ 0.006	
10 Sep. '99		0.807 $\pm$ 0.009
15 Oct. '99		0.868 $\pm$ 0.009

Table 4.4: *Summary of the results for the extraction of κ by using the cell temperature scan method and the HERA beam loss method.*

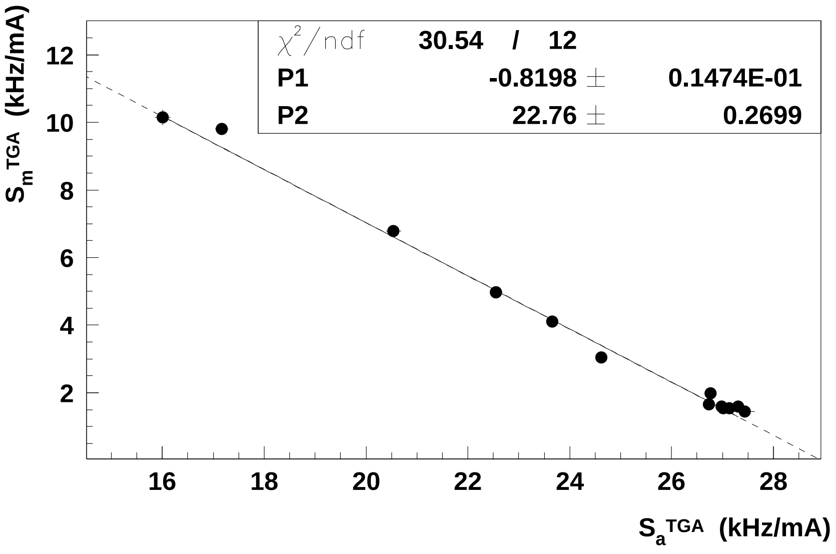

Figure 4.18: *Result of a TGA calibration for the cell temperature scan method: the molecular signal, S_m^{TGA}, is plotted versus the atomic signal S_a^{TGA}. The data points are fitted with a first order polynomial. The parameter P1 of the fit is equal to $-1/\sqrt{2}\kappa$.*

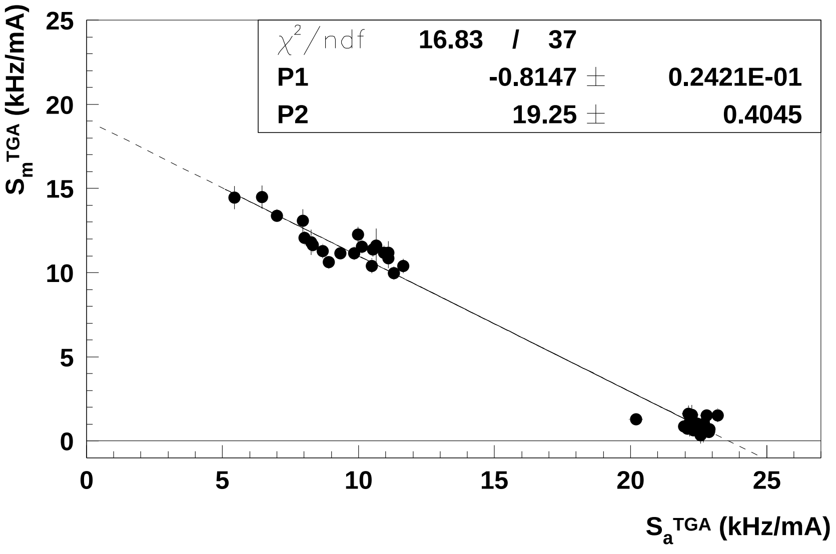

Figure 4.19: *Example of TGA calibration after a HERA beam loss. The molecular signal S_m^{TGA} is shown as a function of the atomic signal S_a^{TGA}. The data points are fitted with a first order polynomial, and the fit parameter P1 corresponds to $-1/\sqrt{2}\kappa$.*

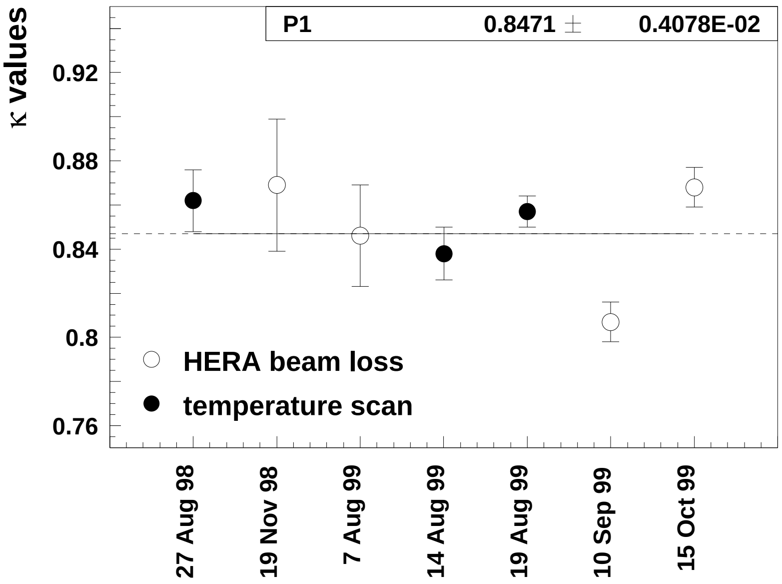

Figure 4.20: *Comparison of the values of κ extracted with the temperature scan method (filled circles) with the values obtained after a HERA beam loss (open circles). The parameter P1 shows the resulting weighted average.*

4.5 The Breit–Rabi polarimeter

The basic function of the Breit-Rabi polarimeter is to measure the relative occupation of the hyperfine states of the gas sampled from the cell. Figure 4.21 shows a schematic view of the BRP components.

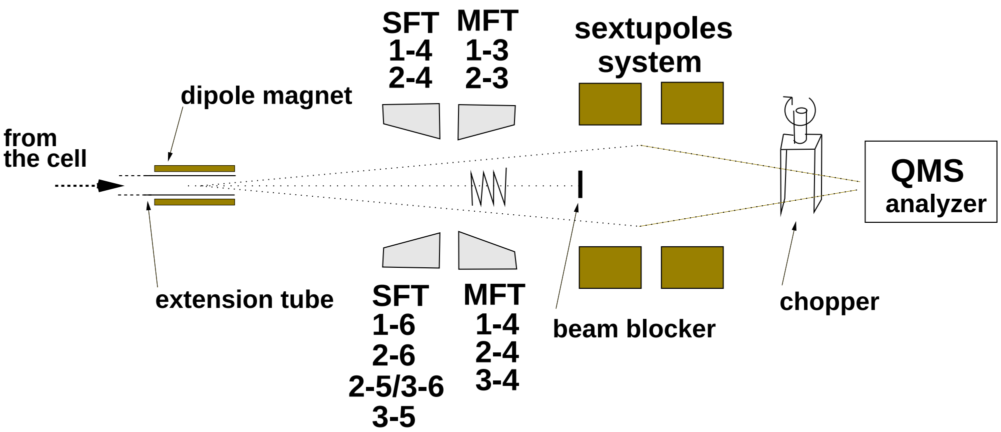

Figure 4.21: *Schematic drawing of the BRP. The same RFT units can be tuned for operating with polarized hydrogen or deuterium target: in the upper part of the drawing the RF transitions are indicated for hydrogen, in the lower part the setting for deuterium are given.*

The BRP consists of a set of two RF transition units followed by two sextupole magnets and an atomic beam detector. A dipole magnet is placed around the extension tube in order to preserve the orientation of the spin of the atoms diffusing from the target cell. The beam detector is placed after the sextupoles and it is realized in the same way as the one used in the TGA: a chopper allows for background suppression, a crossed beam ionizer and a quadrupole mass spectrometer select the atomic content of the beam, and a CDEM gives a signal that is proportional to the intensity of the detected beam. Similarly to the ABS, the sextupole magnets select the atoms according to their electron spin state and focus the $m_J = +\frac{1}{2}$ states into the atomic beam detector. The RF units are used to interchange the population between the hyperfine states of the sampled beam, leading to a change in the atomic beam signal. A beam blocker located on the axis of the first sextupole magnet completely suppresses the transmission of the $m_J = -\frac{1}{2}$ states, reducing the systematic uncertainties for the polarization measurements [103]. With different combinations of the RF transitions and measuring the relative intensities of the detected atomic beam, the relative populations of all the hyperfine states can be determined. The average nuclear polarization of the atomic beam can then be calculated according to Eq. (4.6) for hydrogen atoms and to Eq. (4.8) for deuterium atoms, respectively.

The BRP system is divided into two differentially pumped chambers: the first chamber contains the RF units and the magnets. A typical pressure of 2×10^{-9}mbar is achieved by applying two cryo-pumps. The atomic beam detector is placed in the second chamber, which is pumped by a titanium sublimation pump and an ion getter pump to a typical pressure of 2.5×10^{-10}mbar.

The principle of operation of the BRP is illustrated in the following example. Consider a sample of hydrogen atoms n_i (with i = 1-4) representing the population of the i^{th} hyperfine state. The transmission of atoms effusing from the target cell into the BRP and through the sextupole magnet is described by the following equation, assuming a separation efficiency of 100% by the sextupole magnet:

$$\begin{pmatrix} n_1 \\ n_2 \\ n_3 \\ n_4 \end{pmatrix} \xrightarrow{sextupole} \begin{pmatrix} n_1 \\ n_2 \\ 0 \\ 0 \end{pmatrix} . \tag{4.29}$$

The signal measured in the QMS of the BRP is proportional to the sum of the hyperfine states n_1 and n_2. If the RF transition SFT(2-4) is applied to the atoms entering the BRP, then the hyperfine population of the state $|2\rangle$ and $|4\rangle$ are exchanged:

$$\begin{pmatrix} n_1 \\ n_2 \\ n_3 \\ n_4 \end{pmatrix} \xrightarrow{SFT_{(2-4)}} \begin{pmatrix} n_1 \\ n_4 \\ n_3 \\ n_2 \end{pmatrix} \xrightarrow{sextupole} \begin{pmatrix} n_1 \\ n_4 \\ 0 \\ 0 \end{pmatrix} , \tag{4.30}$$

and the measured signal is proportional to $n_1 + n_4$. The ratio R_{24} of the two measured intensities is given by

$$R_{24} = \frac{n_1 + n_4}{n_1 + n_2} = 1 - \frac{n_2 - n_4}{n_1 + n_2} \tag{4.31}$$

and it differs from unity only if $n_2 \neq n_4$. In general, by proper selection of RF transitions, it is possible to realize the ratio R_{ij} which is sensitive to the difference in the population of the ith and jth hyperfine state. With the normalization condition $\sum_i n_i = 1$, the values of the all four relative occupation numbers n_i of the analyzed atomic beam are determined by solving the following equations:

$$\begin{pmatrix} 1 & 1 & 1 & 1 \\ -R_{14} & 1-R_{14} & 0 & 1 \\ 1-R_{24} & -R_{24} & 0 & 1 \\ 1-R_{23} & -R_{23} & 1 & 0 \end{pmatrix} \begin{pmatrix} n_1 \\ n_2 \\ n_3 \\ n_4 \end{pmatrix} = \begin{pmatrix} 1 \\ 0 \\ 0 \\ 0 \end{pmatrix} . \tag{4.32}$$

For a sample of deuterium atoms ($i = $ 1-6) a set of six independent equations is required. The efficiency of the RF transitions and the transmission probability of the different hyperfine states through the sextupole magnet must be taken into account in the real experimental set-up compared to the ideal case described above. These quantities are measured [103, 111] for both hydrogen and deuterium settings and included in the formalism for the determination of the relative occupation numbers leading a more general matrix equation than given in Eq. (4.32).

4.6 Determination of the target polarization

For a hydrogen (or deuterium) internal gas target, the evaluation of the total polarization requires the knowledge of the relative content of atoms and molecules present in the target and their polarization. At HERMES, these quantities are measured by the TGA and the BRP: the TGA determines the atomic fraction, and the BRP provides a measurement of the polarization of the atoms in the cell.
The contributions to the total nucleon density inside the target cell, ρ^{TC}_{tot}, can be separated as follows

$$\rho^{TC}_{tot} = \rho^a + 2\rho^m_{rec} + 2\rho^m_{rg} + 2\rho^m_{bal} + 2\rho^m_{dif} . \tag{4.33}$$

Here, the distinction has been made between the contribution due to atoms, ρ^a (indicated by the superscript a), and the contributions due to different sources of molecules (indicated by the superscript m). The latter terms are counted double to account for a double number of nuclei in a molecule compared to an atom. Specifically, the terms ρ^m_{bal} and ρ^m_{dif} define the density of unpolarized molecules coming from the ABS ballistically and diffusively, respectively. These quantities depend on specific running conditions of the ABS: the power of the RF discharge, the degree of dissociation in the dissociator, and the pressure in the ABS chambers. Another source of unpolarized molecules, ρ^m_{rg}, originates from the residual gas in the target chamber. Finally, the term ρ^m_{rec} gives the density of molecules coming from recombination of polarized atoms. These molecules may preserve the nuclear polarization of the constituent atoms and therefore may be polarized to a certain degree.
In order to evaluate the target polarization it is useful to define the terms α_0 and α_r which account for the different sources of atoms and molecules descibed previously. By using Eq. (4.33), the fraction of nuclei present as unpolarized molecules in the cell can be expressed as

$$1 - \alpha_0 \;=\; \frac{2\rho^m_{rg} + 2\rho^m_{bal} + 2\rho^m_{dif}}{\rho^{TC}_{tot}} , \tag{4.34}$$

and the fraction of nuclei surviving recombination is evaluated according to

$$\alpha_r = \frac{\rho^a}{\rho^a + 2\rho^m_{rec}} \ . \tag{4.35}$$

From Eqs. (4.34) and (4.35), the fraction of atoms in the target is given by

$$\alpha_0 \cdot \alpha_r = \frac{\rho^a}{\rho^{TC}_{tot}} \ , \tag{4.36}$$

thus the fraction of molecules coming from recombination is

$$\alpha_0(1 - \alpha_r) = \frac{2\rho^m_{rec}}{\rho^a + 2\rho^m_{rec}} \ . \tag{4.37}$$

Indicating with P^a and P^m the polarization of atoms and of molecules respectively, the target polarization can be defined as

$$P_T = \alpha_0\alpha_r P^a + \alpha_0(1 - \alpha_r)P^m \ . \tag{4.38}$$

It is important to notice that the polarization of the atoms measured by the BRP, P^a_{BRP}, and the degree of dissociation measured by the TGA, α_{TGA}, are quantities that characterize the gas sampled from the center of the cell. In general, the properties of the analyzed gas differ from the average properties of the atoms and molecules inside the total length of the cell. Therefore, Monte Carlo simulations have been developed [103, 105] in order to relate the measured polarization and degree of dissociation to the corresponding average quantities of the gas in the target. The simulations comprise an analytical model for the diffusion process inside the HERMES target cell geometry and the modeling of processes and conditions leading to recombination and spin relaxation on the cell wall. In this way, the influence of non-uniformities of the cell surface on the quantities measured by BRP and by TGA can be investigated, and the following relations are derived

$$\alpha_r = c_\alpha \cdot \alpha_{TGA} \ , \tag{4.39}$$

$$P^a = c_P \cdot P^a_{BRP} \ , \tag{4.40}$$

where c_α and c_P are the sampling corrections. In Fig. 4.22, the corrected degree of dissociation α_r is shown as a function of the measured degree of dissociation, α_{TGA}, in the TGA. The shaded area in the plot corresponds to the uncertainties in the sampling correction due to the assumptions made in the simulations. The expression for the upper an lower limits are given in Ref. [112] and are assumed to be valid for both hydrogen and deuterium targets.

Finally, the average polarization in the target cell is determined from the observed quantities modified by the sampling corrections according to the following formula:

$$P_T = \alpha_0(\alpha_r + (1 - \alpha_r)\beta)P^a \ , \tag{4.41}$$

where the quantity related to the polarization of the molecules, $\beta = P^a/P^m$, is the only unknown.

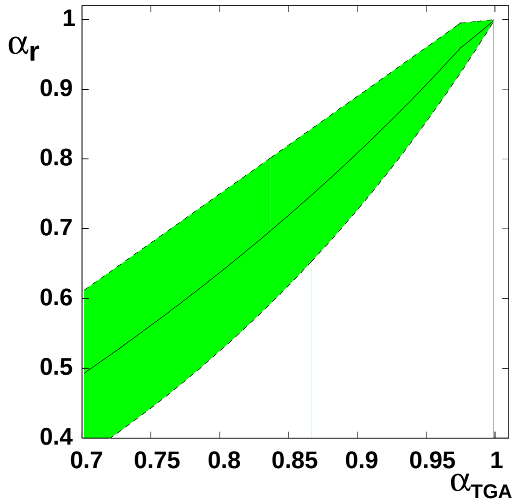

Figure 4.22: *The degree of dissociation in the target, α_r, is shown as a function of the degree of dissociation, α_{TGA}, measured by the TGA. The dashed curves indicate the upper and lower limits of α_r for a measured value of α_{TGA} as determined by MC simulation. The solid curve is the average of the upper and lower limits.*

One way to determine the polarization of molecules that are formed by recombination of polarized atoms is to perform an asymmetry measurement sensitive to the target nuclear polarization for a high value of α_r and a low value of α_r. HERMES performed this measurement with nuclear polarized hydrogen atoms [104]. The recombination of atoms into molecules was enhanced by increasing the cell temperature to 270 K, while the magnetic holding field was kept at the working point of 335 mT. The value obtained for the ratio between the atomic and molecular polarization was $\beta = 0.56 \pm 0.16$. An extrapolation of β to the operating target temperature (100 K) yielded a constraint on $\beta \in [0.25,1.0]$. An experiment performed at the Amsterdam Pulse Stretcher (AmPS) at NIKHEF investigated the tensor polarization of deuterium molecules with elastic electron-deuteron scattering. The molecules were obtained by recombination of nuclear-tensor polarized deuterium atoms on a copper surface [113]. The magnetic holding field was 23 mT. The nuclear tensor polarization of the molecules from recombined atoms resulted in a value of 0.81 ± 0.32. At the Indiana University Cyclotron Facility (IUCF) measurements of the nuclear polarization of hydrogen molecules formed by recombination of polarized hydrogen on a copper surface were performed [114]. The observed nuclear polarization of the molecules was 0.42 ± 0.02 for a magnetic field of 0.66 T and at a temperature of 300 K. It was shown that the fraction of polarization retained by the molecules has a strong dependence on the applied magnetic field, but almost no dependence on the temperature for $T > 70$ K.
The results of the IUCF measurements cannot be applied directly to HERMES conditions, as the recombination at IUCF was done on a copper surface, while the HERMES target is coated with a non-metallic layer. The relaxation time of polarized atoms on the cell wall is different for different surface properties. Therefore, in the calculation of the target polarization the value $\beta = 0.65 \pm 0.4$ is used.

The systematic uncertainty in the determination of the target polarization may be derived by rewriting Eq. (4.41) as

$$P_T = \alpha_{tot} \cdot P^a \, . \tag{4.42}$$

The two terms of the equation are independent, thus the uncertainty on P_T is given by

$$\delta P_T = \sqrt{(\delta\alpha_{tot})^2 + (\delta P^a)^2)} \, . \tag{4.43}$$

The breakdown of the systematic uncertainty on α_{tot} follows by applying the error propagation formalism to the different contributions (α_0, α_r and β) which are uncorrelated. Therefore, even if the uncertainty associated to β is considerably large, its contribution to the total target polarization uncertainty is suppressed by a factor $(1 - \alpha_r)$. During normal running conditions, $(1-\alpha_r)$ is typically of the order of 2%. For the 2000 running period (with a polarized deuterium target) the total uncertainty on α_{tot} was evaluated $\delta\alpha_{tot} = 3\%$ [115]
The uncertainty associated to P^a arises from the uncertainty on the BRP calibration. As this contribution is of statistical nature only, it can be deduced from the precision of the signal-to-background ratio in the BRP. This is evaluated with an accuracy of less that 2% [103, 115].

4.7 Feasibility study for a transversely polarized target

The HERMES physics program for the years 2002-2006 includes a broad range of studies of spin observables on a transversely polarized target [116, 117]. Measurements of the virtual photon cross section asymmetry A_2 and the structure function $g_2(x)$ are considered with proton and deuteron targets. Furthermore, the capability of HERMES to investigate semi-inclusive hadron production might allow to probe for the first time the transversity distribution $h_1^q(x)$. This distribution function only appears in semi-inclusive DIS structure functions multiplied by a (chirally-odd) fragmentation function [118].

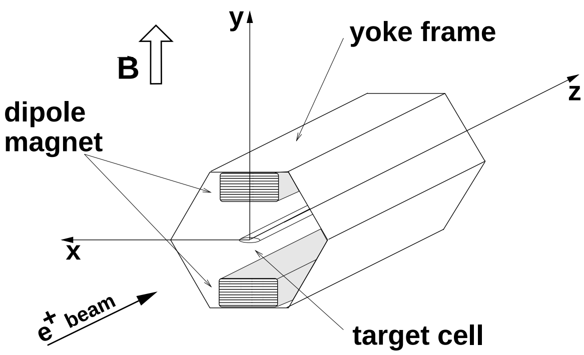

Figure 4.23: *Schematic drawing of the dipole magnet within the HERMES coordinate system: the z direction is along the positron beam axis.*

In order to accomplish the proposed studies, the feasibility of a transversely polarized hydrogen target for the HERMES experiment has been investigated. In 1999 a test dipole electromagnet was installed in the existing HERMES hydrogen target setup. This dipole was designed [77] to generate a magnetic field of up to 0.2 T in the transverse direction with respect to the HERA beam axis. The choice of the maximum value of the field strength was mainly motivated by the fact that a higher magnetic field would yield too much synchrotron radiation. The dipole, which consists of two conventional water-cooled coils, is characterized by a high field uniformity along its length and a low hysteresis curve. This was accomplished by using decarburized steel for the inner ferromagnetic core (less than 0.03% of carbon present). The shape of the core provides a field uniformity of 0.5 mT. Figure 4.23 shows a schematic drawing of the dipole magnet within the HERMES target coordinate system. The beam axis, z, is defined at the position x = 0 and y = 0. The magnitude of the magnetic field has been carefully measured as a function of the position for different current settings. Field profiles for a current of 190 A are presented in Fig. 4.24 and Fig. 4.25. The magnet is characterized by the hysteresis curve shown in Fig. 4.26. The measured residual field equals 0.55 mT.

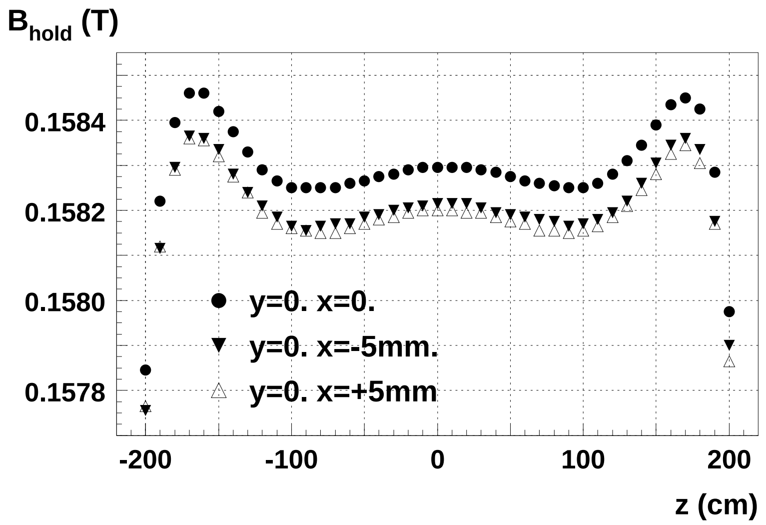

Figure 4.24: *Magnetic holding field, B_{hold}, versus the direction z in the target at y = 0 for different values of x at a current of 190 A.*

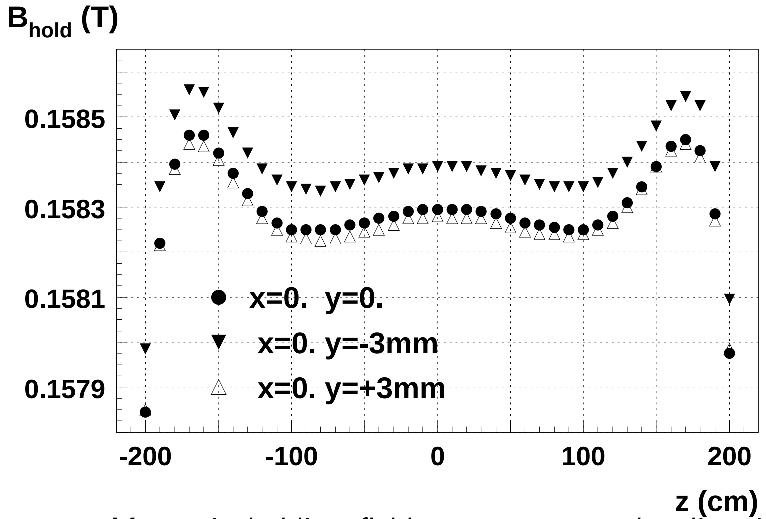

Figure 4.25: *Magnetic holding field, B_{hold}, versus the direction z in the target at x = 0 for different values of y at a current of 190 A.*

The use of a transverse magnetic field in the HERMES target region in combination with the HERA beam environment has to take into account several constraints:

- Displacement of the beam trajectory at the target interaction point.
- Production of synchrotron radiation associated with the deflection of the beam.
- Depolarization of the target induced by the positron beam.

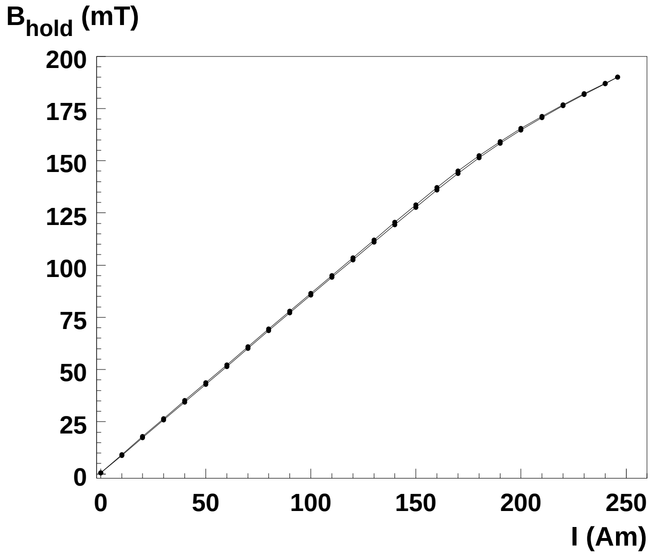

Figure 4.26: *Hysteresis curve of the dipole magnet measured at the coordinates x = y = z = 0. The data points are connected with a solid curve.*

The above constraints were investigated, with the test dipole magnet, during two days of dedicated beam operation. Here, the results are discussed.

Beam displacement

Considering a uniform field of $B_\perp = 0.17$ T along the longitudinal direction of the dipole (0.6 m long), the integrated field amounts to $\int Bdl = 0.102$ Tm. For a 27.5 GeV electron beam this corresponds to an orbital kick of 1.1 mrad. In order to compensate for the beam displacement, two correction dipole magnet are installed upstream (z = -1.27 m) and downstream (z = 2.19 m) with respect to the interaction point at the center of the target (z = 0 m). The integrated field provided is 0.065 Tm for the first dipole and 0.038 Tm for the second. In this configuration the maximum horizontal excursion of the beam at z = 0 amounts to 0.9 mm. This value is small compared to the length of the semi-major axis of the elliptical cell (12 mm), and, therefore, does not represent a problem for the operation of the transversely polarized target.

Synchrotron radiation

A consequence of the bending of the electron beam in a dipole magnet is the emission of synchrotron radiation. For the configuration of correction dipoles and target magnet described above, the total power dissipated by the beam when passing through the system was evaluated [119] assuming an average beam current of 30 A. For a field value of $B_\perp = 0.17$ T, the estimated power is $P_T^{beam} \approx 435$ W, and taking into account also the correcting dipoles, the resulting total power is $P_{tot}^{beam} \approx 700$ W. Considering the deflection angles of the emitted radiation for the three bending magnets, the first point of impact with the beam pipe is located 20 m downstream of the HERMES target. The luminosity monitor (located at z = 8 m downstream of the interaction point) is the closest detector

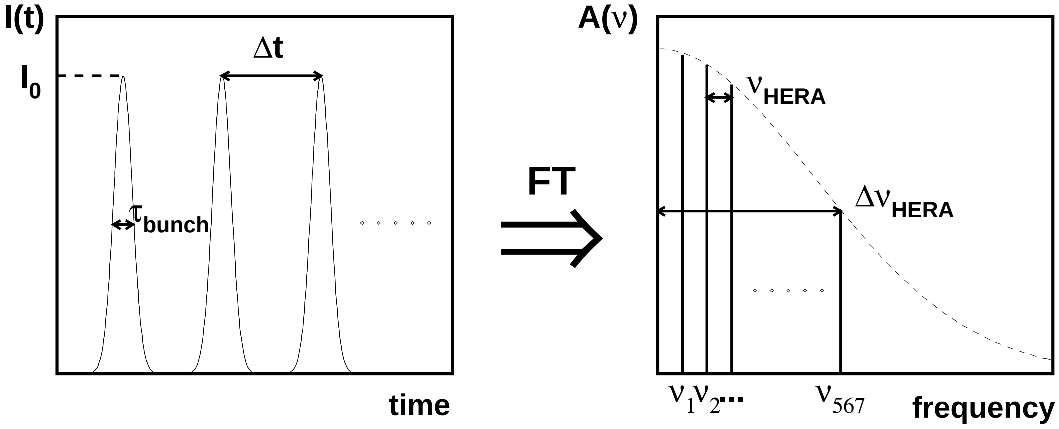

Figure 4.27: *Left panel: schematic of the time structure of the HERA positron beam: the bunches are approximated with a Gaussian of width τ_{bunch}. Right panel: Fourier transformation of the positron beam structure.*

to the beam pipe covering the smallest angles with a distance of 32 mm from the beam axis. At this location the region covered by the opening angle of the incident radiation is less than 7 mm wide. Therefore, the synchrotron radiation produced by the described magnets settings does not irradiate any part of the HERMES detector.

Target depolarization induced by the HERA positron beam

In this section the depolarization effect caused by a resonant interaction of the nuclear spin of the atoms in the target with the transient RF-field generated by the HERA positron beam is discussed. This mechanism was investigated for the HERMES longitudinal polarized target for the case of hydrogen [104, 120] and deuterium atoms [103]. Studies of the depolarization effect for nuclear polarized atoms in a transverse magnetic field are presented in Ref. [121, 122].
The HERA positron beam is optimized for operating in collider mode with the proton beam. Therefore, it consists of short bunches with high peak currents. Positrons in the HERA ring are arranged in 220 bunches, and for a typical average current of 35 mA each bunch contains about 4×10^{10} particles. The time distance, Δt, between two subsequent bunches is 96 ns, corresponding to the fundamental frequency of $\nu_{\text{HERA}} = 10.42$ MHz. To a good approximation at the energy of 27.5 GeV the distribution of positrons in a single bunch has a Gaussian shape in space in each of the transverse and longitudinal coordinates, with $\sigma_x \simeq 0.32$ mm, $\sigma_y \simeq 0.05$ mm, and $\sigma_z \simeq 11.3$ mm, respectively. The resulting bunch length in time is $\tau_{bunch} = 37.7$ ps, corresponding to a bunch frequency $\Delta\nu_{\text{HERA}} \simeq 6$ GHz. A scheme of the time structure of the positron beam and its Fourier decomposition is depicted in Fig. 4.27. Usually, the current in the HERA positron beam is built up in such a way that not all the bunches are filled with the same amount of charge. A typical configuration of the beam current is described by 3 sets of 63 completely filled bunches alternated by 3 sets of almost empty bunches. However, for the purpose of our studies the assumption holds that all bunches are equally filled and the charges in each bunch are Gaussian distributed. The current of the beam, I_{HERA}, as a function of time

can be therefore decomposed in its Fourier terms as follows

$$I_{\text{HERA}}(t) = \sum_{n=0} I_n cos(2\pi n \nu_{\text{HERA}} t) \ , \tag{4.44}$$

where I_0 is the DC component of the positron beam current.
The amplitudes of the nth harmonic of the fundamental frequency is given by

$$I_n = 2 I_0 e^{-(2\pi n \nu_{\text{HERA}} \tau_{bunch})^2/2} \ . \tag{4.45}$$

Therefore, the amplitude of the HERA RF field has decreased by 50% compared to I_1 only at the harmonic $n \simeq$ 500, corresponding to $n\nu_{\text{HERA}} \simeq$ 5.2 GHz. As consequence of the fact that the bunch length τ_{bunch} is short compared to the separation between bunches, the Fourier envelope contains a high number of fundamental harmonics ν_{HERA} with significant amplitude.
The charges in the bunches produce a strong transient magnetic field transverse to the beam direction (up to 80 mT at 35 mA of electron beam). The interaction of the nuclear and electron spins of the atoms in the target with this field is described by the Hamiltonian given in Eq. (4.13). At a certain value B_{hold} of the magnetic holding field, transitions between hyperfine states $|a\rangle$ and $|b\rangle$ can be induced whenever a harmonic of the RF field matches the transition frequency ν_{ab}

$$h n \nu_n = h \nu_{ab} = \Delta E_{ab} \ . \tag{4.46}$$

Considering the case of the longitudinal polarized hydrogen target, the direction of the perturbing RF field is always transverse to the holding field direction. Therefore, only transitions with $\Delta m_F = \pm$ 1 are allowed. In the strong field limit the transitions $\pi 12$ and $\pi 34$ only change the nuclear polarization, while the transitions $\pi 14$ and $\pi 23$ only change the electron polarization (see Table 4.2). In a transverse holding field also the transition $\sigma 24$ with $\Delta m_F = \pm$ 0 has to be considered. This transition changes both the electron and the proton polarization. The same kind of arguments hold in the case of polarized deuterium atoms in the target. The values of B_{hold} for which the HERA beam harmonics match the resonance condition in Eq. (4.46) are indicated in Fig. 4.28 for hydrogen and deuterium atoms. In Table 4.5 the field values of B_{hold}, for which nuclear depolarizing resonances occur, are given for both hydrogen and deuterium together with the corresponding beam harmonic number. It is clear that in normal target operation (nuclear polarized atoms) the value of the magnetic field in the target has to be such as to avoid depolarizing resonance conditions within the effective target volume.
In HERMES, the magnet used for the longitudinal field is designed to have sufficient strength and field uniformity to operate in a region where no nuclear resonance conditions are matched for both hydrogen and deuterium atoms. In the case of a transverse magnet with $B_{hold} =$ 170 mT, the target holding field is 15 times the deuterium critical field, but only 3 times the critical field for hydrogen atoms. Therefore, comparing the values of magnetic field for two subsequent resonance conditions, the choice of B_{hold} is more critical in the case of a hydrogen target. For deuterium no resonance is matched for $B_{hold} \geq$ 60 mT up to $B_{hold} =$ 219.03 mT, where the 10th harmonic of the $\pi 45$ transition is encountered (see Table 4.5). In addition, a lower B_{hold} value for the transverse hydrogen target, compared

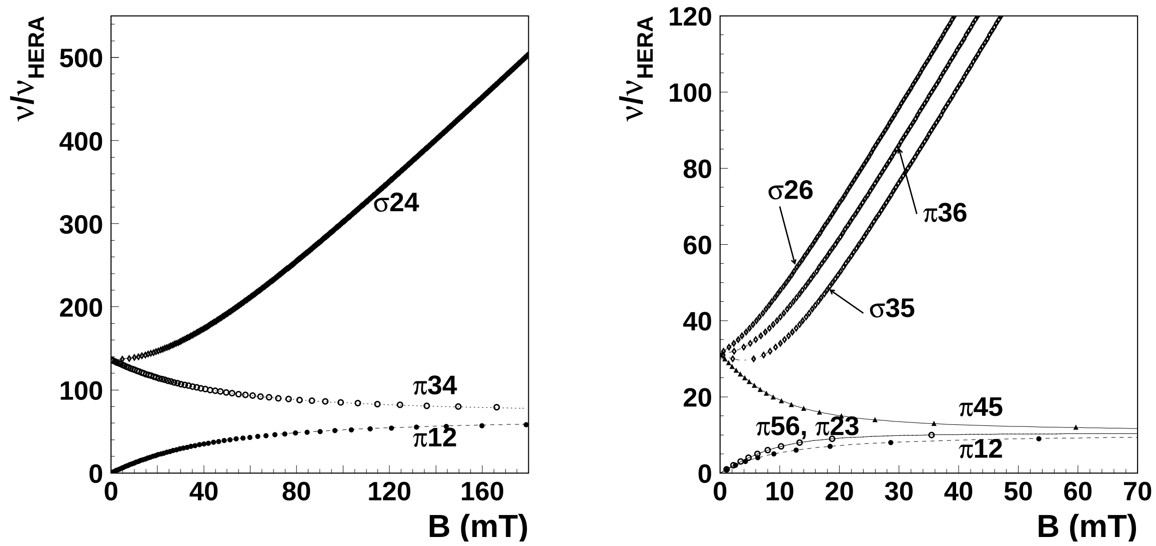

Figure 4.28: *Resonance conditions in harmonics of the HERA beam as a function of the magnetic holding field for hydrogen atoms (left panel) and deuterium atoms (right panel).*

Hydrogen resonances		Deuterium resonances		
$\pi 12$	$\pi 34$	$\pi 12$	$\pi 45$	$\pi 23,\ \pi 56$
103.64 (52)	98.99 (85)	1.19 (1)	219.03 (11)	1.12 (1)
111.71 (53)	106.42 (84)	2.58 (2)	58.57 (12)	2.26 (2)
120.98 (54)	114.88 (83)	4.25 (3)	35.87 (13)	3.47 (3)
131.78 (55)	124.66 (82)	6.31 (4)	25.95 (14)	4.78 (4)
144.56 (56)	136.12 (81)	8.99 (5)	20.35 (15)	6.26 (5)
159.99 (57)	149.76 (80)	12.73 (6)	16.66 (16)	8.01 (6)
179.10 (58)		18.44 (7)	14.01 (17)	10.22 (7)
203.57 (59)		28.62 (8)	11.96 (18)	13.35 (8)
236.51 (60)		53.45 (9)	10.31 (19)	18.77 (9)
284.50 (61)		242.61 (10)	8.93 (20)	35.44 (10)

Table 4.5: *Magnitude of the magnetic field B_{hold} (in mT) at which nuclear spin-flip resonances occur for hydrogen and deuterium atoms. The numbers in brackets correspond to the number of the matched resonance.*

to the longitudinal hydrogen target, results in a loss of nuclear polarization due to the electron spin-flip mechanism. The measurements performed with the hydrogen target transversely polarized had the objective to determine the values of the magnetic holding field for which resonant nuclear transitions are matched in the target. The resonances were observed experimentally by injecting selected hyperfine states in the target while the stored HERA positron beam was circulating in the ring. The Breit-Rabi polarimeter monitored the atomic beam intensity of the injected states, for different values of B_{hold}. In order to observe the nuclear resonances $\pi 12$ and $\pi 34$, the hyperfine states $|2>$ and $|3>$ are injected into the cell and the RF transition W13 in the BRP is turned on. After the BRP sextupole magnet, the measured signal is proportional to the population of the first two occupation numbers. The injection of states $|2>$ and $|3>$ has the

advantage that the measurement is insensitive to the transitions $\pi 14$ and $\pi 23$. The study is performed both in the case of circulating beam and in absence of beam.
The following schemes illustrate the procedure of the measurement:

- Without HERA beam:

$$\underbrace{\begin{pmatrix} 0 \\ n_2 \\ n_3 \\ 0 \end{pmatrix}}_{ABS\ INJECTED} \Rightarrow \underbrace{\begin{pmatrix} n_3 \\ n_2 \\ 0 \\ 0 \end{pmatrix}}_{after\ W13} \Rightarrow \underbrace{\begin{pmatrix} n_3 \\ n_2 \\ 0 \\ 0 \end{pmatrix}}_{after\ sextupole} \tag{4.47}$$

$\Longrightarrow$ BRP signal $S_0^{BRP} \propto n_2 + n_3$.

- With HERA beam:

$$\underbrace{\begin{pmatrix} 0 \\ n_2 \\ n_3 \\ 0 \end{pmatrix}}_{ABS\ INJECTED} \Rightarrow \underbrace{\begin{pmatrix} \epsilon_{12} \\ n_2 - \epsilon_{12} - \epsilon_{24} \\ n_3 - \epsilon_{34} \\ \epsilon_{34} + \epsilon_{24} \end{pmatrix}}_{\substack{RESONANCES \\ \pi 12\,,\pi 34\,,\sigma 24}} \Rightarrow \underbrace{\begin{pmatrix} n_3 - \epsilon_{34} \\ n_2 - \epsilon_{12} - \epsilon_{24} \\ \epsilon_{12} \\ \epsilon_{34} + \epsilon_{24} \end{pmatrix}}_{after\ W13} \Rightarrow \underbrace{\begin{pmatrix} n_3 - \epsilon_{34} \\ n_2 - \epsilon_{12} - \epsilon_{24} \\ 0 \\ 0 \end{pmatrix}}_{after\ sextupole} \tag{4.48}$$

$\Longrightarrow$ BRP signal $S_1^{BRP} \propto n_2 + n_3 - \epsilon_{34} - \epsilon_{12} - \epsilon_{24}$.

A decrease of intensity in the signal S_1^{BRP} measured in the BRP in the presence of the beam compared to the signal S_0^{BRP} without beam indicates that a hyperfine transition occurred in the target for that value of the holding field. In addition, since the transitions $\pi 12$ and $\pi 34$ do not occur for the same value of magnetic field, they can be observed separately. The result of the measurement is presented in Fig. 4.29, where the signal measured in the BRP is shown as a function of the value of the magnetic field in the target. The position of the resonances expected from calculation according to Eq. (4.46) are also shown for comparison. When the HERA positron beam is present in the ring a decrease of about 10% of the BRP signal is observed in the region of magnetic field corresponding to a resonance condition. It must be noted that since the state n_2 is populated, also the transition $\sigma 24$ could be induced (see Eq. (4.48)). In this measurement the target magnetic field was ramped from 110 mT to 162 mT with a step size of 4.0 mT. However, the distance in between two subsequent $\sigma 24$ transitions is 0.37 mT, and therefore the single $\sigma 24$ transitions cannot be resolved. The signal from the BRP comprises the contribution from these transitions, whose strength is proportional to the corresponding transition probability (see Fig. 4.6) and the RF power induced by the beam. The difference of the BRP signals with and without HERA beam allows for the quantification of the $\sigma 24$ contribution. Unfortunately, the result of the measurement in absence of beam was compromised by the non-stable performance of the QMS in the BRP. As a consequence, the evaluation of the magnitude of the $\sigma 24$ transitions is not possible. The limited time given for these studies did not allow for the repair of the faulty device, and the repetition of the measurements was not possible.

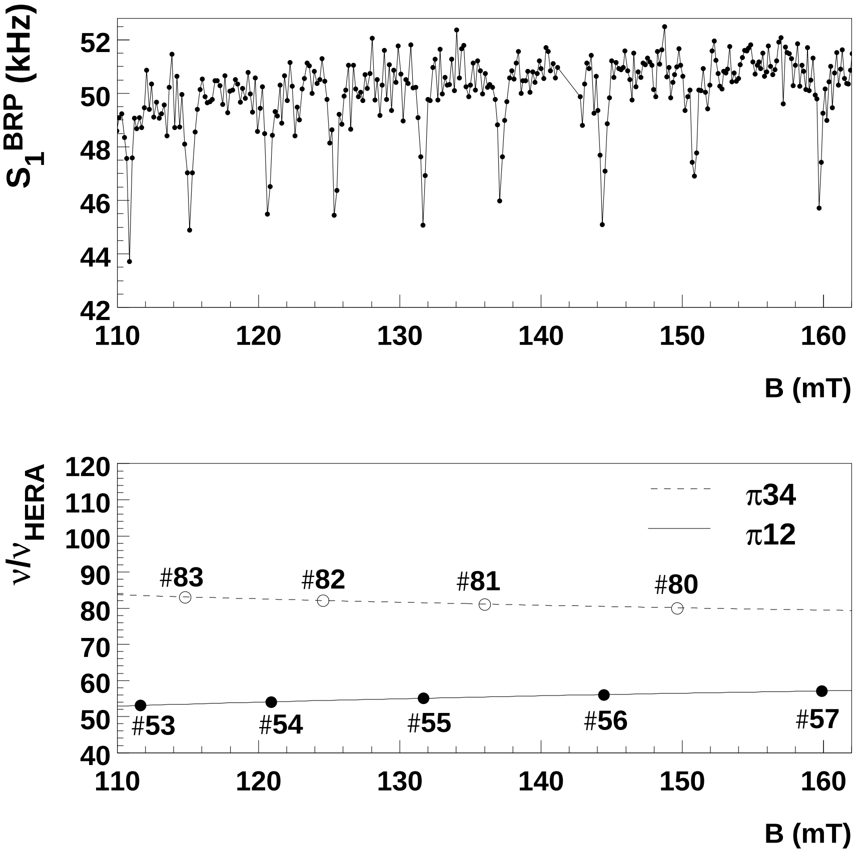

Figure 4.29: *Signal measured in the BRP as a function of the magnetic field in the target when hydrogen states $|2>$ and $|3>$ are injected in the cell and HERA beam is circulating in the ring. The observed nuclear resonances $\pi 12$ and $\pi 34$ are compared to the expected position (see Eq. (4.46)).*

4.7.1 Conclusions

The studies performed with the test dipole magnet, in combination with the HERMES hydrogen target, have shown that the effects related to the interaction of the HERA beam with a transverse magnetic field of $B_{hold} = 170$ mT do not represent a problem for the target and spectrometer performance. In addition, a higher value of the magnetic field up to $B_{hold} = 350$ mT seems feasible: the calculated beam displacement at the center of the cell amounts to 1.7 mm, and the produced synchrotron radiation does not damage the cell surface and any component of the HERMES detector. Although the strength of the transition $\sigma 24$ induced by the beam could not be observed with this test set-up, it must be noted that a magnetic field of $B_{hold} = 350$ mT in the target region would suppress the probability for the $\sigma 24$ resonances by a factor four compared to $B_{hold} = 160$ mT.

5 Extraction of the inclusive and semi-inclusive double-spin asymmetries

Here, the evaluation of the inclusive and semi-inclusive cross-section asymmetries, $A_\parallel$, for polarized hydrogen and deuterium targets is discussed. The criteria to select the events with which the asymmetries are formed, are given in Section 5.1. Section 5.2 describes the formalism used to derive the virtual photon asymmetry A_1 from $A_\parallel$. The various corrections applied to the measured asymmetries are treated in Section 5.3, and the data are presented in Section 5.4. A discussion of the systematic uncertainties to the measured asymmetries is contained in Section 5.5. Further systematic studies for the time-dependence of the measured quantities are discussed in Section 5.6. Finally, in Section 5.7 the resulting proton and deuteron asymmetries are presented and compared to data from CERN and SLAC experiments.

5.1 Data selection

Not all the data acquired by the experiment are suitable for the extraction of inclusive and semi-inclusive spin-correlation parameters. Selection criteria are applied to the whole data set to ensure the minimization of systematic uncertainties while maximizing the statistical precision.
The basic unit of time that characterizes the detector stability is the length of a *fill* of positrons in the HERA ring. A fill corresponds to a period of typically 6-8 hours in which the experiment acquires data in an undisturbed manner. Between fills, hardware and software changes to the experimental setup may occur, introducing variation in the detector conditions from one fill to the next. As explained in Section 3.5, the HERMES DAQ-system separates the data collected within a fill in *runs*. When an accidental failure of a component of the detector is recorded, the corresponding runs are marked in the logbook. The rejection of these runs is the first step in the data quality selection. The smallest subdivision of the data is represented by a *burst*, corresponding to 10 seconds of data taking. Within a run, the DAQ-system generates trigger signals that define the boundaries of each burst and enable the read-out of the slow-control data. Although the detector is read out for every triggered event, each burst contains the complete information of the experimental status (*e.g.* beam and target polarizations, and luminosity

monitor rates) integrated over the 10 seconds. Events acquired within these 10 seconds consequently belong to the set of information defined in the burst. Hence, most studies of data quality focus on this subdivision. Due to the random reversal of the polarization in the target, a burst of 10 seconds can eventually be split in 2 or 3 parts. In these cases, each part is called a *record*, and it corresponds to a well defined state of the target polarization. For data quality purposes the concepts of burst and record are identical. The following paragraphs detail the criteria applied for the selection of data suitable for polarized cross-section analysis.

5.1.1 Burst and record quality

At burst level, the quality criteria are used to reject data due to detector instability and, for the extraction of double-spin asymmetries, records with low beam and target polarizations. By construction the HERMES spectrometer allows the distinction of possible detector failures for top and bottom parts separately. However, for semi-inclusive physics a multi-track coincidence is necessary in the detector, thus the following selection criteria are applied to both detector halves simultaneously. A summary of the data quality selection criteria for the analyzed data sets is given in Table 5.1. Table 5.2 summarizes the number of analyzed records in each year after the selection criteria have been applied.

Data Acquisition conditions
The HERMES DAQ controls the online collection of data. Failures of this system can compromise the quality of the collected data. To ensure an optimal working condition of the system several criteria are applied at the run and burst level. At the beginning and at the end of each run, the DAQ performs a variety of initialization and clean up operations which affect the information recorded in a burst. For this reason, the first three bursts and the final burst of each run are rejected. To ensure good synchronization between the flipping of the target state and the acquired events, the length of a record is required to be between 0 and 11 seconds. The DAQ *live time* is defined as the time in which the DAQ is not busy and is able to collect new data. Bursts where the ratio between the accepted triggers and the generated triggers were below 70% are excluded. Both the burst length and the live time enter directly in the normalization of the experimental count rates.

Beam conditions
Necessary requirements for the analysis of spin observables are a stable and high beam current, and a large and well-measured beam polarization. Limits on the minimum beam current of $I_B > 5$ mA, and on the beam polarization value of $|P_B| > 40\%$ were placed on the data records to ensure both conditions. In addition, the good operation of at least one polarimeter is required.

Target conditions
High polarization and stable performance of the target are requirements as important as the beam conditions in order to achieve a precise measurement of spin observables. For the selected bursts, the nuclear polarization of the target has to be high ($P_T > 70\%$)

and in a well-defined spin state, either parallel or antiparallel to the beam polarization direction. Also the allowed ranges for the initial fraction of injected atoms, α_0, and the fraction of atoms surviving recombination in the cell, α_r, (see Section 4.6) are constrained to ensure a highly polarized target with small systematic uncertainty ($0.97 < \alpha_0 < 1.0$ and $0.7 < \alpha_r < 1.0$).

Detector and tracking conditions
All the PID detectors in both spectrometer halves were required to be operational. The proper functioning of the tracking system in the spectrometer is required, therefore records acquired during trips of the high voltage of the tracking chambers are rejected.

Luminosity
The rate in the luminosity monitor is sensitive to variations in the beam current and of the target density. The requirement for the rate to remain within a nominal operating range (5 Hz $\leq \mathcal{L}_{fit} \leq$ 60 Hz) is a test of the stability for the HERA positron beam and the target density.

5.1.2 Target polarization schemes

In the following the various schemes for the target polarization adopted for the different years are summarized. The averaged values of the target polarization, $\langle P_T \rangle$, are shown in Table 5.2.
A new analysis of the 1997 hydrogen data yielded improved values for the nuclear target polarization compared to the value used in the HERMES publication [123]. Hence, the constant value $\langle P_T \rangle = \pm$ 0.85 was used for the 1997 data set.
In 1996 the fraction $(1 - \alpha_r)$ of atoms recombined as molecules was measured to be (12 $\pm$ 3)%. This value would lead to a relatively large systematic uncertainty in the target polarization due to the large uncertainty in the value of molecular polarization ratio β (see Section 4.6). To reduce the systematic uncertainty, the inclusive asymmetry measured in 1996 was normalized to the asymmetry measured in 1997, where the molecular fraction was small and did not dominate the systematic error in the measured target polarization. For the 1996 asymmetries the averaged target polarization $\langle P_T \rangle = \pm$ 0.75 was obtained. For the 1998 and 1999 data the standard formula for the determination of the target nuclear polarization in Eq. (4.41) was used, where the values for α_0, α_r and P^a were taken from the μDST tables. The sampling correction, c_α, was applied as described in Section 4.6.
For the 2000 data taking period the values used for the nuclear target polarization were $\langle P_{z+} \rangle$ = 0.851 and $\langle P_{z-} \rangle = -$ 0.840 [115].

Parameter	Quality Selection Criterium
DAQ:	
Initialization	Exclude first 3 and last bursts
Efficiency	$0.7 \leq T_{Acc}/T_{Gen} \leq 1$
Record Length	0 s $\leq \Delta_{Record} \leq 11$ s
Beam:	
Current	5 mA $< I_B < 50$ mA
Polarimeter	OK
Polarization	$40\% \leq \lvert P_B \rvert \leq 80\%$
Target:	
Status	Defined
Polarization	$\lvert P_T \rvert \geq 70\%$
α_0-fraction	$0.97 \leq \alpha_0 \leq 1.$
α_r-fraction	$0.7 \leq \alpha_r \leq 1.$
Detector:	
HV Trips	Excluded
Calorimeter	OK
TRD	OK
Čerenkov / RICH	OK
Luminosity Rate	5 Hz $\leq \mathcal{L}_{fit} \leq 60$ Hz

Table 5.1: *Summary of the data quality criteria applied to the HERMES data.*

	1996	1997	1998	1999	2000
$\langle P_B \rangle$	0.54	0.53	0.51	0.53	0.54
$\langle P_T \rangle$	0.75	0.85	0.81	0.80	0.85
Good Runs	3112	8025	5622	8643	22545
Good records, spin $\uparrow\Downarrow$	75802	208936	158189	159309	295938
Good records, spin $\uparrow\Uparrow$	75732	208837	161135	158370	294025
Fractional luminosity	62.2%	79.2%	85.7%	66.2%	81.9%

Table 5.2: *Summary of the records analyzed for each production year after the data quality selection. The averaged polarization values of beam, $\langle P_B \rangle$, and target, $\langle P_T \rangle$, are indicated as well.*

5.1.3 Event selection criteria

At event level, each track that belongs to the event is considered separately. Selection criteria take care of particle identification and kinematic quantities in order to determine the DIS candidates and the semi-inclusive hadrons that are to be used for evaluation of the asymmetries. Table 5.3 summarizes the criteria applied on a track-by-track level.

Track selection
For the analysis, events that generated a DIS-trigger (trigger 21) were selected. Bursts with an overall trigger efficiency lower than 50% were excluded. The reconstruction method of the tracks called $FC\ only$ requires a partial track in the front detector region by using FC only, and a back partial track by using the BC. Tracks for which only the front partial track is available (short tracks) were rejected.

Geometry requirements
The geometry selection criteria ensure that the particle originated from an interaction with target gas within the cell. The particle trajectories were required to be contained within the fiducial volume of the spectrometer. This condition guarantees a proper track reconstruction and identification also for those particles whose trajectories are close to the edges of the acceptance. Additionally, the position of the particle trajectory at the calorimeter was selected to be within $|x_{calo}| \leq$ 175 cm and 30 cm $\leq |y_{calo}| \leq$ 100 cm. These criteria ensure an optimal cluster energy reconstruction and negligible energy loss outside the calorimeter volume for the selected tracks.

Particle identification
As explained in Section 3.4, the relevant quantities for particle identification are the expressions $PID_3 + PID_5$ (for the 1996 and 1997 data sets), and $PID_2 + PID_5$ (for the 1998 to 2000 data sets), which refer to the summed likelihood parameter from the various PID detectors. The separation of leptonic tracks from charged hadronic tracks was performed as follows

$$\begin{aligned} \text{Leptons} &: \quad PID_l \equiv PID_{3(2)} + PID_5 - \log\ \phi \geq 2\,; \\ \text{Hadrons} &: \quad PID_h \equiv PID_{3(2)} + PID_5 - \log\ \phi \leq 0\,. \end{aligned}$$

DIS leptons were further selected in each event by applying the kinematic DIS criteria to the leptonic track with the highest energy. For each event, in coincidence with the DIS lepton, hadrons that passed the kinematic criteria are selected for the formation of the semi-inclusive asymmetries.
For the analysis of hydrogen data (1996-1997) the identification of pions was performed with the threshold Čerenkov detector. A high efficiency for pion identification (>85%) was achieved within a particle momentum window of 4.9 GeV $< p_{track} <$ 13.5 GeV.
Particle identification with the RICH detector for the 1998-2000 data sets makes use of the IRT reconstruction method. A cut on the $quality\ parameter\ rQp >$ 0.0 was applied, and the additional requirement on the particle momentum 4.0 GeV $< p_{track} <$ 13.5 GeV

Criterium	Inclusive asymm.	Semi-inclusive asymm.
Track reconstruction requirements:		
Trigger pattern	T21 fired	
Reconstruction method	FC only	
Track reconstruction	Full tracks only	
Geometry requirements:		
Longitudinal vertex position	-18 cm $\leq z_{vertex} \leq$ +18 cm	
Transverse vertex position	$d_{vertex} \leq$ 0.75 cm	
Horizontal scattering angle	$\|\theta_x\| \leq$ 170 mrad	
Vertical scattering angle	40 mrad $\leq \|\theta_y\| \leq$ 140 mrad	
Position at the calorimeter	$\|x_{calo}\| \leq$ 175 cm	
	30 cm $\leq \|y_{calo}\| \leq$ 100 cm	
PID requirements (1996-1997):		
Lepton identification	$PID \geq 2$	
Hadron identification		$PID \leq 0$
π candidates momentum		4.9 GeV $< p_{track} <$ 13.5 GeV
π candidates Čerenkov signal		$S_{Cer} >$ 0.25NPE
PID requirements (1998-2000):		
Lepton identification	$PID \geq 2$	
Hadron identification		$PID \leq 0$
π, K candidates momentum		4.0 GeV $< p_{track} <$ 13.5 GeV
RICH reconstruction method		IRT, $rQp > 0.0$
Kinematic cuts:		
Calorimeter cluster energy	$E_{calo} \geq$ 3.5 GeV	
Momentum transfer	$Q^2 \geq$ 1.0 GeV^2	
Fractional energy transfer	$y \leq$ 0.85	
Invariant mass	$W^2 \geq$ 4.0 GeV^2	$W^2 \geq$ 10.0 GeV^2
Hadron energy fraction		$z \geq$ 0.2
Feynman variable		$x_F \geq$ 0.1

Table 5.3: *Summary of the criteria used in the analysis to select the inclusive and semi-inclusive events.*

was made. Contaminations are taken into account for the extraction of the pions and kaons semi-inclusive asymmetries with the Q-matrix as weight for the number of events as explained in Section 3.4

Kinematic selection criteria for DIS events and semi-inclusive hadrons
After leptonic tracks have been discriminated from hadronic tracks, the scattered positrons from the DIS processes were selected applying kinematic criteria that define the phase-space associated with the deep-inelastic scattering events. At this point of the selection, no distinction was made between electrons and positrons, as electrons measure charge-symmetric background in the positron sample for a positron beam. Within all the identified positrons in the event, the one with highest momentum (leading lepton) that additionally deposited an energy in the calorimeter greater than 3.5 GeV was selected for the determination of the kinematic variables x, y, Q^2 and W^2. These kinematic variables were calculated by from the particle momenta and the scattering angles. An upper limit of $y \leq 0.85$ suppresses radiative corrections to the cross-section. The criterion on the invariant mass of the final hadronic state, $W^2 \geq 4$ GeV^2, was used to select the deep-inelastic region, where the nucleon breaks apart incoherently. The requirement $Q^2 \geq 1$ GeV^2 allows the modeling of the events within the perturbative QCD framework, and it also suppresses higher twist effects. These requirements define a base sample of inclusive DIS candidates. The distribution of the selected DIS in the kinematic (x, Q^2)-plane is shown in Fig. 5.1.
For the semi-inclusive analysis, the hadrons in the event in coincidence with the DIS candidate were selected. These events form a subsample of the inclusive sample. Hadron fragmentation is analyzed assuming factorization. Monte Carlo studies suggested that a selection criterion of $W^2 \geq 10$ GeV^2 is a good choice for ensuring the validity of this assumption at HERMES [124]. Further requirements on a lower limit for the energy fraction of the hadron ($z \geq 0.2$) and on the Feynman variable ($x_F \geq 0.1$) enhance the correlation between the recorded hadrons and the struck quark in the event.

5.1.4 Summary

For each year of analyzed data, the total numbers of inclusive e^+ and e^-, and semi-inclusive hadrons found after all the selection criteria are summarized in Table 5.4.
Particle multiplicities for the 1995 data set (from Ref. [124]) are shown for completeness.

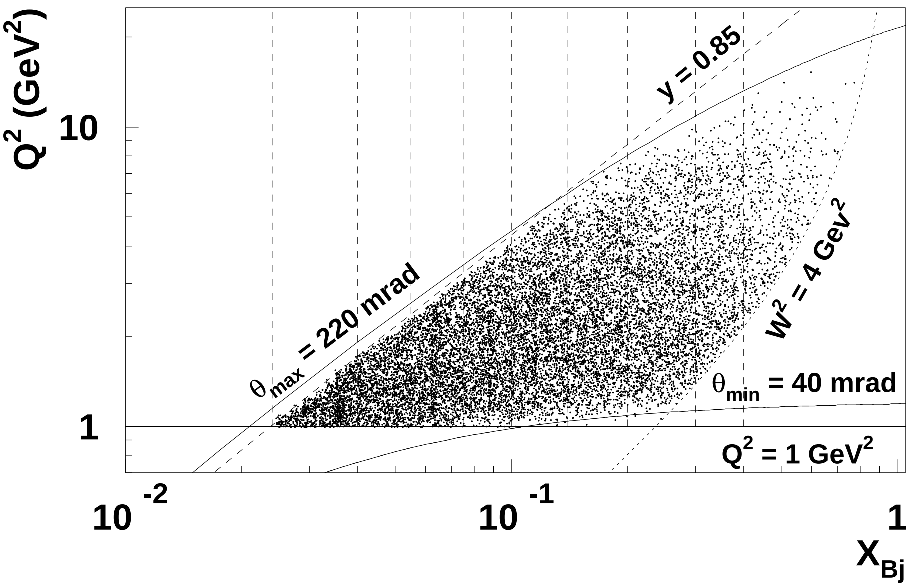

Figure 5.1: *Distribution of the selected DIS candidates in the x and Q^2 kinematic plane. The curves define the applied kinematic selection criteria. The vertical dashed lines show the boundaries of the x-binning as used in the analysis.*

	1995 (^{3}He)	1996 (H)	1997 (H)	1998 (D)	1999 (D)	2000 (D)
e^+	2143301	645295	1707019	976983	12971	6110432
e^-	21784	7336	19971	11229	1169961	62103
h^+	269958	84747	225204	122112	143481	782398
h^-	169666	48299	126898	81509	97662	491371
π^+	-	28878	83939	59632	69521	364339
π^-	-	19552	57146	47995	57251	297233
K^+	-	-	-	10894	13012	67538
K^-	-	-	-	4175	5391	28280

Table 5.4: *Summary of particle multiplicities obtained after all the described selection criteria for the different years of data taking. In brackets, next to the year, the kind of polarized target used is indicated. For the ^{3}He data sample, the particle multiplicities from Ref. [124] are shown for comparison. Note that for the 1998 data period an electron beam was used instead of positrons in the experiment.*

5.2 Determination of the double-spin asymmetries

The longitudinal double-spin asymmetry $A_{\parallel}^{(h)}(x,Q^2)$ is defined by the cross-sections for antiparallel ($\rightleftarrows$) and parallel ($\rightrightarrows$) alignment of the beam and target helicities as:

$$A_{\parallel}^{(h)}(x,Q^2) = \frac{\sigma^{\leftrightarrows} - \sigma^{\rightrightarrows}}{\sigma^{\leftrightarrows} + \sigma^{\rightrightarrows}}\,, \tag{5.1}$$

where h may represent any of the inclusive or semi-inclusive event channels considered for either hydrogen, deuterium or ^{3}He targets. The total yield of events of type h measured per spin state,$N_h^{\rightleftarrows\,(\rightrightarrows)}$, is related to $A_{\parallel}^{(h)}(x,Q^2)$ by

$$N_{(h)}^{\rightleftarrows\,(\rightrightarrows)} = \int_{\rightleftarrows\,(\rightrightarrows)} \mathcal{A}(t,x,Q^2,z)\;\sigma^{\mathrm{unpol}}(x,Q^2,z)\;\mathcal{L}(t)\;\Big(1 \overset{+}{\scriptstyle(-)} A_{\parallel}^{(h)}(x,Q^2,z)\;P_B(t)\;P_T(t)\Big)\;dt\;. \tag{5.2}$$

Here, the integration is performed over time periods with target polarization in a state anti-parallel ($\int_{\rightleftarrows}$) or parallel ($\int_{\rightrightarrows}$) to the longitudinal beam polarization. The HERMES detector acceptance and efficiency factors for events of type h are included in the term $\mathcal{A}(t,x,Q^2,z)$, and $\sigma^{unpol}(x,Q^2,z) = (\sigma^{\rightleftarrows} + \sigma^{\rightrightarrows})/2$ is the unpolarized DIS cross-section. The term $\mathcal{L}(t)$ represents the effective luminosity at the experiment for each spin state. The lifetime of the DAQ-system is accounted for in this quantity. Note that the indicated z dependence of the cross-section is valid in the semi-inclusive case only. Target and beam polarizations are indicated by $P_T(t)$ and $P_B(t)$, respectively. Assuming that acceptance and efficiency are constant on the time-scale of a target spin-flip, $\mathcal{A}(x,Q^2,z)$ is time independent, and can be factorized out of the integral together with $\sigma^{unpol}(x,Q^2,z)$. Equation (5.2) is further integrated over the Q^2 and z dependence, leaving only the dependence on the quark momentum fraction x. Integrating over the time-length of a burst i, the time dependent quantities can be rewritten as

$$L_i^{\rightleftarrows\,(\rightrightarrows)} = \int_{\rightleftarrows\,(\rightrightarrows)} \mathcal{L}(t)\;dt\;, \tag{5.3}$$

$$P_i^{\rightleftarrows\,(\rightrightarrows)} = \int_{\rightleftarrows\,(\rightrightarrows)} \mathcal{L}(t)\;|P_B(t)\;P_T(t)|\,dt\;. \tag{5.4}$$

With the definitions

$$N_{(h)}^{\rightleftarrows\,(\rightrightarrows)} \equiv \sum_i (n_h^{\rightleftarrows\,(\rightrightarrows)})_i\,, \tag{5.5}$$

$$L^{\rightleftarrows\,(\rightrightarrows)} \equiv \sum_i L_i^{\rightleftarrows\,(\rightrightarrows)}\,, \tag{5.6}$$

$$P^{\rightleftarrows\,(\rightrightarrows)} \equiv \sum_i P_i^{\rightleftarrows\,(\rightrightarrows)}\,, \tag{5.7}$$

where $n_i^{\rightleftarrows\,(\rightrightarrows)}$ represents the number of events in burst i for each kinematic x-bin, and the sum is performed over all the collected bursts in the experiment for each defined spin state, the raw count rate asymmetry $A_{\parallel}^{(h)}(x)$ is experimentally determined from

$$A_{\parallel}^{(h)}(x) = \frac{N_{(h)}^{\rightleftarrows} L^{\rightrightarrows} - N_{(h)}^{\rightrightarrows} L^{\rightleftarrows}}{N_{(h)}^{\rightleftarrows} P^{\rightrightarrows} + N_{(h)}^{\rightrightarrows} P^{\rightleftarrows}} \,. \tag{5.8}$$

Assuming $g_2^{(h)} = 0$, the virtual photon-nucleon asymmetry $A_1^{(h)}$ in Eq. (2.89) equals

$$A_1^{(h)} = \frac{1}{(1+\eta\gamma)} \frac{A_{\parallel}^{(h)}}{D} \,. \tag{5.9}$$

The uncertainty associated with this assumption is included in the systematic uncertainty of $A_1^{(h)}$, and it is discussed in section 5.5.4. In Eq. (5.9), $\eta(x,Q^2)$ and $\gamma(x,Q^2)$ are the kinematic factors defined in Section 2.2.2, and are determined in each x-bin from their average values for the two spin states. The depolarization factor, $D(x,Q^2)$, may slightly vary for the two spin target states due to statistics, and it is evaluated for each spin state separately ($D^{\rightleftarrows}$ and $D^{\rightrightarrows}$). The Tables in Appendix A list the values of η, γ and D averaged for each x-bin for the inclusive and the semi-inclusive events.
The statistical uncertainty $\delta A_1^{(h)}$ on the measured asymmetry $A_1^{(h)}$ is calculated from the statistical uncertainties in the number of events, which follows a Poisson distribution. For sufficiently large numbers of scattering events one has $\delta N = \sqrt{N}$ (the index h is implicitly assumed), and

$$\begin{aligned} \delta A_1^{(h)} &= \sqrt{\left(\frac{\partial A_{\parallel}}{\partial N^{\rightrightarrows}}\,\delta N^{\rightrightarrows}\right)^2 + \left(\frac{\partial A_{\parallel}}{\partial N^{\rightleftarrows}}\,\delta N^{\rightleftarrows}\right)^2} \\ &= \frac{1}{(1+\eta\gamma)} \cdot \frac{L^{\rightleftarrows} P^{\rightrightarrows} D^{\rightrightarrows} + L^{\rightrightarrows} P^{\rightleftarrows} D^{\rightleftarrows}}{\left(N^{\rightleftarrows} P^{\rightrightarrows} D^{\rightrightarrows} + N^{\rightrightarrows} P^{\rightleftarrows} D^{\rightleftarrows}\right)^2} \sqrt{\left(N^{\rightrightarrows}\right)^2 N^{\rightleftarrows} + \left(N^{\rightleftarrows}\right)^2 N^{\rightrightarrows}} \,. \end{aligned} \tag{5.10}$$

The binning in x is chosen such that the number of events is about equally distributed in each bin. Table 5.5 lists the boundaries of the x-bins as used in the analysis.

x-bin	x-range	$\langle x \rangle$
1	0.023-0.040	0.033
2	0.040-0.055	0.047
3	0.055-0.075	0.065
4	0.075-0.100	0.087
5	0.100-0.140	0.119
6	0.140-0.200	0.168
7	0.200-0.300	0.244
8	0.300-0.400	0.342
9	0.400-0.600	0.464

Table 5.5: *Definition of the boundaries of the x kinematic binning as used in the analysis. The average x value within each bin is shown as well.*

5.3 Corrections to the raw asymmetries

In this section, the corrections applied to the extracted inclusive asymmetries, A_1, and semi-inclusive asymmetries, $A_1^{(h)}$, are discussed in order to derive the corresponding Born asymmetries.

5.3.1 Background corrections

The dominant source of background in the DIS positron (electron) sample arises from misidentified positrons (electrons) coming from charge-symmetric processes such as e^+e^- pair production. Photo-produced π^0 may decay via $\pi^0 \rightarrow \gamma\gamma$ with subsequent conversion of one or both photons into a e^+e^- pair. Additionally, high energy Bremsstrahlung photons can produce e^+e^- pairs and contribute to the DIS lepton misidentification.
Assuming equal probability for positron and electron identification from the charge-symmetric background processes, the misidentified DIS lepton can be removed from the data sample by subtracting events where the leading lepton passing the DIS kinematic criteria is of opposite charge with respect to the beam charge. Therefore, if a lepton with opposite beam charge passed all the DIS kinematic cuts, then one event with the charge of the beam and with the same kinematics is subtracted from the DIS event sample. In addition, the hadrons in coincidence with the misidentified DIS lepton passing the selection for semi-inclusive candidates, are also subtracted from the semi-inclusive hadron sample.
The hadron contamination in the DIS sample is small compared to the correction from the charge-symmetric background processes, and was therefore neglected.
In Fig. 5.2, the fraction of background events subtracted to the DIS sample in each x-bin is shown for the 1999 data set as example.

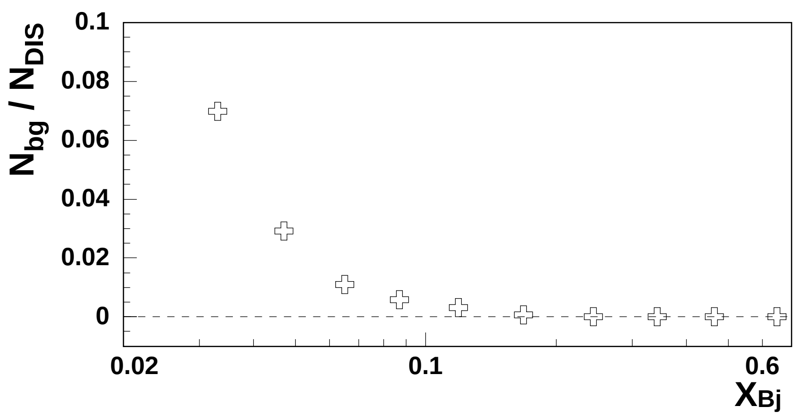

Figure 5.2: *Fraction of background events found in each x-bin with respect to the number of DIS candidates after background subtraction.*

5.3.2 Smearing corrections

In any detector, a systematic difference between the measured kinematic quantities and the true kinematics is observed due to the interaction of the particles with the detector material. This effect is called *kinematic smearing*. The loss of energy due to Bremsstrahlung and multiple scattering can alter the kinematics of the observed tracks. In addition, biases from detector misalignment or calibration offsets, and from the track reconstruction algorithm itself, must be considered. The contributions to the measured asymmetries of these smearing effects and of the detector acceptance have been estimated over the x range with the HERMES Monte Carlo (HMC) [125]. A large sample of DIS events was generated with HMC, in which a representation of the HERMES detector is implemented based on the Geant package [126]. The same angular acceptance and kinematic selection criteria as used in the extraction of the experimental asymmetry are applied to the generated events. For each x-bin, an acceptance correction factor was estimated for the inclusive asymmetries as follows

$$\kappa_{ACC} = \frac{A_{1,MC}^{4\pi}}{A_{1,MC}^{ACC}} , \tag{5.11}$$

where the asymmetry $A_{1,MC}^{4\pi}$ was determined from all the generated positron kinematics, and $A_{1,MC}^{ACC}$ takes into account only those events inside HERMES acceptance. A smearing correction factor was evaluated for each x-bin by comparing the previous asymmetry , $A_{1,MC}^{ACC}$, with the asymmetry $A_{1,MC}^{ACC,REC}$ extracted from the events with kinematics reconstructed considering detector effects

$$\kappa_{smear} = \frac{A_{1,MC}^{ACC}}{A_{1,MC}^{ACC,REC}} . \tag{5.12}$$

The overall correction factor $\kappa_{MC} = \kappa_{smear} \cdot \kappa_{ACC}$ is applied to the measured inclusive asymmetries as a multiplicative term

$$A_{\parallel}^{corr} = A_{\parallel}^{exp} \cdot \kappa_{MC} . \tag{5.13}$$

In a similar way, acceptance and smearing correction factors for the semi-inclusive asymmetries have been determined by extracting $A_{1,MC}^{h}$ from the generated hadrons in coincidence with the DIS positrons. Monte Carlo multiplicities have been weighted by the experimental hadron multiplicities $n^{h^+}(x)$ and $n^{h^-}(x)$. The estimated corrections for the proton target are listed in Table 5.6 (from Ref. [127]). Smearing corrections for semi-inclusive π^+ and π^- events have not been calculated, and they are assumed to be identical to the hadron corrections.
At the time of this analysis, the corrections for the deuterium data have not been determined. Therefore, the same systematic uncertainties associated with the smearing corrections on the proton asymmetries have been applied to the deuteron asymmetries. Note that during the data taking period with deuterium target the silicon vertex chambers have been removed from the detector set-up. These chambers induce a major part of the smearing.

$\langle x \rangle$	$\kappa_{smear} \pm stat.$	$\kappa^{h^+}_{smear} \pm stat.$	$\kappa^{h^-}_{smear} \pm stat.$
0.033	0.946 $\pm$ 0.009	0.913 $\pm$ 0.011	0.981 $\pm$ 0.027
0.047	0.975 $\pm$ 0.009	0.931 $\pm$ 0.011	0.967 $\pm$ 0.025
0.065	0.967 $\pm$ 0.009	0.930 $\pm$ 0.010	0.944 $\pm$ 0.022
0.087	0.955 $\pm$ 0.009	0.925 $\pm$ 0.009	0.930 $\pm$ 0.018
0.119	0.937 $\pm$ 0.009	0.929 $\pm$ 0.007	0.931 $\pm$ 0.011
0.168	0.931 $\pm$ 0.008	0.960 $\pm$ 0.005	0.961 $\pm$ 0.007
0.245	0.934 $\pm$ 0.007	0.996 $\pm$ 0.004	1.000 $\pm$ 0.005
0.342	0.966 $\pm$ 0.008	1.019 $\pm$ 0.004	1.019 $\pm$ 0.005
0.465	0.989 $\pm$ 0.005	1.026 $\pm$ 0.004	1.023 $\pm$ 0.005

Table 5.6: *Kinematic smearing corrections for the inclusive and semi-inclusive proton asymmetries from Ref. [127].*

5.3.3 Radiative corrections

In Chapter 1 the lepton-nucleon scattering process was discussed in the approximation of one-photon exchange, also called Born approximation. However, the cross-sections measured in deep-inelastic scattering experiments have large contributions from processes other than the first-order Born diagram depicted in Fig. 5.3 (a). The formalism used to remove the contributions to the DIS cross-sections from non-Born processes is known as *radiative corrections* (RC). The Feynman diagrams representing the second-order radiative corrections to the Born diagram are depicted in Fig. 5.3 (b,c,d,e).

At the lowest order the cross-section that takes into account radiative effects can be decomposed in terms of specific contributions as

$$\sigma_{RC} = \sigma_{in} + \sigma_{el} + \sigma_{qel} + \sigma_v \; . \tag{5.14}$$

Here, each σ denotes the double differential cross-section $d^2\sigma/dxdy$, and $\sigma_{in},\ \sigma_{el}$ and σ_{qel} represent respectively the contributions of radiative tails from continuous spectrum, the elastic scattering radiative tail, and quasi-elastic scattering. The term σ_v contains the contribution of virtual photon radiation and vacuum polarization effects. Each scattering channel dominates in a different region of the kinematic $(\nu, Q^2)-$plane. Electroweak corrections due to photon-Z^0 interference are negligible at the HERMES Q^2 range, where Q^2 is small compared to the mass of the Z^0 boson (m_{Z^0} = 91 GeV).
The radiative corrections were calculated, for the different targets, with the code POLRAD [128, 129]. The program models the radiative effects that are needed to calculate the polarized Born asymmetries by using as input the measured asymmetries on hydrogen, deuterium and ^{3}He targets. With POLRAD, the Born asymmetry is obtained as a result of an iterative procedure, where at each next step a fit of the experimental asymmetry A_1^{measured}, corrected for radiative effects estimated at the previous step, is used to calculate a model for the structure function $g_1(x)$:

$$g_1^{(n)}(x) = \frac{F_2(x,Q^2)}{2x(1+R)} \left(A_1^{\mathrm{measured}} - \Delta A_1^{RC} \cdot g_1^{(n-1)}(x) \right) \; . \tag{5.15}$$

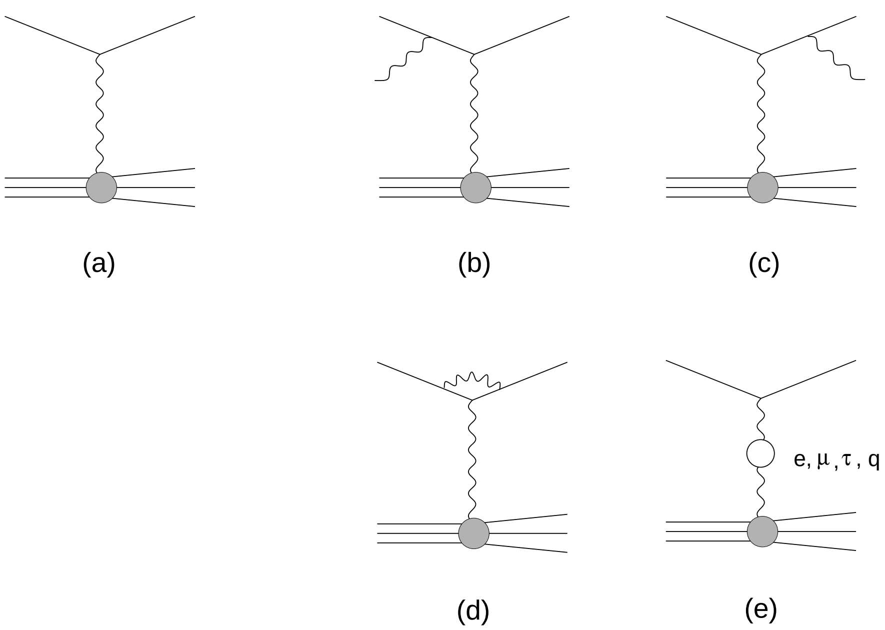

Figure 5.3: *Born diagram (a) and first-order Feynman diagrams which contribute to the radiative corrections to the asymmetries A_1. Diagrams (b) and (c) represents the corrections from Bremsstrahlung effects. Virtual photon contributions are determined from the vertex correction of diagram (d) and the vacuum polarization depicted by diagram (e).*

Here, n indicates the iteration index. POLRAD requires input for the structure functions F_2 and $R = \sigma_L/\sigma_T$. For F_2 the parametrization given in Ref. [130], and for R the Whitlow parametrization given in Ref. [26] were used. Additionally, $g_2(x) = 0$ is assumed. The magnitude of the radiative corrections are determined after convergence of the procedure (usually within a few steps). The corrections are applied as an additive term to the measured asymmetries A_1^{measured} as follows

$$A_1^{\mathrm{Born}} = A_1^{\mathrm{measured}} - \Delta A_1^{RC} , \tag{5.16}$$

where $A_1^{\mathrm{B}orn}$ is the Born asymmetry and the ΔA_1^{RC} spin asymmetry comprises the contributions from the radiative processes shown in Fig. 5.3. The results for the radiative corrections ΔA_1^{RC} to the inclusive proton and deuteron asymmetries are presented in Table 5.7 with their associated systematic uncertainties. The dominating sources of systematic uncertainties in the RC are related to the choice of different parametrizations of the structure functions and to the elastic and quasi-elastic form factors. Corrections to the semi-inclusive asymmetries have been determined to be small enough to be negligible [131], and are therefore not applied.

$\langle x \rangle$	$\Delta A_1^{RC} \pm$ syst. unc.		
	Helium-3	Hydrogen	Deuterium
0.033	0.00571± 0.00292	-0.00337 ± 0.00016	0.00878 ± 0.00033
0.047	0.00494± 0.00134	-0.00311 ± 0.00010	0.00737 ± 0.00023
0.065	0.00474± 0.00064	-0.00302 ± 0.00010	0.00662 ± 0.00018
0.087	0.00439± 0.00023	-0.00247 ± 0.00007	0.00606 ± 0.00010
0.119	0.00423± 0.00062	-0.00215 ± 0.00011	0.00556 ± 0.00012
0.168	0.00404± 0.00100	-0.00143 ± 0.00012	0.00533 ± 0.00018
0.245	0.00389± 0.00138	-0.00039 ± 0.00005	0.00376 ± 0.00017
0.342	0.00399± 0.00181	0.00047 ± 0.00002	0.00212 ± 0.00010
0.465	0.00384± 0.00196	0.00084 ± 0.00008	0.00082 ± 0.00010

Table 5.7: *Additive radiative corrections ΔA_1^{RC} to the inclusive ^{3}He, proton and deuterium asymmetries A_1, and associated systematic uncertainties.*

5.4 Measured proton and deuteron asymmetries

The $A_1^{(h)}$ asymmetries for proton (1996 and 1997) are shown in Fig. 5.4 and for deuteron (1998 – 2000) in Fig. 5.5. The data samples belonging to the corresponfing type of target are consistent with each other. The values of the asymmetries with statistical and total systematic uncertainties are listed in the Tables in Appendix A.
The extracted inclusive and semi-inclusive hadron asymmetries for the proton data have been combined and compared to the results of the E155 experiment at SLAC [132] for the inclusive case, and the SMC experiment at CERN [133] for the semi-inclusive case (see Fig. 5.6).
The combined Hermes inclusive and semi-inclusive hadron asymmetries on deuterium are compared in Fig. 5.7 to E155 [17] and SMC results [133].

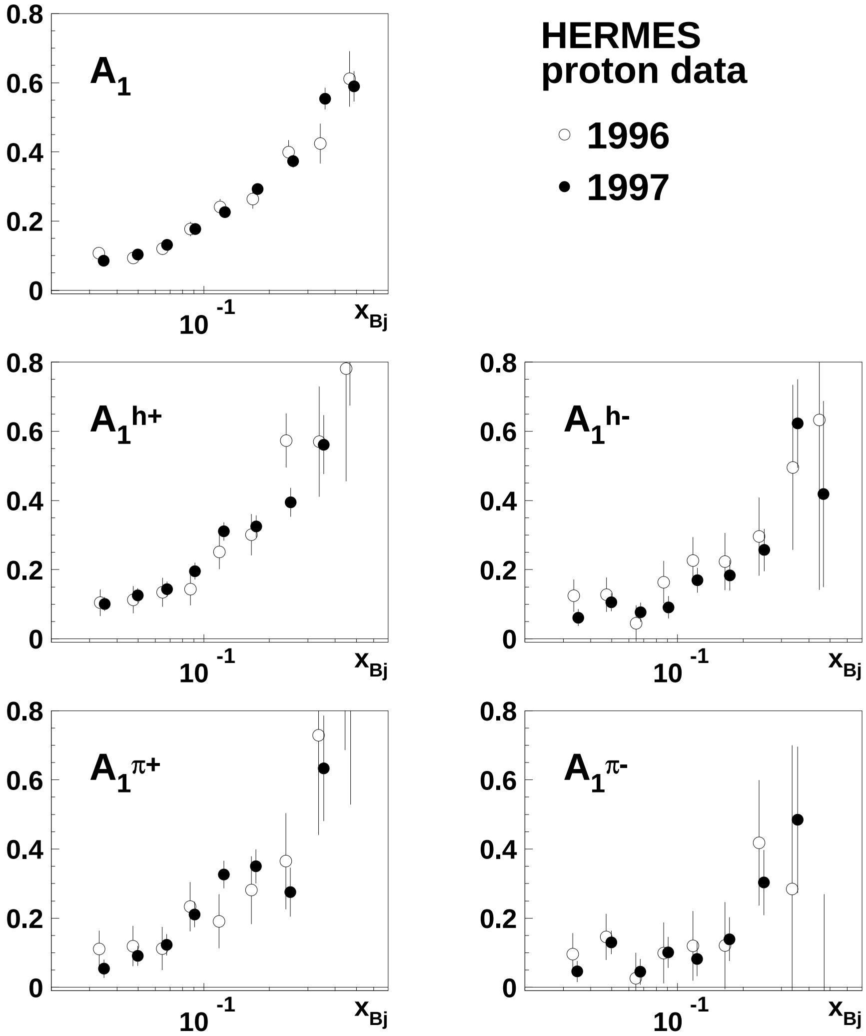

Figure 5.4: *Comparison of inclusive and semi-inclusive proton asymmetries extracted from 1996 and 1997 data sets. The error bars on the data points correspond to the statistical uncertainties.*

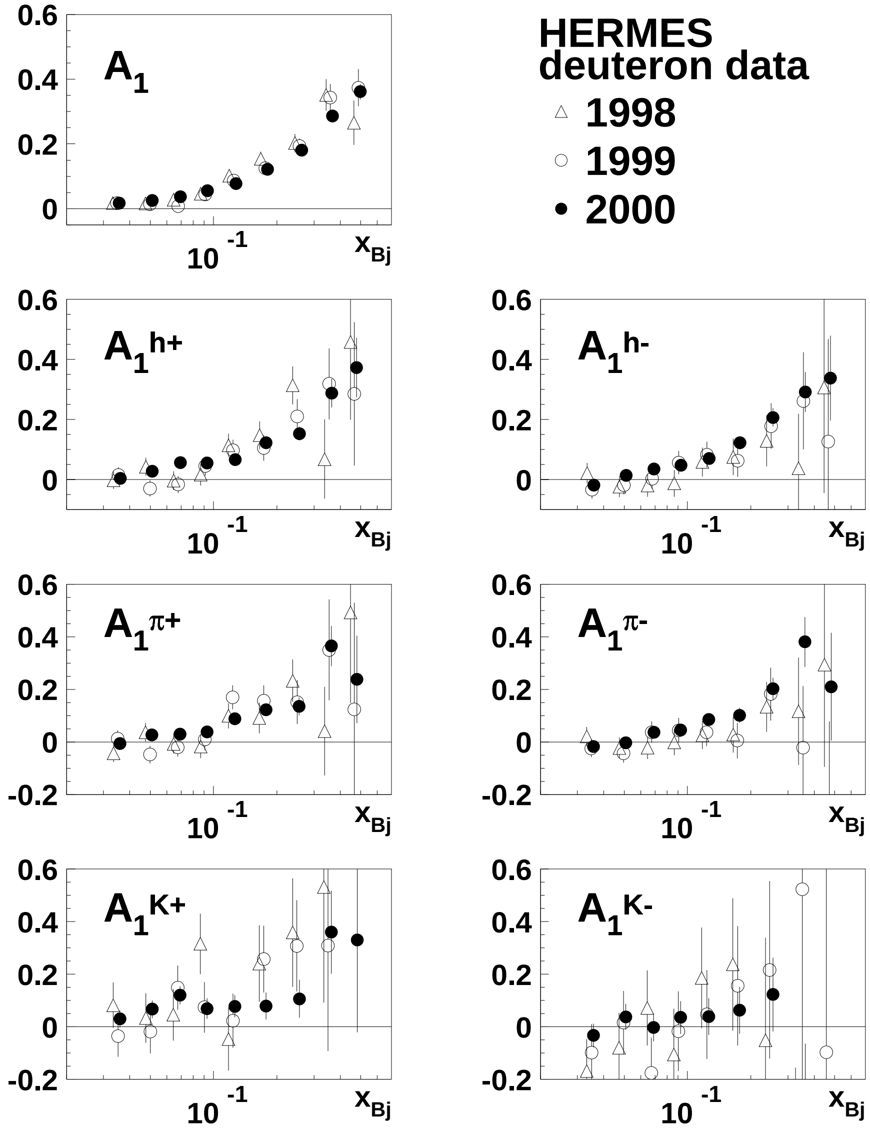

Figure 5.5: *Comparison of inclusive and semi-inclusive deuteron asymmetries extracted from 1998, 1999, and 2000 data sets. The error bars on the data points correspond to the statistical uncertainties.*

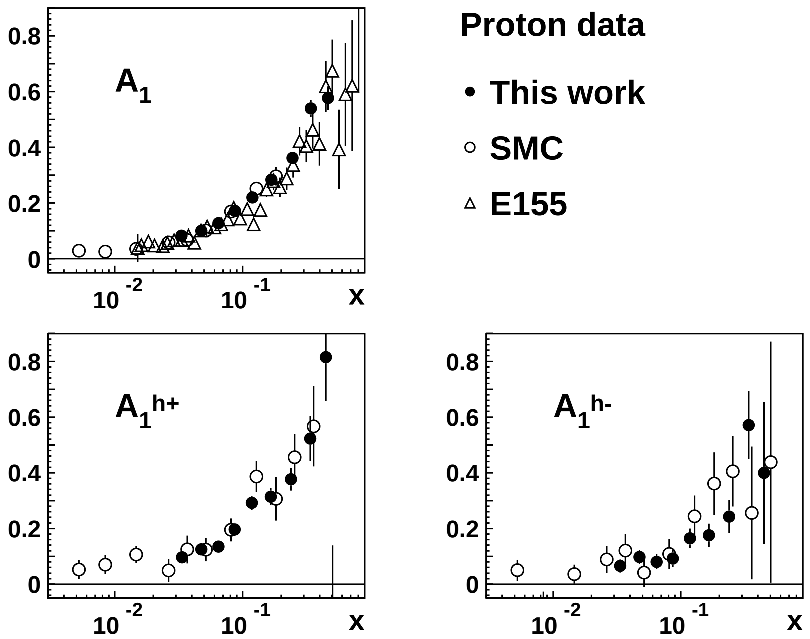

Figure 5.6: *The combined* HERMES *proton asymmetries are compared to results of E155 [132] and SMC [133]. For E155 and SMC data only the statistical errors are shown.*

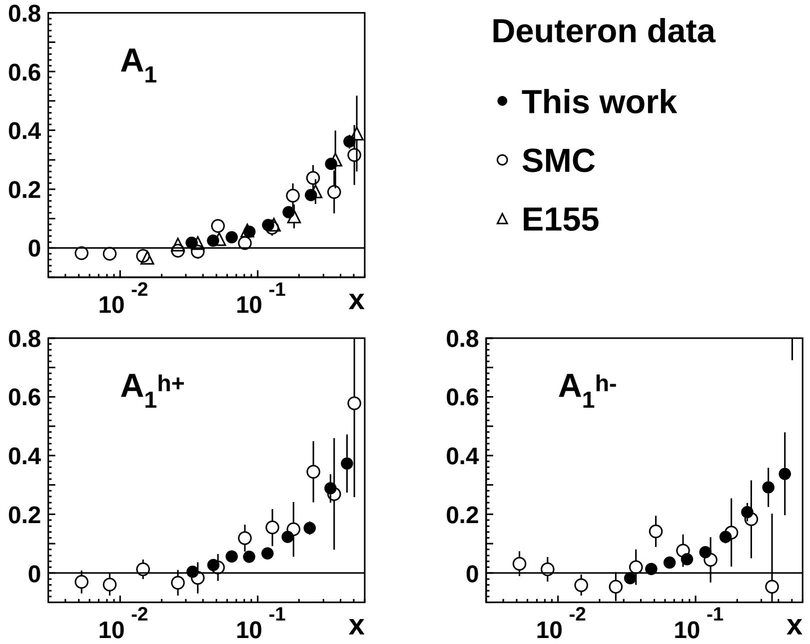

Figure 5.7: *The combined* HERMES *deuteron asymmetries are compared to results of E155 [132] and SMC [133]. Only the statistical errors are shown.*

5.5 Systematic uncertainties in the asymmetries

The contributions to the systematic uncertainty in $A_1^{(h)}$ are outlined in this section. The errors related to the HERMES experiment comprise the systematic uncertainties in the beam and target polarization measurements, and the smearing and radiative corrections discussed in section 5.3.2. Additional systematic uncertainties in $A_1^{(h)}$ are related to external contributions such as the uncertainties in the measurements of R and g_2. In the following, the formulae are applied for each x-bin and, unless explicitly stated otherwise, they hold in the same way for inclusive and semi-inclusive asymmetries. A summary of the sources of the systematic uncertainties in $A_1^{(h)}$ are given in the Tables in Appendix A separately for the different data sets. The largest contribution over the entire x range originates from the target and beam polarizations. The error in each contributing term was added in quadrature to evaluate the total systematic uncertainty in the final asymmetry measurement.

5.5.1 Beam polarization uncertainty

For the 1996 and 1997 data taking periods, the information on the beam polarization was taken from the measurement of the transverse polarimeter only. The fractional systematic uncertainty associated with the absolute calibration of this device was determined as $[\delta P_B/P_B]_{\text{calib}} = 3.3\%$ [124]. This value is fully correlated between measurements of different years. Additional systematic uncertainties arise from corrections to point-to-point instabilities of the raw polarization measurements. This contribution was estimated independently for 1996 and 1997, and is equal to $[\delta P_B/P_B]_{\text{corr}} = 0.9\%$ for both years [124]. Hence, the two contributions added in quadrature give the total fractional uncertainty in the beam polarization measurement of $[\delta P_B/P_B]_{(1996,1997)} = 3.4\%$.
Also for the 1998 data the transverse polarimeter was taken as the default polarimeter, delivering an uncertainty of $[\delta P_B/P_B]_{(1998)} = 3.4\%$. Measurements from the longitudinal polarimeter were used instead for the 1999 and 2000 data. The associated fractional uncertainties are respectively, $[\delta P_B/P_B]_{(1999)2} = 1.8\%$, and $[\delta P_B/P_B]_{(2000)} = 1.9\%$. The systematic uncertainty in the asymmetry A_1 from this contribution is given by

$$[\delta A_1]_{P_B} = \sqrt{\left(\frac{\partial A_1}{\partial P_B}\right)^2 (\delta P_B)^2} = \left| A_1 \cdot \frac{\delta P_B}{P_B} \right| . \tag{5.17}$$

5.5.2 Target polarization uncertainty

In Section 5.1.2 the values of the target polarization were given for the different years. Here, the associated systematic uncertainties are summarized.
For the 1997, the relative target polarization uncertainty was estimated to be $[\delta P_T/P_T]_{1997} = 5.9\%$. For the 1996 data, the fractional uncertainty arising from the

normalization procedure to the 1997 asymmetry evaluated in an overall relative polarization uncertainty of $[\delta P_T/P_T]_{1996} = 7.6\%$.
The fractional uncertainties associated with the 1998 and 1999 running periods were $[\delta P_T/P_T]_{1998,1999} = 8.0\%$. For the 2000 data set the value $[\delta P_T/P_T]_{2000} = 4.0\%$ was estimated.
For each year the systematic uncertainty in the asymmetries was calculated according to

$$[\delta A_1]_{P_T} = \left| A_1 \cdot \frac{\delta P_T}{P_T} \right| . \tag{5.18}$$

5.5.3 Smearing and radiative corrections uncertainties

The systematic uncertainties associated with the smearing and radiative corrections have been estimated during the discussion of the correction procedure in Sections 5.3.2 and 5.3.3. Since the smearing correction factors κ_{smear} are determined from MC studies, their uncertainties are related to the number of generated events, and are thus of statistical nature. On the other hand, κ_{smear} depends on the value of the asymmetry itself. Therefore, the systematic uncertainty in the smearing correction was associated with $\delta\kappa_{smear}$. The resulting uncertainties in the asymmetries are given by

$$[\delta A_1]_{\kappa_{smear}} = |A_1 \cdot \delta\kappa_{smear}| , \tag{5.19}$$
$$[\delta A_1]_{RC} = \left|\delta(\Delta A_1^{RC})\right| . \tag{5.20}$$

The smearing corrections are assumed to be fully correlated between years characterized by the same target. For the semi-inclusive pion asymmetries the uncertainties associated with the smearing corrections are evaluated from the corresponding uncertainties for the hadron asymmetries. The systematic uncertainties for the radiative corrections were accounted only for the inclusive asymmetries, since this correction was not applied to the semi-inclusive asymmetries.

5.5.4 Model for the spin structure function g_2

The derivation of Eq. (5.9) assumes that the structure function $g_2(x)$ equals zero. Figure 5.8 shows the presently available data for direct measurements of the function $xg_2(x)$ performed with inclusive DIS at SLAC [134, 16, 18]. The data were obtained in a similar x and Q^2 range as covered in Hermes . The data are consistent with $g_2(x) = 0$ within statistical uncertainties. The systematic bias due to the assumption for $g_2(x)$ has been evaluated by parametrizing the experimental uncertainties, $x\delta g_2(x)$, of $xg_2(x)$ as

$$x\tilde{g}_2^p(x) = \pm 0.055 \cdot (1-x)^{0.7} , \tag{5.21}$$
$$x\tilde{g}_2^d(x) = \pm 0.065 \cdot (1-x)^{0.98} , \tag{5.22}$$
$$x\tilde{g}_2^n(x) = \pm 0.110 \cdot (1-x)^{0.98} . \tag{5.23}$$

For $x \to 1$ these parametrizations follow the behaviour of the twist-2 Wanzura-Wilczek term $xg_2^{WW}(x)$ which approaches zero in this limit. The systematic uncertainty δg_2 associated with the model used for $g_2(x)$ follows from Eq. (2.41) as

$$[\delta A_1]_{g_2} = \left| \frac{(\eta\gamma - \gamma^2)}{1+\eta\gamma} \left(\frac{\tilde{g}_2}{F_1} \right) \right| , \tag{5.24}$$

for proton and deuteron asymmetries. The semi-inclusive asymmetries are assumed to have the same systematic uncertainty as the measured uncertainty in the inclusive case. The contributions due to δg_2 are completely correlated for each target, but not between different targets. The values of δg_2 in the HERMES kinematic region are listed in the Tables in Appendix A for the different data sets.

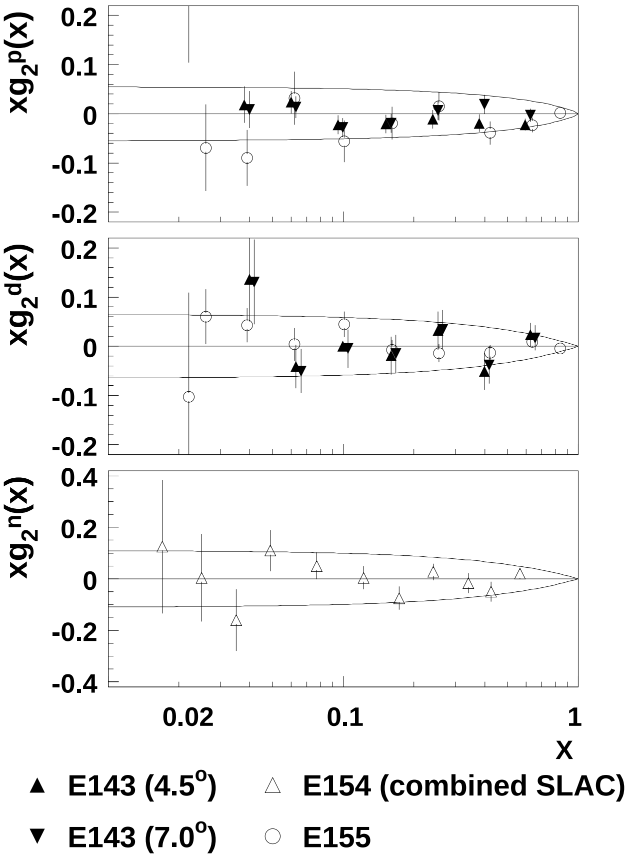

Figure 5.8: *The spin structure function $xg_2(x)$ measured at SLAC on different targets. The proton and deuteron data refer to the results of the experiments E143 [134] (separately for the 4.5° and 7.0° spectrometers, at the average Q^2 of 3 GeV^2) and E155 [18] (average $Q^2 \sim 5$ GeV^2). Neutron data refer to the combined results of the SLAC experiments E142, E143 and E154 [16] (average $Q^2 \sim 3$ GeV^2). The error bars on the data points indicate the statistical uncertainties only. The systematic uncertainties are negligible and not shown. The curves drawn symmetrically around $xg_2(x) = 0$ were used to parametrize the uncertainties associated with the assumption $g_2(x) = 0$.*

5.5.5 Uncertainty in the parametrization of R

The ratio $R = \sigma_L/\sigma_T$ of the longitudinal (σ_L) and transverse (σ_T) photon absorption cross-sections enters the asymmetry calculation through the depolarization factor D (see Eq. (2.35)). The uncertainty, δR, of the world-averaged parametrization of R is presented in Ref. [26] and contributes to the measured asymmetries as

$$[\delta A_1]_R = \frac{\epsilon}{1+\epsilon R} A_1 \delta R \, , \tag{5.25}$$

where ϵ is the kinematic factor in Eq. (2.36). In the Tables in Appendix A the values of R in the HERMES kinematic region are given.

5.5.6 Uncertainty in the RICH hadron identification

To assess the stability of the RICH particle identification the semi-inclusive asymmetries for pions and kaons have been extracted from the 2000 deuterium data by using the RPS method (see Section 3.3.2) and compared to those extracted applying the IRT method. Within statistical uncertainties the asymmetries were found to be consistent with each other. Therefore, a conservative systematic error of 2% was assigned to the RICH PID based on the maximum difference of the asymmetries determined with the two methods.

5.5.7 Total systematic uncertainty

The total systematic uncertainty assigned to the asymmetries comprises all the contributions described in the previous sections. Each systematic uncertainty was added in quadrature for each x-bin,

$$\delta A_1^{tot}(x) = \sqrt{\sum_i ([\delta A_1(x)]_i)^2} \, . \tag{5.26}$$

The Tables in Appendix A present the resulting systematic uncertainties in the asymmetries for each contribution and for each year separately. For the years 1996 and 1997 (hydrogen target) the dominating source over almost the entire x-range is given by the uncertainty in the target polarization. The uncertainty associated with the spin structure function g_2 is strongly dependent on kinematics and becomes the dominant contribution to the bins at highest x. The same considerations hold for the deuterium data in the years 1998 and 1999. For the data obtained in the year 2000 the uncertainty assigned to g_2 is the most important component.

5.6 Systematic studies in the deuteron asymmetries

A number of studies have been performed for the asymmetries extracted from the deuterium data in order to test the coherence of the analyzed data for the different years. Systematic studies related to the data obtained with the hydrogen target are summarized in Refs. [135, 136].
In this Section, the results of the following studies are presented:

- Time dependence of normalized particle yields (Sections 5.6.1 and 5.6.2);
- Time dependence of the measured asymmetries (Section 5.6.3);

- Dependence of the semi-inclusive asymmetries on the fractional hadron energy z (Section 5.6.4).

To ensure that the measurements were not biased by time-dependent effects in the experiment, each year of collected data (except 1998) was subdivided into several independent sets. The basic time unit chosen to characterize the detector stability is the HERA fill. During each year of data taking, apart for for 1998, the helicity of the beam was reversed several times. Therefore, the criteria used to divide the collected data were chosen such that a well-defined beam helicity corresponds to each data set. Defining $+1$ as the sign of the beam helicity used for the year 1996, periods with beam helicity opposite to that used in 1996 have beam helicity -1. Data from periods with the same beam helicity were merged together to define two periods: $Pol+$, corresponding to beam helicity $+1$, and $Pol-$, corresponding to beam helicity -1.
The definition of the time periods chosen for the studies are summarized in Table 5.8.

Year	Period	Fills	Beam Helicity
1996	all		$+1$
1998	all	189−319	-1
1999	all	10 − 190	
	P1	10 − 51	$+1$
	P2	57 − 85	-1
	P3	89 − 158	$+1$
	P4	159 − 190	-1
	Pol+	P1 + P3	$+1$
	Pol−	P2 + P4	-1
2000	all	7 − 335	
	P1	7 − 69	$+1$
	P2	71 − 105	-1
	P3	110 − 151	$+1$
	P4	152 − 203	-1
	P5	204 − 244	$+1$
	P6	245 − 290	-1
	P7	291 − 335	$+1$
	Pol+	P1 + P3 + P5 + P7	$+1$
	Pol−	P2 + P4 + P6	-1

Table 5.8: *Definition of the time periods used in the division of the data sets. The fill numbers of the data passing the quality criteria and used in the analysis are listed. The beam helicity corresponding to each period is indicated. The beam helicity for the year 1996 is shown only as reference.*

5.6.1 Luminosity normalized DIS yields

The luminosity normalized yields of DIS events have been calculated separately for each fill and for each target spin state. Using the notation of Eqs. (5.6) and (5.7), the yield $Y_i^{\rightleftarrows}$ calculated for fill i and for antiparallel spin state target is defined as

$$Y_i^{\rightleftarrows} = \frac{N^{\rightleftarrows}}{L^{\rightleftarrows}}\,, \tag{5.27}$$

where $L^{\rightleftarrows}$ is the integrated luminosity. The uncertainty in $Y_i^{\rightleftarrows}$ is given by the statistical uncertainty in the number of DIS events, $\sigma_{i,\rightleftarrows} = \sqrt{N^{\rightleftarrows}}/L^{\rightleftarrows}$.
The yield $Y_i^{\rightleftarrows}$ for each fill was then compared to the error-weighted mean of the total yield, $\langle Y_{year}\rangle$, for the year under study, calculated as

$$\langle Y_{year}\rangle = \frac{\sum_i^n \frac{Y_i}{\sigma_i^2}}{\sum_i \frac{1}{\sigma_i^2}}\,. \tag{5.28}$$

Here, n is the total number of fills for the year. The statistical uncertainty of the total yield is given by

$$\sigma_{year}^2 = \frac{1}{\sum_i^n \frac{1}{\sigma_i^2}}\,. \tag{5.29}$$

Figures 5.9 to 5.11 show the yields Y_i for each year versus fill number. It can be seen that the 1998 yields for fills 189−210 are considerably higher than the remaining fills in the year. It was found that this fluctuation is highly correlated to the position of the beam with respect to the interaction point (IP) at the target.
The beam position at the HERMES IP is estimated by a combination of a beam position monitor (BPM) located several meters upstream the target IP, and a BPM placed downstream (one meter after the luminosity monitor). The two lower panels of Fig. 5.9 show the fill-averaged beam position along the x coordinate at the IP, and the y-projection of the beam slope. The y position and x slope of the beam do not exhibit significant fluctuations throughout the year. Different beam positions at the IP can result in a variation of the coincidence rates of the Møller pairs in the luminosity detector. Monte Carlo-based corrections are applied to the detected rates to take into account acceptance dependence of the Møller cross-section. However, extreme conditions for the beam position can lead to the necessity of correcting for contributions not related to the reconstructed beam parameters at the luminosity monitor [137].
Note that the 1998 yields (electron beam) are in general lower than the yields in 1999 and 2000 (positron beam). This is probably due to the different corrections for Møller and Bhabha cross-sections applied to the rates measured in the luminosity monitor.
The yields for the 1999 period also show fluctuations, although in this case these are not related to the position of the beam. Trigger studies [138] reported a significant change

in the H0 hodoscope efficiency due to an increase of the high voltage in the H0 photomultipliers. Four periods could be identified characterized by different voltage settings in correspondence to fills 30, 51 and 85.
For 2000 data taking, a slightly lower yield for fills 7−97 compared to the remaining fills can be observed. In this case, the H0 threshold was changed, resulting in an overall increase of the efficiency of the trigger.
In this analysis, a normalization of the yield in each year was not applied since the fluctuations were characteristic of periods much longer than the time scale of a target spin-flip. In the measured asymmetries, for instance, the trigger efficiency cancels out in the ratio of the cross-sections. Instead, an evaluation of the impact of the yield fluctuations on the calculated asymmetries was performed by extracting the asymmetries on a fill-by-fill basis. A consistency test of the variation in the observed values is presented in Section 5.6.3.

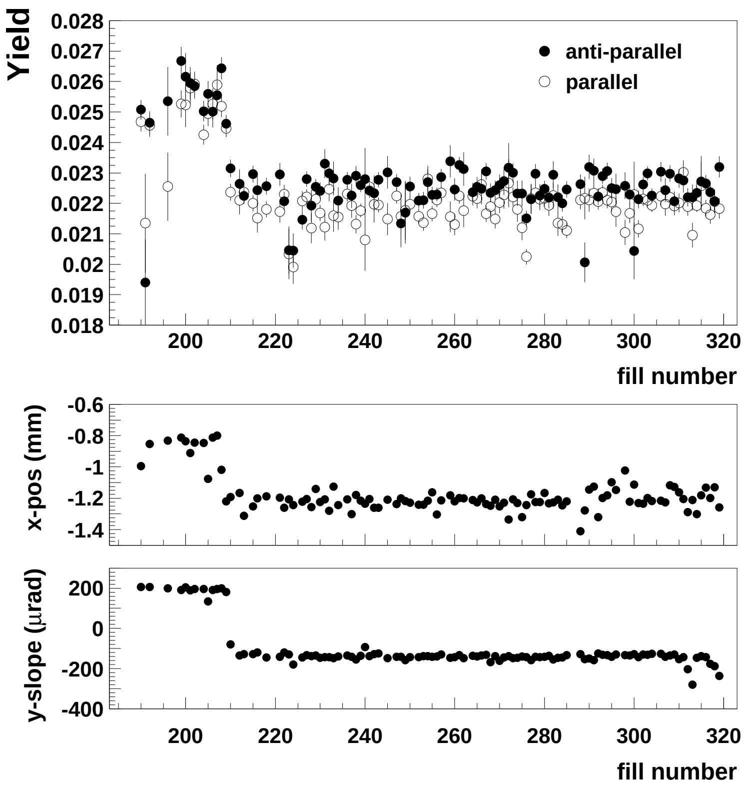

Figure 5.9: *Normalized DIS yields for the year 1998 (upper panel) for antiparallel spin states (filled circles) and for parallel spin states (open circles) are shown versus fill number. In the lower panels, the fill-averaged x-position and the y-slope of the beam are shown.*

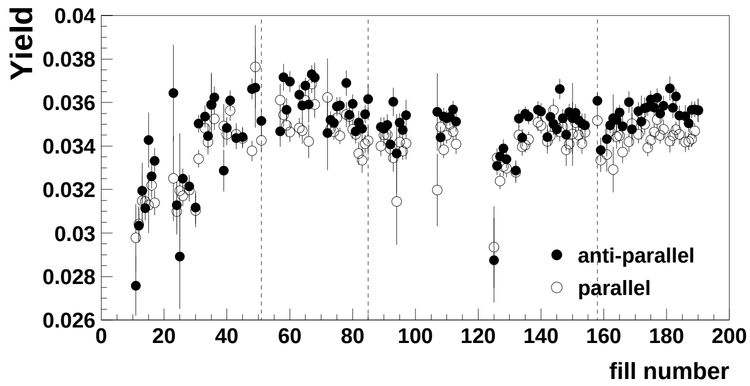

Figure 5.10: *Normalized DIS yields for the year 1999 versus fill number. Filled circles: data taken with antiparallel spin states. Open circles: data taken with parallel spin states. The vertical dashed lines indicate periods with different beam helicity.*

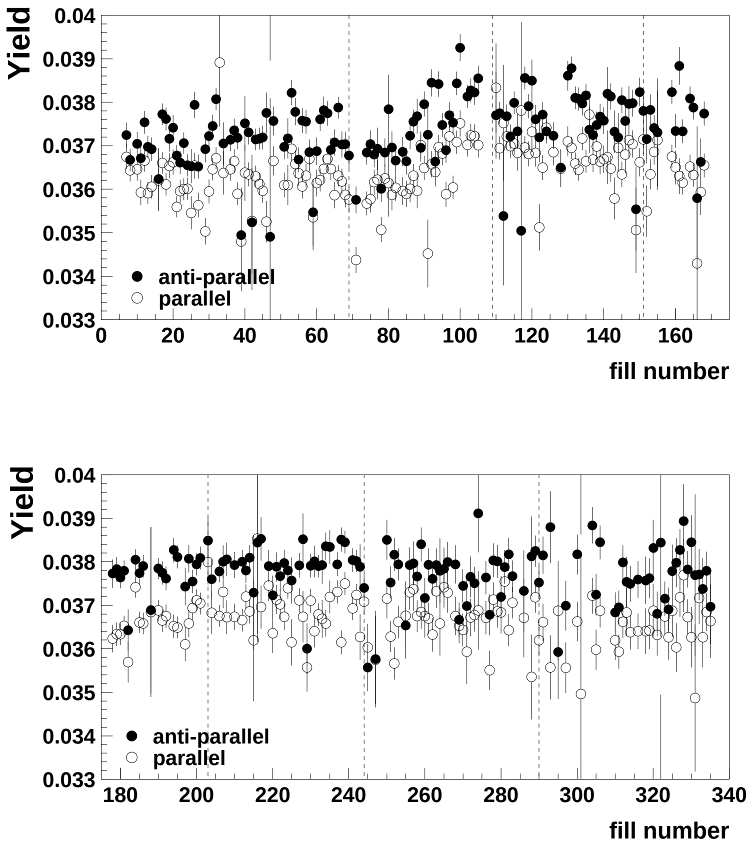

Figure 5.11: *Normalized DIS yields for the year 2000. The yields are shown for antiparallel spin states (filled circles) and for parallel spin states (open circles) versus fill number. The vertical dashed lines define periods with the same beam helicity.*

5.6.2 Particle yields

The stability of the PID detectors over time has been investigated by examining the multiplicities of all tracks passing the selection criteria for hadron identification described in Section 5.1.3. The number of identified particles normalized to the number of DIS events was calculated for each fill. Figure 5.12 shows the detected particle yields for positive hadrons, positive pions, and positive kaons versus fill number from 1998 data set. No significant time dependence of the multiplicities could be observed for this year and for the other years. This test underlines the overall good performance of the HERMES PID detectors during all the data taking periods and the reliability of the applied selection criteria.

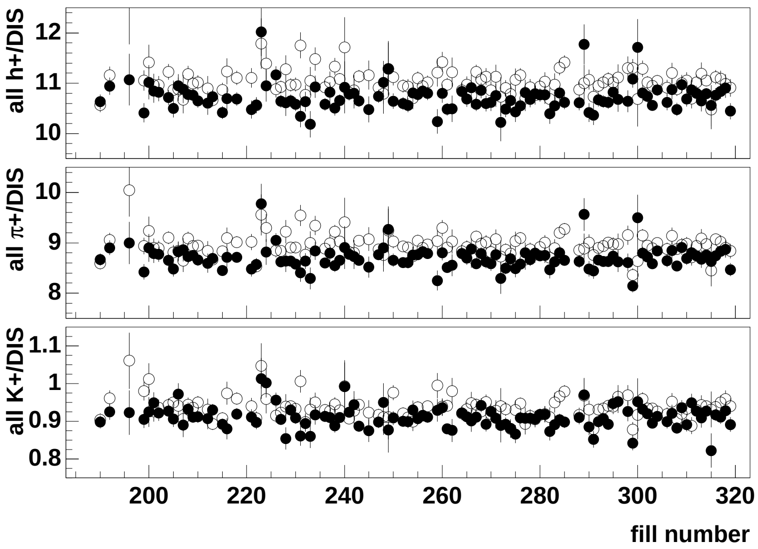

Figure 5.12: *Particle multiplicities for the year 1998 for antiparallel spin states (open circles) and for parallel spin states (filled circles) are shown versus fill number.*

5.6.3 Time dependence of the measured asymmetries

To check for any time fluctuation, the inclusive asymmetry $A_1^i(x)$ was extracted for each fill i and the weighted mean was calculated by summing over the x-bins,

$$A_1^i = \frac{\displaystyle\sum_{j=1}^{9} \frac{A_1^i(x_j)}{\sigma_i^2(A_1(x_j))}}{\displaystyle\sum_{j=1}^{9} \frac{1}{\sigma_i^2(A_1(x_j))}}\,. \tag{5.30}$$

Here, $\sigma_i^2(A_1(x_j))$ is the statistical uncertainty in the asymmetry $A_1^i(x)$ for the x-bin j. The corresponding statistical error σ_i in the mean is calculated similarly to Eq. (5.29).

Figures 5.13 and 5.14 show the asymmetries $A_1^i(x)$ versus fill number. In each year the distribution of the asymmetries is random with respect to the average for the year. The latter was calculated by fitting the data with a constant. From the results of the χ^2 test of the fits, it can be concluded that there is no significant systematic fluctuation of the extracted asymmetries.
Subsequently, the weighted mean of the asymmetries, measured for a combination of fills as defined for the periods in Table 5.8, was calculated. Figure 5.15 shows the results for the inclusive data sample. The distribution of the weighted mean for the measured semi-inclusive asymmetries is shown in Fig. 5.16 for positive hadrons and in Fig. 5.17 for negative hadrons. The observed fluctuations are statistically consistent.

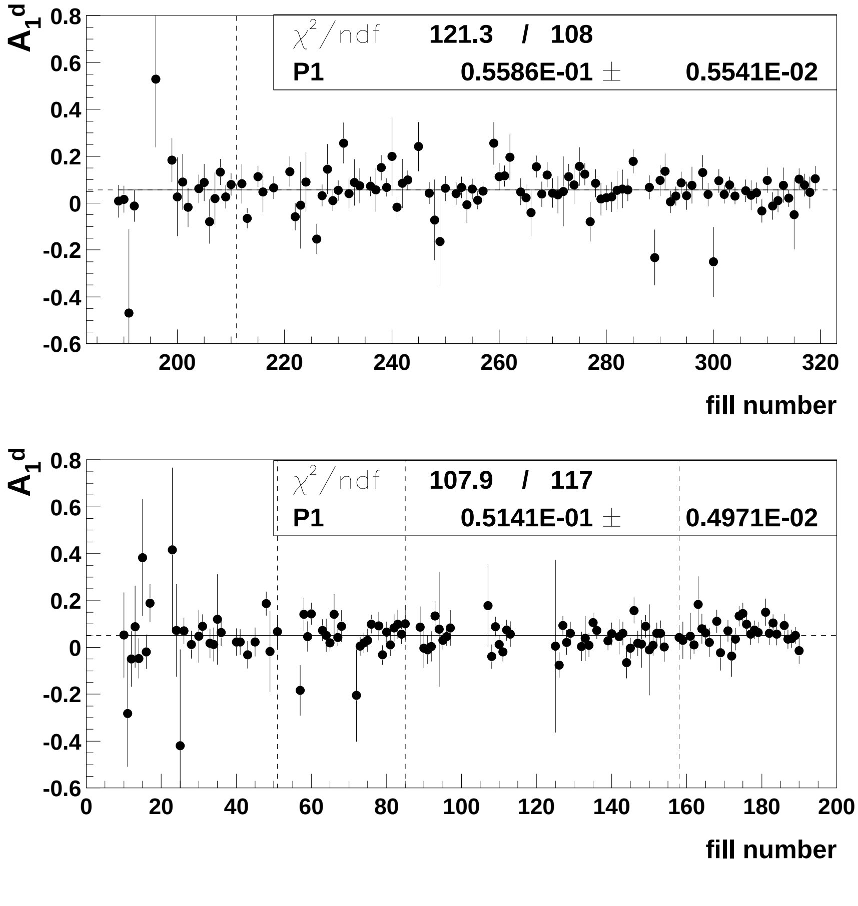

Figure 5.13: *The fill-averaged asymmetry A_1^d versus fill number is shown for the years 1998 (top panel), and 1999 (bottom panel). The horizontal straight line represent a fit with a constant to the asymmetries. The result of the fit is shown for each year together with the corresponding χ^2. The dashed vertical lines indicate periods with different beam helicity. For the 1998 the vertical line separates the higher luminosity period form the lower luminosity period.*

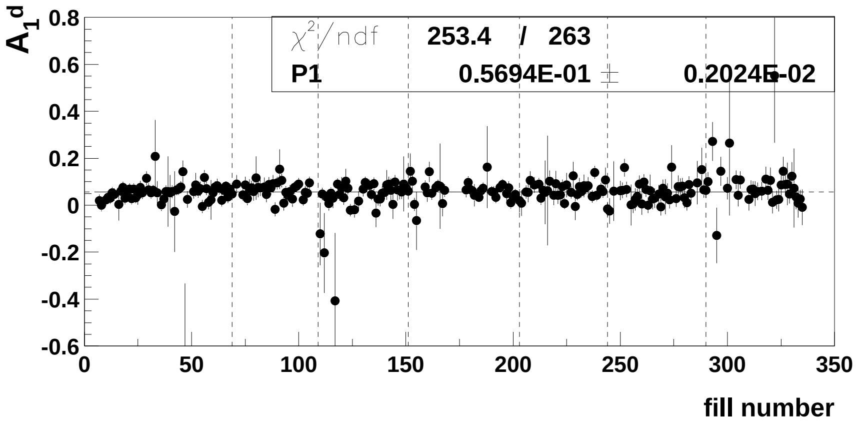

Figure 5.14: *The fill-averaged asymmetry A_1^d versus fill number for the 2000 data set. The horizontal straight line indicates a fit with a constant to the asymmetries. The result of the fit is shown for each year together with the χ^2. The dashed vertical lines indicate periods with different beam helicity.*

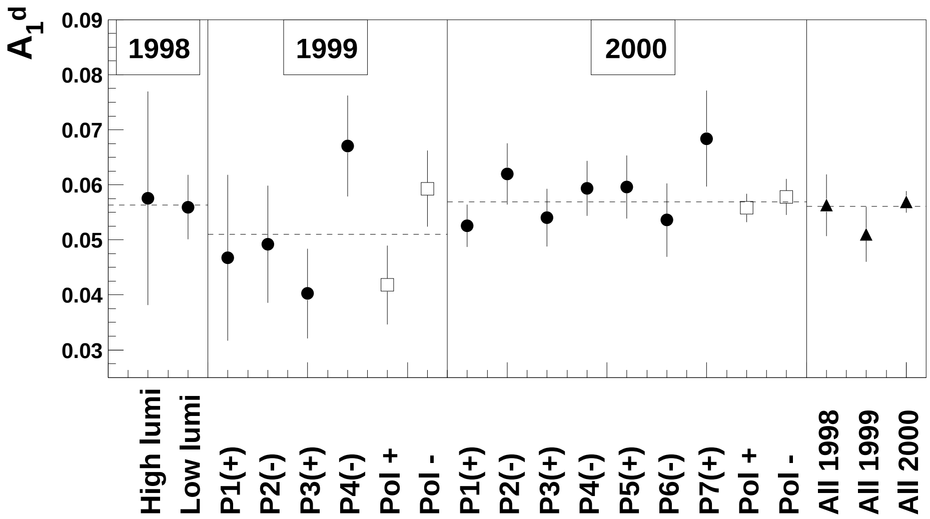

Figure 5.15: *Distribution of the weighted mean asymmetries extracted for the different periods indicated in Tab. 5.8. The dashed horizontal lines represent the weighted means for each year.*

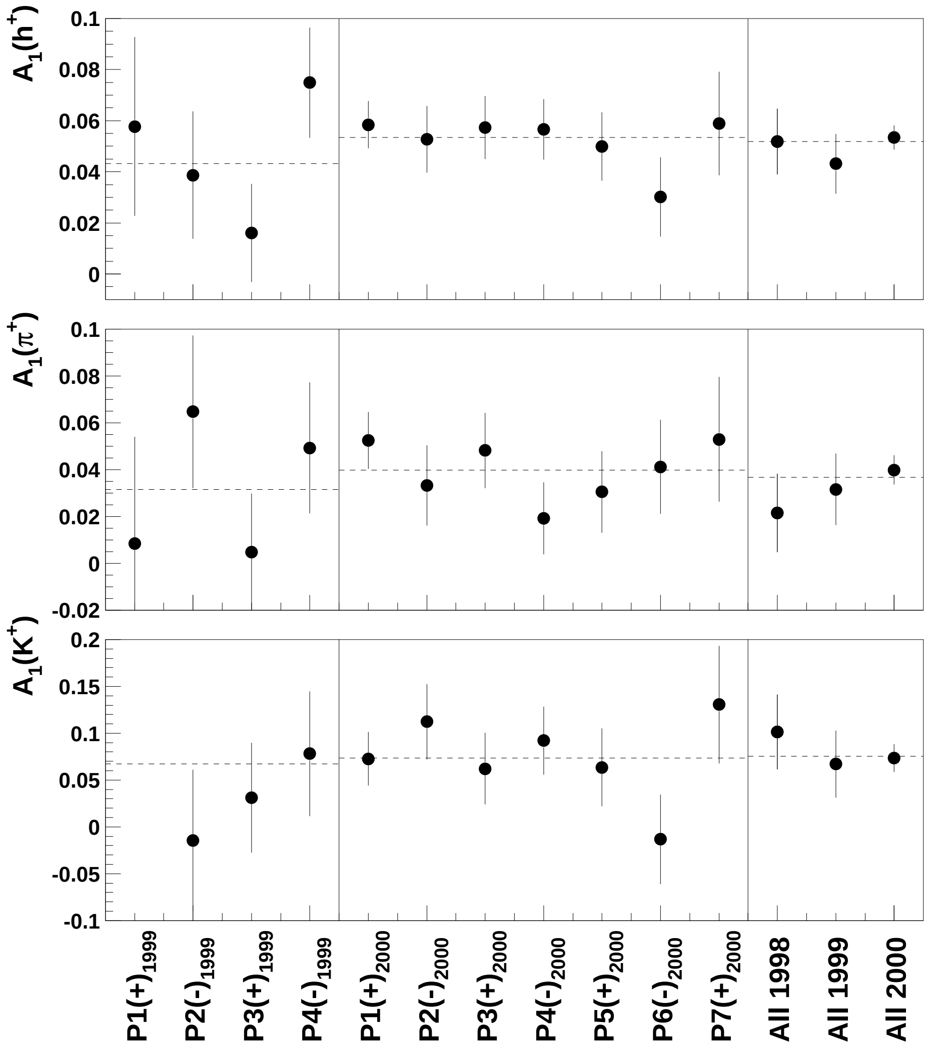

Figure 5.16: *Distribution of the weighted means of the semi-inclusive asymmetries measured for positive hadrons in different periods (see Table 5.8). The dashed horizontal lines represent the weighted means for each year.*

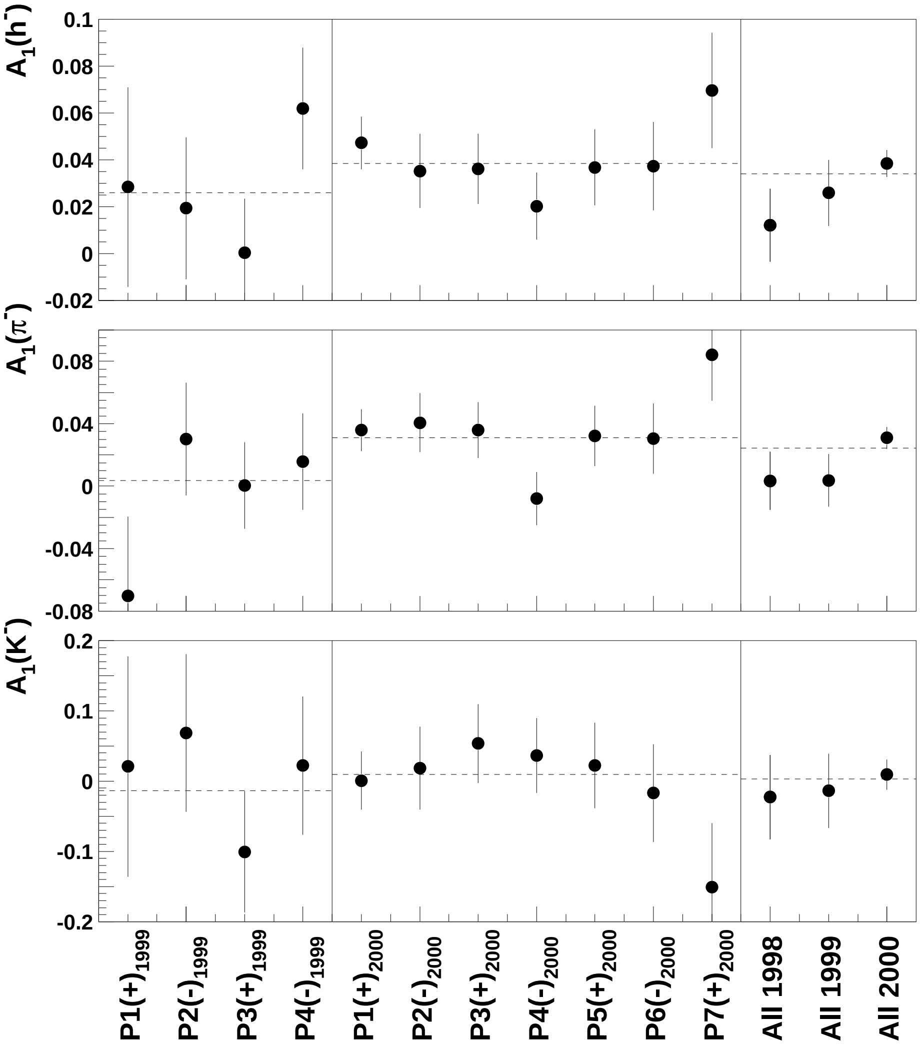

Figure 5.17: *Distribution of the weighted means of the semi-inclusive asymmetries measured for negative hadrons in different periods (see Table 5.8). The dashed horizontal lines represent the weighted means for each year.*

5.6.4 Study of the dependence on the fractional hadron energy z

The semi-inclusive asymmetries presented in Section 5.4 are formed by the count rates of the hadrons which were selected requiring $z \geq 0.2$. The effect of the z-dependence of the semi-inclusive asymmetries was investigated because of the expectation that the purity of the sample of hadrons generated from the fragmentation of the struck quark improves with high values of z. Figure 5.18 shows the comparison for both positive and negative hadrons, selected with $z \geq 0.0$, 0.2, and 0.4. The mean z value for the three data sets is 0.35, 0.41, and 0.57, respectively. For $z \geq 0.4$ the hadron sample statistics is reduced by about 60% with respect to $z \geq 0.2$. Within statistics, the results from the three values of z are equivalent.

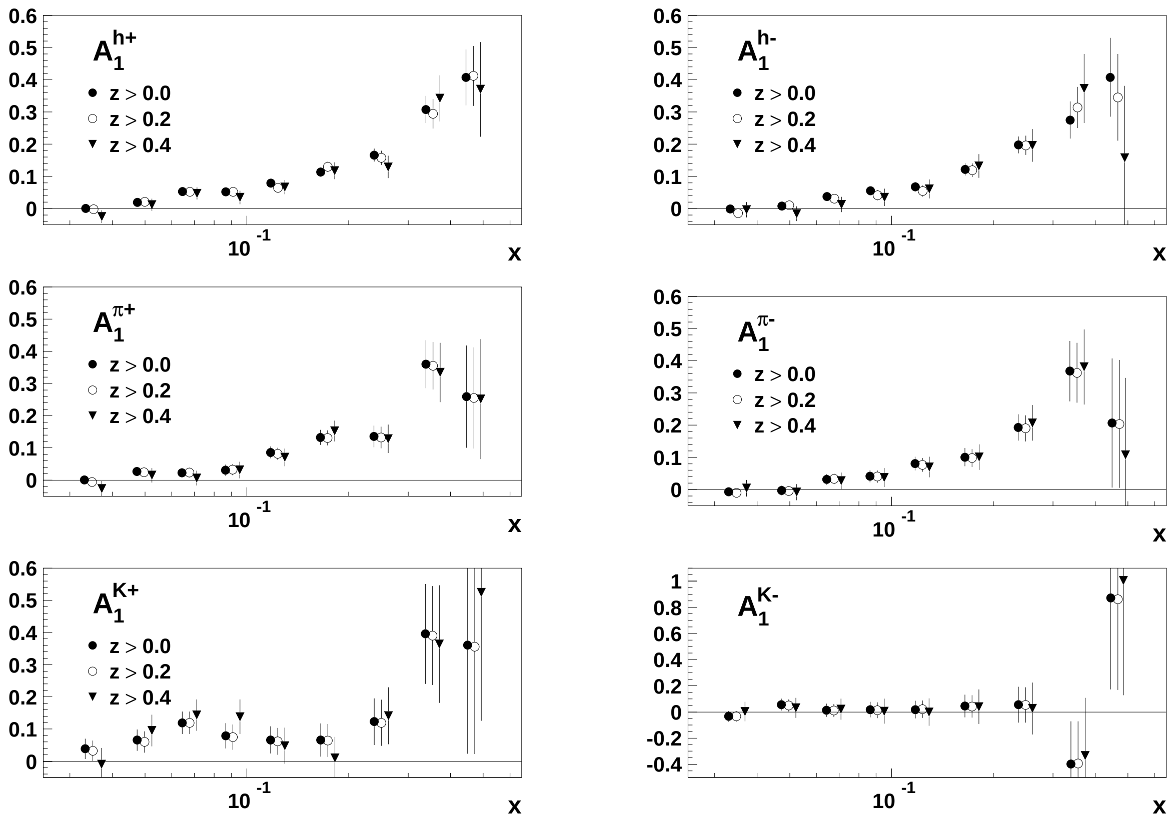

Figure 5.18: *Comparison of the semi-inclusive asymmetries extracted from the 2000 data sample for different choices of the z kinematic variable.*

5.7 Conclusions

Inclusive and semi-inclusive asymmetries have been extracted from HERMES data collected on a proton target (1996 and 1997), and on a deuteron target (1998, 1999, and 2000). For both targets the asymmetries for different years are in statistical agreement with each other. Systematic studies have verified that the measurements were not biased by time dependent effects or by the choice of kinematic constrains.

For both targets separately, the combined asymmetries were formed and compared to results from other experiments. Agreement is observed between all the measurements.

In the next chapter, the measured proton and deuteron asymmetries are used to extract the polarized quark distributions.

6 Extraction of polarized quark distributions

In Chapter 1, the asymmetries extracted from spin-dependent DIS processes were interpreted within the Quark-Parton Model as quantities related to a sum of quark distributions inside the nucleon. Here, the analysis procedure used to derive the quark spin distributions from the measured inclusive and semi-inclusive asymmetries on ^{3}He, hydrogen and deuterium targets is described.
The extraction method is based on the generation of a matrix (called *purity matrix*) that depends on the unpolarized quark distributions and the fragmentation functions. The purity formalism was introduced by Niczyporuk and Bruins [66], and already used by the HERMES collaboration for the results published in Ref. [123]. Also the SMC experiment used a similar *purity method* for their extraction of the polarized density functions [133]. The basic formalism of the method is described in Section 6.1. A Monte Carlo approach for the generation of the purity matrix is presented in Section 6.2. The results obtained for the polarization of the quarks are shown in Section 6.4, and the treatment of the associated systematic uncertainties is given in Section 6.5. The first moments of the polarized quark distributions are computed and compared to predictions in Section 6.6.

6.1 The purity formalism

At leading order QCD, the double-spin asymmetries A_1^h measured at HERMES in the semi-inclusive cross-section for production of a hadron of type h are written as (see Eq. (2.89))

$$A_1^h(x,Q^2,z) \overset{g_2=0}{=} \frac{(1+R(x,Q^2))}{(1+\gamma^2)} \cdot \frac{\sum_f e_f^2 \Delta q_f(x,Q^2)\ \tilde{D}_f^h(x,Q^2,z)}{\sum_f e_f^2 q_f(x,Q^2)\ \tilde{D}_f^h(x,Q^2,z)}\,, \tag{6.1}$$

where, the contribution from the spin structure function $g_2(x,Q^2)$ has been neglected, and $\Delta q_f(x,Q^2)$ and $q_f(x,Q^2)$ are the polarized and unpolarized quark distributions, respectively. The term $\tilde{D}_f^h(x,Q^2,z)$ represents an effective fragmentation function, where the effect of the limited HERMES acceptance is taken into account.
Note that Eq. (6.1) presents the additional factor $(1+R(x,Q^2))/(1+\gamma^2)$ compared to Eq. (2.89). In fact, the LO parametrization of the unpolarized structure function $F_2(x,Q^2)$ is obtained from measurements which use non-vanishing values for the cross-section ratio $R(x,Q^2)$ and for γ^2. As a consequence, the parametrizations of the unpolarized quark

distributions $q_f(x, Q^2)$ in Eq. (6.1), which are extracted from a global analysis to world data which include also data on F_2, are related to the structure function F_1 according to Eq. (2.22)

$$F_1(x, Q^2) = \frac{(1+\gamma^2)}{(1+R(x,Q^2))} \cdot \frac{1}{2} \sum_f e_f^2 q_f(x, Q^2) \,. \tag{6.2}$$

In order to use parton distributions extracted from data on F_2 consistently, a correction for non-zero values of R and γ^2 are included in the purity formalism.
The measured inclusive and semi-inclusive asymmetries depend on the acceptance $\mathcal{A}$ of the detector. In fact, the asymmetries $A_1^h(x)$ are the result of the integration of the asymmetries $A_1^h(x, Q^2, z)$ in each x-bin over the corresponding Q^2-range and z-range.
In the same way, the functions $\tilde{D}_f^h(x, Q^2, z)$ in Eq. (6.1) are defined as

$$\tilde{D}_f^h(x, z_{min}, Q^2_{min}) = \int_{z_{min}}^1 dz \int_{Q^2_{min}} dQ^2 \mathcal{A}(x, Q^2, z) D_f^h(z, Q^2) \,, \tag{6.3}$$

where the effective multiplicity of events of type h coming from a quark of flavor f is considered for the HERMES acceptance. Convoluting the fragmentation function $\tilde{D}_f^h(x, z_{min}, Q^2_{min})$ with the unpolarized distribution functions $q_f(x)$ defined at the scale Q^2, the so-called *quark flavor purity* can be defined for events of type h as

$$P_f^h(x) = \frac{e_f^2\, q_f(x)\, \tilde{D}_f^h(x, z_{min}, Q^2_{min})}{\sum_{f'} e_{f'}^2\, q_{f'}(x)\, \tilde{D}_{f'}^h(x, z_{min}, Q^2_{min})} \,. \tag{6.4}$$

The *purity* function, $P_f^h(x)$, describes the probability that a semi-inclusive event of type h was recorded when a scattering occurred at the kinematic point (x, Q^2) on a quark of flavor f. In particular, the purity provides information concerning the sensitivity of the measured asymmetries to the polarization of the different quark flavors. The efficacy of this formalism for the extraction of the polarized quark distributions becomes clear when Eq. (6.1) is rewritten introducing the purity functions:

$$A_1^h(x) = \frac{(1+R(x))}{(1+\gamma^2)} \cdot \sum_{f=u,\bar{u},d,\bar{d},s,\bar{s}} P_f^h(x) \cdot \frac{\Delta q_f}{q_f}(x) \,, \tag{6.5}$$

where the terms of the summation are explicitly indicated for the index f. In the previous equation, the quark polarizations are assumed to be independent of Q^2 within each x-bin:

$$\Delta q_f(x, Q^2) = \frac{\Delta q_f(x, Q^2)}{q_f(x, Q^2)} \cdot q_f(x, Q^2) \approx \frac{\Delta q_f}{q_f}(x) \cdot q_f(x, Q^2) \,. \tag{6.6}$$

This assumption is justified considering the weak dependence of the measured asymmetries on Q^2. Equation (6.5) is used to extract polarized quark distribution functions from the measured semi-inclusive asymmetries. The validity of this formalism relies on the independence of the fragmentation process on the quark polarization.
Purities for inclusive DIS events are defined as

$$P_f^{inc}(x) = \frac{e_f^2\, q_f(x)}{\sum_{f'} e_{f'}^2\, q_{f'}(x)} \,, \tag{6.7}$$

and the same kind of relation expressed by Eq. (6.5) holds for the inclusive asymmetries with the label $h \equiv inc$.
Considering all the types of measured semi-inclusive asymmetries and including also the inclusive ones, Eq. (6.5) can be conveniently rewritten in matrix form as

$$\vec{\mathbf{A}}(x) = c_R \cdot \mathcal{P}(x) \cdot \vec{\mathbf{Q}}(x) \; . \tag{6.8}$$

Here, $c_R = (1 + R(x))\,(1 + \gamma^2)$ has been used. For each x-bin, the vector $\vec{\mathbf{A}}(\mathbf{x})$ contains m measured asymmetries, and the vector $\vec{\mathbf{Q}}(\mathbf{x})$ contains n parameters for the quark polarizations,

$$\vec{\mathbf{A}}(x) = \begin{pmatrix} A_1^{h_1}(x) \\ A_1^{h_2}(x) \\ \vdots \\ A_1^{h_m}(x) \end{pmatrix} , \quad \vec{\mathbf{Q}}(x) = \begin{pmatrix} \frac{\Delta q_1(x)}{q_1(x)} \\ \frac{\Delta q_2(x)}{q_2(x)} \\ \vdots \\ \frac{\Delta q_n(x)}{q_n(x)} \end{pmatrix} . \tag{6.9}$$

The purities are arranged in a $m \times n$ matrix as

$$\mathcal{P}(x) = c_R \cdot \begin{pmatrix} P_{q_1}^{h_1}(x) & \ldots & P_{q_1}^{h_m}(x) \\ \vdots & \ddots & \vdots \\ P_{q_n}^{h_1}(x) & \ldots & P_{q_n}^{h_m}(x) \end{pmatrix} . \tag{6.10}$$

The expression in Eq. (6.8) can in principle be generalized to any number of parameters, allowing for the extraction of different combinations of quark polarizations. As the number m of measured asymmetries is typically larger than the number n of independent quark polarizations chosen as parameters, the system in Eq. (6.8) is over-constrained.
Introducing the vector $\vec{\mathbf{A}}_{\mathbf{m}}$ containing the measured asymmetries, a solution for the vector $\vec{\mathbf{Q}}$ is provided by the minimization of the equation

$$\chi^2 = \left(\vec{\mathbf{A}}_{\mathbf{m}} - \vec{\mathbf{A}}\right)^{\mathrm{T}} \mathcal{C}_{\mathbf{A}}{}^{-1} \left(\vec{\mathbf{A}}_{\mathbf{m}} - \vec{\mathbf{A}}\right) \; . \tag{6.11}$$

The matrix $\mathcal{C}_{\mathbf{A}}$ is the covariance matrix of the asymmetry vector $\vec{\mathbf{A}}_{\mathbf{m}}$, and $\vec{\mathbf{A}}$ contains the asymmetries calculated from Eq. (6.8) as a function of the fit parameters $\Delta q_f/q_f(x)$. The statistical correlations between the different types of asymmetries which enter into the covariance matrix $\mathcal{C}_{\mathbf{A}}$ are given in Appendix B.
The χ^2-minimization algorithm of the MINUIT package [139] was used to obtain the best possible agreement of the calculated asymmetries vector with the experimental asymmetries vector.
For each hadron type, five independent parameters were chosen to express the corresponding asymmetry $A_1^h(x)$. Therefore, the parameters vector

$$\vec{\mathbf{Q}}(x) = \left(\frac{\Delta d}{d}(x),\ \frac{\Delta u}{u}(x),\ \frac{\Delta \bar{d}}{\bar{d}}(x),\ \frac{\Delta \bar{u}}{\bar{u}}(x),\ \frac{\Delta s + \Delta \bar{s}}{s + \bar{s}}(x) \right) \tag{6.12}$$

gives the solution for the polarized quark distributions. The known unpolarized quark distributions $q_f(x, Q^2)$ used to form $\vec{\mathbf{Q}}$ were taken from the parametrization CTEQ5L at Leading Order [35].
The nuclear corrections which were applied to construct the ^{3}He and the deuteron asymmetries from the proton and neutron asymmetries are discussed in Section 6.3. The statistical correlations between the different types of asymmetries which enter into the covariance matrix $\mathcal{C}_{\mathbf{A}}$ are discussed in Appendix B.1.

6.2 Generating the purities

The purities defined in Eq. (6.4) depend on the unpolarized parton distributions, $q_f(x)$, and on the effective fragmentation functions, $\tilde{D}_f^h(z, Q^2)$, in Eq. (6.3). Measurements of fragmentation functions at HERMES are available only for u and d quarks into charged pions [70]. However, the purity formalism requires as input for each hadron of type h a purity function $P_f^h(x)$ determined for each flavor f with $f = u, \bar{u}, d, \bar{d}, s, \bar{s}$. Therefore, due to the spin-independence of the fragmentation processes, the elements of the probability matrix $\mathcal{P}$ have been calculated from a Monte Carlo code for unpolarized scattering.
The general procedure implemented in the Monte Carlo is schematically depicted in Fig. 6.1. In the first step, the unpolarized DIS event is generated by the LEPTO program [140], which uses first order QCD matrix elements for the calculation of the parton states after the hard-scattering subprocess occurred. The event is generated at a given point in the kinematic plane (x, Q^2), according to the lepton-nucleon cross-section for the interaction of the virtual photon on a quark of flavor f. The unpolarized quark densities define the probability of scattering from a certain quark flavor. Due to the low energies involved, the simulation in Leading Logarithmic Approximation of the parton shower is not included.

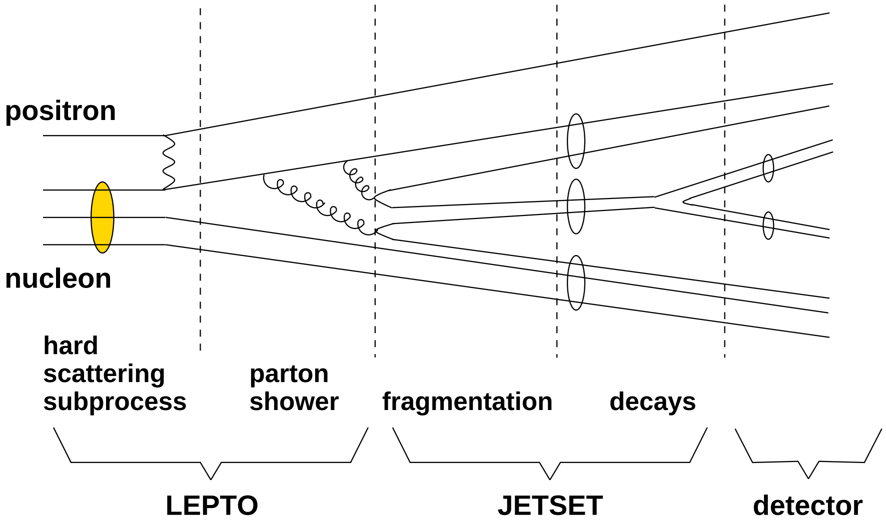

Figure 6.1: *Scheme of the different parts implemented in the Monte Carlo used for the generation of the purities.*

The kinematic quantities of the struck quark as well as the structure of the target remnant are passed to the second part of the Monte Carlo, defined by JETSET [74], which generates the hadronic final states and particle decays. In JETSET, the LUND string fragmentation model was chosen to handle the fragmentation process of quarks into hadrons, as it was found to be applicable in the HERMES regime [70, 75, 76]. The free LUND-parameters have been tuned to fit the measured hadron multiplicities at HERMES [76]. The values of the tuned parameters are given in Table 6.1, and are discussed in Section 6.2.2. The dependence of the extracted polarizations from the hadronization model was included in the systematic uncertainties.

It is important to point out that the MC needs as input the acceptance of the spectrometer and the fragmentation model, as in the MC the hadrons are generated in the full phase space. The detector acceptance was modeled by applying rectangular angle criteria: $|\theta_x| \leq 170$mrad and 40mrad $\leq |\theta_y| \leq 140$mrad.

The effective fragmentation functions $\tilde{D}_f^h(x, Q^2, z)$ in Eq. (6.3) are defined on a 3-dimensional grid (x, Q^2, z) by the ratio of the number N_A of accepted hadrons h and the number N_G of generated DIS events where a lepton l scattered from a quark q_f in the nucleon N,

$$\tilde{D}_f^h(x, Q^2, z) = \frac{N_A : [l(N, q_f) \longrightarrow l'hX](x, Q^2, z)}{N_G : [l(N, q_f) \longrightarrow l'X](x, Q^2, z)} \,. \tag{6.13}$$

The quantity $\tilde{D}_f^h(x, Q^2, z)$ is different for proton and neutron targets, and a separate computation is made for both target types. With this MC method an effective fragmentation function $\tilde{D}_f^h(x, Q^2, z)$ is defined for all the quark and antiquark flavors $f = u,\ \bar{u},\ d,\ \bar{d},\ s,\ \bar{s}$ and hadrons types $h = h^+, h^-, \pi^+, \pi^-, K^+, K^-$. In particular, the same criteria on the particle kinematics and acceptance used for the selection of the semi-inclusive candidates were applied for the selection of the MC hadrons to generate the functions $\tilde{D}_f^h(x, Q^2, z)$.

In the case of inclusive events, the functions $\tilde{D}_f^h(x, Q^2)$ were similarly determined from the ratio of accepted over generated inclusive DIS events for scattering from a quark q_f.

Finally, the purities in Eq. (6.4) are obtained from the fragmentation functions introducing a parametrization for the quark distribution functions $q_f(x, Q^2)$. The quark distribution functions for the neutron are obtained from the proton functions by isospin rotation of the quark flavors ($i.e.$ $u \leftrightarrow d$, $\bar{u} \leftrightarrow \bar{d}$, while strangeness stays the same $s \leftrightarrow s$).

6.2.1 Unpolarized parton distribution

Different sets of parametrizations for the unpolarized parton distributions are currently available. The CTEQ [35], GRV [46], and MRST [141] groups have fitted parton distribution functions (PDFs) to the results of a variety of experiments. The extrapolation of these fits to the HERMES kinematic region provides a precise description of the unpolarized parton distributions in the nucleon.

HERMES alone does not determine DIS cross-sections well enough to constrain unpolarized parton distributions. However, the world parametrizations have been checked at HERMES directly with measurements of F_2^n/F_2^p [142], and $\bar{d} - \bar{u}$ [143, 144].

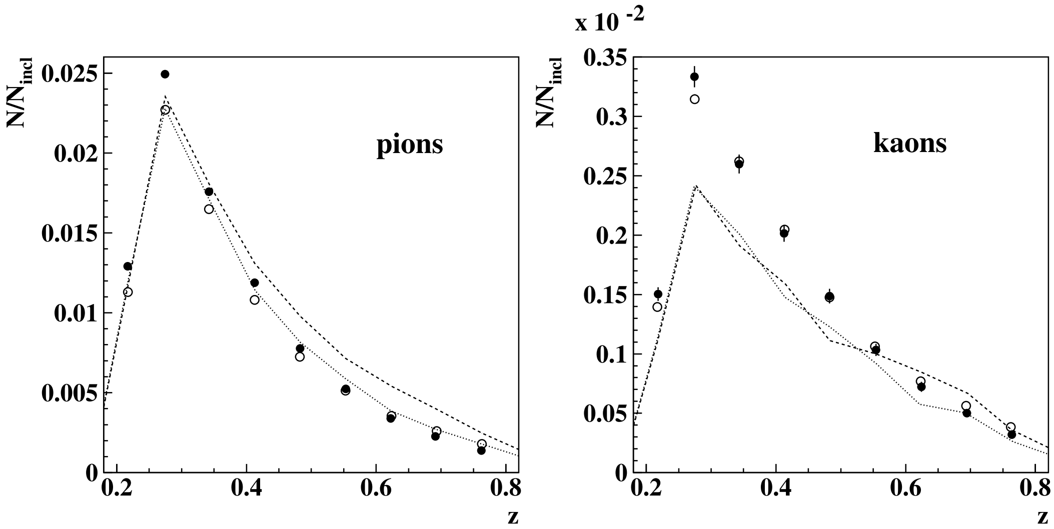

Figure 6.2: *Comparison of the normalized z-distributions for charged pions and kaons extracted from the 2000 data set (open circles) and from the tuned HERMES MC SF1 scheme (filled circles) from Ref. [76]. The dashed curves indicate the distributions obtained with the JETSET parameters setting of the PETRA scheme, and the dotted curves with the values of the SF2 scheme (see Table 6.1) which corresponds to a previous MC-tune performed for HERMES [70, 75].*

For this analysis, the PDF set from CTEQ5 at Leading Order and low Q^2 (CTEQ5L) [35] is used (see Fig. 2.5). The choice of the PDF set employed in the extraction method introduces a systematic uncertainty which is accounted for in the uncertainties associated to the purities. This contribution is discussed in Section 6.5.2.

6.2.2 Fragmentation models

The present understanding of the hadronization process is based on phenomenological models. Each model uses different assumptions to describe the experimental particle multiplicities (see Section 2.6.1).

In this analysis, the quark polarizations have been extracted by using purities generated by the JETSET Monte Carlo package which employs the LUND-based fragmentation model. The fragmentation parameters have been tuned to reproduce the multiplicities of charged particles at HERMES. The standard fragmentation settings used in the extraction of the polarized quark distributions is labeled SF1 scheme and is taken from Ref. [76]. A comparison of the normalized z-distributions between SF1-tuned MC and experimental data for charged pions and kaons is shown in Fig. 6.2.

In addition, two different settings of MC parameters were selected in order to generate different sets of purities. The first set (SF2 scheme) was used for the HERMES results in Ref. [123], while the second (PETRA scheme) was introduced to model the e^+e^- collision events in PETRA at DESY (where the energy in the c.m.s. is $\sqrt{s} \approx$ 35 GeV).

The comparison of the results obtained with the different settings is used to evaluate the systematic uncertainty associated with the choice of the fragmentation parameters in the Monte Carlo code and will be discussed in Section 6.5.2. In Table 6.1 the JETSET tuned parameters are listed for the different setting.

JETSET parameters	Standard setting	Scheme SF1	SF2	PETRA
PARJ(1)	0.10	0.02	0.10	0.10
PARJ(2)	0.30	0.20	0.10	0.30
PARJ(5)	0.50	0.00	0.00	0.50
PARJ(21)	0.36	0.37	0.34	0.36
PARJ(23)	0.01	0.03	0.01	0.01
PARJ(24)	2.00	2.50	2.00	2.00
PARJ(41)	0.30	1.74	0.82	1.00
PARJ(42)	0.58	0.23	0.24	0.70
PARL(3)	0.44	0.78	0.44	0.44

Table 6.1: *The JETSET parameters for the three sets of fragmentation scheme used in the analysis. The standard JETSET setting is given as reference. The parameters are described in Ref. [74].*

6.2.3 Resulting purities

The semi-inclusive purities for charged pions and kaons calculated according to Eq. (6.4) are shown in Figs. 6.3 and 6.4 as a function of x for proton and neutron targets, respectively, together with the purities extracted from the inclusive DIS events. The strong x dependence of the purities is mainly caused by the x-dependence of the unpolarized parton distributions. For a proton target, both inclusive and semi-inclusive events are primarily dominated by the sensitivity to the u quark. Scattering from d quarks is suppressed, compared to u quarks, by a factor of about 5 to 10 depending on x. Less than 10% of the inclusive events originate from other quark species. For the case of purities determined from semi-inclusive events, for each quark flavor, the fragmentation functions either enhance or suppress the purities compared to the inclusive ones. For $x < 0.1$ the purities for the $\bar{u}$ quarks become important. In the same x range, the s quark flavor contribution is enhanced in the case of K^- purities, and the $\bar{s}$ contribution for the K^+ purities. This makes the kaon asymmetries particularly sensitive to the strange sea influences, while the pion asymmetries would favor the sensitivity to the light quark flavors in the low-x region. In the case of a neutron target, the scattering from the d quarks dominates at low values of x for the inclusive case. The combined use of inclusive and semi-inclusive data for both targets in the extraction procedure allows one to exploit the different sensitivities exhibited by the purities to the different quark flavors as a function on the x value.

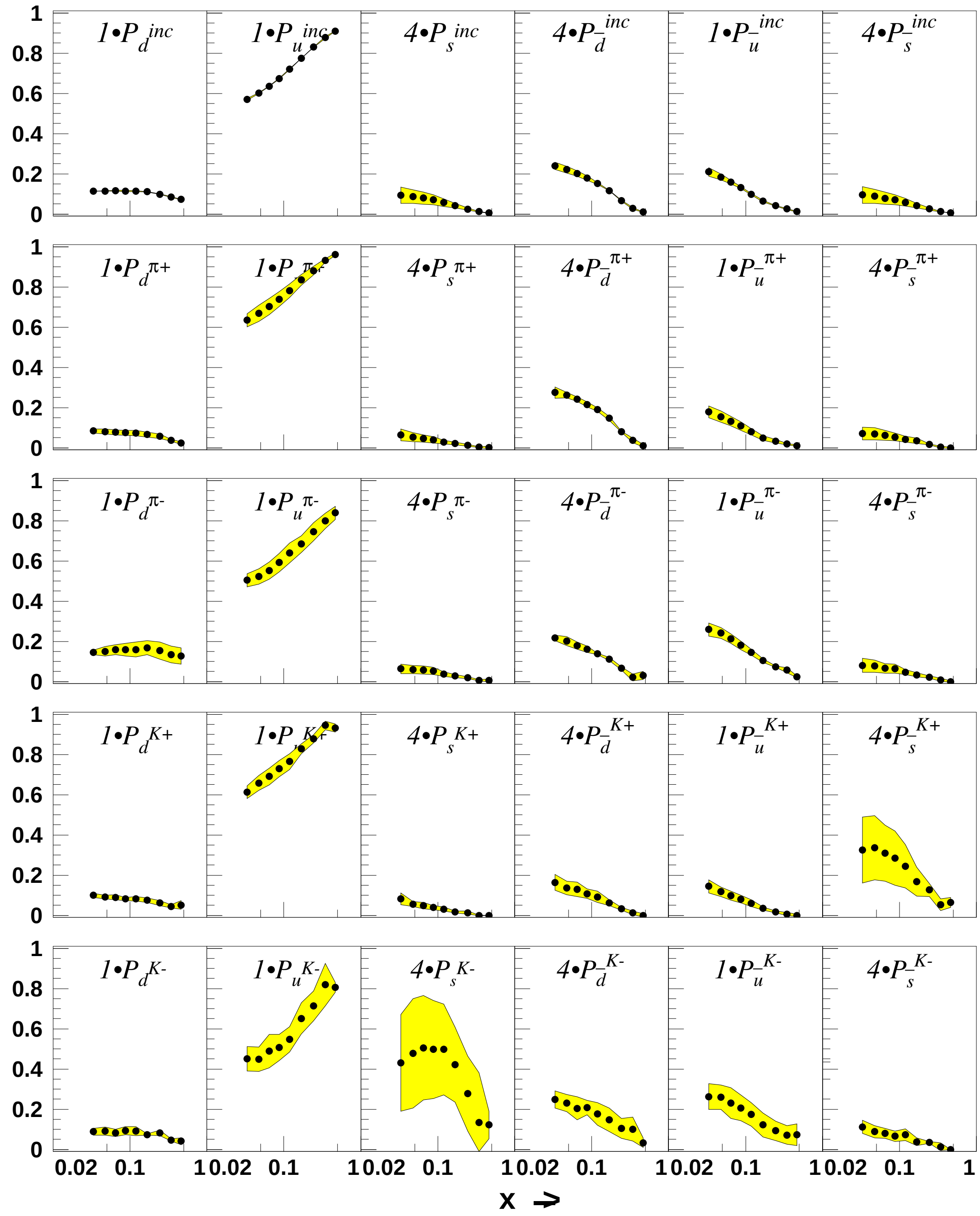

Figure 6.3: *Quark flavor purities $P_f^h(x)$ for a proton target as a function of x for inclusive and semi-inclusive charged pions and kaons events and for $f = u, \bar{u}, d, \bar{d}, s, \bar{s}$. The tuned LUND fragmentation model SF1 and the CTEQ5L parametrizations of the unpolarized quark distributions have been used in the MC for the generation of the extracted events. The shaded bands represents the systematic uncertainties in the purities which were estimated by extracting the fragmentation functions with the SF2 and PETRA schemes as input parameters. Note that for some quark flavors a multiplicative term was introduced to make the purities clearly visible.*

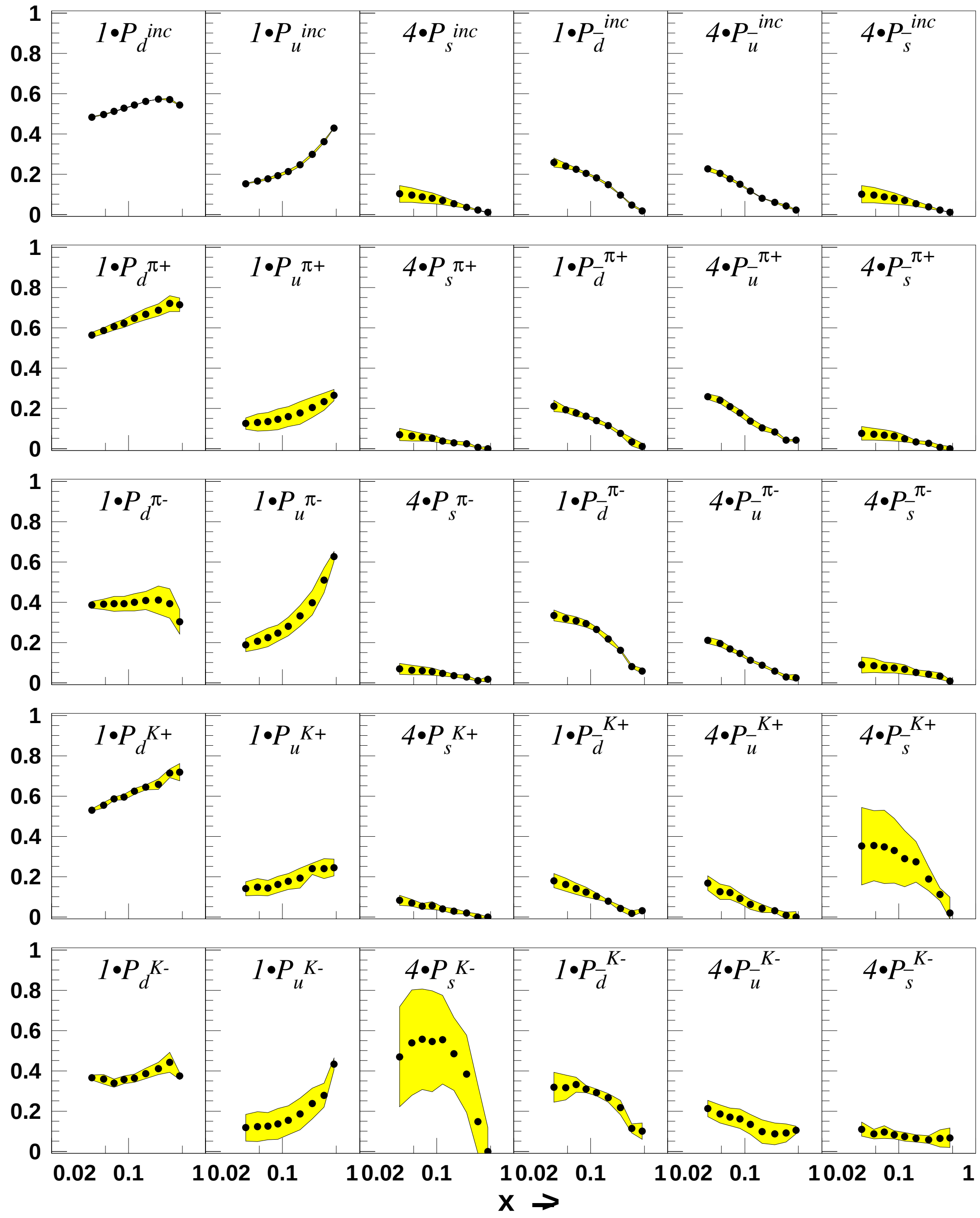

Figure 6.4: *Quark flavor purities $P_f^h(x)$ for a neutron target as a function of x for inclusive and semi-inclusive charged pions and kaons events and for $f = u, \bar{u}, d, \bar{d}, s, \bar{s}$. The labels for the quark flavor refer to the proton, by using isospin symmetry. The tuned LUND fragmentation model SF1 and the CTEQ5L parametrization for the unpolarized quark distributions have been used in the MC for the generation of the extracted events. The shaded bands represents the systematic uncertainties in the purities which were estimated by extracting the fragmentation functions with the SF2 and PETRA schemes as input parameters. Note that for some quark flavor a multiplicative term was introduced to make the purities clearly visible.*

6.3 Nuclear corrections

Assuming that DIS cross-sections for lepton scattering from deuterium are incoherent superpositions of proton and neutron cross-sections, the asymmetry for events of type h, $A_{1,\mathrm{d}}^{(h)}$, measured for a deuterium target can be split into the corresponding asymmetries for proton, $A_{1,\mathrm{p}}^{(h)}$, and neutron, $A_{1,\mathrm{n}}^{(h)}$:

$$A_{1,\mathrm{d}}^{(h)}(x,Q^2) = f_{\mathrm{p,d}}^{(h)}(x,Q^2) \cdot p_{\mathrm{p,d}} \cdot A_{1,\mathrm{p}}^{(h)}(x,Q^2) + f_{\mathrm{n,d}}^{(h)}(x,Q^2) \cdot p_{\mathrm{n,d}} \cdot A_{1,\mathrm{n}}^{(h)}(x,Q^2) \; . \tag{6.14}$$

Here, $p_{\mathrm{p,d}}$ and $p_{\mathrm{n,d}}$ are the effective polarizations of the proton and neutron in the deuterium nucleus, and the *dilution factors* $f_{\mathrm{p,d}}^{(h)}$ and $f_{\mathrm{n,d}}^{(h)}$ account for the probability of scattering from either the proton or the neutron. The wave function of deuteron, described as a two-nucleon system, contains a dominant S-state and a small D-state component. In the D-state the nucleons are mainly anti-aligned relative to the deuteron spin. This results in a slight depolarization of proton and neutron.
Here, the value used for the D-state probability is $\omega_{\mathrm{D}} = 0.05 \pm 0.01$ [145], given by N-N potential calculations. Assuming isospin symmetry, the effective polarizations in the deuteron can be written as

$$p_{\mathrm{p,d}} = p_{\mathrm{n,d}} = (1 - \frac{3}{2}\,\omega_{\mathrm{D}}) = 0.925 \; , \tag{6.15}$$

where the exact relation between nucleon and nuclear polarizations was calculated taking Clebsh-Gordan coefficients into account [146].
The dilution factors $f_{\mathrm{p,d}}^{(h)}$ and $f_{\mathrm{n,d}}^{(h)}$ define a probability, therefore $f_{\mathrm{p,d}}^{(h)} + f_{\mathrm{n,d}}^{(h)} = 1$ by definition. Under the assumption that $\sigma_{\mathrm{d}}^{(h)} = \sigma_{\mathrm{p}}^{(h)} + \sigma_{\mathrm{n}}^{(h)}$ for the unpolarized DIS cross-section the dilution factors can be written as

$$f_{\mathrm{p,d}}^{(h)} = \frac{\sigma_{\mathrm{p}}^{(h)}}{\sigma_{\mathrm{d}}^{(h)}} \; , \qquad f_{\mathrm{n,d}}^{(h)} = \frac{\sigma_{\mathrm{n}}^{(h)}}{\sigma_{\mathrm{d}}^{(h)}} = 1 - f_{\mathrm{p,d}}^{(h)} \; . \tag{6.16}$$

Introducing explicitly the quantities that are measured to form the cross-sections, it follows that

$$f_{\mathrm{p,d}}^{(h)} \;=\; \frac{N_{\mathrm{p}}^{(h)}}{\mathcal{L}_{\mathrm{p}}} \cdot \frac{\mathcal{L}_{\mathrm{d}}}{N_{\mathrm{d}}^{(h)}} = \frac{N_{\mathrm{p}}^{(h)}}{N_{\mathrm{p}}^{DIS}} \cdot \frac{N_{\mathrm{d}}^{DIS}}{N_{\mathrm{d}}^{(h)}} \cdot \frac{\sigma_{\mathrm{p}}^{DIS}}{\sigma_{\mathrm{d}}^{DIS}} \; , \tag{6.17}$$

$$\;=\; \frac{n_{\mathrm{p}}^{(h)}}{n_{\mathrm{d}}^{(h)}} \cdot \frac{\sigma_{\mathrm{p}}^{DIS}}{\sigma_{\mathrm{n}}^{DIS}} = \frac{n_{\mathrm{p}}^{(h)}}{n_{\mathrm{d}}^{(h)}} \cdot \frac{F_2^{\mathrm{p}}}{2\,F_2^{\mathrm{d}}} \; , \tag{6.18}$$

where $N_{\mathrm{p}}^{(h)}$ and $N_{\mathrm{d}}^{(h)}$ are the detected number of events of type h, and $\mathcal{L}_{\mathrm{p}}$ and $\mathcal{L}_{\mathrm{d}}$ define the integrated luminosities. In the previous equation, the inclusive DIS cross sections, $\sigma^{DIS} = N^{DIS}/\mathcal{L}$, for proton and deuteron targets were introduced to derive the DIS-normalized multiplicities, $n_{\mathrm{p}}^{(h)}$ and $n_{\mathrm{d}}^{(h)}$, for hadrons of type h. This allows for a direct measurement of semi-inclusive dilution factors from HERMES unpolarized data, such that acceptance and systematic uncertainties cancel. The NMC parametrizations in Ref. [130]

for the proton and deuteron structure functions were used for F_2^{p} and F_2^{d}.
The same kind of approach was applied to the asymmetries $A^{(h)}_{1,{}^3\mathrm{He}}$ measured with the ^{3}He target (see *e.g.* Ref. [124]). In the ^{3}He nucleus the polarizations of proton and neutron take into account the admixture of S' and D states to the ^{3}He ground-state wave function. They result in $p_{\mathrm{p},{}^3\mathrm{He}} = -0.027$ and $p_{\mathrm{n},{}^3\mathrm{He}} = 0.865$, respectively [147, 148]. The dilution factor for the proton in ^{3}He becomes

$$f^{(h)}_{\mathrm{p},{}^3\mathrm{He}} = \frac{2\sigma^{(h)}_{\mathrm{p}}}{\sigma^{(h)}_{{}^3\mathrm{He}}} = \frac{2\sigma^{(h)}_{\mathrm{p}}}{\sigma^{(h)}_{\mathrm{d}} + \sigma^{(h)}_{\mathrm{p}}} = 2\frac{n^{(h)}_{\mathrm{p}} \cdot F_{2,\mathrm{p}}}{n^{(h)}_{\mathrm{d}} \cdot 2F_{2,\mathrm{d}} + n^{(h)}_{\mathrm{p}} \cdot F_{2,\mathrm{p}}}\,. \tag{6.19}$$

6.4 Results for the polarized quark distributions

6.4.1 Quark polarizations from a five-parameter fit

The flavor decomposition of the quark polarizations was obtained for each x-bin by solving Eq. (6.11) for the five quark polarization parameters defined by the vector $\vec{\mathbf{Q}}$ in Eq. (6.12).
The unpolarized quark distributions for the sea quarks rapidly decrease as a function of x. This is due to the fact that in the region $x > 0.3$ the number density of sea quarks carrying a large fraction of the nucleon momentum is small. As a consequence, the positivity limit

$$|\Delta q_s(x)| \leq \frac{1+\gamma^2}{1+R}\,|q_s(x)| \tag{6.20}$$

provides a strong constraint on the contribution of the sea quarks to the nucleon spin in this x-range. Thus, in the extraction procedure the polarization of all the sea quarks was set to zero for $x > 0.3$. The corresponding effect on the results for the non-sea quark polarizations was included in their systematical uncertainties. The result of the fit is shown in Fig. 6.5 as a function of x. The values for the quark polarizations for each x-bin are given in Table 6.3 together with the $\chi^2/n.d.f.$ of the fit. The number of degrees of freedom equals 29, which resulted from the difference between the number of measured asymmetries as input and the number of parameters used for the fit. Table B.3 summarizes the correlation coefficients of the five-fit parameters.
In the proton, the d-quark polarization is negative while the u-quark polarization is positive. This means that the u-quarks are polarized in the same direction as the parent nucleon spin, while the d-quarks are polarized in the opposite direction to the parent nucleon, with generally smaller polarization values compared to the u-quarks. Both polarizations increase with increasing x. The $\bar{d}$-quark distribution shows a negative polarization for $x < 0.07$, and the $\bar{u}$-quark polarization is consistent with zero within statistical uncertainties. The polarization of the strange sea assumes positive values for $x < 0.1$, while it is zero over the remaining x range.

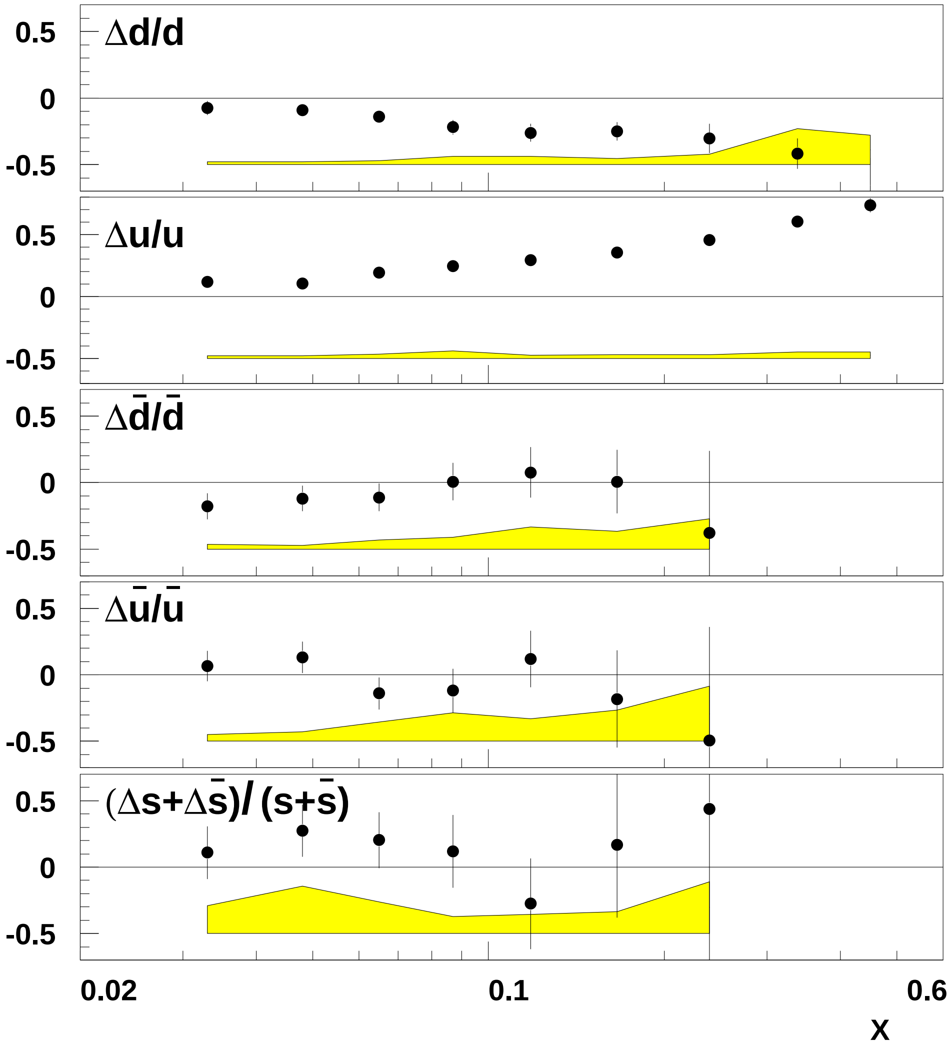

Figure 6.5: *The flavor decomposition of the quark polarization as a function of x for five-parameter as defined by Eq. (6.12). For $x > 0.3$ the sea polarization is assumed to be zero. The error bars represent the statistical uncertainties and the shaded areas represent the systematic uncertainties.*

x-bin	$\langle x\rangle$	$\chi^2/n.d.f.$
1	0.033	1.15
2	0.047	1.09
3	0.065	0.78
4	0.087	0.76
5	0.119	1.23
6	0.168	0.83
7	0.245	1.37
8	0.342	1.16
9	0.465	0.85

Table 6.2: *Values of the χ^2 divided by the number of degrees of freedom for the five-parameter fit in each x-bin.*

	$\frac{\Delta u}{u}$	$\frac{\Delta d}{d}$	$\frac{\Delta\bar{u}}{\bar{u}}$	$\frac{\Delta\bar{d}}{\bar{d}}$	$\frac{\Delta s+\Delta\bar{s}}{s+\bar{s}}$
1	0.120 ± 0.043	-0.075 ± 0.053	0.066 ± 0.116	-0.177 ± 0.097	0.108 ± 0.200
2	0.106 ± 0.039	-0.092 ± 0.057	0.133 ± 0.119	-0.120 ± 0.101	0.245 ± 0.196
3	0.191 ± 0.039	-0.142 ± 0.048	-0.139 ± 0.120	-0.113 ± 0.114	0.203 ± 0.210
4	0.243 ± 0.032	-0.219 ± 0.056	-0.119 ± 0.166	0.007 ± 0.142	0.119 ± 0.275
5	0.293 ± 0.033	-0.261 ± 0.068	0.118 ± 0.214	0.075 ± 0.191	-0.275 ± 0.342
6	0.355 ± 0.034	-0.251 ± 0.070	-0.182 ± 0.367	0.006 ± 0.240	0.167 ± 0.549
7	0.454 ± 0.047	-0.303 ± 0.111	-0.495 ± 0.855	-0.380 ± 0.618	0.438 ± 1.052
8	0.606 ± 0.039	-0.417 ± 0.116	–	–	–
9	0.736 ± 0.056	-0.655 ± 0.203	–	–	–

Table 6.3: *Extracted quark polarizations as a function of x for the five-parameter fit. The errors quoted correspond to the statistical uncertainties only.*

6.4.2 Polarized parton distributions

The quark polarizations deduced from the fitting procedure were obtained at the experimental measured $\langle x\rangle$ and $\langle Q^2\rangle$ values in each x-bin. The polarized parton distributions may be derived by multiplying the extracted quark polarization parameters with unpolarized parton distributions evaluated at the $\langle x\rangle$ value in each bin and evolved at a common $Q_0^2 = 2.5$ GeV^2:

$$\Delta q(\langle x\rangle, Q_0^2) = \left(\frac{\Delta q}{q}\right)\bigg|_{Q^2_{exp}} \cdot q(\langle x\rangle, Q_0^2)\,. \tag{6.21}$$

The measured quark polarizations are assumed to be Q^2 independent, which is motivated by the absence of a significant Q^2 dependence in the measured asymmetries. Figure 6.6 shows the resulting polarized parton distribution multiplied by x. In the same figure a comparison with different parametrizations for the polarized parton distributions to world data on polarized DIS is presented. Glück *et al.* (parametrization GRSV 2000, [149]) have extracted polarized parton distributions at Leading Order QCD within the common "standard" scenario in which the flavor-asymmetries in the polarized antiquark sector are neglected. In this model a flavor-symmetric light sea distribution $\Delta\bar{q}$ is, therefore, assumed together with the results for hyperon decay constants. This is motivated by the

fact that the polarized semi-inclusive DIS data used in the GRSV analysis (which include up to SLAC-E155 data [132] and HERMES neutron [150] and proton [151] data) cannot discriminate univocally between a flavor-broken light sea model ("valence" scenario) or a flavor-symmetric polarized light sea model. In addition, the GRSV extraction is performed for the world data on the spin asymmetries A_1 with the ratio $R = \sigma_L/\sigma_T$ equal to zero. Thus, for consistency with the treatment adopted in this work the comparison with the measured Δq is performed applying a $(1+R)$ correction to the GRSV parametrizations. The polarized parton distributions presented in Fig. 6.6 have been compared also to the results of a LO QCD analysis by Blümlein and Böttcher [152]. In their analysis a fit to the world data on the inclusive cross-section asymmetries A_1 and g_1/F_1 on hydrogen, deuterium and ^{3}He targets is performed which requires $SU(3)_f$ flavor-symmetry assumptions between the polarized distributions of the sea quarks, as inclusive data alone cannot sufficiently constrain all the polarized quark distributions independently.
Note that the kind of analyses performed by both the GRSV group and Blümlein and Böttcher do not need any knowledge of fragmentation functions. A good agreement is observed between the results from the LO QCD fits and the quark polarizations extracted with the five-parameter fit by using semi-inclusive asymmetries. Therefore, it is unlikely that further contributions to the semi-inclusive data samples have a large impact on the final result. This particularly excludes any sizeable effect in the HERMES kinematic domain from a potential spin-dependent contribution to the fragmentation function, as it was suggested by Glück and Reya in Ref. [153].
A direct fit to the extracted polarized quark distributions has been performed by using a parametrization of the same functional form used by the GRSV group in Ref. [149]

$$\Delta q_f(x) = N_f \cdot x^{\alpha_f}(1-x)^{\beta_f} \cdot q_f(x) \; , \tag{6.22}$$

with $f = u,\ d,\ \bar{u},\ \bar{d},\ s = \bar{s}$. The term x^{α_f} controls the low-x behavior of the polarized parton distributions and the term $(1-x)^{\beta_f}$ the high-x region. The CTEQ5L parametrization was used for the unpolarized parton distributions $q_f(x)$ at the $\langle x\rangle$ and $\langle Q^2\rangle$ values in each x-bin. The results from the fit are also shown in Fig. 6.6 and the fit parameters are listed in Table 6.4.2. Consistency with the parametrizations from world data is observed within uncertainties.

Quark distribution	fit parameters N_f	α_f	β_f	$\chi^2/d.o.f.$
Δd	-1.19 ± 0.68	0.76 ± 0.21	0.48 ± 0.79	1.66
Δu	1.47 ± 0.66	0.75 ± 0.18	0.46 ± 0.64	1.94
$\Delta\bar{d}$	-6.56 ± 10.34	0.99 ± 0.42	26.11 ± 20.98	0.85
$\Delta\bar{u}$	-57.94 ± 132.8	2.44 ± 1.24	6.39 ± 9.22	0.95
$\Delta s+\Delta\bar{s}$	7963 ± 2926	2.63 ± 1.13	52.34 ± 39.38	0.58

Table 6.4: *Parameters for a fit of the x-dependence of the extracted polarized parton distributions.*

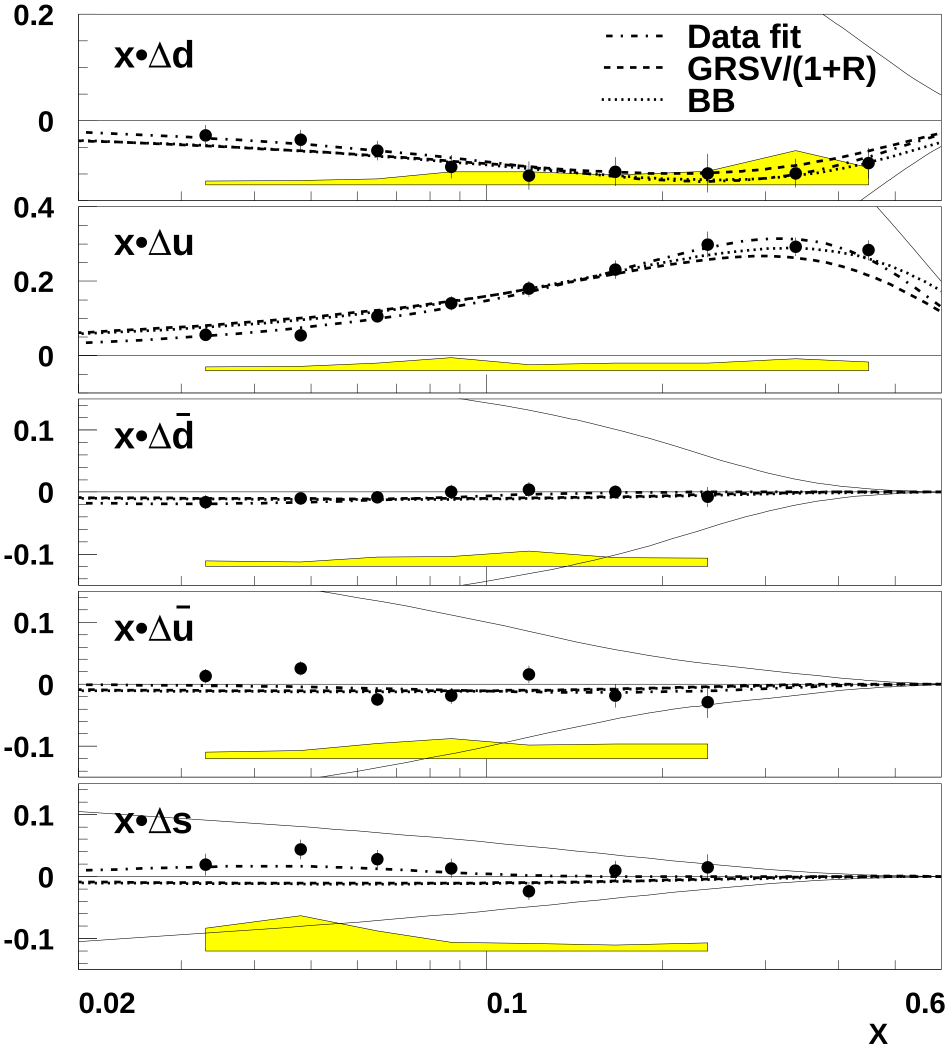

Figure 6.6: *Polarized quark distributions $x\Delta q(x)$ evaluated at a common Q^2 = 2.5 GeV^2. The error bars represent the statistical uncertainties and the shaded areas represent the systematic uncertainties. The solid curves correspond to the upper and lower limits $\pm xq(x)$ from the CTEQ5L unpolarized quark distributions [35] evaluated at Q^2 =2.5 GeV^2. The dashed curves show the GRSV prediction (LO, standard scenario) [149] for the polarized quark distributions, and the dotted curves represent the distributions obtained from a LO QCD analysis by J.Blümlein and H.Böttcher [152]. The GRSV parametrizations are divided by $(1+R)$ to allow a direct comparison to the data as explained in the text. The dot-dashed curves indicate the result of a fit to the data.*

6.4.3 The valence quark polarizations

The extraction of the valence quark polarizations, $\Delta u_v = \Delta u - \Delta\bar{u}$ and $\Delta d_v = \Delta d - \Delta\bar{d}$, was performed by using in the fit procedure the alternative parameters vector

$$\vec{\mathbf{Q}}(x) = \left(\frac{\Delta d - \Delta\bar{d}}{d - \bar{d}}(x),\ \frac{\Delta u - \Delta\bar{u}}{u - \bar{u}}(x),\ \frac{\Delta\bar{d}}{\bar{d}}(x),\ \frac{\Delta\bar{u}}{\bar{u}}(x),\ \frac{\Delta s + \Delta\bar{s}}{s + \bar{s}}(x) \right). \qquad (6.23)$$

The fitted sea polarization is identical for the valence and for the flavor decomposition. As in the case of the flavor decomposition, in the valence decomposition the sea distribution was set to zero for $x > 0.3$ and the effect on the results of the valence distributions was included in the systematic uncertainties. The polarized valence quark distributions $x \cdot \Delta d_v$, $x \cdot \Delta u_v$, and $x \cdot \Delta\bar{u}$ are shown in Fig. 6.7. The distributions were calculated from the extracted quark polarizations by multiplication with the CTEQ5L parametrization of unpolarized quark distributions evaluated at $Q^2 = 2.5$ GeV^2. Figure 6.7 includes a comparison to the SMC results [133] obtained at $Q^2 = 10$ GeV^2 and evolved at $Q^2 = 2.5$ GeV^2 by assuming Q^2-independent quark polarizations. In particular, the SMC data have been extracted assuming a $SU(3)_f$ symmetric sea

$$\Delta q_s(x) = \Delta u_s(x) = \Delta\bar{u}(x) = \Delta d_s(x) = \Delta\bar{d}(x) = \Delta s(x) = \Delta\bar{s}(x). \qquad (6.24)$$

The results of the fit for the valence decomposition are given in Table 6.4.3. The statistical correlations between the quark polarizations are listed in Table B.4 together with the corresponding value of $\chi^2/n.d.f.$ in each x-bin.
The results obtained for the valence decomposition have been compared also to the polarized parton distributions extracted by Leader, Sidorov and Stamenov [154]. The LSS group performed a fit to world data on inclusive DIS spin asymmetry A_1. The LO QCD analysis comprises updated values for the baryonic decay constants and the MRST99 set for the unpolarized parton densities in Ref. [155] is taken as input for the parametrizations of the polarized distributions. In addition, the SLAC-E155 proton data [132] are incorporated in the analysis. The extracted LO polarized parton distributions for the valence sector, Δu_v and Δd_v, assume a $SU(3)$ flavor-symmetric sea and the adopted parametrization has the form

$$\delta q_f(x, Q_0^2) = \eta_f A_f x^f q_f(x, Q_0^2), \qquad (6.25)$$

where $f = u_v,\, d_v,\, sea$ and $Q_0^2 = 1$ GeV^2. Here, the terms η_u and η_d are the first moments of the polarized distributions and are constrained in the fit to satisfy the sum rules for the axial charges a_3 and a_8 in Eq. (2.76). The extrapolation of the proton spin structure function g_1^p in the unmeasured small-x region predicts for this parametrization a change in sign for $x < 10^{-3}$. The value of g_1^p becomes negative in the case the gluon polarization is positive. This behavior is substantially different from the usually Regge-type functional form adopted for g_1^p at small x.
In analogy to the GRSV parametrizations, a $(1 + R)$ correction was applied to the LSS parametrizations to allow for a direct comparison with the values extracted in this analysis.

x-bin	$x \cdot \Delta d_v$	$x \cdot \Delta u_v$	$x \cdot \Delta \bar{u}$
1	0.016 ± 0.033 ± 0.007	0.036 ± 0.025 ± 0.010	0.014 ± 0.023 ± 0.043
2	−0.013 ± 0.033 ± 0.008	0.033 ± 0.029 ± 0.013	0.023 ± 0.025 ± 0.043
3	−0.029 ± 0.032 ± 0.008	0.103 ± 0.028 ± 0.025	−0.005 ± 0.024 ± 0.043
4	−0.088 ± 0.035 ± 0.013	0.145 ± 0.030 ± 0.031	−0.008 ± 0.026 ± 0.043
5	−0.097 ± 0.038 ± 0.012	0.156 ± 0.032 ± 0.018	0.011 ± 0.028 ± 0.043
6	−0.072 ± 0.082 ± 0.014	0.218 ± 0.050 ± 0.017	−0.005 ± 0.040 ± 0.043
7	−0.033 ± 0.077 ± 0.012	0.272 ± 0.039 ± 0.028	−0.001 ± 0.032 ± 0.043
8	−0.059 ± 0.027 ± 0.026	0.314 ± 0.025 ± 0.017	–
9	−0.071 ± 0.028 ± 0.013	0.290 ± 0.025 ± 0.011	–

Table 6.5: *Extracted values of the polarized quark distributions for the valence decomposition. The first (second) error corresponds the stistical (systematic) uncertainty.*

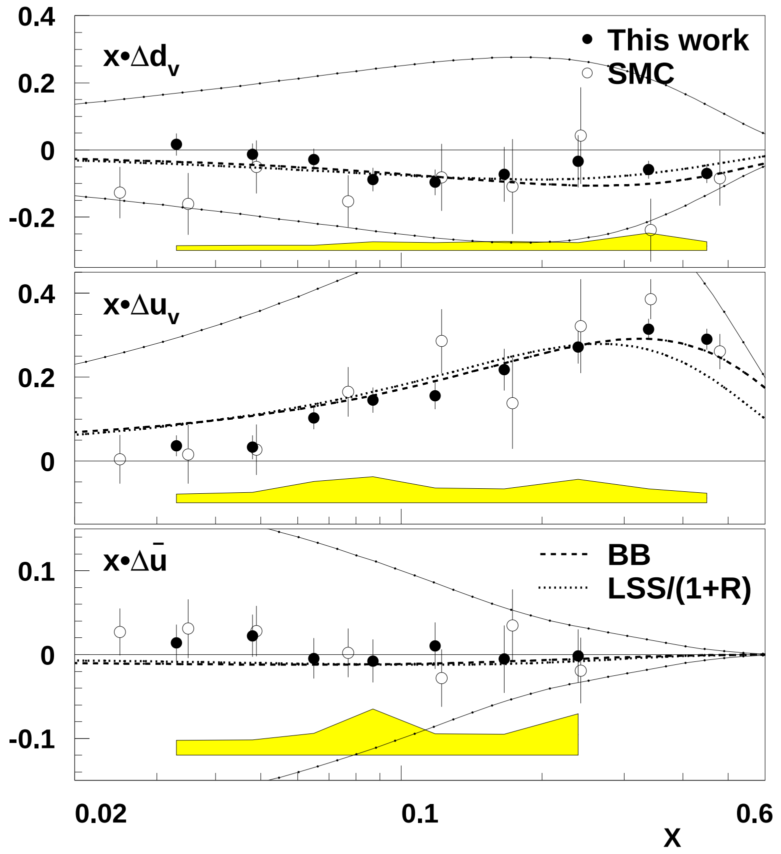

Figure 6.7: *Polarized quark distributions for valence quarks, $x\Delta d_v$ and $x\Delta u_v$, and for $x\Delta\bar{u}$ at $Q^2 = 2.5$ GeV^2 as a function of x. The error bars refer to the statistical uncertainties and the shaded bands to the systematic uncertainties. The distributions are compared to the results from SMC [133], at the same scale. The error bars of the SMC results correspond to the total uncertainty. The solid curves indicate the positivity limit. The dashed curves represent the parametrization of the polarized parton densities from Blümlein and Böttcher (BB) [152] and the dotted curves indicate the parametrization from Leader, Sidorov and Stamenov (LSS) [154] at LO.*

6.4.4 Light-quark polarization difference $\Delta\bar{u} - \Delta\bar{d}$

Parametrizations of polarized quark distributions extracted from inclusive data alone cannot provide information on the polarization of the antiquark distributions for the separate flavors.

In the unpolarized case, a flavor asymmetry in the antiquark sector ($\bar{d} > \bar{u}$) has been confirmed by several experiments, and its x-dependence has been studied (see $e.g.$ [143, 156]). The question of whether this asymmetry extends also to the polarized light-sea distributions, $i.e.$ $\Delta\bar{d} \neq \Delta\bar{u}$ is addressed by several nucleon models. For example, a large asymmetry for $\Delta\bar{d} - \Delta\bar{u}$ as a function of x is predicted by calculations in the chiral quark-soliton model (CQSM) [157, 158] and by the statistical model of the nucleon by Soffer $et\ al.$ [159].

Calculations within the CQSM show that the flavor asymmetry of the polarized light-sea distributions should be larger than the corresponding unpolarized distributions: $|\Delta\bar{u} - \Delta\bar{d}| > |\bar{u} - \bar{d}|$. In the model, the nucleon is characterized as a bound state of N_c quarks where N_c defines the number of colors. The large-N_c limit technique is exploited in the calculation to control the corrections (of the order $(1/N_c)^n$) of the evolution of the quark distributions. In addition, the initial evolution condition is characterized by a relatively low normalization point ($\mu^2 = 0.36$ GeV^2) [160].

In the model the nearly massless quarks develop a non-zero dynamical mass due to the spontaneous breaking of the chiral QCD Lagrangian. Then, the dynamical quark fields in the nucleon interact with Goldstone pions. The chiral soliton of the model is the solution for the minimization of the nucleon mass expressed in terms of pion fields.

Static properties of the nucleon obtained from CQSM calculations (such as masses, magnetic moments and form factors) are in reasonable agreement with the experimental results. In addition, due to its field theoretical nature, the quark and antiquark distributions obtained in this model satisfy the general QCD requirements like positivity, sum rules, $etc.$, and are in good qualitative accordance with phenomenological parametrizations.

A different approach is adopted by Soffer, Bourrely and Bucella [159]. Based on a statistical physical picture, the nucleon is viewed as a gas of massless partons (quarks, antiquarks and gluons) in equilibrium at a given temperature in a finite size volume. The initial energy scale Q_0^2 of this system depends on a thermodynamical potential for the partons and a universal temperature $T_U \approx 50$ MeV. The parton potentials are the fitting parameters of the model. The formalism is based on the direct construction of the quark and antiquark distributions for both helicity states separately. Unpolarized and polarized distributions follow from the simple combination of the different helicity states for each flavor. The potential of a quark in a certain helicity state is opposite to the potential of the corresponding antiquark in the opposite helicity state. The potential of the gluons is zero. From the previous assumptions several relations can be deduced between the potentials reducing the number of free parameters. In particular, a consequence of the ordering of the potentials is that

$$\Delta\bar{u} - \Delta\bar{d} \simeq \bar{d} - \bar{u}\,, \tag{6.26}$$

with the flavor symmetry breaking almost the same for unpolarized and polarized quark distributions. A selection of polarized and unpolarized DIS data are fitted in order to determine the eight free parameters of the model.
The x-dependence of the polarized structure functions obtained within the statistical model is in fair agreement with the data. A fast rising behavior for g_1^p and a fast decrease for g_1^n in the small-x region are predicted by this model due to the antiquark contributions. In the extraction of $\Delta\bar{d} - \Delta\bar{u}$ the parameters vector used for the fitting procedure was

$$\vec{\mathbf{Q}}(x) = \left(\frac{\Delta d}{d}(x),\ \frac{\Delta u}{u}(x),\ \frac{\Delta\bar{u} - \Delta\bar{d}}{\bar{u} - \bar{d}}(x),\ \frac{\Delta\bar{d}}{\bar{d}}(x),\ \frac{\Delta s + \Delta\bar{s}}{s + \bar{s}}(x) \right) . \tag{6.27}$$

Figure 6.8 shows the results of the fit. The extracted values for $\Delta\bar{u}-\Delta\bar{d}$ at $Q^2 = 2.5$ GeV^2 are listed in Table B.5 together with the corresponding value of $\chi^2/n.d.f.$ in each x-bin. The CTEQ5L parametrizations of the unpolarized quark distributions were used for the evolution at $Q^2 = 2.5$ GeV^2. In Figure 6.8, the data are compared to results from CQSM calculations at $Q^2 = 2.5$ GeV^2 as well as results from the statistical model at the same scale. Even if the data do not seem to favor the CQSM, the size of the experimental uncertainties (as well as the model uncertainties) does not allow for a definitive statement concerning the distinction between the two models.

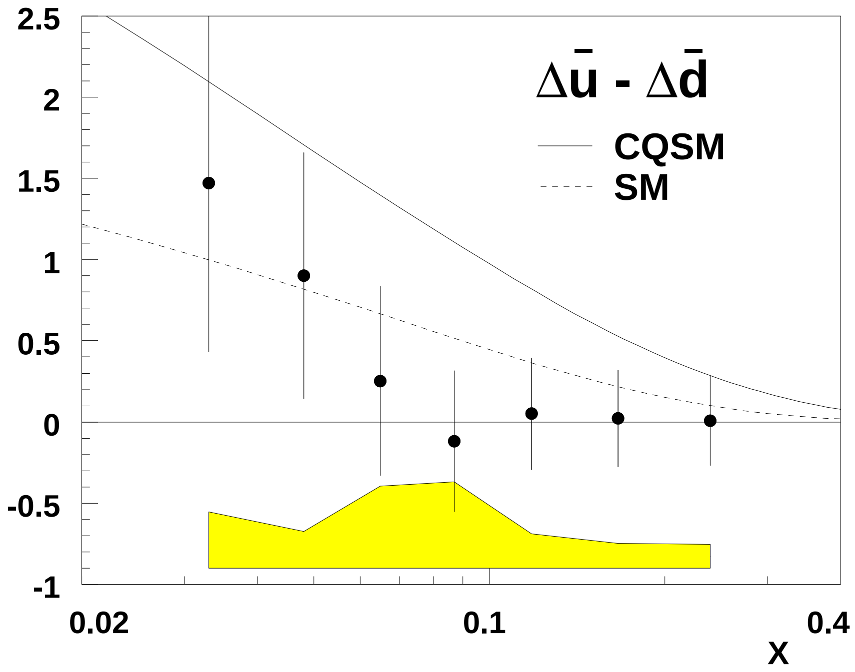

Figure 6.8: *Result for the $\Delta\bar{u} - \Delta\bar{d}$ as a function of x for $Q^2 = 2.5$ GeV^2. The solid curve indicates the prediction from the CQSM [160], the dashed curve represent the prediction from the Statistical Model [159].*

6.5 Systematic uncertainty in the polarized quark distributions

The systematic uncertainties in the extracted quark polarizations have contributions from the systematic uncertainties in the measured asymmetries and the uncertainties in the fragmentation model used to generate the purities. Additional contributions arise from the choice of the unpolarized quark distributions, and from the assumption of a zero sea-quark polarizations for $x > 0.3$. In this Section the different parts are discussed.
For the extraction of the flavor decomposition, the dominant contribution to the systematic uncertainty is due to the uncertainties in the fragmentation model in the Monte Carlo. Beam and target polarization uncertainties are also relevant.

6.5.1 Propagation of the asymmetry uncertainties

The systematic uncertainties in the extracted quark polarizations arising from the systematic uncertainties in the measured asymmetries (discussed in Section 5.5) can be determined by using the same covariance matrix method as was used for the statistical uncertainties (see Appendix A). The constructed covariance matrix C_A^{syst} contains the systematic error in the asymmetry vector $\vec{\mathbf{A}}_{\mathbf{m}}$ in Eq. (6.9). The covariance matrix is then added to the covariance matrix C_A^{stat}

$$C_A^{TOT} = C_A^{syst} + C_A^{stat}\,, \tag{6.28}$$

and the minimization Eq. (6.11) is solved by using the total covariance matrix. The systematic errors σ_{syst} of the quark polarization is defined as

$$\sigma^{syst} = \sqrt{(\sigma^{tot})^2 - (\sigma^{stat})^2}\,, \tag{6.29}$$

where σ^{tot} is the error in the extracted quark polarization with C_A^{TOT}, and σ^{stat} is the error obtained from C_A^{stat}.
In the following the construction of $C_A^{syst,\,k}$ for each systematic error source k is presented. The elements of the matrix are defined for row i and column j, with i, $j = 1, \ldots, 9$. The full covariance matrix is then obtained as $C_A^{syst} = \sum_k C_A^{syst,\,k}$.

Beam polarization
The contribution of the fractional error of the beam polarization error to the systematic covariant matrix was calculated as

$$[C_A^{syst,\,p_B}]_{ij} = \left[\left(\frac{\delta p_B}{p_B}\right)^2_{rise} + [\rho^{p_B}]_{ij}\left(\frac{\delta p_B}{p_B}\right)_{corr,i}\left(\frac{\delta p_B}{p_B}\right)_{corr,j}\right] A_i A_j\,, \tag{6.30}$$

where the correlation coefficient $[\rho^{p_B}]_{ij}$ was taken to be one for asymmetries of the same year and zero for asymmetries of different years. Here, $(\delta p_B/p_B)_{rise}$ denotes the systematic error obtained from the rise time calibration of the polarimeter and $(\delta p_B/p_B)_{corr}$

refers to the systematic error due to the corrections which are applied to the measured raw polarization. The values for both systematic uncertainties are given for each year of data taking in Section 5.5.1.

Target polarization
The fractional systematic uncertainties in the target polarization were given in Section 5.5.2 for each year of data taking. In analogy to $[C_A^{syst,\, p_B}]$, the covariance matrix for this contribution was determined as

$$[C_A^{syst,\, p_T}]_{ij} = \left[[\rho^{p_T}]_{ij} \left(\frac{\delta p_T}{p_T}\right)_i \left(\frac{\delta p_T}{p_T}\right)_j \right] A_i A_j \,, \tag{6.31}$$

where $[\rho^{p_T}]_{ij} = 1$ for asymmetries of the same target and zero for asymmetries for different targets.

Cross section ratio R
Two contributions from the cross-section ratio R are accounted for in the systematic error in the quark polarizations. The first one arises from the depolarization factor D which depends on R, and the second one from the $(1+R)$ factor in Eq. (6.1). It follows from Eqs. (2.35), (2.41) and (6.1) that the contribution to the covariance matrix can be written as

$$[C_A^{syst,\, R}]_{ij} = \left[\frac{1-\epsilon}{(1+R)(1+\epsilon R)} \delta R \right]^2 A_i A_j \,, \tag{6.32}$$

where both R and δR are taken from Ref. [26].

Radiative corrections
The systematic uncertainty, $\delta(\Delta A_1^{RC})$, associated with the radiative correction term ΔA_1^{RC} is given in Table 5.7 for the inclusive asymmetries. This contribution was included in the covariance matrix according to

$$[C_A^{syst,\, RC}]_{ij} = [\rho^{RC}]_{ij} \delta(\Delta A_i^{RC}) \delta(\Delta A_j^{RC}) \,, \tag{6.33}$$

where $[\rho^{RC}]_{ij} = 1$ for the inclusive asymmetries of the same target and zero otherwise.

Smearing corrections
Smearing corrections were applied to the proton asymmetries only. The statistical uncertainty $\Delta\kappa_{smear}$ in the correction factor κ_{smear} in Table 5.6 was used as its systematic error. This contribution was then included into the proton and the deuteron parts of the covariance matrix as follows

$$[C_A^{syst,\, SM}]_{ij} = [\rho^{SM}]_{ij} (\delta(\Delta\kappa_{smear}^i) A_i)(\delta(\Delta\kappa_{smear}^j) A_j) \,, \tag{6.34}$$

where $[\rho^{SM}]_{ij} = 1$ when i and j are both proton, deuteron, or ^{3}He asymmetries and zero otherwise.

Spin structure function g_2
In Section 5.5.4 the systematic uncertainty in the asymmetry A_1 due to the assumption $g_2 = 0$ was discussed. The extraction of the polarized quark distributions is based on the ratio g_1/F_1, therefore the systematic error due to g_2 has to be calculated for this quantity. Although the asymmetry A_1 equals the ratio g_1/F_1 for $g_2 = 0$, the systematic error in both quantities due to this assumption is different. From Eq. (2.41) the systematic uncertainty arising from g_2 is given by

$$\delta(g_1/F_1)_{g_2} = \frac{\gamma(\gamma-\eta)}{1+\gamma\eta} \cdot \frac{\delta g_2}{F_1} . \tag{6.35}$$

The contribution of the uncertainty in g_2 to the covariance matrix is

$$[C_A^{syst,\,g_2}]_{ij} = \left[[\rho^{g_2}]_{ij} \delta\left(\frac{g_1}{F_1}\right)_{g_2,\,i} \delta\left(\frac{g_1}{F_1}\right)_{g_2,\,j} \right] A_i A_j \,, \tag{6.36}$$

where $[\rho^{g_2}]_{ij} = 1$ for asymmetries of the same target and zero otherwise.

Yield fluctuations
The yield of the 1995 data on ^{3}He target exhibited a small non-statistical fluctuation. The size of these fluctuations and their contributions to the systematic uncertainty in $A_1^{(h)}$ is discussed for instance in Ref. [75]. For the inclusive and semi-inclusive charged hadron asymmetries obtained with ^{3}He the systematic error $[\delta A_1]_{Yield}$ due to the observed yield fluctuations is given by

$$[\delta A_1]_{Yield} = 0.00256 \,, \tag{6.37}$$
$$[\delta A_1^{h^+}]_{Yield} = 0.00575 \,, \tag{6.38}$$
$$[\delta A_1^{h^-}]_{Yield} = 0.00547 \,. \tag{6.39}$$

The systematic contributions were included in the ^{3}He sector of the covariance matrix according to

$$[C_A^{syst,\,Yield}]_{ij} = [\delta A_i]_{Yield}[\delta A_j]_{Yield} \,. \tag{6.40}$$

No yield fluctuation were observed for the proton data. In addition, it is assumed that the non-statistical yield fluctuations observed for the deuterium data are due to known systematics effects (such as beam position). However, it has been shown (see Section 5.6.1) that they do not occurr within a fill. Hence, in a fill-based analysis the extracted asymmetries are not affected (see Fig. 5.13).

6.5.2 Systematic uncertainty from the purities

Two sources of uncertainty for the determination of the purities have been considered: the contributions from uncertainties in the unpolarized parton density functions and the fragmentation model implemented to reproduce particle yields at HERMES.
The uncertainty in the choice of the unpolarized parton distributions was estimated considering the difference of the results obtained for two alternative unpolarized PDF

sets. For this purpose the parametrizations of $q_f(x, Q^2)$ from CTEQ5L [35] and from GRV98 [46] were used as input in Eq. (6.4). The LUND string fragmentation model fitted to HERMES distributions (scheme SF1 in Table 6.1) was used to determine the fragmentation functions in Eq. (6.3). To estimate the systematic uncertainty associated with the fragmentation model SF1, other sets of fragmentation functions were generated from two alternative JETSET parametrizations: the independent fragmentation model (IF) and the PETRA tune. The systematic uncertainty in the polarized quark distributions was then derived from the maximum deviation of the results obtained for either of the alternative models compared to those extracted from SF1. The systematic uncertainty in the spectrometer acceptance function is assumed to be negligible.

6.5.3 Uncertainty in the unpolarized sea model

The polarization of the sea quarks was set to zero for $x > 0.3$. The systematic effect on the polarization of the u and d quarks due to this assumption was determined by setting the sea polarization to the upper and lower positivity limits given by the unpolarized quark distributions. In practice, this corresponds to a modification of the input asymmetries for $x > 0.3$ as

$$\left(A^h\right)' = A^h \pm P_f^h \left(\frac{1-\gamma^2}{1+R}\right) , \tag{6.41}$$

where P_f are the purities for the sea flavors. The extraction of the quark polarizations was performed by using the modified asymmetries $(A^h)'$. The maximum difference between the results obtained with this assumption and the setting $\Delta q_{sea}/q_{sea} = 0$ was taken as the systematic uncertainty in the u and d quarks polarizations for $x > 0.3$ (see Table B.6).

6.6 Determining moments of the distributions

The n^{th} moment $\Delta^{(n)} q_f(Q^2)$ of a polarized quark distribution $\Delta q_f(x, Q^2)$ is determined as

$$\Delta^{(n)} q_f(Q^2)\big|_{Q^2=2.5\ \text{GeV}^2} = \int_0^1 dx\ x^{n-1}\ \Delta q(x, Q^2)\big|_{Q^2=2.5\ \text{GeV}^2} \tag{6.42}$$

where the extracted polarized quark distributions have been evaluated at a fixed scale $Q_0^2 = 2.5$ GeV^2.

For the first moments, $n = 1$, the total contribution of each quark flavor to the nucleon spin is determined by integrating the measured parton distributions over the entire x range. In practice, the total integration comprises three pieces: the HERMES measured region ($0.023 < x < 0.6$), the low-x region ($x < 0.023$), and the high-x region ($x > 0.6$). The integral of the quark spin distribution in the measured x-region is calculated by integrating the product of the quark polarization at a given x-bin, x_i, and the parametrization of the unpolarized distribution $q_f(x, Q_0^2)$ as

$$\Delta^{(1)} q_f(Q_0^2) = \int_{0.023}^{0.6} dx \Delta q(x, Q_0^2) = \sum_i \left(\frac{\Delta q_f}{q_f}(x_i) \int_{\xi_i}^{\xi_{i+1}} q_f(x, Q_0^2) dx\right) , \tag{6.43}$$

where $\frac{\Delta q_f}{q_f}(x_i)$ was assumed constant within each x-bin, i, and independent of Q^2. The integration was performed for $x \in [\xi_i, \xi_{i+1}]$ which defines the boundaries of the bin. The parametrizations from CTEQ5L at $Q_0^2 = 2.5$ GeV^2 were taken for the unpolarized parton distributions $q_f(x, Q_0^2)$. The statistical uncertainties in the integral in the measured region was obtained by adding the statistical uncertainties in quadrature in each x-bin. The systematic uncertainties were assumed to be completely correlated among x-bins and thus added linearly.

Outside the measured region $0.023 < x < 0.6$, assumptions are required on the integrals for the extrapolations in the low and high-x regions. The low-x extrapolation depends heavily on the theoretical model. Unfortunately, there is no clear prediction for the behavior of the polarized parton distributions in this region [15]. Previous analyses on $g_1(x)$ assumed that the spin structure function exhibits Regge-behavior at small x. According to the treatment in Ref. [161], the polarized parton distributions exhibit an x-dependence at low-x of the form $\Delta q_f(x) \propto x^{-\alpha}$. Here, the exponent $-\alpha$ is the intercept of the axial vector Regge trajectory, and it is expected to be in the range $-0.5 < -\alpha < 0.0$. In Ref. [161], a value of $\alpha = -0.07^{+0.42}_{-0.32}$ has been obtained from a fit to EMC data. In this analysis $\alpha = 0$ was taken and a constant value was fitted to the first three x-bins for each quark flavor. The results of the fit were then integrated in the range $0.0 < x < 0.023$. A relative uncertainty of 100% in the fitted constant was taken as systematic uncertainty associated with the low-x extrapolation.

Absolute upper limits for the low-x contribution to the integrals of the polarized quark distributions can be derived from the unpolarized distributions. Using the CTEQ5L parametrization, at $Q^2 = 2.5$ GeV^2 these limits for the valence quark distributions are

$$\int_{0.0}^{0.023} d_v(x)dx = 0.25 \,, \tag{6.44}$$

$$\int_{0.0}^{0.023} u_v(x)dx = 0.41 \,, \tag{6.45}$$

while for the d and u flavors one has

$$\int_{0.0}^{0.023} d(x)dx = 1.13 \,, \tag{6.46}$$

$$\int_{0.0}^{0.023} u(x)dx = 1.25 \,. \tag{6.47}$$

The same integration for the $s + \bar{s}$ quarks gives a value of 0.94. However, it is possible to infer from Fig. 6.6 that the extracted quark polarizations do not reach the positivity limits in the small x range. Therefore in the framework of the Regge model there is no reason to assume that the low-x extrapolation could be close to these absolute limits. The high-x extrapolation ($0.6 < x < 1.0$) was performed assuming that for the polarized parton distributions the functional form given in Eq. (6.22) can be used. The steep decrease of the unpolarized parton distributions for $x > 0.6$ ensures that the contribution to the integral coming from this kinematic region remains small. As a conservative estimate, for each flavor the value obtained from the extrapolation was used as the systematic uncertainty in the integral for $0.6 < x < 1.0$. The polarized parton distributions of the

sea quarks in the region $x > 0.3$ are assumed zero, with the positivity limits providing the systematic uncertainties.
The results for the first moment[1] $\Delta q_f(Q_0^2)$ in the range $0.0 < x < 1.0$ are listed in Table 6.6. The separate contributions from the three integrated x-regions are shown together with the total integral which was calculated by summing the three pieces for each flavor. The statistical error for the measured region was taken as the statistical uncertainty in the total integral. The total systematic uncertainty was obtained adding in quadrature the systematic contributions of the three regions.

	Integrated x-regions			First moment
	0.0 – 0.023	0.023 – 0.6	0.6 – 1.0	0.0 – 1.0
Δu	0.034	0.557 ± 0.022 ± 0.061	0.020	0.611 ± 0.022 ± 0.079
Δd	−0.019	−0.218 ± 0.027 ± 0.068	−0.002	−0.239 ± 0.027 ± 0.071
$\Delta \bar{u}$	0.001	0.038 ± 0.034 ± 0.065	0.000	0.039 ± 0.034 ± 0.065
$\Delta \bar{d}$	−0.004	−0.010 ± 0.031 ± 0.052	0.000	−0.014 ± 0.031 ± 0.052
$\Delta s + \Delta \bar{s}$	0.013	0.032 ± 0.033 ± 0.072	0.000	0.045 ± 0.033 ± 0.073
$\Delta u + \Delta \bar{u}$	0.035	0.595 ± 0.017 ± 0.045	0.020	0.650 ± 0.017 ± 0.060
$\Delta d + \Delta \bar{d}$	−0.023	−0.228± 0.019 ± 0.047	−0.002	−0.253 ± 0.019 ± 0.052
Δu_v	0.029	0.526 ± 0.041 ± 0.114	0.020	0.575 ± 0.041 ± 0.119
Δd_v	−0.012	−0.212 ± 0.042 ± 0.095	−0.002	−0.226 ± 0.042 ± 0.096

Table 6.6: *First moments of polarized quark distributions at $Q_0^2 = 2.5$ GeV^2. The results are given for the measured region $0.023 < x < 0.6$, and for the low-x and high-x extrapolation regions. The total integral is given by the sum of the results in the three x regions. For the integrals in the measured range and for the total integrals the first (second) error is the statistical (systematic) uncertainty.*

Using the previous results, at leading order QCD the $SU(3)_f$ singlet component $\Delta\Sigma$ was determined according to Eq. (2.75), as well as the triplet and octet components Δq_3 and Δq_8. The obtained total integrals and the separate contributions from the different x-regions are given in Table 6.7.

	Integrated x-regions			First moment
	0.0 – 0.023	0.023 – 0.6	0.6 – 1.0	0.0 – 1.0
$\Delta\Sigma$	0.025	0.399 ± 0.026 ± 0.072	0.018	0.442 ± 0.026 ± 0.078
Δq_3	0.058	0.823 ± 0.028 ± 0.087	0.022	0.903 ± 0.028 ± 0.106
Δq_8	−0.014	0.303 ± 0.077 ± 0.143	0.018	0.307 ± 0.077 ± 0.145

Table 6.7: *First moments of the $SU(3)_f$ singlet ($\Delta\Sigma$), triplet (Δq_3) and octet (Δq_8) at $Q_0^2 = 2.5$ GeV^2. The contributions to the total integral from the measured region ($0.023 < x < 0.6$) and from the extrapolations at low-x and high-x are shown as well. For the integrals in the measured range and for the total integrals the first (second) term behind the value is the statistical (systematic) uncertainty.*

[1] In the following, the first moment $\Delta^{(1)} q_f$ is referred to as Δq_f.

6.7 Comparison of results to other measurements and theoretical predictions

Here, the moments of the quark polarizations obtained in the previous section are compared to other experimental results and to theoretical predictions.

6.7.1 Results from semi-inclusive measurements

The SMC experiment measured the polarized quark distributions [133] by using semi-inclusive DIS data in a way similar to the analysis procedure employed in this thesis. The extracted polarized valence quark distributions have been shown already in Fig. 6.7 together with the SMC data evolved at $Q^2 = 2.5$ GeV^2. The results for the integrals in the measured region for the valence quarks were compared directly to those from the SMC experiment over the common x range $0.023 < x < 0.6$. The integrals of the polarized quark distributions from SMC were extrapolated to $Q^2 = 2.5$ GeV^2 (assuming Q^2-independent quark polarizations) and integrated according to Eq. (6.43). For the integration of the SMC results, the LO GRV94 parametrization [162] was used as input for the unpolarized distributions since this is the parametrization originally used in the analysis by SMC. In Table 6.8 the first and the second moments are compared. The results obtained with the two analyses are compatible within the quoted uncertainties. With the addition of the deuterium data, the statistical precision of the d_v quarks is comparable to that of the u_v quarks.

	This analysis	SMC
Δu_v	$0.53 \pm 0.04 \pm 0.11$	$0.59 \pm 0.08 \pm 0.07$
Δd_v	$-0.21 \pm 0.04 \pm 0.10$	$-0.33 \pm 0.11 \pm 0.09$
$\Delta^{(2)} u_v$	$0.13 \pm 0.01 \pm 0.01$	$0.15 \pm 0.02 \pm 0.01$
$\Delta^{(2)} d_v$	$-0.04 \pm 0.01 \pm 0.01$	$-0.05 \pm 0.02 \pm 0.02$

Table 6.8: *The integrals in the measured x-region obtained from this analysis are compared to SMC results [133]. The SMC values have been evolved at $Q^2 = 2.5$ GeV^2 and integrated over the interval $0.023 < x < 0.6$, which corresponds to the HERMES integration region.*

6.7.2 $SU(3)_f$ analysis predictions

The first moments of the polarized quark distributions presented in Tables 6.6 and 6.7 can be compared to results obtained from hyperon decay analyses as discussed in Section 2.5. In particular, the Bjorken sum rule is directly related to the first moment of the $SU(3)_f$ triplet Δq_3

$$\Delta q_3(Q^2) = \left|\frac{g_A}{g_V}\right| \Delta C_{NS}(Q^2)\,, \tag{6.48}$$

where the Q^2 dependence is driven by the scale dependence of $\alpha_s(Q^2)$ included in the first moment of the non-singlet coefficient ΔC_{NS}. The term ΔC_{NS} was determined according to Eq. (2.72) for a number of active flavors $n_f = 3$ and in the $\overline{\text{MS}}$ scheme. Using the value $\alpha_s^{(3)}(2.5\ \text{GeV}^2) = 0.339 \pm 0.018$ (which corresponds to $\alpha_s(M_{Z^0}) = 0.118 \pm 0.002$ [39]) one obtains at the $\mathcal{O}((\alpha_s/\pi)^3)$ correction order:

$$\Delta C^{NS}(2.5\ \text{GeV}^2) = 0.825 \pm 0.015\,, \tag{6.49}$$

where the error on ΔC^{NS} was calculated from the error on $\alpha_s^{(3)}$. The theoretical value of the Bjorken sum rule in Eq. (2.80) at the same Q^2-scale is $\Gamma_{Bj} = 0.174 \pm 0.003$, where $|g_A/g_V| = 1.2670 \pm 0.0035$ was taken from Ref. [39]. Therefore, the right hand side of Eq. (6.48) equals 1.044 ± 0.019 and has to be compared to the measured value $\Delta q_3(2.5\ \text{GeV}^2) = 0.903 \pm 0.028 \pm 0.106$ obtained in this analysis. Therefore, the Bjorken sum rule is confirmed to the level of 1.3 standard deviation.

In Ref. [163] Ellis and Karliner determined the decomposition of the nucleon spin under $SU(3)_f$ symmetry assumption. From a global fit of the available values on the first moment for proton (Γ_1^p) and neutron (Γ_1^n) from inclusive data, the polarized quark combinations $\Delta u + \Delta\bar{u}$, $\Delta d + \Delta\bar{d}$, and $\Delta s + \Delta\bar{s}$ were derived at an evolution scale of $Q^2 = \infty$. Using the quoted result $\Delta\Sigma(\infty) = 0.27 \pm 0.04$ together with $\Delta q_3(\infty) = |g_A/g_V|$ and $\Delta q_8(\infty) = 3F - D$, it is possible to evolve the singlet and non-singlet contributions at $Q^2 = 2.5\ \text{GeV}^2$ according to

$$\begin{aligned}
\Delta\Sigma(2.5\ \text{GeV}^2) &= \Delta\Sigma(\infty)\Delta C^S(2.5\ \text{GeV}^2)\,, && (6.50)\\
\Delta q_3(2.5\ \text{GeV}^2) &= \Delta q_3(\infty)\Delta C^{NS}(2.5\ \text{GeV}^2)\,, && (6.51)\\
\Delta q_8(2.5\ \text{GeV}^2) &= \Delta q_8(\infty)\Delta C^{NS}(2.5\ \text{GeV}^2)\,. && (6.52)
\end{aligned}$$

Here, ΔC^S is the first moment of the singlet coefficient function in Eq. (2.72), which at $\alpha_s^{(3)}(2.5\ \text{GeV}^2)$ and $\mathcal{O}((\alpha_s/\pi)^2)$ order equals

$$\Delta C^S(2.5\ \text{GeV}^2) = 0.879 \pm 0.007\,. \tag{6.53}$$

The resulting $SU(3)_f$ predictions for the polarized quark distribution at $Q^2 = 2.5\ \text{GeV}^2$ are presented in Table 6.9. Note that the results in the Ellis-Karliner analysis contain further theoretical and systematic uncertainties which include higher twist effects, low-x extrapolation and a possible Q^2-dependence of the spin asymmetry A_1. These uncertainties were estimated by the authors to have the same order of magnitude as the quoted errors [163].
The result for $\Delta u + \Delta\bar{u}$ obtained in this thesis by using semi-inclusive data is in good agreement with the prediction from the inclusive $SU(3)_f$ analysis. Instead, both measured $\Delta d + \Delta\bar{d}$ and $\Delta s + \Delta\bar{s}$ values are higher than the $SU(3)_f$ prediction. In particular, the value of $\Delta s + \Delta\bar{s}$ differs by 1.7 standard deviations from the Ellis-Karliner analysis, in which the polarization value for the strange sea is derived from $SU(3)_f$ symmetry. In the semi-inclusive approach the polarization of the strange sea is found to be compatible with zero within the quoted uncertainties. A difference of 2.5 standard deviation is observed

for the measured value of the first moment of the singlet distribution $\Delta\Sigma$. A graphical comparison with the predictions from $SU(3)_f$ symmetry analysis is presented in Fig. 6.9. First moments of the polarized quark distributions determined from the GRSV analysis at Leading Order [149] are shown in Table 6.9 for a scale of $Q^2 = 2.5$ GeV^2. Both the "standard" scenario results (in which a flavor-symmetric light sea distribution is considered) and the "valence" scenario results (which is based on a totally flavor-asymmetric light sea) are presented. The moments of the singlet and non-singlet distributions determined with the "valence" parametrizations seem to agree better with the corresponding measured values. However, if symmetry-breaking is considered, then the value of $\Delta\Sigma$ does not change significantly, while $\Delta s + \Delta\bar{s}$ becomes closer to zero.
The predictions for the Ellis-Jaffe sum rule for both the proton and neutron under the assumptions of $SU(3)_f$ symmetry and zero strange quark polarization (see Section 2.5.2) has been found to be violated by several measurements. The different scenarios proposed to account for this discrepancy either invoke $SU(3)_f$ symmetry breaking, $SU(3)_f$ asymmetric polarized sea distributions, or a large negative strange quark polarization. The results obtained in this semi-inclusive analysis, which was performed without any assumption for the polarization of the sea quarks, cannot yet uniquely discriminate between the different polarized sea models.

	This analysis	Predictions at $Q^2 = 2.5$ GeV^2		
$\Delta u + \Delta\bar{u}$	0.65 ± 0.02 ± 0.06	0.68 ± 0.02	$SU(3)_f$	[163]
		0.79	LO Standard	[149]
		0.74	LO Valence	[149]
$\Delta d + \Delta\bar{d}$	−0.25 ± 0.02 ± 0.05	−0.36 ± 0.01	$SU(3)_f$	[163]
		−0.42	LO Standard	[149]
		−0.44	LO Valence	[149]
$\Delta s + \Delta\bar{s}$	0.05 ± 0.03 ± 0.07	−0.08 ± 0.01	$SU(3)_f$	[163]
		−0.11	LO Standard	[149]
		0.007	LO Valence	[149]
$\Delta\Sigma$	0.44 ± 0.03 ± 0.08	0.24 ± 0.04	$SU(3)_f$	[163]
		0.27	LO Standard	[149]
		0.31	LO Valence	[149]
Δq_3	0.90 ± 0.03 ± 0.11	1.04 ± 0.02	Bjorken	
Δq_8	0.31 ± 0.08 ± 0.16	0.48 ± 0.03	$SU(3)_f$	[163]
		0.59	LO Standard	[149]
		0.31	LO Valence	[149]

Table 6.9: *The first moments of various spin distributions compared to predictions from $SU(3)_f$ symmetry analysis by Ellis and Karliner [163] and from LO analyses by Glück et al. [149] with two different scenarios for the symmetry of the light-sea quarks.*

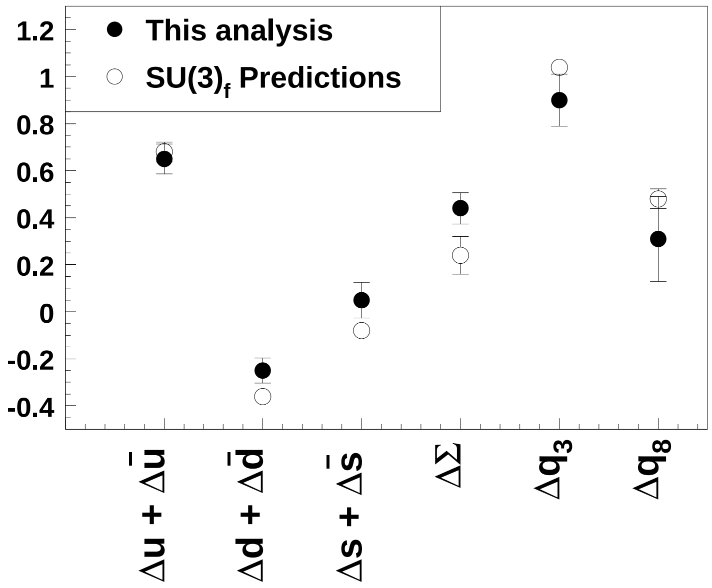

Figure 6.9: *Comparison of the polarized quark distributions obtained in this analysis and the predictions from an $SU(3)_f$ symmetry analysis [163].*

6.7.3 Gluon spin contribution

As explained in Section 2.5, due to the contribution of the axial anomaly, the singlet axial charge a_0 does not coincide with the interpretation of $\Delta\Sigma$ in terms of the sum of the quark spins. In addition, the mixing of the quark and gluon contributions is scheme dependent. Equation (2.77) shows the decomposition of a_0 (in the AB scheme) as a function of $\Delta\Sigma$ and Δg, where Δg is the first moment of the gluon spin. In this scheme $\Delta\Sigma$ is conserved and therefore independent of Q^2. The axial coupling a_0 extrapolated at $Q^2 = 2.5$ GeV^2 can be extracted from the Ellis-Jaffe sum rule in Eq. (2.69)

$$a_0(2.5\ \text{GeV}^2) = 9\left[\Gamma_1^{p\,(n)} - \left(\frac{1}{36}\Delta q_8 - (+)\frac{1}{12}\Delta q_3\right)\right] . \tag{6.54}$$

Using the HERMES published values for Γ_1^p and Γ_1^n at $Q^2 = 2.5$ GeV^2 together with the measured Δq_3 and Δq_8, the resulting axial couplings are $a_0 = 0.48 \pm 0.17$ for the proton and $a_0 = 0.27 \pm 0.17$ for the neutron, in agreement with each other.
The first moment of the gluon spin at this scale can now be evaluated from Eq. (2.77) as follows

$$\Delta g(2.5\ \text{GeV}^2) = \frac{2\pi}{3\alpha_s(2.5\ \text{GeV}^2)}\left(\Delta\Sigma - a_0(2.5\ \text{GeV}^2)\right) = 1.08 \pm 0.76_{(\text{stat.})} \pm 0.81_{(\text{syst.})} . \tag{6.55}$$

This result can be compared to the QCD analysis from Glück *et al.* [149], whose parametrization was used to determine a value of $\Delta g(2.5\ \text{GeV}^2) = 1.01$. However, the NLO fits to the world data performed to extract the polarized gluon distribution strongly depends on the assumption made about the x-dependence of the parametrization at the initial evolution scale. Therefore, the agreement of the extracted value for Δg with the GRSV result should not be considered as a confirmation of the measurement.

The phenomenological QCD fits, which exploit the Q^2 dependence of the data to separate the singlet quark distribution and the gluon distribution, represent an indirect measurement of the gluon polarization and are constrained by the limited Q^2 coverage of the data. A first direct observation of Δg was performed at HERMES by measuring the spin asymmetry in the photoproduction of pairs of high-p_T hadrons [164]. The production of jets with high transverse momentum p_T is an experimental signature of the photon-gluon fusion process (see Section 2.4). At HERMES energy, jets are replaced by hadrons with $p_T \geq 1$ GeV^2. The extracted value of $\langle \Delta g/g \rangle$ averaged over the range $0.06 < x_G < 0.28$ (x_G is the fraction of the nucleon momentum carried by the struck gluon) was determined to be $0.41 \pm 0.18_{\text{(stat.)}} \pm 0.03_{\text{(syst.)}}$. The systematic uncertainty represents the experimental contribution only. This value is found comparable with the GRSV parametrization within uncertainties.

6.7.4 Lattice QCD calculations predictions

Finally, in Table 6.10 first and second moments for the valence quark distributions over the entire x-range have been compared to values determined from lattice QCD calculations in the quenched approximation [165, 166]. In the theoretical framework of the OPE, the Wilson coefficients can be computed perturbatively. However, the determination of the forward matrix elements of the nucleon operators is a non-perturbative problem. The lattice QCD techniques offers a way to approach the calculation of the matrix elements. Both measured values for Δu_v and Δd_v at the scale $Q^2 = 5$ GeV^2 are lower than the lattice calculation at the same scale. The deviation of Δd_v from the prediction is less significant than for Δu_v.
The observed discrepancy for the first moment are also present for the second moments which were evaluated at $Q^2 = 4$ GeV^2. However, in this case the measured value of $\Delta^{(2)} d_v$ is in better agreement with the lattice prediction within uncertainties.
While a reasonable description of the phenomenological results is obtained in the unpolarized sector [165], the lattice computation in the quenched approximation is still not able to provide a satisfactory agreement with the experimental polarized moment distributions.
Recently, attempts have been made to incorporate an analytical expression for the extrapolation of the QCD calculations to the physical value of the pion mass [167, 168]. The developed theoretical framework in which the extrapolation is performed seems promising for the resolution of the discrepancy of the calculations with the experimental results.

	Total integral	Prediction		Q^2 (GeV^2)
Δu_v	$0.54 \pm 0.03 \pm 0.08$	0.84 ± 0.05	[165]	5
Δd_v	$-0.18 \pm 0.05 \pm 0.09$	-0.25 ± 0.02	[165]	5
$\Delta^{(2)} u_v$	$0.13 \pm 0.01 \pm 0.02$	0.198 ± 0.008	[166]	4
$\Delta^{(2)} d_v$	$-0.03 \pm 0.01 \pm 0.01$	-0.048 ± 0.003	[166]	4

Table 6.10: *First and second moments of valence quark distributions compared to predictions of lattice QCD calculations [165, 166]. In the last column the Q^2 values used for the comparison are quoted in GeV^2.*

7 Summary

The study of the nucleon structure via inclusive deep-inelastic scattering has played and still plays an important role in the establishment of the Quark-Parton Model in the composition of hadrons and subsequently of QCD as the theory of strong interactions. With polarized DIS the spin observables of the nucleon become accessible. A unique insight into the nucleon spin structure is provided by the semi-inclusive DIS process where both the scattered lepton and hadrons produced from the struck quark are detected.
In this thesis, inclusive and semi-inclusive double-spin asymmetries have been extracted from data collected by the HERMES experiment by using deep-inelastic scattering of a longitudinally polarized positron beam of 27.5 GeV from a longitudinally polarized gas target.
The analyzed data comprise the polarized proton target data from the 1996-1997 running period and the data on a polarized deuteron target which was operated from 1998 to 2000. The covered kinematic range is 1 GeV$^2 < Q^2 <$ 10 GeV^2 and 0.023 $< x <$ 0.6. In this x-range the average Q^2 value is $\langle Q^2 \rangle \simeq$ 2.5 GeV^2.
For the proton data, pion identification has been possible in a momentum window from 4 GeV to 13.5 GeV by using a threshold Čerenkov detector. In 1998 the Čerenkov detector was converted into a dual-radiator Ring Imaging Čerenkov detector, allowing pions, kaons and protons to be identified over a wide momentum range (2-15 GeV).
Systematic studies have been carried out for the extracted deuteron asymmetries. Consistency was found with the previous asymmetry measurements made by the SMC experiment at CERN and the E155 experiment at SLAC.
The ^{3}He inclusive and semi-inclusive hadron asymmetries from the 1995 HERMES data were combined with the proton and deuteron asymmetries to determine the contribution of each quark flavor to the spin of the nucleon. The extraction procedure is based on a LO QCD fromalism in which effective hadron fragmentation functions were generated within the HERMES acceptance. A Monte Carlo code employing the LUND string fragmentation model and tuned to reproduce HERMES multiplicities has been used. Polarized quark distributions were determined for all the flavors separately without imposing constraints on the sea polarization. The polarization of the u-quarks is found to be positive over the measured x kinematic range, and increases for increasing values for x. The polarization of the d-quarks is negative and smaller in magnitude compared to that of the u-flavor. The light sea quarks exhibit a polarization which is consistent with zero within the experimental uncertainties over the measured x-range. In the low-x region, where the sensitivity to the sea quarks is higher, $\Delta\bar{d}$ is negative, while $\Delta\bar{u}$ is positive. The polarization of the strange quarks is found also to be positive in this x-range.
The polarized light-sea difference $\Delta\bar{u} - \Delta\bar{d}$ was extracted as a function of x at the scale Q^2 = 2.5 GeV^2. The result has been compared to predictions from the Chiral

Quark-Soliton Model and from the Statistical Model. The latter seems to give a better description of the functional behavior of the data.
The first moments of the polarized quark distributions have been determined at $Q^2 = 2.5$ GeV^2. For the integrals, a Regge-type trajectory behavior was assumed for the extrapolation to $x = 0$, and the parametrization of the measured polarized quark distributions was used for $x > 0.6$. The fraction of the nucleon spin carried by the separate flavors was found to equal

$$\begin{aligned}
\Delta u &= 0.61 \pm 0.02 \pm 0.08 \ , \\
\Delta d &= -0.24 \pm 0.03 \pm 0.07 \ , \\
\Delta \bar{u} &= 0.04 \pm 0.03 \pm 0.07 \ , \\
\Delta \bar{d} &= -0.01 \pm 0.03 \pm 0.05 \ , \\
\Delta s + \Delta \bar{s} &= 0.05 \pm 0.03 \pm 0.07 \ .
\end{aligned}$$

The total fraction of the nucleon spin carried by the quarks is

$$\Delta\Sigma = 0.442 \pm 0.026 \pm 0.064 \ .$$

The extraction of the polarized valence quark distributions resulted in

$$\begin{aligned}
\Delta u_v &= 0.58 \pm 0.04 \pm 0.12 \ , \\
\Delta d_v &= -0.23 \pm 0.04 \pm 0.10 \ ,
\end{aligned}$$

which is consistent, within the overlapping x-region measured by HERMES, with results of previous SMC measurements extrapolated to $Q^2 = 2.5$ GeV^2.
Relative to the previously published HERMES results a higher statistical accuracy is achieved in the present analysis due to the addition of the deuterium data. However, the increased number of fitted quark-polarization parameters in the extraction procedure, together with a conservative estimate of some uncertainty contributions, induces a larger systematic uncertainty in the final results. A direct measurement of fragmentation functions at HERMES and an improved estimate of the target polarization will reduce the systematic uncertainty in the polarized quark distributions in future analyses.
The first moment of the triplet flavor component

$$\Delta q_3 = \Delta u + \Delta \bar{u} - (\Delta d + \Delta \bar{d}) = 0.903 \pm 0.028 \pm 0.106$$

agrees with the prediction of the Bjorken sum rule, which at $Q^2 = 2.5$ GeV^2 equals $\Gamma_{Bj} = 0.104 \pm 0.003$. At the same scale, the measured value of the octet flavor combination

$$\Delta q_8 = \Delta u + \Delta \bar{u} + \Delta d + \Delta \bar{d} - 2(\Delta s + \Delta \bar{s}) = 0.31 \pm 0.08 \pm 0.15$$

is in disagreement with the prediction from an $SU(3)$ flavor symmetry analysis. Instead, the analysis at LO of Glück *et al.* [149] which uses inclusive data and a broken light-sea symmetry ("valence" scenario) is in better agreement with the obtained results.
Predictions from lattice QCD calculations in the quenched approximation overestimate the results obtained in this thesis for the first and the second moments of the polarized u-valence quark, while the agreement is better for the polarized d-valence quark.
With the result of the integral for the spin structure function of the neutron measured at HERMES, the first moment of the polarized gluon contribution at $Q^2 = 2.5$ GeV^2 has been evaluated in the AB scheme: $\Delta g = 1.08 \pm 0.76_{(\mathrm{stat})} \pm 0.81_{(\mathrm{syst})}$. This result is in good agreement with the prediction from Glück *et al.*

8 Samenvatting

De studie van de structuur van het nucleon door middel van diep-inelastische verstrooiing (DIS) heeft een belangrijke rol gespeeld in het tot stand brengen van het Quark-Parton Model voor de samenstelling van hadronen, en vervolgens van QCD als theorie van de sterke wisselwerking. Met gepolariseerde DIS worden ook spinobservabelen meetbaar. Het semi-inclusieve DIS proces, waarbij zowel het verstrooide elektron als de uit het aangeslagen quark geproduceerde hadronen gedetecteerd worden, geeft een uniek inzicht in de spin-structuur van het nucleon.

In dit proefschrift zijn inclusieve en semi-inclusieve dubbele spin-asymmetriën bepaald uit data, verzameld bij het HERMES experiment, door middel van diep-inelastische verstrooiing van een longitudinaal gepolariseerde positronenbundel van 27.5 GeV aan een longitudinaal gepolariseerd gas target.
De geanaliseerde data omvatten de gepolariseerde proton target data uit de run-periode 1996-1997, en de data verkregen met een gepolariseerd deuterium target, welke tussen 1998 en 2000 in gebruik was.

Het behaalde kinematische bereik is 1 GeV$^2 < Q^2 <$ 10 GeV^2 en $0.023 < x < 0.6$. De gemiddelde waarde van Q^2 in dit x-bereik is $\langle Q^2 \rangle \simeq 2.5$ GeV^2.
Voor de proton data is pion-identificatie mogelijk geweest voor momenta tussen 4 GeV en 13.5 GeV middels een zogenaamde threshold Čerenkov detector. Deze Čerenkov detector is in 1998 omgezet in een dual-radiator Ring Imaging Čerenkov detector, wat de identificatie mogelijk maakte van pionen, kaonen en protonen in een breed impulsbereik (2-15 GeV).
Systematische studies zijn gedaan voor de gemeten deuterium-asymmetrieën. De resultaten zijn consistent met de eerdere asymmetrieë-metingen van het SMC experiment op CERN en het E155 experiment op SLAC.

De ^{3}He inclusieve and semi-inclusieve hadron asymmetrieën uit de HERMES data van 1995 zijn gecombineerd met deze proton- en deuterium-asymmetrieën om voor elk type quark de bijdrage aan de spin van het nucleon te bepalen. De meetmethode is gebaseerd op een LO QCD formalisme, waarbij effectieve hadron-fragmentatiefuncties gegenereerd zijn binnen de acceptantie van HERMES . Hierbij is gebruik gemaakt van een Monte Carlo programma dat het LUND string-fragmentatiemodel uitvoert, en dat zo aangepast is, dat de deeltjesmultipliciteiten van HERMES gereproduceerd werden.

Gepolariseerde quarkverdelingen zijn bepaald voor alle types apart, zonder het beperkingen op te leggen aan de polarisatie van de "sea". De gevonden polarisatie van de u-quarks is positief over het gemeten bereik in x, en neemt toe voor hogere waarden van x. De polarisatie van de d-quarks is negatief en kleiner in sterkte dan die van de u-quarks. De lichte "sea" quarks vertonen een polarisatie die, binnen de experimentele onzekerheid, consistent is met nul in het gemeten x-bereik. In het lage-x gebied, waar de gevoeligheid voor de "sea" quarks hoger is, is $\Delta\bar{d}$ negatief en $\Delta\bar{u}$ positief. De polarisatie van de s-quarks is ook positief in dit x-bereik.

Het verschil voor de gepolariseerde lichte "sea", $\Delta\bar{u} - \Delta\bar{d}$, is gemeten als functie van x bij een schaalgrootte van $Q^2 = 2.5$ GeV^2. Het resultaat is vergeleken met voorspellingen van het Chirale Quark-Soliton Model en met die van het Statistische Model. Het laatste model lijkt een betere beschrijving te geven van het functionele gedrag van de data.

De eerste momenten van de gepolariseerde quarkverdelingen zijn bepaald bij $Q^2 = 2.5$ GeV^2. Voor de integralen is een 'Regge traject'-achtig gedrag aangenomen voor de extrapolatie naar $x = 0$, en een parametrisatie van de gemeten gepolariseerde quarkverdelingen is gebruikt voor $x > 0.6$. De gevonden fractionele bijdrage van de diverse quark-soorten aan de nucleon-spin is

$$\begin{aligned}
\Delta u &= 0.61 \pm 0.02 \pm 0.08 \ , \\
\Delta d &= -0.24 \pm 0.03 \pm 0.07 \ , \\
\Delta\bar{u} &= 0.04 \pm 0.03 \pm 0.07 \ , \\
\Delta\bar{d} &= -0.01 \pm 0.03 \pm 0.05 \ , \\
\Delta s + \Delta\bar{s} &= 0.05 \pm 0.03 \pm 0.07 \ .
\end{aligned}$$

De totale fractionele bijdrage van de quarks aan de spin van het nucleon is De bepaling

$$\Delta\Sigma = 0.442 \pm 0.026 \pm 0.064 \ .$$

van de gepolariseerde valentiequarkverdelingen heeft geleid tot

$$\begin{aligned}
\Delta u_v &= 0.58 \pm 0.04 \pm 0.12 \ , \\
\Delta d_v &= -0.23 \pm 0.04 \pm 0.10 \ ,
\end{aligned}$$

wat, binnen het overlappende x-bereik, consistent is met resultaten van eerdere metingen van SMC, geëxtrapoleerd tot $Q^2 = 2.5$ GeV^2.
In vergelijking tot eerder gepubliceerde resultaten van HERMES is in deze analyse, door het toevoegen van de deuterium data, een hogere statistische nauwkeurigheid bereikt. Echter, de toegenomen hoeveelheid fitparameters voor de quarkpolarisatie en een meer behoudende afschatting van een aantal bijdragen aan de onzekerheid, leiden tot een hogere systematische onzekerheid in de uiteindelijke resultaten. Een directe meting van de fragmentatiefuncties bij HERMES, en een verbeterde afschatting van de targetpolarisatie, zullen de systematische onzekerheid in de gepolariseerde quarkverdelingen bij toekomstige analyses reduceren.
Het eerste moment van de "triplet flavor" component

$$\Delta q_3 = \Delta u + \Delta\bar{u} - (\Delta d + \Delta\bar{d}) = 0.903 \pm 0.028 \pm 0.106 \ ,$$

stemt overeen met de voorspelling van de somregel van Bjorken, waar, bij $Q^2 = 2.5$ GeV^2, $\Gamma_{Bj} = 0.104 \pm 0.003$. Bij dezelfde schaal stemt de gemeten waarde voor de "octet flavor" combinatie,

$$\Delta q_8 = \Delta u + \Delta \bar{u} + \Delta d + \Delta \bar{d} - 2(\Delta s + \Delta \bar{s}) = 0.31 \pm 0.08 \pm 0.15 \ ,$$

niet overeen met de voorspelling uit $SU(3)$ flavor symmetrie analyse. Daarentegen is de LO analyse van Glück *et al.* [149], welke gebruik maakt van inclusieve data en een gebroken lichte "sea" symmetrie (het "valentie" scenario), beter in overeenstemming met de verkregen resultaten.

Voorspellingen uit berekeningen met Lattice QCD in de 'quenched' benadering voor het eerste en tweede moment van het gepolariseerde u-valentie quark liggen hoger dan de in dit proefschrift gevonden resultaten, terwijl de resultaten voor het gepolariseerde d-valentie quark beter overeenstemmen.

Met de integraal van de bij HERMES gemeten spin-structuurfunctie van het neutron, is het eerste moment van de gepolariseerde gluon-structuurfunctie bij $Q^2 = 2.5$ GeV^2 bepaalt in het AB schema: $\Delta g = 1.08 \pm 0.76_{\text{(stat)}} \pm 0.81_{\text{(syst)}}$. Dit resultaat komt goed overeen met de voorspelling van Glück *et al.*

Appendix A
Tables of results for the measured asymmetries

Table A.1: *Averaged values of kinematic quantities for the measured inclusive and semi-inclusive charged hadron asymmetries on the hydrogen target (1996-1997 data).*

Inclusive asymmetry							
Bin	x	Q^2	y	η	γ	D	R
1	0.033	1.210	0.713	0.025	0.057	0.718	0.339
2	0.047	1.451	0.597	0.043	0.075	0.587	0.332
3	0.065	1.724	0.514	0.063	0.095	0.498	0.322
4	0.087	1.991	0.444	0.087	0.121	0.426	0.307
5	0.119	2.309	0.378	0.120	0.155	0.362	0.283
6	0.168	2.675	0.310	0.171	0.207	0.300	0.251
7	0.244	3.091	0.247	0.246	0.285	0.242	0.215
8	0.342	3.795	0.215	0.318	0.361	0.214	0.175
9	0.464	5.206	0.216	0.353	0.404	0.221	0.129

Semi-inclusive asymmetry h^+								
Bin	x	Q^2	y	z	η	γ	D	R
1	0.034	1.205	0.701	0.364	0.027	0.057	0.704	0.339
2	0.048	1.449	0.592	0.392	0.044	0.075	0.581	0.333
3	0.065	1.740	0.522	0.408	0.061	0.094	0.506	0.321
4	0.087	2.136	0.477	0.418	0.080	0.116	0.463	0.304
5	0.118	2.705	0.444	0.418	0.101	0.140	0.437	0.273
6	0.166	3.640	0.425	0.412	0.124	0.169	0.432	0.218
7	0.239	5.165	0.418	0.408	0.149	0.203	0.444	0.151
8	0.338	7.182	0.411	0.401	0.177	0.241	0.451	0.103
9	0.448	9.805	0.422	0.380	0.195	0.271	0.474	0.074

Semi-inclusive asymmetry h^-								
Bin	x	Q^2	y	z	η	γ	D	R
1	0.033	1.202	0.701	0.352	0.027	0.057	0.704	0.339
2	0.047	1.453	0.595	0.378	0.043	0.075	0.584	0.333
3	0.065	1.766	0.529	0.394	0.060	0.094	0.515	0.321
4	0.087	2.153	0.482	0.399	0.079	0.115	0.468	0.304
5	0.118	2.733	0.448	0.401	0.100	0.140	0.441	0.272
6	0.165	3.744	0.438	0.395	0.120	0.167	0.447	0.215
7	0.237	5.187	0.424	0.385	0.146	0.201	0.450	0.151
8	0.338	7.285	0.417	0.378	0.174	0.239	0.459	0.101
9	0.447	9.795	0.422	0.407	0.194	0.270	0.475	0.075

Table A.2: *Measured asymmetries, $A_1^{(h)} = \frac{A_\parallel^{(h)}}{D(1+\eta\gamma)}$, in each x-bin for the hydrogen target for the year 1996.*

Inclusive asymmetry		
Bin	x	$A_1 \pm \sigma_{stat} \pm \sigma_{syst}$
1	0.033	0.107 ± 0.015 ± 0.010
2	0.047	0.094 ± 0.017 ± 0.009
3	0.065	0.120 ± 0.018 ± 0.011
4	0.087	0.175 ± 0.021 ± 0.015
5	0.119	0.236 ± 0.023 ± 0.021
6	0.168	0.255 ± 0.027 ± 0.023
7	0.244	0.373 ± 0.032 ± 0.033
8	0.342	0.380 ± 0.052 ± 0.033
9	0.465	0.534 ± 0.070 ± 0.046

Semi-inclusive asymmetry h^+		
Bin	x	$A_1^{h^+} \pm \sigma_{stat} \pm \sigma_{syst}$
1	0.034	0.104 ± 0.039 ± 0.009
2	0.048	0.113 ± 0.040 ± 0.010
3	0.065	0.134 ± 0.042 ± 0.012
4	0.087	0.143 ± 0.047 ± 0.013
5	0.118	0.247 ± 0.049 ± 0.023
6	0.166	0.295 ± 0.059 ± 0.026
7	0.239	0.556 ± 0.076 ± 0.048
8	0.338	0.547 ± 0.152 ± 0.048
9	0.448	0.742 ± 0.310 ± 0.065

Semi-inclusive asymmetry h^-		
Bin	x	$A_1^{h^-} \pm \sigma_{stat} \pm \sigma_{syst}$
1	0.033	0.125 ± 0.047 ± 0.012
2	0.047	0.128 ± 0.049 ± 0.012
3	0.065	0.045 ± 0.052 ± 0.004
4	0.087	0.163 ± 0.060 ± 0.015
5	0.118	0.223 ± 0.066 ± 0.020
6	0.165	0.220 ± 0.081 ± 0.020
7	0.237	0.288 ± 0.110 ± 0.025
8	0.338	0.476 ± 0.230 ± 0.042
9	0.447	0.602 ± 0.467 ± 0.053

Semi-inclusive asymmetry π^+		
Bin	x	$A_1^{\pi^+} \pm \sigma_{stat} \pm \sigma_{syst}$
1	0.033	0.111 ± 0.053 ± 0.010
2	0.047	0.119 ± 0.058 ± 0.011
3	0.064	0.112 ± 0.063 ± 0.010
4	0.086	0.231 ± 0.070 ± 0.021
5	0.118	0.189 ± 0.077 ± 0.017
6	0.165	0.277 ± 0.097 ± 0.025
7	0.238	0.356 ± 0.136 ± 0.031
8	0.336	0.704 ± 0.278 ± 0.061
9	0.444	1.332 ± 0.677 ± 0.117

Semi-inclusive asymmetry π^-		
Bin	x	$A_1^{\pi^-} \pm \sigma_{stat} \pm \sigma_{syst}$
1	0.033	0.096 ± 0.060 ± 0.009
2	0.047	0.146 ± 0.067 ± 0.014
3	0.064	0.026 ± 0.073 ± 0.003
4	0.086	0.098 ± 0.087 ± 0.009
5	0.118	0.119 ± 0.100 ± 0.011
6	0.165	0.119 ± 0.124 ± 0.011
7	0.236	0.408 ± 0.177 ± 0.035
8	0.335	0.276 ± 0.401 ± 0.024
9	0.444	1.607 ± 0.734 ± 0.141

Table A.3: *Total systematic uncertainties in the inclusive and semi-inclusive charged hadron asymmetries for the year 1996 in each x-bin. The source of the uncertainties are indicated: polarization measurements of target (P_T) and beam (P_B), cross section ratio R, spin structure function g_2, radiative corrections, and the combinded acceptance and smearing corrections.*

Inclusive asymmetry A_1							
Bin	Total	P_T	P_B	R	g_2	Rad. Corr	Smear. Corr.
1	0.0097	0.0081	0.0036	0.0037	0.0005	0.0002	0.0010
2	0.0085	0.0071	0.0032	0.0033	0.0006	0.0001	0.0008
3	0.0107	0.0091	0.0041	0.0036	0.0008	0.0001	0.0011
4	0.0154	0.0133	0.0060	0.0047	0.0010	0.0001	0.0016
5	0.0211	0.0180	0.0080	0.0071	0.0012	0.0001	0.0021
6	0.0230	0.0194	0.0087	0.0085	0.0015	0.0001	0.0020
7	0.0326	0.0284	0.0127	0.0094	0.0020	0.0000	0.0026
8	0.0330	0.0289	0.0129	0.0081	0.0028	0.0000	0.0030
9	0.0464	0.0406	0.0182	0.0122	0.0045	0.0001	0.0027

Semi-inclusive asymmetry $A_1^{h^+}$							
Bin	Total	P_T	P_B	R	g_2	Rad. Corr	Smear. Corr.
1	0.0095	0.0079	0.0035	0.0037	0.0005	0.0000	0.0011
2	0.0103	0.0086	0.0038	0.0040	0.0006	0.0000	0.0012
3	0.0120	0.0102	0.0046	0.0039	0.0008	0.0000	0.0013
4	0.0126	0.0108	0.0049	0.0038	0.0010	0.0000	0.0013
5	0.0226	0.0188	0.0084	0.0090	0.0012	0.0000	0.0017
6	0.0265	0.0224	0.0100	0.0097	0.0015	0.0000	0.0015
7	0.0484	0.0423	0.0189	0.0138	0.0020	0.0000	0.0022
8	0.0477	0.0415	0.0186	0.0138	0.0029	0.0000	0.0022
9	0.0653	0.0564	0.0252	0.0204	0.0048	0.0000	0.0030

Semi-inclusive asymmetry $A_1^{h^-}$							
Bin	Total	P_T	P_B	R	g_2	Rad. Corr	Smear. Corr.
1	0.0118	0.0095	0.0042	0.0044	0.0005	0.0000	0.0034
2	0.0120	0.0097	0.0043	0.0046	0.0006	0.0000	0.0032
3	0.0041	0.0034	0.0015	0.0013	0.0008	0.0000	0.0010
4	0.0146	0.0124	0.0055	0.0044	0.0010	0.0000	0.0029
5	0.0204	0.0169	0.0076	0.0081	0.0012	0.0000	0.0025
6	0.0198	0.0167	0.0075	0.0072	0.0016	0.0000	0.0015
7	0.0251	0.0219	0.0098	0.0071	0.0020	0.0000	0.0014
8	0.0416	0.0362	0.0162	0.0120	0.0030	0.0000	0.0024
9	0.0530	0.0457	0.0205	0.0166	0.0048	0.0000	0.0030

Table A.4: *Contributions to the systematic uncertainties for the semi-inclusive charged pion asymmetries for the year 1996.*

Semi-inclusive asymmetry $A_1^{\pi^+}$							
Bin	Total	P_T	P_B	R	g_2	Rad. Corr	Smear. Corr.
1	0.0101	0.0084	0.0038	0.0038	0.0005	0.0000	0.0012
2	0.0108	0.0090	0.0040	0.0040	0.0007	0.0000	0.0013
3	0.0099	0.0085	0.0038	0.0030	0.0008	0.0000	0.0011
4	0.0205	0.0176	0.0079	0.0066	0.0010	0.0000	0.0021
5	0.0174	0.0144	0.0064	0.0072	0.0013	0.0000	0.0013
6	0.0245	0.0210	0.0094	0.0082	0.0016	0.0000	0.0014
7	0.0310	0.0271	0.0121	0.0085	0.0021	0.0000	0.0014
8	0.0614	0.0535	0.0240	0.0176	0.0030	0.0000	0.0028
9	0.1169	0.1012	0.0453	0.0365	0.0048	0.0000	0.0053

Semi-inclusive asymmetry $A_1^{\pi^-}$							
Bin	Total	P_T	P_B	R	g_2	Rad. Corr	Smear. Corr.
1	0.0090	0.0073	0.0033	0.0033	0.0005	0.0000	0.0026
2	0.0136	0.0111	0.0049	0.0049	0.0006	0.0000	0.0036
3	0.0025	0.0020	0.0009	0.0007	0.0008	0.0000	0.0006
4	0.0089	0.0075	0.0033	0.0028	0.0010	0.0000	0.0018
5	0.0110	0.0090	0.0040	0.0045	0.0013	0.0000	0.0013
6	0.0107	0.0091	0.0041	0.0035	0.0016	0.0000	0.0008
7	0.0355	0.0310	0.0139	0.0098	0.0020	0.0000	0.0020
8	0.0242	0.0209	0.0094	0.0069	0.0030	0.0000	0.0014
9	0.1411	0.1221	0.0546	0.0440	0.0048	0.0000	0.0080

Table A.5: *Measured asymmetries,* $A_1^{(h)} = \frac{A_{\parallel}^{(h)}}{D(1+\eta\gamma)}$*, in each x-bin for the hydrogen target for the year 1997.*

Inclusive asymmetry		
Bin	x	$A_1 \pm \sigma_{stat} \pm \sigma_{syst}$
1	0.034	0.085 ± 0.008 ± 0.007
2	0.048	0.104 ± 0.009 ± 0.008
3	0.065	0.130 ± 0.010 ± 0.010
4	0.087	0.175 ± 0.011 ± 0.013
5	0.119	0.222 ± 0.012 ± 0.017
6	0.168	0.283 ± 0.014 ± 0.022
7	0.245	0.348 ± 0.018 ± 0.026
8	0.342	0.497 ± 0.028 ± 0.036
9	0.465	0.516 ± 0.039 ± 0.037

Semi-inclusive asymmetry h^+		
Bin	x	$A_1^{h^+} \pm \sigma_{stat} \pm \sigma_{syst}$
1	0.034	0.101 ± 0.020 ± 0.008
2	0.048	0.126 ± 0.021 ± 0.010
3	0.065	0.143 ± 0.022 ± 0.011
4	0.087	0.194 ± 0.025 ± 0.014
5	0.118	0.307 ± 0.026 ± 0.024
6	0.166	0.318 ± 0.030 ± 0.024
7	0.238	0.383 ± 0.041 ± 0.028
8	0.338	0.538 ± 0.082 ± 0.039
9	0.446	0.802 ± 0.162 ± 0.059

Semi-inclusive asymmetry h^-		
Bin	x	$A_1^{h^-} \pm \sigma_{stat} \pm \sigma_{syst}$
1	0.033	0.061 ± 0.025 ± 0.005
2	0.047	0.106 ± 0.026 ± 0.009
3	0.064	0.077 ± 0.028 ± 0.006
4	0.087	0.090 ± 0.033 ± 0.007
5	0.118	0.168 ± 0.035 ± 0.013
6	0.165	0.179 ± 0.043 ± 0.014
7	0.238	0.250 ± 0.059 ± 0.018
8	0.339	0.597 ± 0.123 ± 0.044
9	0.445	0.396 ± 0.255 ± 0.030

Semi-inclusive asymmetry π^+		
Bin	x	$A_1^{\pi^+} \pm \sigma_{stat} \pm \sigma_{syst}$
1	0.033	0.054 ± 0.027 ± 0.004
2	0.047	0.091 ± 0.029 ± 0.007
3	0.064	0.122 ± 0.031 ± 0.009
4	0.086	0.209 ± 0.037 ± 0.016
5	0.118	0.323 ± 0.040 ± 0.025
6	0.165	0.344 ± 0.049 ± 0.026
7	0.237	0.269 ± 0.069 ± 0.019
8	0.338	0.611 ± 0.148 ± 0.044
9	0.448	0.812 ± 0.307 ± 0.060

Semi-inclusive asymmetry π^-		
Bin	x	$A_1^{\pi^-} \pm \sigma_{stat} \pm \sigma_{syst}$
1	0.033	0.046 ± 0.030 ± 0.004
2	0.047	0.130 ± 0.034 ± 0.010
3	0.064	0.045 ± 0.037 ± 0.004
4	0.086	0.100 ± 0.045 ± 0.008
5	0.117	0.081 ± 0.050 ± 0.006
6	0.165	0.137 ± 0.062 ± 0.010
7	0.237	0.296 ± 0.092 ± 0.021
8	0.339	0.467 ± 0.205 ± 0.034
9	0.447	−0.187 ± 0.444 ± 0.015

Table A.6: *Total systematic uncertainties in the inclusive and semi-inclusive charged hadron asymmetries for the year 1997 in each x-bin. The breakdown of the uncertainties is indicated: polarization measurements of target (P_T) and beam (P_B), cross section ratio R, spin structure function g_2, radiative corrections, and the combinded acceptance and smearing corrections.*

Inclusive asymmetry A_1							
Bin	Total	P_T	P_B	R	g_2	Rad. Corr	Smear. Corr.
1	0.0065	0.0050	0.0029	0.0029	0.0005	0.0002	0.0008
2	0.0080	0.0061	0.0035	0.0037	0.0006	0.0001	0.0009
3	0.0098	0.0077	0.0044	0.0040	0.0008	0.0001	0.0012
4	0.0129	0.0103	0.0060	0.0047	0.0010	0.0001	0.0016
5	0.0167	0.0131	0.0075	0.0066	0.0012	0.0001	0.0020
6	0.0216	0.0167	0.0096	0.0095	0.0015	0.0001	0.0023
7	0.0255	0.0205	0.0118	0.0087	0.0020	0.0000	0.0024
8	0.0358	0.0293	0.0169	0.0106	0.0028	0.0000	0.0040
9	0.0374	0.0305	0.0176	0.0118	0.0045	0.0001	0.0026

Semi-inclusive asymmetry $A_1^{h^+}$							
Bin	Total	P_T	P_B	R	g_2	Rad. Corr	Smear. Corr.
1	0.0078	0.0059	0.0034	0.0035	0.0005	0.0000	0.0011
2	0.0098	0.0074	0.0043	0.0045	0.0006	0.0000	0.0014
3	0.0107	0.0084	0.0049	0.0042	0.0008	0.0000	0.0014
4	0.0144	0.0115	0.0066	0.0052	0.0010	0.0000	0.0017
5	0.0238	0.0181	0.0104	0.0111	0.0013	0.0000	0.0021
6	0.0242	0.0188	0.0108	0.0104	0.0015	0.0000	0.0016
7	0.0279	0.0226	0.0130	0.0095	0.0021	0.0000	0.0015
8	0.0392	0.0317	0.0183	0.0136	0.0030	0.0000	0.0022
9	0.0592	0.0473	0.0273	0.0220	0.0051	0.0000	0.0032

Semi-inclusive asymmetry $A_1^{h^-}$							
Bin	Total	P_T	P_B	R	g_2	Rad. Corr	Smear. Corr.
1	0.0050	0.0036	0.0021	0.0021	0.0005	0.0000	0.0016
2	0.0086	0.0062	0.0036	0.0038	0.0006	0.0000	0.0026
3	0.0060	0.0045	0.0026	0.0022	0.0008	0.0000	0.0017
4	0.0069	0.0053	0.0031	0.0024	0.0010	0.0000	0.0016
5	0.0131	0.0099	0.0057	0.0061	0.0012	0.0000	0.0018
6	0.0137	0.0106	0.0061	0.0059	0.0016	0.0000	0.0013
7	0.0183	0.0147	0.0085	0.0062	0.0021	0.0000	0.0012
8	0.0436	0.0352	0.0203	0.0151	0.0030	0.0000	0.0030
9	0.0295	0.0234	0.0135	0.0109	0.0050	0.0000	0.0020

Table A.7: *Contributions to the systematic uncertainties for the semi-inclusive charged pion asymmetries for the year 1997.*

Semi-inclusive asymmetry $A_1^{\pi^+}$							
Bin	Total	P_T	P_B	R	g_2	Rad. Corr	Smear. Corr.
1	0.0042	0.0032	0.0018	0.0018	0.0005	0.0000	0.0006
2	0.0070	0.0054	0.0031	0.0031	0.0006	0.0000	0.0010
3	0.0091	0.0072	0.0042	0.0032	0.0008	0.0000	0.0012
4	0.0156	0.0124	0.0071	0.0060	0.0010	0.0000	0.0019
5	0.0253	0.0190	0.0110	0.0123	0.0013	0.0000	0.0023
6	0.0257	0.0203	0.0117	0.0102	0.0016	0.0000	0.0017
7	0.0195	0.0158	0.0091	0.0065	0.0021	0.0000	0.0011
8	0.0445	0.0361	0.0208	0.0153	0.0031	0.0000	0.0024
9	0.0599	0.0479	0.0276	0.0223	0.0052	0.0000	0.0032

Semi-inclusive asymmetry $A_1^{\pi^-}$							
Bin	Total	P_T	P_B	R	g_2	Rad. Corr	Smear. Corr.
1	0.0037	0.0027	0.0016	0.0016	0.0005	0.0000	0.0012
2	0.0104	0.0076	0.0044	0.0043	0.0006	0.0000	0.0032
3	0.0035	0.0026	0.0015	0.0012	0.0008	0.0000	0.0010
4	0.0077	0.0059	0.0034	0.0029	0.0010	0.0000	0.0018
5	0.0065	0.0048	0.0028	0.0031	0.0013	0.0000	0.0009
6	0.0103	0.0081	0.0047	0.0040	0.0016	0.0000	0.0010
7	0.0215	0.0175	0.0101	0.0071	0.0021	0.0000	0.0015
8	0.0341	0.0276	0.0159	0.0117	0.0031	0.0000	0.0023
9	0.0147	0.0110	0.0063	0.0051	0.0052	0.0000	0.0009

Table A.8: *Averaged values of kinematic quantities for the measured inclusive and semi-inclusive charged hadron asymmetries on the deuterium target (1998-2000 data).*

Inclusive asymmetry							
Bin	x	Q^2	y	η	γ	D	R
1	0.034	1.206	0.706	0.027	0.057	0.703	0.339
2	0.048	1.448	0.591	0.044	0.075	0.580	0.333
3	0.065	1.731	0.525	0.061	0.094	0.501	0.321
4	0.087	2.017	0.459	0.080	0.115	0.424	0.304
5	0.118	2.332	0.379	0.110	0.143	0.357	0.272
6	0.165	2.704	0.310	0.152	0.192	0.293	0.216
7	0.242	3.124	0.250	0.221	0.257	0.236	0.151
8	0.342	3.819	0.214	0.287	0.326	0.208	0.102
9	0.465	5.226	0.217	0.322	0.381	0.218	0.075

Semi-inclusive asymmetry h^+								
Bin	x	Q^2	y	z	η	γ	D	R
1	0.034	1.206	0.701	0.364	0.027	0.057	0.703	0.339
2	0.048	1.448	0.591	0.391	0.044	0.075	0.580	0.333
3	0.065	1.751	0.525	0.406	0.061	0.094	0.510	0.321
4	0.087	2.147	0.479	0.415	0.080	0.115	0.465	0.304
5	0.118	2.732	0.449	0.418	0.100	0.140	0.442	0.272
6	0.165	3.704	0.433	0.416	0.122	0.167	0.442	0.216
7	0.238	5.174	0.420	0.411	0.148	0.202	0.446	0.151
8	0.338	7.229	0.413	0.405	0.176	0.240	0.453	0.102
9	0.445	9.616	0.417	0.402	0.197	0.272	0.468	0.075

Semi-inclusive asymmetry h^-								
Bin	x	Q^2	y	z	η	γ	D	R
1	0.033	1.206	0.703	0.355	0.026	0.057	0.706	0.339
2	0.047	1.452	0.593	0.380	0.043	0.075	0.583	0.333
3	0.065	1.761	0.529	0.397	0.060	0.094	0.514	0.321
4	0.087	2.173	0.486	0.404	0.078	0.114	0.473	0.303
5	0.118	2.766	0.455	0.406	0.098	0.139	0.449	0.271
6	0.165	3.733	0.438	0.402	0.120	0.166	0.447	0.215
7	0.237	5.224	0.425	0.395	0.146	0.200	0.453	0.150
8	0.338	7.257	0.416	0.386	0.175	0.239	0.457	0.102
9	0.445	9.629	0.418	0.388	0.196	0.271	0.469	0.075

Table A.9: *Measured asymmetries,* $A_1^{(h)} = \frac{A_{\parallel}^{(h)}}{D(1+\eta\gamma)}$*, in each* x*-bin for a deuteron target for the year 1998.*

Inclusive asymmetry		
Bin	x	$A_1 \pm \sigma_{stat} \pm \sigma_{syst}$
1	0.034	0.017 ± 0.012 ± 0.002
2	0.048	0.015 ± 0.013 ± 0.002
3	0.065	0.027 ± 0.014 ± 0.003
4	0.087	0.046 ± 0.016 ± 0.005
5	0.118	0.101 ± 0.018 ± 0.010
6	0.165	0.151 ± 0.021 ± 0.014
7	0.238	0.196 ± 0.027 ± 0.018
8	0.337	0.337 ± 0.047 ± 0.031
9	0.444	0.252 ± 0.065 ± 0.026

Semi-inclusive asymmetry h^+		
Bin	x	$A_1^{h^+} \pm \sigma_{stat} \pm \sigma_{syst}$
1	0.034	−0.002 ± 0.029 ± 0.001
2	0.048	0.043 ± 0.030 ± 0.004
3	0.065	−0.003 ± 0.031 ± 0.002
4	0.087	0.017 ± 0.036 ± 0.003
5	0.118	0.113 ± 0.038 ± 0.011
6	0.165	0.145 ± 0.046 ± 0.014
7	0.238	0.305 ± 0.061 ± 0.028
8	0.337	0.066 ± 0.127 ± 0.009
9	0.447	0.434 ± 0.245 ± 0.041

Semi-inclusive asymmetry h^-		
Bin	x	$A_1^{h^-} \pm \sigma_{stat} \pm \sigma_{syst}$
1	0.033	0.022 ± 0.034 ± 0.002
2	0.047	−0.023 ± 0.035 ± 0.003
3	0.065	−0.019 ± 0.038 ± 0.002
4	0.087	−0.012 ± 0.045 ± 0.002
5	0.118	0.058 ± 0.047 ± 0.006
6	0.165	0.074 ± 0.060 ± 0.008
7	0.238	0.125 ± 0.083 ± 0.012
8	0.337	−0.018 ± 0.174 ± 0.007
9	0.446	0.291 ± 0.334 ± 0.029

Semi-inclusive asymmetry π^+		
Bin	x	$A_1^{\pi^+} \pm \sigma_{stat} \pm \sigma_{syst}$
1	0.033	−0.043 ± 0.034 ± 0.004
2	0.047	0.037 ± 0.036 ± 0.004
3	0.065	−0.007 ± 0.038 ± 0.002
4	0.087	−0.018 ± 0.044 ± 0.003
5	0.118	0.098 ± 0.046 ± 0.010
6	0.165	0.089 ± 0.057 ± 0.009
7	0.238	0.227 ± 0.079 ± 0.021
8	0.337	0.039 ± 0.162 ± 0.008
9	0.448	0.468 ± 0.327 ± 0.045

Semi-inclusive asymmetry π^-		
Bin	x	$A_1^{\pi^-} \pm \sigma_{stat} \pm \sigma_{syst}$
1	0.033	0.021 ± 0.036 ± 0.002
2	0.047	−0.022 ± 0.039 ± 0.002
3	0.064	−0.022 ± 0.042 ± 0.003
4	0.087	−0.001 ± 0.049 ± 0.002
5	0.118	0.026 ± 0.053 ± 0.004
6	0.165	0.028 ± 0.067 ± 0.004
7	0.238	0.130 ± 0.092 ± 0.013
8	0.337	−0.035 ± 0.196 ± 0.007
9	0.448	0.281 ± 0.370 ± 0.029

Semi-inclusive asymmetry K^+		
Bin	x	$A_1^{K^+} \pm \sigma_{stat} \pm \sigma_{syst}$
1	0.033	0.083 ± 0.087 ± 0.008
2	0.048	0.034 ± 0.095 ± 0.004
3	0.064	0.046 ± 0.098 ± 0.004
4	0.087	0.314 ± 0.114 ± 0.029
5	0.118	−0.046 ± 0.119 ± 0.005
6	0.165	0.237 ± 0.143 ± 0.022
7	0.238	0.350 ± 0.202 ± 0.033
8	0.334	0.514 ± 0.424 ± 0.048
9	0.455	1.495 ± 0.838 ± 0.140

Semi-inclusive asymmetry K^-		
Bin	x	$A_1^{K^-} \pm \sigma_{stat} \pm \sigma_{syst}$
1	0.033	−0.168 ± 0.122 ± 0.016
2	0.047	−0.080 ± 0.133 ± 0.008
3	0.064	0.073 ± 0.142 ± 0.007
4	0.086	−0.103 ± 0.172 ± 0.010
5	0.117	0.184 ± 0.190 ± 0.018
6	0.164	0.234 ± 0.248 ± 0.022
7	0.234	−0.050 ± 0.381 ± 0.006
8	0.326	−1.071 ± 0.920 ± 0.099
9	0.438	1.168 ± 1.412 ± 0.196

Table A.10: *Total systematic uncertainties in the inclusive and semi-inclusive charged hadron asymmetries for the year 1998 in each x-bin. The separate contributions of the systematic uncertainty are indicated: polarization measurements of target (P_T) and beam (P_B), cross section ratio R, spin structure function g_2, radiative corrections, smearing corrections and RICH PID.*

Inclusive asymmetry A_1							
Bin	Total	P_T	P_B	R	g_2	Rad. Corr	Smear. Corr.
1	0.0018	0.0013	0.0006	0.0006	0.0009	0.0003	0.0001
2	0.0019	0.0013	0.0005	0.0006	0.0012	0.0002	0.0001
3	0.0029	0.0022	0.0009	0.0008	0.0015	0.0002	0.0002
4	0.0046	0.0037	0.0016	0.0012	0.0020	0.0001	0.0004
5	0.0098	0.0081	0.0034	0.0036	0.0024	0.0001	0.0009
6	0.0144	0.0121	0.0051	0.0050	0.0032	0.0002	0.0012
7	0.0184	0.0157	0.0167	0.0049	0.0044	0.0002	0.0014
8	0.0313	0.0269	0.0115	0.0085	0.0066	0.0001	0.0027
9	0.0259	0.0202	0.0086	0.0069	0.0118	0.0001	0.0013

Semi-inclusive asymmetry $A_1^{h^+}$							
Bin	Total	P_T	P_B	R	g_2	Rad. Corr	Smear. Corr.
1	0.0010	0.0002	0.0001	0.0001	0.0009	0.0000	0.0000
2	0.0042	0.0034	0.0015	0.0015	0.0012	0.0000	0.0004
3	0.0016	0.0002	0.0001	0.0001	0.0015	0.0000	0.0000
4	0.0025	0.0013	0.0006	0.0005	0.0020	0.0000	0.0002
5	0.0109	0.0091	0.0039	0.0041	0.0024	0.0000	0.0008
6	0.0138	0.0116	0.0049	0.0048	0.0032	0.0000	0.0007
7	0.0279	0.0244	0.0104	0.0076	0.0044	0.0000	0.0012
8	0.0089	0.0053	0.0023	0.0017	0.0063	0.0000	0.0003
9	0.0414	0.0347	0.0148	0.0119	0.0120	0.0000	0.0017

Semi-inclusive asymmetry $A_1^{h^-}$							
Bin	Total	P_T	P_B	R	g_2	Rad. Corr	Smear. Corr.
1	0.0023	0.0018	0.0007	0.0008	0.0009	0.0000	0.0006
2	0.0025	0.0018	0.0008	0.0008	0.0012	0.0000	0.0006
3	0.0024	0.0015	0.0006	0.0005	0.0016	0.0000	0.0004
4	0.0022	0.0010	0.0004	0.0003	0.0019	0.0000	0.0002
5	0.0061	0.0047	0.0020	0.0021	0.0025	0.0000	0.0006
6	0.0076	0.0060	0.0025	0.0024	0.0032	0.0000	0.0005
7	0.0122	0.0100	0.0043	0.0031	0.0044	0.0000	0.0006
8	0.0068	0.0015	0.0006	0.0005	0.0066	0.0000	0.0001
9	0.0291	0.0233	0.0099	0.0080	0.0119	0.0000	0.0014

Table A.11: *Contributions to the systematic uncertainties for the semi-inclusive charged pion and kaon asymmetries for the year 1998.*

Semi-inclusive asymmetry $A_1^{\pi^+}$								
Bin	Total	P_T	P_B	R	g_2	Rad. Corr	Smear. Corr.	RICH PID
1	0.0042	0.0034	0.0015	0.0015	0.0009	0.0000	0.0005	0.0009
2	0.0037	0.0030	0.0013	0.0013	0.0012	0.0000	0.0004	0.0007
3	0.0016	0.0006	0.0002	0.0002	0.0015	0.0000	0.0001	0.0001
4	0.0026	0.0014	0.0006	0.0005	0.0020	0.0000	0.0002	0.0004
5	0.0098	0.0078	0.0033	0.0036	0.0025	0.0000	0.0007	0.0020
6	0.0091	0.0071	0.0030	0.0029	0.0033	0.0000	0.0004	0.0018
7	0.0214	0.0181	0.0077	0.0056	0.0044	0.0000	0.0009	0.0045
8	0.0077	0.0032	0.0013	0.0010	0.0068	0.0000	0.0002	0.0008
9	0.0454	0.0375	0.0159	0.0129	0.0121	0.0000	0.0019	0.0094

Semi-inclusive asymmetry $A_1^{\pi^-}$								
Bin	Total	P_T	P_B	R	g_2	Rad. Corr	Smear. Corr.	RICH PID
1	0.0023	0.0017	0.0007	0.0007	0.0009	0.0000	0.0006	0.0004
2	0.0025	0.0018	0.0007	0.0008	0.0012	0.0000	0.0005	0.0004
3	0.0026	0.0018	0.0007	0.0006	0.0015	0.0000	0.0005	0.0004
4	0.0019	0.0001	0.0000	0.0000	0.0019	0.0000	0.0001	0.0000
5	0.0035	0.0021	0.0009	0.0010	0.0024	0.0000	0.0003	0.0005
6	0.0041	0.0022	0.0009	0.0009	0.0032	0.0000	0.0002	0.0005
7	0.0129	0.0104	0.0044	0.0032	0.0044	0.0000	0.0007	0.0026
8	0.0075	0.0028	0.0012	0.0009	0.0067	0.0000	0.0002	0.0007
9	0.0288	0.0225	0.0095	0.0077	0.0119	0.0000	0.0014	0.0056

Semi-inclusive asymmetry $A_1^{K^+}$								
Bin	Total	P_T	P_B	R	g_2	Rad. Corr	Smear. Corr.	RICH PID
1	0.0080	0.0066	0.0028	0.0029	0.0009	0.0000	0.0009	0.0017
2	0.0035	0.0027	0.0012	0.0011	0.0013	0.0000	0.0004	0.0007
3	0.0046	0.0037	0.0016	0.0012	0.0016	0.0000	0.0005	0.0009
4	0.0296	0.0251	0.0107	0.0090	0.0020	0.0000	0.0028	0.0063
5	0.0052	0.0037	0.0016	0.0018	0.0025	0.0000	0.0003	0.0009
6	0.0226	0.0190	0.0081	0.0071	0.0033	0.0000	0.0012	0.0047
7	0.0327	0.0280	0.0119	0.0084	0.0045	0.0000	0.0014	0.0070
8	0.0481	0.0411	0.0175	0.0129	0.0067	0.0000	0.0021	0.0103
9	0.1403	0.1196	0.0508	0.0414	0.0124	0.0000	0.0060	0.0299

Semi-inclusive asymmetry $A_1^{K^-}$								
Bin	Total	P_T	P_B	R	g_2	Rad. Corr	Smear. Corr.	RICH PID
1	0.0167	0.0134	0.0057	0.0056	0.0009	0.0000	0.0045	0.0034
2	0.0079	0.0064	0.0027	0.0026	0.0012	0.0000	0.0020	0.0016
3	0.0071	0.0058	0.0025	0.0018	0.0016	0.0000	0.0016	0.0015
4	0.0101	0.0083	0.0035	0.0030	0.0019	0.0000	0.0019	0.0021
5	0.0181	0.0147	0.0063	0.0070	0.0025	0.0000	0.0020	0.0037
6	0.0222	0.0187	0.0079	0.0067	0.0033	0.0000	0.0016	0.0047
7	0.0064	0.0040	0.0017	0.0012	0.0044	0.0000	0.0002	0.0010
8	0.0995	0.0857	0.0364	0.0265	0.0065	0.0000	0.0053	0.0214
9	0.1250	0.0977	0.0290	0.0332	0.0118	0.0000	0.0214	0.0594

Table A.12: *Measured asymmetries, $A_1^{(h)} = \frac{A_\parallel^{(h)}}{D(1+\eta\gamma)}$, in each x-bin for the year 1999 on the deuterium target.*

Inclusive asymmetry		
Bin	x	$A_1 \pm \sigma_{stat} \pm \sigma_{syst}$
1	0.034	0.017 ± 0.010 ± 0.002
2	0.048	0.013 ± 0.011 ± 0.002
3	0.065	0.008 ± 0.012 ± 0.002
4	0.087	0.043 ± 0.014 ± 0.004
5	0.118	0.085 ± 0.015 ± 0.008
6	0.165	0.122 ± 0.018 ± 0.011
7	0.238	0.188 ± 0.023 ± 0.017
8	0.337	0.329 ± 0.039 ± 0.029
9	0.444	0.355 ± 0.055 ± 0.033

Semi-inclusive asymmetry h^+		
Bin	x	$A_1^{h^+} \pm \sigma_{stat} \pm \sigma_{syst}$
1	0.034	0.016 ± 0.026 ± 0.002
2	0.048	−0.029 ± 0.027 ± 0.003
3	0.065	−0.016 ± 0.028 ± 0.002
4	0.087	0.045 ± 0.032 ± 0.004
5	0.118	0.097 ± 0.034 ± 0.009
6	0.165	0.104 ± 0.041 ± 0.010
7	0.238	0.205 ± 0.055 ± 0.018
8	0.337	0.306 ± 0.113 ± 0.027
9	0.444	0.272 ± 0.227 ± 0.026

Semi-inclusive asymmetry h^-		
Bin	x	$A_1^{h^-} \pm \sigma_{stat} \pm \sigma_{syst}$
1	0.033	−0.033 ± 0.030 ± 0.003
2	0.047	−0.018 ± 0.031 ± 0.002
3	0.065	0.003 ± 0.034 ± 0.002
4	0.087	0.057 ± 0.039 ± 0.005
5	0.118	0.082 ± 0.042 ± 0.008
6	0.165	0.062 ± 0.053 ± 0.006
7	0.238	0.173 ± 0.074 ± 0.015
8	0.339	0.251 ± 0.155 ± 0.023
9	0.444	0.120 ± 0.325 ± 0.016

Semi-inclusive asymmetry π^+		
Bin	x	$A_1^{\pi^+} \pm \sigma_{stat} \pm \sigma_{syst}$
1	0.033	0.012 ± 0.031 ± 0.001
2	0.047	−0.048 ± 0.033 ± 0.004
3	0.064	−0.019 ± 0.036 ± 0.002
4	0.087	0.010 ± 0.042 ± 0.002
5	0.117	0.168 ± 0.045 ± 0.016
6	0.165	0.154 ± 0.057 ± 0.014
7	0.238	0.148 ± 0.081 ± 0.014
8	0.337	0.339 ± 0.186 ± 0.031
9	0.444	0.118 ± 0.386 ± 0.016

Semi-inclusive asymmetry π^-		
Bin	x	$A_1^{\pi^-} \pm \sigma_{stat} \pm \sigma_{syst}$
1	0.033	−0.024 ± 0.033 ± 0.002
2	0.047	−0.043 ± 0.036 ± 0.004
3	0.064	0.038 ± 0.040 ± 0.004
4	0.086	0.045 ± 0.047 ± 0.004
5	0.117	0.037 ± 0.052 ± 0.004
6	0.165	0.005 ± 0.067 ± 0.003
7	0.237	0.178 ± 0.099 ± 0.016
8	0.338	−0.020 ± 0.226 ± 0.007
9	0.450	−0.392 ± 0.467 ± 0.037

Semi-inclusive asymmetry K^+		
Bin	x	$A_1^{K^+} \pm \sigma_{stat} \pm \sigma_{syst}$
1	0.034	−0.035 ± 0.079 ± 0.003
2	0.048	−0.019 ± 0.081 ± 0.002
3	0.064	0.148 ± 0.085 ± 0.013
4	0.086	0.073 ± 0.096 ± 0.007
5	0.118	0.024 ± 0.102 ± 0.003
6	0.165	0.254 ± 0.125 ± 0.023
7	0.237	0.301 ± 0.170 ± 0.027
8	0.333	0.299 ± 0.389 ± 0.027
9	0.434	1.540 ± 0.688 ± 0.137

Semi-inclusive asymmetry K^-		
Bin	x	$A_1^{K^-} \pm \sigma_{stat} \pm \sigma_{syst}$
1	0.033	−0.097 ± 0.108 ± 0.009
2	0.047	0.016 ± 0.120 ± 0.002
3	0.064	−0.173 ± 0.133 ± 0.015
4	0.086	−0.016 ± 0.150 ± 0.003
5	0.118	0.046 ± 0.167 ± 0.005
6	0.165	0.154 ± 0.225 ± 0.014
7	0.234	0.212 ± 0.331 ± 0.019
8	0.335	0.506 ± 0.719 ± 0.045
9	0.436	−0.093 ± 2.224 ± 0.014

Table A.13: *Total systematic uncertainties in the inclusive and semi-inclusive charged hadron asymmetries for the year 1999 in each x-bin. The various uncertainties are indicated: polarization measurements of target (P_T) and beam (P_B), cross section ratio R, spin structure function g_2, radiative corrections, smearing corrections and the RICH PID.*

Inclusive asymmetry A_1							
Bin	Total	P_T	P_B	R	g_2	Rad. Corr	Smear. Corr.
1	0.0018	0.0014	0.0003	0.0006	0.0009	0.0003	0.0002
2	0.0017	0.0011	0.0002	0.0005	0.0012	0.0002	0.0001
3	0.0017	0.0006	0.0001	0.0002	0.0015	0.0002	0.0001
4	0.0042	0.0035	0.0008	0.0012	0.0019	0.0001	0.0004
5	0.0081	0.0068	0.0015	0.0031	0.0024	0.0001	0.0008
6	0.0113	0.0098	0.0022	0.0040	0.0032	0.0002	0.0010
7	0.0168	0.0150	0.0034	0.0047	0.0044	0.0002	0.0013
8	0.0292	0.0264	0.0059	0.0083	0.0068	0.0001	0.0026
9	0.0329	0.0284	0.0064	0.0097	0.0119	0.0001	0.0018

Semi-inclusive asymmetry $A_1^{h^+}$							
Bin	Total	P_T	P_B	R	g_2	Rad. Corr	Smear. Corr.
1	0.0017	0.0013	0.0003	0.0006	0.0009	0.0000	0.0002
2	0.0029	0.0023	0.0005	0.0010	0.0012	0.0000	0.0003
3	0.0021	0.0013	0.0003	0.0005	0.0015	0.0000	0.0002
4	0.0043	0.0036	0.0008	0.0012	0.0019	0.0000	0.0004
5	0.0090	0.0077	0.0017	0.0035	0.0024	0.0000	0.0007
6	0.0097	0.0083	0.0019	0.0034	0.0032	0.0000	0.0005
7	0.0181	0.0164	0.0037	0.0051	0.0044	0.0000	0.0008
8	0.0271	0.0245	0.0055	0.0077	0.0066	0.0000	0.0012
9	0.0263	0.0217	0.0049	0.0074	0.0117	0.0000	0.0011

Semi-inclusive asymmetry $A_1^{h^-}$							
Bin	Total	P_T	P_B	R	g_2	Rad. Corr	Smear. Corr.
1	0.0032	0.0026	0.0006	0.0012	0.0009	0.0000	0.0009
2	0.0021	0.0014	0.0003	0.0006	0.0012	0.0000	0.0004
3	0.0016	0.0002	0.0001	0.0001	0.0016	0.0000	0.0001
4	0.0053	0.0045	0.0010	0.0015	0.0019	0.0000	0.0010
5	0.0078	0.0066	0.0015	0.0030	0.0025	0.0000	0.0009
6	0.0063	0.0049	0.0011	0.0020	0.0032	0.0000	0.0004
7	0.0155	0.0138	0.0031	0.0043	0.0045	0.0000	0.0009
8	0.0226	0.0201	0.0045	0.0063	0.0067	0.0000	0.0012
9	0.0156	0.0096	0.0022	0.0033	0.0116	0.0000	0.0006

Table A.14: *Contributions to the systematic uncertainties for the semi-inclusive charged pion asymmetries for the year 1999.*

Semi-inclusive asymmetry $A_1^{\pi^+}$								
Bin	Total	P_T	P_B	R	g_2	Rad. Corr	Smear. Corr.	RICH PID
1	0.0015	0.0010	0.0002	0.0004	0.0009	0.0000	0.0001	0.0002
2	0.0046	0.0038	0.0009	0.0016	0.0012	0.0000	0.0005	0.0010
3	0.0023	0.0015	0.0003	0.0005	0.0015	0.0000	0.0002	0.0004
4	0.0022	0.0008	0.0002	0.0003	0.0020	0.0000	0.0001	0.0002
5	0.0158	0.0135	0.0030	0.0064	0.0024	0.0000	0.0011	0.0034
6	0.0142	0.0124	0.0028	0.0046	0.0032	0.0000	0.0008	0.0031
7	0.0138	0.0119	0.0027	0.0036	0.0044	0.0000	0.0006	0.0030
8	0.0306	0.0271	0.0061	0.0085	0.0068	0.0000	0.0013	0.0068
9	0.0160	0.0095	0.0021	0.0032	0.0120	0.0000	0.0005	0.0024

Semi-inclusive asymmetry $A_1^{\pi^-}$								
Bin	Total	P_T	P_B	R	g_2	Rad. Corr	Smear. Corr.	RICH PID
1	0.0025	0.0019	0.0004	0.0008	0.0010	0.0000	0.0006	0.0005
2	0.0041	0.0034	0.0008	0.0014	0.0012	0.0000	0.0011	0.0009
3	0.0038	0.0030	0.0007	0.0010	0.0015	0.0000	0.0008	0.0008
4	0.0045	0.0036	0.0008	0.0013	0.0020	0.0000	0.0008	0.0009
5	0.0042	0.0029	0.0007	0.0014	0.0025	0.0000	0.0004	0.0007
6	0.0033	0.0004	0.0001	0.0001	0.0032	0.0000	0.0000	0.0001
7	0.0163	0.0142	0.0032	0.0043	0.0045	0.0000	0.0009	0.0036
8	0.0071	0.0016	0.0004	0.0005	0.0068	0.0000	0.0001	0.0004
9	0.0370	0.0314	0.0071	0.0108	0.0123	0.0000	0.0020	0.0078

Semi-inclusive asymmetry $A_1^{K^+}$								
Bin	Total	P_T	P_B	R	g_2	Rad. Corr	Smear. Corr.	RICH PID
1	0.0034	0.0028	0.0006	0.0012	0.0010	0.0000	0.0004	0.0007
2	0.0021	0.0015	0.0003	0.0006	0.0012	0.0000	0.0002	0.0004
3	0.0133	0.0119	0.0027	0.0039	0.0016	0.0000	0.0015	0.0030
4	0.0069	0.0059	0.0013	0.0021	0.0020	0.0000	0.0007	0.0015
5	0.0034	0.0019	0.0004	0.0009	0.0025	0.0000	0.0002	0.0005
6	0.0230	0.0203	0.0046	0.0076	0.0033	0.0000	0.0013	0.0051
7	0.0268	0.0241	0.0054	0.0072	0.0045	0.0000	0.0012	0.0060
8	0.0272	0.0239	0.0054	0.0075	0.0066	0.0000	0.0012	0.0060
9	0.1371	0.1232	0.0277	0.0419	0.0114	0.0000	0.0006	0.0308

Semi-inclusive asymmetry $A_1^{K^-}$								
Bin	Total	P_T	P_B	R	g_2	Rad. Corr	Smear. Corr.	RICH PID
1	0.0093	0.0077	0.0017	0.0033	0.0010	0.0000	0.0026	0.0019
2	0.0020	0.0013	0.0003	0.0005	0.0012	0.0000	0.0004	0.0003
3	0.0158	0.0139	0.0031	0.0045	0.0015	0.0000	0.0038	0.0035
4	0.0025	0.0013	0.0003	0.0005	0.0020	0.0000	0.0003	0.0003
5	0.0050	0.0037	0.0008	0.0018	0.0026	0.0000	0.0005	0.0009
6	0.0141	0.0123	0.0028	0.0044	0.0033	0.0000	0.0011	0.0031
7	0.0192	0.0170	0.0038	0.0050	0.0045	0.0000	0.0011	0.0042
8	0.0451	0.0404	0.0091	0.0127	0.0067	0.0000	0.0025	0.0101
9	0.0143	0.0074	0.0017	0.0025	0.0117	0.0000	0.0005	0.0019

Table A.15: *Measured asymmetries, $A_1^{(h)} = \frac{A_\parallel^{(h)}}{D(1+\eta\gamma)}$, in each x-bin for the year 2000 on the deuterium target.*

Inclusive asymmetry		
Bin	x	$A_1 \pm \sigma_{stat} \pm \sigma_{syst}$
1	0.034	0.017 ± 0.004 ± 0.001
2	0.048	0.025 ± 0.005 ± 0.002
3	0.065	0.036 ± 0.005 ± 0.003
4	0.087	0.054 ± 0.006 ± 0.004
5	0.118	0.077 ± 0.006 ± 0.005
6	0.165	0.118 ± 0.008 ± 0.007
7	0.244	0.168 ± 0.009 ± 0.010
8	0.342	0.257 ± 0.015 ± 0.014
9	0.464	0.317 ± 0.021 ± 0.019

Semi-inclusive asymmetry h^+		
Bin	x	$A_1^{h^+} \pm \sigma_{stat} \pm \sigma_{syst}$
1	0.034	0.004 ± 0.011 ± 0.001
2	0.048	0.028 ± 0.011 ± 0.002
3	0.065	0.057 ± 0.011 ± 0.003
4	0.087	0.054 ± 0.013 ± 0.003
5	0.118	0.066 ± 0.014 ± 0.004
6	0.165	0.121 ± 0.017 ± 0.007
7	0.238	0.149 ± 0.022 ± 0.009
8	0.338	0.276 ± 0.046 ± 0.016
9	0.445	0.354 ± 0.094 ± 0.022

Semi-inclusive asymmetry h^-		
Bin	x	$A_1^{h^-} \pm \sigma_{stat} \pm \sigma_{syst}$
1	0.033	−0.018 ± 0.012 ± 0.001
2	0.047	0.014 ± 0.013 ± 0.002
3	0.065	0.036 ± 0.014 ± 0.003
4	0.087	0.047 ± 0.016 ± 0.003
5	0.118	0.070 ± 0.017 ± 0.005
6	0.165	0.121 ± 0.022 ± 0.007
7	0.237	0.201 ± 0.030 ± 0.011
8	0.338	0.280 ± 0.064 ± 0.016
9	0.445	0.321 ± 0.134 ± 0.020

Semi-inclusive asymmetry π^+		
Bin	x	$A_1^{\pi^+} \pm \sigma_{stat} \pm \sigma_{syst}$
1	0.033	−0.006 ± 0.013 ± 0.001
2	0.047	0.027 ± 0.014 ± 0.002
3	0.064	0.029 ± 0.015 ± 0.002
4	0.087	0.039 ± 0.017 ± 0.003
5	0.118	0.088 ± 0.019 ± 0.006
6	0.165	0.121 ± 0.024 ± 0.008
7	0.238	0.133 ± 0.033 ± 0.009
8	0.338	0.352 ± 0.073 ± 0.020
9	0.446	0.227 ± 0.159 ± 0.018

Semi-inclusive asymmetry π^-		
Bin	x	$A_1^{\pi^-} \pm \sigma_{stat} \pm \sigma_{syst}$
1	0.033	−0.017 ± 0.014 ± 0.001
2	0.047	−0.003 ± 0.015 ± 0.001
3	0.064	0.037 ± 0.016 ± 0.003
4	0.086	0.045 ± 0.019 ± 0.003
5	0.117	0.085 ± 0.022 ± 0.006
6	0.165	0.099 ± 0.028 ± 0.007
7	0.237	0.198 ± 0.040 ± 0.012
8	0.337	0.367 ± 0.092 ± 0.021
9	0.448	0.200 ± 0.195 ± 0.017

Semi-inclusive asymmetry K^+		
Bin	x	$A_1^{K^+} \pm \sigma_{stat} \pm \sigma_{syst}$
1	0.033	0.030 ± 0.032 ± 0.002
2	0.047	0.067 ± 0.034 ± 0.004
3	0.064	0.120 ± 0.035 ± 0.007
4	0.087	0.069 ± 0.040 ± 0.004
5	0.118	0.077 ± 0.042 ± 0.005
6	0.165	0.079 ± 0.050 ± 0.005
7	0.238	0.104 ± 0.070 ± 0.007
8	0.337	0.347 ± 0.152 ± 0.020
9	0.449	0.315 ± 0.334 ± 0.021

Semi-inclusive asymmetry K^-		
Bin	x	$A_1^{K^-} \pm \sigma_{stat} \pm \sigma_{syst}$
1	0.033	−0.033 ± 0.045 ± 0.002
2	0.047	0.038 ± 0.049 ± 0.003
3	0.064	−0.002 ± 0.053 ± 0.002
4	0.086	0.036 ± 0.062 ± 0.003
5	0.118	0.040 ± 0.069 ± 0.004
6	0.165	0.062 ± 0.088 ± 0.005
7	0.237	0.120 ± 0.137 ± 0.008
8	0.338	−0.385 ± 0.324 ± 0.022
9	0.445	1.315 ± 0.689 ± 0.074

Table A.16: *Total systematic uncertainties on the inclusive and semi-inclusive charged hadron asymmetries for the year 2000 in each x-bin. The sources of the uncertainty are indicated: polarization measurements of target (P_T) and beam (P_B), cross section ratio R, spin structure function g_2, radiative corrections, and the RICH PID.*

Inclusive asymmetry A_1							
Bin	Total	P_T	P_B	R	g_2	Rad. Corr	Smear. Corr.
1	0.0014	0.0007	0.0003	0.0006	0.0010	0.0003	0.0001
2	0.0019	0.0010	0.0005	0.0009	0.0012	0.0002	0.0002
3	0.0025	0.0014	0.0007	0.0017	0.0015	0.0002	0.0003
4	0.0035	0.0022	0.0010	0.0015	0.0019	0.0001	0.0005
5	0.0048	0.0031	0.0015	0.0023	0.0024	0.0001	0.0007
6	0.0073	0.0047	0.0022	0.0040	0.0031	0.0002	0.0009
7	0.0097	0.0067	0.0032	0.0043	0.0044	0.0002	0.0012
8	0.0143	0.0103	0.0049	0.0055	0.0063	0.0001	0.0021
9	0.0190	0.0127	0.0060	0.0072	0.0105	0.0001	0.0016

Semi-inclusive asymmetry $A_1^{h^+}$							
Bin	Total	P_T	P_B	R	g_2	Rad. Corr	Smear. Corr.
1	0.0010	0.0002	0.0001	0.0001	0.0010	0.0000	0.0000
2	0.0020	0.0011	0.0005	0.0010	0.0012	0.0000	0.0003
3	0.0034	0.0023	0.0011	0.0017	0.0015	0.0000	0.0006
4	0.0034	0.0022	0.0010	0.0015	0.0019	0.0000	0.0005
5	0.0046	0.0026	0.0013	0.0024	0.0025	0.0000	0.0005
6	0.0074	0.0049	0.0023	0.0040	0.0031	0.0000	0.0006
7	0.0087	0.0059	0.0028	0.0037	0.0043	0.0000	0.0006
8	0.0156	0.0111	0.0053	0.0070	0.0065	0.0000	0.0011
9	0.0215	0.0142	0.0067	0.0097	0.0110	0.0000	0.0014

Semi-inclusive asymmetry $A_1^{h^-}$							
Bin	Total	P_T	P_B	R	g_2	Rad. Corr	Smear. Corr.
1	0.0015	0.0007	0.0003	0.0006	0.0009	0.0000	0.0005
2	0.0015	0.0006	0.0003	0.0005	0.0012	0.0000	0.0003
3	0.0026	0.0014	0.0007	0.0010	0.0016	0.0000	0.0008
4	0.0032	0.0019	0.0009	0.0013	0.0019	0.0000	0.0008
5	0.0048	0.0028	0.0013	0.0026	0.0025	0.0000	0.0008
6	0.0074	0.0048	0.0023	0.0039	0.0032	0.0000	0.0008
7	0.0111	0.0080	0.0038	0.0050	0.0043	0.0000	0.0010
8	0.0157	0.0112	0.0053	0.0071	0.0066	0.0000	0.0014
9	0.0201	0.0128	0.0061	0.0088	0.0117	0.0000	0.0016

Table A.17: *Contributions to the systematic uncertainties for the semi-inclusive charged pion and kaon asymmetries for the year 2000.*

Semi-inclusive asymmetry $A_1^{\pi^+}$								
Bin	Total	P_T	P_B	R	g_2	Rad. Corr	Smear. Corr.	RICH PID
1	0.0010	0.0002	0.0001	0.0002	0.0010	0.0000	0.0001	0.0001
2	0.0021	0.0011	0.0005	0.0009	0.0013	0.0000	0.0003	0.0005
3	0.0022	0.0012	0.0005	0.0008	0.0015	0.0000	0.0003	0.0006
4	0.0030	0.0015	0.0007	0.0011	0.0020	0.0000	0.0003	0.0008
5	0.0060	0.0035	0.0017	0.0034	0.0024	0.0000	0.0006	0.0018
6	0.0076	0.0048	0.0023	0.0036	0.0032	0.0000	0.0006	0.0024
7	0.0084	0.0053	0.0025	0.0032	0.0044	0.0000	0.0005	0.0027
8	0.0205	0.0141	0.0067	0.0089	0.0067	0.0000	0.0014	0.0070
9	0.0170	0.0091	0.0043	0.0062	0.0114	0.0000	0.0009	0.0045

Semi-inclusive asymmetry $A_1^{\pi^-}$								
Bin	Total	P_T	P_B	R	g_2	Rad. Corr	Smear. Corr.	RICH PID
1	0.0015	0.0007	0.0003	0.0006	0.0010	0.0000	0.0005	0.0003
2	0.0012	0.0001	0.0001	0.0001	0.0012	0.0000	0.0001	0.0001
3	0.0027	0.0015	0.0007	0.0010	0.0015	0.0000	0.0008	0.0007
4	0.0033	0.0018	0.0008	0.0013	0.0020	0.0000	0.0008	0.0009
5	0.0059	0.0034	0.0016	0.0033	0.0024	0.0000	0.0009	0.0017
6	0.0066	0.0040	0.0019	0.0030	0.0032	0.0000	0.0007	0.0020
7	0.0116	0.0079	0.0038	0.0048	0.0043	0.0000	0.0010	0.0040
8	0.0213	0.0147	0.0070	0.0092	0.0067	0.0000	0.0018	0.0074
9	0.0159	0.0080	0.0038	0.0055	0.0113	0.0000	0.0010	0.0040

Semi-inclusive asymmetry $A_1^{K^+}$								
Bin	Total	P_T	P_B	R	g_2	Rad. Corr	Smear. Corr.	RICH PID
1	0.0021	0.0012	0.0006	0.0010	0.0009	0.0000	0.0003	0.0006
2	0.0042	0.0027	0.0013	0.0023	0.0013	0.0000	0.0007	0.0013
3	0.0070	0.0048	0.0023	0.0032	0.0016	0.0000	0.0012	0.0024
4	0.0044	0.0027	0.0013	0.0020	0.0020	0.0000	0.0006	0.0014
5	0.0054	0.0031	0.0015	0.0030	0.0025	0.0000	0.0005	0.0015
6	0.0055	0.0031	0.0015	0.0023	0.0032	0.0000	0.0004	0.0016
7	0.0072	0.0042	0.0020	0.0025	0.0045	0.0000	0.0004	0.0021
8	0.0202	0.0139	0.0066	0.0087	0.0068	0.0000	0.0014	0.0069
9	0.0210	0.0126	0.0060	0.0087	0.0113	0.0000	0.0013	0.0063

Semi-inclusive asymmetry $A_1^{K^-}$								
Bin	Total	P_T	P_B	R	g_2	Rad. Corr	Smear. Corr.	RICH PID
1	0.0024	0.0013	0.0006	0.0011	0.0010	0.0000	0.0009	0.0007
2	0.0027	0.0015	0.0007	0.0013	0.0012	0.0000	0.0009	0.0008
3	0.0016	0.0001	0.0000	0.0001	0.0016	0.0000	0.0000	0.0000
4	0.0029	0.0014	0.0007	0.0011	0.0019	0.0000	0.0006	0.0007
5	0.0035	0.0016	0.0008	0.0015	0.0025	0.0000	0.0004	0.0008
6	0.0047	0.0025	0.0012	0.0018	0.0032	0.0000	0.0004	0.0012
7	0.0079	0.0048	0.0023	0.0029	0.0044	0.0000	0.0006	0.0024
8	0.0222	0.0154	0.0073	0.0097	0.0067	0.0000	0.0019	0.0077
9	0.0745	0.0526	0.0250	0.0360	0.0113	0.0000	0.0066	0.0263

Appendix B
Tables of results for the quark polarizations

B.1 Construction of the covariance matrix $\mathcal{C}_A$

The variance of the inclusive DIS events $\sigma^2_{N_{e^+}}$ is equal to the number of detected DIS positrons N_{e^+} as they are Poisson distributed. In the case of semi-inclusive hadrons it is possible to derive [169]:

$$\sigma^2_{N_i} = N_{e^+} = \langle\, (n_i)^2\, \rangle = N_i \frac{\langle\, (n_i)^2\, \rangle}{\langle\, n_i\, \rangle}\,, \tag{B.1}$$

where $\langle n_i \rangle = N_i/N_{e^+}$ is the multiplicity for hadrons of type i and N_i is the number of detected hadrons of the same type. The symbol $\langle f \rangle$ denotes the expectation value of the quantity f. The statistical covariances for the numbers of observed particles can be written as

$$\begin{aligned} \mathsf{cov}(N_i, N_j) &= N_{e^+}\langle n_i n_j\rangle\ ; \\ \mathsf{cov}(N_{e^+}, N_i) &= N_{e^+}\langle n_i\rangle\ , \end{aligned} \tag{B.2}$$

where $n_{e^+} = 1$ by definition. The statistical correlation coefficients, which are determined from the measured hadron multiplicities, are then defined as follows

$$\begin{aligned} \mathsf{corr}(N_i, N_j) &= \frac{\mathsf{cov}(N_i, N_j)}{\sigma_{N_i}\cdot\sigma_{N_j}} = \frac{\langle n_i n_j\rangle}{\sqrt{\langle (n_i)^2\rangle\langle (n_j)^2\rangle}}\ ; \\ \mathsf{corr}(N_{e^+}, N_i) &= \frac{\mathsf{cov}(N_{e^+}, N_i)}{\sigma_{N_{e^+}}\cdot\sigma_{N_i}} = \frac{\langle n_i\rangle}{\sqrt{\langle (n_i)^2\rangle}}\ . \end{aligned} \tag{B.3}$$

By selection of the semi-inclusive hadronic events, the semi-inclusive asymmetries are a subsample of the inclusive asymmetries. Therefore, a significant positive correlation is expected between the inclusive and the semi-inclusive measurements. The statistical covariance $\mathsf{cov}(A_i, A_j)$ for two types of asymmetries A_i and A_j can be defined as

$$\mathsf{cov}(A_i, A_j) \equiv \langle\, (A_i - \langle A_i\rangle)\cdot(A_j - \langle A_j\rangle)\, \rangle\ . \tag{B.4}$$

Assuming that the asymmetry A_i for a given particle type i depends only on the number of observed events in both spin states (denoted as N_{i^+} and N_{i^-}), the covariance, $\mathsf{cov}(A_i, A_j)$, can be related to the covariance for the number of observed particles for each asymmetry type and each spin state as

$$\begin{aligned} \mathsf{cov}(A_i, A_j) &= \sum_{\mu,\nu} \frac{\delta A_i}{\delta N^\mu}\frac{\delta A_j}{\delta N^\nu} \\ &= \frac{\delta A_i}{\delta N_{i^+}}\frac{\delta A_j}{\delta N_{j^+}}\cdot\mathsf{cov}(N_{i^+}, N_{j^+}) + \frac{\delta A_i}{\delta N_{i^-}}\frac{\delta A_j}{\delta N_{j^-}}\cdot\mathsf{cov}(N_{i^-}, N_{j^-}) \end{aligned}$$

$$\simeq \frac{1}{2}\left[\frac{\delta A_i}{\delta N_{i^+}}\frac{\delta A_j}{\delta N_{j^+}} + \frac{\delta A_i}{\delta N_{i^-}}\frac{\delta A_j}{\delta N_{j^-}}\right]\cdot \mathsf{cov}(N_i, N_j)$$

$$\simeq \frac{\delta A_i}{\delta N_{i^\pm}}\frac{\delta A_j}{\delta N_{j^\pm}}\cdot \mathsf{cov}(N_i, N_j) \ , \qquad \text{(B.5)}$$

where Greek indices run over both spin states. In addition, it was assumed that the particles in the two spin states are uncorrelated, and the approximation $N_{i^\pm} \simeq N_i/2$ was used. Under the same assumptions, the errors on the asymmetries can be rewritten as

$$\sigma_A = \left|\frac{\delta A_i}{\delta N_{i^\pm}}\right| \sigma_{N_i} \ . \qquad \text{(B.6)}$$

Therefore, from Eq. (B.3) the covariance for the extracted asymmetries are calculated from the measured particle multiplicities which are used to form the statistical covariance matrix $\mathcal{C}_A$ according to

$$\mathcal{C}_A^{ij} = \mathsf{cov}(A_i, A_j) \simeq \sigma_{A_i}\sigma_{A_j}\mathsf{corr}(N_i, N_j) \ . \qquad \text{(B.7)}$$

Tables B.1 and B.2 summarize the correlation values obtained from the count rates of inclusive and semi-inclusive DIS events on proton and deuteron targets, respectively. The correlation coefficients for the asymmetries on the ^{3}He target were taken from Ref.[124].

Table B.1: *Correlations coefficients of particles for proton target.*

$\langle x\rangle$	(N_e, N_{h^+})	(N_e, N_{h^-})	(N_e, N_{π^+})	(N_e, N_{π^-})
0.033	0.446	0.395	0.295	0.261
0.047	0.492	0.417	0.291	0.250
0.065	0.507	0.411	0.273	0.229
0.087	0.497	0.386	0.246	0.201
0.119	0.452	0.336	0.211	0.166
0.168	0.365	0.260	0.168	0.130
0.245	0.260	0.178	0.122	0.091
0.342	0.183	0.120	0.087	0.063
0.465	0.127	0.080	0.061	0.045

$\langle x\rangle$	(N_{h^+}, N_{h^-})	(N_{h^+}, N_{π^+})	(N_{h^+}, N_{π^-})	(N_{h^-}, N_{π^+})	(N_{h^-}, N_{π^-})	(N_{π^+}, N_{π^-})
0.033	0.173	0.545	0.076	0.078	0.558	0.069
0.047	0.141	0.530	0.069	0.067	0.543	0.058
0.065	0.126	0.514	0.060	0.058	0.534	0.053
0.087	0.109	0.494	0.052	0.051	0.511	0.048
0.119	0.094	0.468	0.041	0.044	0.486	0.044
0.168	0.084	0.434	0.028	0.030	0.462	0.040
0.245	0.063	0.391	0.024	0.026	0.420	0.023
0.342	0.042	0.337	0.018	0.020	0.369	0.011
0.465	0.023	0.276	0.011	0.013	0.304	0.005

Table B.2: *Correlations coefficients of particles for deuteron target.*

$\langle x \rangle$	(N_e, N_{h^+})	(N_e, N_{h^-})	(N_e, N_{π^+})	(N_e, N_{π^-})	(N_e, N_{K^+})	(N_e, N_{K^-})
0.033	0.492	0.455	0.334	0.310	0.142	0.105
0.047	0.504	0.442	0.325	0.296	0.143	0.098
0.065	0.486	0.417	0.302	0.272	0.136	0.088
0.087	0.458	0.386	0.275	0.242	0.126	0.077
0.119	0.415	0.338	0.236	0.206	0.112	0.064
0.168	0.358	0.280	0.190	0.160	0.091	0.050
0.245	0.290	0.216	0.138	0.114	0.068	0.034
0.342	0.238	0.169	0.098	0.079	0.050	0.023
0.465	0.211	0.146	0.073	0.061	0.037	0.017

$\langle x \rangle$	(N_{h^+}, N_{h^-})	(N_{h^+}, N_{π^+})	(N_{h^+}, N_{π^-})	(N_{h^-}, N_{π^+})	(N_{h^-}, N_{π^-})	(N_{π^+}, N_{π^-})
0.033	0.146	0.637	0.118	0.115	0.661	0.064
0.047	0.128	0.619	0.101	0.098	0.649	0.055
0.065	0.126	0.599	0.088	0.087	0.635	0.050
0.087	0.113	0.581	0.075	0.073	0.620	0.048
0.119	0.107	0.555	0.071	0.069	0.599	0.041
0.168	0.087	0.523	0.062	0.058	0.566	0.037
0.245	0.080	0.475	0.050	0.047	0.525	0.027
0.342	0.066	0.413	0.043	0.038	0.465	0.020
0.465	0.054	0.349	0.027	0.025	0.413	0.010

$\langle x \rangle$	(N_{h^+}, N_{K^+})	(N_{h^+}, N_{K^-})	(N_{h^-}, N_{K^+})	(N_{h^-}, N_{K^-})
0.033	0.357	0.063	0.062	0.348
0.047	0.328	0.060	0.061	0.325
0.065	0.319	0.056	0.062	0.318
0.087	0.313	0.051	0.054	0.315
0.119	0.309	0.045	0.049	0.312
0.168	0.298	0.040	0.041	0.302
0.245	0.287	0.030	0.031	0.293
0.342	0.274	0.021	0.028	0.280
0.465	0.271	0.011	0.016	0.275

$\langle x \rangle$	(N_{π^+}, N_{K^+})	(N_{π^+}, N_{K^-})	(N_{π^-}, N_{K^+})	(N_{π^-}, N_{K^-})	(N_{K^+}, N_{K^-})
0.033	0.026	0.021	0.024	0.014	0.054
0.047	0.018	0.014	0.017	0.010	0.051
0.065	0.015	0.012	0.011	0.009	0.050
0.087	0.014	0.011	0.009	0.008	0.045
0.119	0.013	0.009	0.008	0.007	0.037
0.168	0.011	0.009	0.006	0.006	0.035
0.245	0.006	0.006	0.004	0.004	0.032
0.342	0.006	0.003	0.004	0.002	0.031
0.465	0.005	0.002	0.003	0.002	0.026

Table B.3: *Statistical correlation coefficients between the extracted quark polarizations for the flavor decomposition in each x-bin.*

x-bin	$(\frac{\Delta d}{d}, \frac{\Delta u}{u})$	$(\frac{\Delta d}{d}, \frac{\Delta \bar{d}}{\bar{d}})$	$(\frac{\Delta d}{d}, \frac{\Delta \bar{u}}{\bar{u}})$	$(\frac{\Delta d}{d}, \frac{\Delta s+\Delta \bar{s}}{s+\bar{s}})$	$(\frac{\Delta u}{u}, \frac{\Delta \bar{d}}{\bar{d}})$	$(\frac{\Delta u}{u}, \frac{\Delta \bar{u}}{\bar{u}})$	$(\frac{\Delta u}{u}, \frac{\Delta s+\Delta \bar{s}}{s+\bar{s}})$	$(\frac{\Delta \bar{d}}{\bar{d}}, \frac{\Delta \bar{u}}{\bar{u}})$	$(\frac{\Delta \bar{d}}{\bar{d}}, \frac{\Delta s+\Delta \bar{s}}{s+\bar{s}})$	$(\frac{\Delta \bar{u}}{\bar{u}}, \frac{\Delta s+\Delta \bar{s}}{s+\bar{s}})$
1	−0.575	−0.868	0.557	−0.176	0.572	−0.847	−0.209	−0.617	−0.088	−0.154
2	−0.553	−0.816	0.445	−0.081	0.482	−0.772	−0.201	−0.503	−0.204	−0.215
3	−0.573	−0.822	0.452	−0.061	0.485	−0.760	−0.171	−0.516	−0.202	−0.236
4	−0.536	−0.774	0.339	−0.048	0.393	−0.698	−0.172	−0.401	−0.243	−0.277
5	−0.548	−0.771	0.352	−0.030	0.423	−0.719	−0.185	−0.423	−0.262	−0.254
6	−0.587	−0.787	0.385	−0.013	0.466	−0.741	−0.176	−0.430	−0.305	−0.250
7	−0.652	−0.822	0.461	−0.094	0.552	−0.779	−0.208	−0.454	−0.401	−0.229
8	−0.905	–	–	–	–	–	–	–	–	–
9	−0.908	–	–	–	–	–	–	–	–	–

Table B.4: *Statistical correlation coefficients between the extracted quark polarizations for the valence decomposition in each x-bin. The value of $\chi^2/n.d.f.$ is shown as well.*

x-bin	$(\frac{\Delta d_v}{d_v}, \frac{\Delta u_v}{u_v})$	$(\frac{\Delta d_v}{d_v}, \frac{\Delta \bar{u}}{\bar{u}})$	$(\frac{\Delta u_v}{u_v}, \frac{\Delta \bar{u}}{\bar{u}})$	$\chi^2/n.d.f.$
1	−0.570	0.572	−0.969	1.255
2	−0.528	0.507	−0.957	1.098
3	−0.497	0.459	−0.964	0.791
4	−0.459	0.414	−0.959	0.698
5	−0.461	0.405	−0.961	1.291
6	−0.467	0.408	−0.960	0.913
7	−0.469	0.343	−0.923	1.419
8	−0.904	–	–	1.105
9	−0.901	–	–	0.876

Table B.5: *Results for the extracted values of $\Delta\bar{u} - \Delta\bar{d}$ for each x-bin. The first errors are the statistical uncertainty and the second ones are the systematic. The $\chi^2/n.d.f.$ of the fit is shown as well.*

x-bin	$\Delta\bar{u} - \Delta\bar{d}$	$\chi^2/n.d.f.$
1	1.471 ± 1.039 ± 0.347	1.236
2	0.900 ± 0.757 ± 0.226	1.051
3	0.252 ± 0.583 ± 0.505	0.993
4	−0.119 ± 0.435 ± 0.532	1.145
5	0.050 ± 0.346 ± 0.212	1.339
6	0.021 ± 0.297 ± 0.152	0.868
7	0.009 ± 0.278 ± 0.147	1.152

Table B.6: *Contribution to the systematic uncertainties for $\frac{\Delta d}{d}$ and $\frac{\Delta u}{u}$ from the flavor decomposition in each x-bin.*

Systematic uncertainties for $\Delta d/d$													
x-bin	$\langle x\rangle$	Total	Pbeam	Ptarg	Radcor	Smear	RICH	R	g_2	Fragm	PDF	Sea	Yield
1	0.033	0.0193	0.0047	0.0072	0.0021	0.0047	0.0051	0.0016	0.0015	0.0155	0.0011	0.0000	0.0011
2	0.047	0.0196	0.0057	0.0095	0.0018	0.0033	0.0055	0.0010	0.0018	0.0145	0.0009	0.0000	0.0010
3	0.065	0.0284	0.0079	0.0120	0.0011	0.0050	0.0023	0.0013	0.0022	0.0236	0.0025	0.0000	0.0012
4	0.087	0.0613	0.0121	0.0193	0.0009	0.0047	0.0053	0.0018	0.0027	0.0558	0.0079	0.0000	0.0017
5	0.119	0.0606	0.0142	0.0215	0.0017	0.0098	0.0021	0.0022	0.0040	0.0537	0.0018	0.0000	0.0015
6	0.168	0.0460	0.0175	0.0272	0.0011	0.0197	0.0029	0.0004	0.0052	0.0253	0.0013	0.0000	0.0023
7	0.244	0.0778	0.0269	0.0415	0.0027	0.0254	0.0033	0.0006	0.0067	0.0537	0.0042	0.0000	0.0022
8	0.342	0.2692	0.0437	0.0773	0.0022	0.0266	0.0027	0.0006	0.0116	0.0252	0.0034	0.2512	0.0031
9	0.465	0.2228	0.0773	0.1256	0.0021	0.0112	0.0017	0.0005	0.0211	0.0216	0.0031	0.1638	0.0028

Systematic uncertainties for $\Delta u/u$													
x-bin	$\langle x\rangle$	Total	Pbeam	Ptarg	Radcor	Smear	RICH	R	g_2	Fragm	PDF	Sea	Yield
1	0.033	0.0214	0.0044	0.0073	0.0008	0.0011	0.0048	0.0021	0.0013	0.0188	0.0020	0.0000	0.0009
2	0.047	0.0214	0.0053	0.0084	0.0007	0.0009	0.0031	0.0016	0.0011	0.0185	0.0019	0.0000	0.0008
3	0.065	0.0354	0.0067	0.0095	0.0004	0.0014	0.0017	0.0011	0.0009	0.0333	0.0020	0.0000	0.0007
4	0.087	0.0607	0.0103	0.0147	0.0006	0.0013	0.0034	0.0014	0.0011	0.0578	0.0016	0.0000	0.0007
5	0.119	0.0255	0.0098	0.0143	0.0002	0.0011	0.0022	0.0007	0.0012	0.0177	0.0009	0.0000	0.0006
6	0.168	0.0308	0.0111	0.0162	0.0002	0.0012	0.0017	0.0006	0.0017	0.0235	0.0002	0.0000	0.0007
7	0.244	0.0312	0.0139	0.0223	0.0007	0.0026	0.0016	0.0007	0.0025	0.0162	0.0015	0.0000	0.0007
8	0.342	0.0539	0.0175	0.0277	0.0005	0.0021	0.0011	0.0005	0.0027	0.0114	0.0021	0.0411	0.0009
9	0.465	0.0513	0.0263	0.0373	0.0005	0.0022	0.0009	0.0003	0.0032	0.0102	0.0025	0.0205	0.0006

Table B.7: *Contribution to the systematic uncertainties for $\frac{\Delta\bar{d}}{\bar{d}}$, $\frac{\Delta\bar{u}}{\bar{u}}$, and $\frac{\Delta s+\Delta\bar{s}}{s+\bar{s}}$ from the flavor decomposition in each x-bin.*

Systematic uncertainties for $\Delta\bar{d}/\bar{d}$												
x-bin	$\langle x\rangle$	Total	Pbeam	Ptarg	Radcor	Smear	RICH	R	g_2	Fragm	PDF	Yield
1	0.033	0.0338	0.0047	0.0082	0.0033	0.0098	0.0037	0.0025	0.0017	0.0213	0.0219	0.0011
2	0.047	0.0284	0.0042	0.0073	0.0012	0.0113	0.0031	0.0012	0.0022	0.0180	0.0163	0.0014
3	0.065	0.0696	0.0031	0.0059	0.0011	0.0099	0.0020	0.0013	0.0021	0.0673	0.0129	0.0013
4	0.087	0.0883	0.0033	0.0072	0.0012	0.0034	0.0055	0.0008	0.0028	0.0866	0.0136	0.0016
5	0.119	0.1659	0.0034	0.0090	0.0008	0.0076	0.0034	0.0010	0.0036	0.1652	0.0092	0.0019
6	0.168	0.1340	0.0088	0.0143	0.0016	0.0021	0.0045	0.0006	0.0045	0.1321	0.0137	0.0023
7	0.244	0.2267	0.0166	0.0406	0.0025	0.0054	0.0034	0.0007	0.0081	0.2191	0.0369	0.0037

Systematic uncertainties for $\Delta\bar{u}/\bar{u}$												
x-bin	$\langle x\rangle$	Total	Pbeam	Ptarg	Radcor	Smear	RICH	R	g_2	Fragm	PDF	Yield
1	0.033	0.0519	0.0011	0.0052	0.0022	0.0020	0.0036	0.0008	0.0012	0.0513	0.0031	0.0012
2	0.047	0.0706	0.0017	0.0046	0.0017	0.0031	0.0022	0.0003	0.0009	0.0703	0.0016	0.0016
3	0.065	0.1446	0.0033	0.0074	0.0025	0.0046	0.0019	0.0009	0.0007	0.1432	0.0176	0.0013
4	0.087	0.2155	0.0073	0.0143	0.0031	0.0081	0.0013	0.0009	0.0010	0.2136	0.0222	0.0014
5	0.119	0.1680	0.0020	0.0095	0.0008	0.0024	0.0035	0.0004	0.0014	0.1672	0.0125	0.0026
6	0.168	0.2344	0.0142	0.0269	0.0037	0.0172	0.0042	0.0002	0.0036	0.2317	0.0023	0.0036
7	0.244	0.4131	0.0202	0.0535	0.0057	0.0556	0.0076	0.0005	0.0083	0.3955	0.0873	0.0082

Systematic uncertainties for $(\Delta s+\Delta\bar{s})/(s+\bar{s})$												
x-bin	$\langle x\rangle$	Total	Pbeam	Ptarg	Radcor	Smear	RICH	R	g_2	Fragm	PDF	Yield
1	0.033	0.2077	0.0030	0.0102	0.0021	0.0105	0.0506	0.0016	0.0014	0.1022	0.1729	0.0004
2	0.047	0.3561	0.0044	0.0123	0.0011	0.0127	0.0522	0.0012	0.0011	0.1323	0.3259	0.0007
3	0.065	0.2371	0.0061	0.0127	0.0025	0.0153	0.0433	0.0009	0.0016	0.1002	0.2094	0.0005
4	0.087	0.1263	0.0047	0.0109	0.0015	0.0203	0.0689	0.0005	0.0020	0.0867	0.0559	0.0014
5	0.119	0.1428	0.0091	0.0189	0.0011	0.0174	0.0653	0.0004	0.0021	0.1157	0.0446	0.0006
6	0.168	0.1628	0.0037	0.0214	0.0007	0.0102	0.0697	0.0003	0.0039	0.1432	0.0231	0.0012
7	0.244	0.3908	0.0072	0.0265	0.0011	0.0084	0.1283	0.0004	0.0056	0.3615	0.0691	0.0004

Bibliography

[1] R. Hofstadter. *Electron scattering and nuclear and nucleon structure*. W.A. Benjamin, INC., N.Y., (1963).

[2] M. Gell-Mann. *A schematic model of baryons and mesons*. Phys. Lett., **8**, (1964), p. 214.

[3] G. Zweig. *An $SU(3)$ model for strong interaction symmetry and its breaking*. Technical report, **CERN-TH-412**, (1964).

[4] J.D. Bjorken. *Asymptotic sum rules at infinite momentum*. Phys. Rev., **179**, (1969), p. 1547.

[5] H. Fritzsch, M. Gell-Mann, and H. Leutwyler. *Advantages of the color octet picture*. Phys. Lett., **B47**, (1973), p. 365.

[6] M.J. Alguard $et\ al.$ *Deep inelastic scattering of polarized electrons by polarized protons*. Phys. Rev. Lett., **B37**, (1976), p. 1261.

[7] M.J. Alguard $et\ al.$ *Deep inelastic e-p asymmetry measurements and comparison with the Bjorken sum rule and models of the proton spin structure*. Phys. Rev. Lett., **41**, (1978), p. 70.

[8] G. Baum $et\ al.$ *A new measurement of deep inelastic e-p asymmetries*. Phys. Rev. Lett., **51**, (1983), p. 1135.

[9] J. Ashman $et\ al.$ *A measurement of the spin asymmetry and determination of the structure function g_1 in deep-inelastic muon-proton scattering*. Phys. Lett., **B206**, (1988), p. 364.

[10] D. Adams $et\ al.$ *Measurement of the spin-dependent structure function $g_1(x)$ of the proton*. Phys. Lett., **B329**, (1994), p. 399.

[11] F. Bernard for the SMC collaboration. *The spin structure of the deuteron*. In *Spin structure in high energy processes*, SLAC Summer Inst., (1983).

[12] P.L. Anthony $et\ al.$ *Determination of the neutron spin structure function*. Phys. Rev. Lett., **71**, (1993), p. 959.

[13] K. Abe $et\ al.$ *Precision measurement of the proton spin structure function g_1^p*. Phys. Rev. Lett., **74**, (1995), p. 346.

[14] K. Abe $et\ al.$ *Precision measurement of the deuteron spin structure function g_1^d*. Phys. Rev. Lett., **75**, (1995), p. 25.

[15] K. Abe *et al.* *Precision determination of the neutron spin structure function g_1^n*. Phys. Rev. Lett., **79**, (1997), p. 26.

[16] K. Abe *et al.* *Measurement of the neutron spin structure function g_2^n and asymmetry A_2^n*. Phys. Lett., **B404**, (1997), p. 377.

[17] P.L. Anthony *et al.* *Measurement of the deuteron spin structure function g_1^d for 1(GeV/c)$^2 < Q^2 <$ 40(GeV/c)^2*. Phys. Lett., **B463**, (1999), p. 339.

[18] P.L. Anthony *et al.* *Measurement of the proton the deuteron spin structure function g_2 and asymmetry A_2*. Phys. Lett., **B458**, (1999), p. 529.

[19] E. Leader and E. Predazzi. *An introduction to gauge theories and the "new physics"*. Cambridge University Press, (1982).

[20] M. Anselmino, A. Efremov, and E. Leader. *The theory and phenomenology of polarized deep-inelastic scattering*. Phys. Rep., **261**, (1995), p. 1.

[21] A.V. Manohar. *An introduction to spin dependent deep-inelastic scattering*. UCSD-PTH-92, (1992).

[22] L.N. Hand. *An experimental study of the direct production of pions by high-energy electrons*. Phys. Rev., **129**, (1963), p. 1834.

[23] M. G. Doncel and E. de Rafael. *Coincidence electroproduction reactions and positivity restrictions*. Nuovo Cimento, **4A**, (1971), p. 363.

[24] O. Teryaev, B. Pire, and J. Soffer. *Sum rules and positivity constraints on nucleon spin structure*. In *33rd Rencontres de Moriond: QCD and High Energy Hadronic Interactions*, Les Arcs, France, (1998).

[25] M. Arneodo *et al.* *Measurement of the proton and deuteron structure functions, F_2^p and F_2^d, and of the ratio σ_L/σ_T*. Nucl. Phys., **B483**, (1997), p. 3.

[26] L.W. Whitlow *et al.* *A precise extraction of $R = \sigma_L/\sigma_T$ from a global analysis of the SLAC deep inelastic e-p and e-d scattering cross sections*. Phys. Lett., **B250**, (1990), p. 193.

[27] A.C. Benvenuti *et al.* *A comparison of the structure function F_2 of the proton and the neutron from deep-inelastic muon scattering at high Q^2*. Phys. Lett., **B237**, (1990), p. 599.

[28] W.K.H. Panofsky. *Electromagnetic interactions: low Q^2 electrodynamics, elastic and inelastic electron (and muon) scattering*. In *Proc. of the 14th Int. Conf. on High Energy Physics, Vienna*, (1968).

[29] M. Breidenbach *et al.* *Observed behavior of highly inelastic electron-proton scattering*. Phys. Rev. Lett., **23**, (1969), p. 935.

[30] J.D. Bjorken and E.A. Paschos. *Inelastic electron-proton and gamma-proton scattering, and the structure of the nucleon*. Phys. Rev., **185**, (1969), p. 1975.

[31] R.P. Feynman. *Photon-hadron interactions*. Benjamin, Reading, MA, (1972).

[32] R.P. Feynman. *Very high-energy collisions of hadrons*. Phys. Rev. Lett., **23**, (1969), p. 1415.

[33] C.G. Callan and D.J. Gross. *High-energy electroproduction and the constitution of the electric current*. Phys. Rev. Lett., **22**, (1969), p. 156.

[34] J. Visser. *Deep-inelastic scattering off hydrogen and deuterium*. PhD thesis, Groningen Univ., The Netherlands, (2002).

[35] H.L. Lai $et\ al.$ *Global QCD analysis of parton structure of the nucleon: CTEQ5 parton distributions*. Eur. Phys. J., **C12**, (2000), p. 375.

[36] T. Sloan, G. Smadja, and R. Voss. *The quark structure of the nucleon from the CERN muon experiments*. Phys. Rep., **162**, (1988), p. 45.

[37] M. Arneodo $et\ al.$ *Measurement of the proton and the deuteron structure functions, F_2^p and F_2^d*. Phys. Lett., **B364**, (1995), p. 107.

[38] R.K. Ellis, W.J. Stirling, and B.R. Webber. *QCD and collider physics*. Cambridge University Press, (1996).

[39] D.E. Groom $et\ al.$ *Review of Particle Physics*. Eur. Phys. J., **C14**, (2000), p. 1.

[40] V.N. Gribov and L.N. Lipatov. *Deep-inelastic scattering in perturbation theory*. Sov. J. Nucl. Phys., **15**, (1972), p. 438.

[41] G. Altarelli and G. Parisi. *Asymptotic freedom in parton language*. Nucl. Phys., **B126**, (1977), p. 298.

[42] Y.L. Dokshitzer. *Calculation of the structure functions for deep-inelastic scattering and e^+-e^- annihilation by perturbation theory in QCD*. Sov. Phys. JETP, **46**, (1977), p. 641.

[43] G. Altarelli. *Partons in Quantum Chromodynamics*. Phys. Rep., **81**, (1982), p. 1.

[44] R. Mertig and W.L. van Neerven. *The calculation of the two-loop spin splitting functions $P_{ij}^{(1)}(x)$*. Z. Phys., **C70**, (1996), p. 637.

[45] E.B. Zijlstra and W.L. van Neerven. *Order $\alpha(s)^2$ corrections to the polarized structure function $g_1(x, Q^2)$*. Nucl. Phys., **B417**, (1994), p. 61.

[46] M. Glück, E. Reya, and A. Vogt. *Dynamical parton distributions revisited*. Eur. Phys. J., **C5**, (1998), p. 461.

[47] M. Stratmann and W. Vogelsang. *Towards a global analysis of polarized parton distributions*. Phys. Rev., **D64**, (2001), p. 114007.

[48] K.G. Wilson. *Non-lagrangian models of current algebra*. Phys. Rev., **179**, (1969), p. 1499.

[49] W. Zimmermann. *Composite operators in the perturbation theory of renormalizable interactions*. Ann. Phys., **77**, (1973), p. 536.

[50] S.A. Larin and J.A.M. Vermaseren. *The α_s^3 corrections to the Bjorken sum rule for polarized electroproduction and to the Gross-Llewellyn Smith sum rule*. Phys. Lett., **B259**, (1991), p. 345.

[51] S.A. Larin. *The Next-to-leading QCD approximation to the Ellis-Jaffe sum rule*. Phys. Lett., **B334**, (1994), p. 192.

[52] S.I. Adler. *Axial vector vertex in spinor electrodynamics*. Phys. Rev., **177**, (1969), p. 2426.

[53] J.S. Bell and R. Jackiw. *A PCAC puzzle: $\pi^0 \rightarrow \gamma\gamma$ in the sigma model*. Nuovo Cimento, **A60**, (1969), p. 47.

[54] S.I. Adler and W. Bardeen. *Absence of higher order corrections in the anomalous axial vector divergence equation*. Phys. Rev., **182**, (1969), p. 1517.

[55] W. Bardeen, A. Buras, D.W. Duke, and T. Muta. *Deep inelastic scattering beyond the leading order in asymptotically free gauge theories*. Phys. Rev., **D18**, (1978), p. 3998.

[56] G. Altarelli and G.G. Ross. *The anomalous gluon contribution to polarized leptoproduction*. Phys. Lett., **B212**, (1988), p. 391.

[57] S. Wandzura and F. Wilczek. *Sum rules for spin dependent electroproduction: test of relativistic constituent quarks*. Phys. Lett., **B72**, (1977), p. 195.

[58] J.D. Bjorken. *Applications of the chiral $U(6) \otimes U(6)$ algebra of current densities*. Phys. Rev., **148**, (1966), p. 1467.

[59] J. Ellis and R. Jaffe. *Sum rule for deep-inelastic electroproduction from polarized protons*. Phys. Rev., **D9**, (1974), p. 1444.

[60] J. Ashman $et\ al.$ *An investigation of the spin structure of the proton in deep-inelastic scattering of polarized muons on polarized protons*. Phys. Lett., **B328**, (1989), p. 1.

[61] Ya.I. Azimov, Yu.I. Dokshitzer, V.A. Khoze, and S.I. Troian. *The string effect and QCD coherence*. Phys. Lett., **B165**, (1985), p. 147.

[62] H. Albrecht $et\ al.$ *Physics with ARGUS*. Phys. Rep., **276**, (1996), p. 223.

[63] S. Aid $et\ al.$ *A Study of the fragmentation of quarks in e-p collisions at HERA*. Nucl. Phys., **B445**, (1995), p. 3.

[64] E.L. Berger. *Semi-inclusive inelastic electron scattering from nuclei*. In *Proc. of NPAS Workshop on Electronuclear Physics with Internal Targets, Stanford, CA*, ANL-HEP-CP-87-45, (1987).

[65] J.P. Albanese $et\ al.$ *Quark charge retention in final state hadrons from deep-inelastic muon scattering*. Phys. Lett., **B144**, (1984), p. 302.

[66] J.M. Niczyporuk and E.E.W. Bruins. *Quark flavor tagging in polarized hadronic processes*. Phys. Rev., **D58**, (1998), p. 091501.

[67] J. Binnewies. *Fragmentation functions in next-to-leading order QCD*. PhD thesis, Universität Hamburg, Germany, (1997).

[68] A. Airapetian $et\ al.$ *Multiplicity of charged and neutral pions in deep-inelastic scattering of 27.5 GeV positrons on hydrogen*. Eur. Phys. J., **C21**, (2001), p. 599.

[69] M. Arneodo $et\ al.$ *Measurement of the u valence quark distribution function in the proton and u quark fragmentation functions*. Nucl. Phys., **B321**, (1989), p. 541.

[70] P. Geiger. *Measurement of the fragmentation functions at HERMES* . PhD thesis, Ruprecht-Karls Univ. Heidelberg, Germany, (1998).

[71] B.R. Webber. *Fragmentation and hadronization*. J. Mod. Phys., **A15S1**, (2000), p. 577.

[72] R.D. Field and R.P. Feynman. *A parameterization of the properties of quark jets*. Nucl. Phys., **B136**, (1978), p. 1.

[73] B. Andersson, G. Gustafson, G. Ingelmann, and T. Sjöstrand. *Parton fragmentation and string dynamics*. Phys. Rep., **97**, (1983), p. 31.

[74] T. Sjöstrand. *High energy physics event generation with PYTHIA 5.7 and JETSET 7.4*. Comp. Phys. Commun., **82**, (1994), p. 74.

[75] H. Tallini. *Measurement of the quark spin distributions of the nucleon at* HERMES. PhD thesis, Liverpool Univ., Great-Britain, (1998).

[76] F.M. Menden. *Determination of the gluon polarization in the nucleon*. PhD thesis, Albert-Ludwigs-Univ. Freiburg, Germany, (2001).

[77] HERMES collaboration. *HERMES Technical Design Report*. DESY-PRC-93-06, (1993).

[78] A.A. Sokolov and I.M. Ternov. *On polarization and spin effects in the theory of synchrotron radiation*. Sov. Phys. Dokladi, **8**, (1964), p. 1203.

[79] D.P. Barber *et al.* *The HERA polarimeter and the first observation of electron spin polarization*. Nucl. Instr. Meth., **A338**, (2000), p. 21.

[80] D.P. Barber *et al.* *The first achievement of longitudinal spin polarization in a high-energy electron storage ring*. Phys. Lett., **B343**, (1995), p. 436.

[81] M. Dueren. *The HERMES experiment: From the design to the first results*. Friedrich-Alexander-Univ. Erlangen-Nürnberg, (1995).

[82] M. Beckmann *et al.* *The longitudinal polarimeter at HERA*. Nucl. Instr. Meth., **A461**, (2000), p. 21.

[83] M. Beckmann. *Extraction of polarised quark distributions of the nucleon from deep-inelastic scattering at the HERMES experiment*. PhD thesis, Albert-Ludwigs-Univ. Freiburg, Germany, (2000).

[84] W. Haerbeli. *Free and stored stomic beams as internal polarized targets*. In *AIP Conf. Proc. Nucl. Phys. with Stored, Cooled Beams*, Indiana, (1984).

[85] R. Gilman *et al.* *A polarized gas internal target using a storage cell in an electron storage ring*. Nucl. Instr. Meth., **A327**, (1993), p. 277.

[86] J.S. Dunham *et al.* *A H_2 gas jet as internal target*. Nucl. Instr. Meth., **A219**, (1984), p. 46.

[87] D. Adams *et al.* *The polarized double cell target of the SMC*. Nucl. Instr. Meth., **A437**, (1999), p. 23.

[88] S.F. Pate *et al.* *The HERMES polarized internal gas target*. In *Proc. Conf. Int. Workshop on polarized beams and polarized gas targets*, London, England, (1996).

[89] D. de Schepper *et al.* *The HERMES polarized ^{3}He internal gas target*. Nucl. Instr. Meth., **A419**, (1998), p. 16.

[90] K. Ackerstaff *et al.* *The HERMES spectrometer*. Nucl. Instr. Meth., **A417**, (1998), p. 230.

[91] N. Akopov *et al.* *The HERMES dual-radiator ring imaging Cerenkov detector*. Nucl. Instr. Meth., **A479**, (2002), p. 511.

[92] D. de Schepper, R. Kaiser, and E. Cisbani. *Particle identification with the HERMES RICH detector: description of different approaches*. HERMES internal note/98-008, (1998).

[93] A.T. Maas. *Particle identification with RICH detectors: algorithms and their optimization*. PhD thesis, GSI Darmstadt, DESY Zeuthen, Germany, (2000).

[94] Y. Gaerber. *Messung der Proton-Spinstrukturfunktion g_1 bis zu kleinstmöglichen Bjorken-x mit dem HERMES Experiment*. PhD thesis, Humboldt-Univ. Berlin, Germany, (2001).

[95] D. de Schepper *et al.* *The HERMES Čerenkov detector*. HERMES internal note/00-021, (2000).

[96] R. Kaiser. *Likelihood analysis for the RICH IRT method*. HERMES internal note/00-026, (2000).

[97] K. Negodeva. *The PID efficiency of the HERMES RICH detector for the IRT method*. HERMES internal note/00-028, (2000).

[98] R. Kaiser and B. Hommez. *Using the RICH detector for physics analysis*. HERMES internal note/00-003, (2000).

[99] I. McLaren *et al.* *EPIO - Experimental Physics Input Output Package, CERN Program Library Long Writeup* **I-101**. (1993).

[100] CERN Programming Techniques Group. *ADAMO (ALEPH Data Model) - An entity-relationship programming system, Version 3.3*. (1994).

[101] W. Wander. *Rekonstruktion hochenergetischer Streuereignisse im HERMES Experiment*. PhD thesis, Friedrich-Alexander-Univ. Erlangen-Nürnberg, Germany, (1996).

[102] N. Koch. *A study on the Production of Intense Cold Atomic beams for Polarized Hydrogen and Deuterium Targets*. PhD thesis, Friedrich-alexander Univ., Erlangen-Nürnberg, (1999).

[103] C. Baumgarten. *Studies of Spin Relaxation and Recombination at the HERMES Hydrogen/Deuterium Gas Target*. PhD thesis, Ludwig-Maximilians Univ., München, (2000).

[104] H.Kolster. *The HERMES Gaseous Internal Polarized Proton target and its use in the HERA Positron Storage Ring*. PhD thesis, Ludwig-Maximilians Univ., München, (1998).

[105] B. Braun. *Spinrelaxation von Wasserstoff und Deuterium in Speicherzellen*. PhD thesis, Ludwig-Maximilians Univ., München, (1995).

[106] J.S. Price and W. Haerberli. *Polarization measurement of polarized gas targets.* Nucl. Instr. Meth., **A326**, (1993), p. 416.

[107] J.S. Price and W. Haerberli. *Measurement of cell wall depolarization of polarized hydrogen gas targets.* Nucl. Phys., **A349**, (1994), p. 321.

[108] D.S. Eliott M.B. Shah and H.B. Gilbody. *Pulsed crossed-beam study of the ionization of atomic hydrogen and deuterium*. J. Phys., **B20**, (1987), p. 3501.

[109] E. Krishnakumar and S.K. Srivastava. *Cross-sections for dissociative ionization in molecules by electron impact*. J. Phys., **B27**, (1994), p. 251.

[110] C. Baumgarten $et\ al.$ *Molecular flow and wall collision age distributions*. Eur.Phys.J., **D18**, (2002), p. 37.

[111] C. Baumgarten $et\ al.$ *An atomic beam polarimeter to measure the nuclear polarization in the HERMES gaseous polarized hydrogen and deuterium target*. Nucl. Instr. Meth., **A482**, (2002), p. 606.

[112] M. Henoch. *Sampling correction on α_r for 1997*. HERMES internal note/00-04, (2000).

[113] J.F.J van den Brand $et\ al.$ *Evidence for nuclear tensor polarization of deuterium molecules in storage cells*. Phys. Rev. Lett., **78**, (1997), p. 1235.

[114] T. Wise $et\ al.$ *Nuclear polarization of hydrogen molecules from recombination of polarized atoms*. Phys. Rev. Lett., **87**, (2001), p. 64.

[115] HERMES target group. *The polarization of the HERMES target and its error for the deuterium running in 2000*. HERMES internal note/02-010, (2002).

[116] HERMES Collaboration. *The HERMES physics program and plans for 2001-2006*. DESY-PRC 00/096, (2000).

[117] W.D. Nowak for the HERMES Collaboration. *Prospects for the HERMES run II*. In *Proc. Conf. DIS2001*, Bologna, (2001).

[118] P.J. Mulders. *Structure of hadrons in hard scattering processes*. Lecture notes given at the Nijmegen summer school, hep-ph/9912493, (1999).

[119] D. Reggiani. *Studio ed applicazione di un bersaglio trasversalmente polarizzato per l'esperimento HERMES a HERA*. Diploma thesis, Ferrara Univ., Italy, (1999).

[120] A. Airapetian $et\ al.$ *Beam-induced nuclear depolarization in a gaseous polarized hydrogen target*. Phys. Rev. Lett., **82**, (1999), p. 1164.

[121] M.C. Simani for the HERMES Collaboration. *Resonant depolarization of hydrogen and deuterium atoms induced by the 27.5 GeV lepton beam at HERMES* . In *Proc. Conf. Polarized Sources and Targets*, Erlangen-Nürnberg, Germany, (1999).

[122] M. Ferro-Luzzi $et\ al.$ *Zeeman transitions in deuterium atoms induced by ultra-relativistic electrons*. Hyperfine Interactions, **110**, (1997), p. 239.

[123] K. Ackerstaff $et\ al.$ *Flavor decomposition of the polarized quark distributions in the nucleon from inclusive and semi-inclusive deep-inelastic scattering*. Phys. Rev. Lett., **464**, (1999), p. 123.

[124] B.E. Tipton. *Measurement of polarised parton distributions with spin-dependent deep-inelastic scattering*. PhD thesis, Massachusetts Institute of Technology, Boston, Massachusetts, USA, (1999).

[125] M. Düren, P. Geiger, N. Makins, and E. Volk. *The HERMES Monte Carlo*, (1997).

[126] R. Brun *et al.* *Geant - Detector description and simulation tool, CERN program library, Writeup W5013*, (1993).

[127] A. Gute. *Messung der polarisierten Strukturfunktion g_1^p des Protons im HERMES Experiment*. PhD thesis, Friedrich-Alexander-Univ. Erlangen-Nürnberg, Germany, (1999).

[128] I. Akushevich and N.M. Shumeiko. *Radiative effects in deep inelastic scattering of polarized leptons by polarized light nuclei*. J. Phys., **G20**, (1994), p. 513.

[129] I. Akushevich *et al.* *POLRAD 2.0 code for the radiative corrections to DIS of polarized particles*. Comp.Phys.Comm., **104**, (1997), p. 201.

[130] M. Arneodo *et al.* *Measurement of the proton and the deuteron structure functions F_2^p and F_2^d*. Phys. Lett., **B364**, (1995), p. 107.

[131] I. Akushevich, A. Ilyichev, and N.M. Shumeiko. *Radiative effects in scattering of polarized leptons by polarized nucleons and light nuclei*. In *Proc. Lepton-Photon 01*, Roma, (2001).

[132] P.L. Anthony *et al.* *Measurement of the Q^2 dependence of the proton and neutron spin structure function g_1^p and g_1^n*. Phys. Lett., **B493**, (2000), p. 19.

[133] B. Adeva *et al.* *Polarised quark distributions in the nucleon from semi-inclusive spin asymmetries*. Phys. Lett., **B420**, (1998), p. 180.

[134] K. Abe *et al.* *Measurements of the proton and deuteron spin structure functions g_1 and g_2*. Phys. Rev., **D58**, (1998), p. 112003:1.

[135] H. Ihssen *et al.* *Preliminary determination of the charged hadron asymmetries from the 1996 data*. HERMES internal note/97-050, (1997).

[136] B. Bains *et al.* *Determination of the charged hadron asymmetries from the year 1997*. HERMES internal note/99-015, (1999).

[137] U. Elschenbroich. *Bhabha-Streuung and Luminositaetsmessung in HERMES Experiment*. Diploma thesis, Heinrich Heine Univ. Duesseldorf, Germany, (2001).

[138] L. de Nardo. *Trigger efficiencies for 98 and 99 data*. HERMES internal note/01-005, (2001).

[139] F. James and M. Roos. *MINUIT, function minimization and error analysis*, (1997).

[140] G. Ingelman, A. Edin, and J. Rathsman. *LEPTO 6.5 - A Monte Carlo generator for deep-inelastic lepton nucleon scattering*. Comp. Phys. Commun., **101**, (1997), p. 108.

[141] A.D. Martin, R.G. Roberts, W.J. Stirling, and R.S. Thorne. *Parton distributions: A new global analysis*. Eur. Phys. J., **C4**, (1998), p. 463.

[142] K. Ackerstaff. *First results from the* HERMES *experiment using unpolarized targets*. PhD thesis, Hamburg Univ., Germany, (1996).

[143] K. Ackerstaff *et al.* *Flavour asymmetry of the light quark sea from semi-inclusive deep-inelastic scattering*. Phys. Rev. Lett., **81**, (1998), p. 5519.

[144] M.G. Vincter. *A determination of F_2^n/F_2^p, $d_v(x)/u_v(x)$, and $(\bar{d}(x)-\bar{u}(x))/(u(x)-d(x))$ from the 1996 HERMES unpolarized data.* HERMES internal note/97-018, (1997).

[145] B. Desplanques. *Deuteron D-state probability and energy-dependent NN interactions*. Phys. Lett., **B203**, (1988), p. 200.

[146] H. Arenhovel *et al.* *The role of electromagnetic form-factors in meson exchange currents*. Z. Phys., **A331**, (1988), p. 509.

[147] J.L. Friar *et al.* *Neutron polarization in polarized ^{3}He targets*. Phys. Rev., **C42**, (1990), p. 2310.

[148] C. Ciofi degli Atti *et al.* *Nuclear effects in DIS of polarized electrons off polarized ^{3}He and the neutron spin structure functions*. Phys. Rev., **C48**, (1993), p. 968.

[149] M. Glück, E. Reya, M. Stratmann, and W. Vogelsang. *Models for the polarized parton distributions of the nucleon*. Phys. Rev., **D63**, (2001), p. 094005.

[150] K. Ackerstaff *et al.* *Measurement of the neutron spin structure function g_1^n with a polarized ^{3}He internal target*. Phys. Lett., **B404**, (1997), p. 383.

[151] A. Airapetian *et al.* *Measurement of the proton spin structure function g_1^p with a pure hydrogen target*. Phys. Lett., **B442**, (1998), p. 484.

[152] J. Blümlein and H. Böttcher. *QCD analysis of polarized deep inelastic scattering data and parton distributions*. e-print: hep-ph/0203155, (2002).

[153] M. Glück and E. Reya. *On the determination of spin-dependent parton distributions in semi-inclusive deep inelastic scattering*. e-print: hep-ph/0203063, (2002).

[154] E. Leader, A.V. Sidorov, and D.B. Stamenov. *A new evaluation of polarized parton densities in the nucleon*. Eur. Phys. J., **C23**, (2002), p. 479.

[155] A.D. Martin, R.G. Roberts, W.J. Stirling, and R.S. Thorne. *Parton distributions and the LHC: W and Z production*. Eur. Phys. J., **C14**, (2000), p. 133.

[156] E.A. Hawker *et al.* *Measurement of the light antiquark flavor asymmetry in the nucleon sea*. Phys. Rev. Lett., **80**, (1998), p. 3715.

[157] D.I. Diakonov, V.Yu. Petrov, P.V. Pobylitsa, M.V. Polyakov, and C. Weiss. *Nucleon parton distributions at low normalization point in the large-N_c limit*. Nucl. Phys., **B480**, (1996), p. 341.

[158] B. Dressler, K. Goeke, P. Schweitzer, C. Weiss, and M.V. Polyakov. *Can we measure $\Delta\bar{u}-\Delta\bar{d}$ in semi-inclusive e-N or N-N scattering?* Prog. Part. Nucl. Phys., **44**, (2000), p. 293.

[159] C. Bourrely, J. Soffer, and F. Buccella. *A statistical approach for polarized parton distributions*. Eur. Phys. J., **C23**, (2002), p. 487.

[160] K. Goeke, P.V. Pobylitsa, M.V. Polyakov, and D. Urbano. *Polarized antiquark distributions from chiral quark-soliton model: Compilation of the results*. Nucl. Phys., **A680**, (2000), p. 307.

[161] J. Ellis and M. Karliner. *An analysis of the angular momentum of the proton*. Phys. Lett., **B213**, (1988), p. 73.

[162] M. Glück, E. Reya, and A. Vogt. *Dynamical parton distributions of the proton and small-x physics*. Z. Phys., **C67**, (1995).

[163] J. Ellis and M. Karliner. *The strange spin of the nucleon*. Phys. Lett., **B341**, (1995), p. 397.

[164] A. Airapetian $et\ al.$ *Measurement of the spin asymmetry in the photoproduction of pairs of high-p_T hadrons at HERMES*. Phys. Rev. Lett., **84**, (2000), p. 2584.

[165] M. Göckeler $et\ al.$ *Polarized and unpolarized nucleon structure functions from lattice QCD*. Phys. Rev., **D53**, (1996), p. 2317.

[166] M. Göckeler $et\ al.$ *A lattice determination of the second moment of the polarised valence quark distribution*. Phys. Lett., **B414**, (1997), p. 340.

[167] D. Dolgov $et\ al.$ *Moments of nucleon light cone quark distributions calculated in full lattice QCD*. e-print: hep-lat/0201021, (2002).

[168] W. Negele. *Understanding parton distributions from lattice QCD: present limitations and future promise*. In *Proc. Conf. QCD-N'02*, Ferrara, Italy, (2002).

[169] M.A. Funk. *A measurement of the polarised parton densities of the nucleon in deep-inelastic scattering at HERMES* . PhD thesis, Hamburg Univ., Germany, (1998).